Development of a tissue-engineered primary human skin infection model to study the pathogenesis of tsetse fly-transmitted African trypanosomes in mammalian skin

Entwicklung eines primären humanen Hautinfektionsmodells basierend auf Gewebezüchtung zur Erforschung der Pathogenese von Tsetsefliegen-übertragenen Afrikanischen Trypanosomen in der Säugetierhaut

Dissertation

for a doctoral degree (Dr. rer. nat.)

at the *Graduate School of Life Sciences*,

Julius-Maximilians-Universität Würzburg

Section: Infection and Immunity

submitted by

Christian Steffen Reuter

from

Plauen

Würzburg, 2021

Submitted on:

Members of the Thesis Committee:

Chair Person:	Prof. Dr. Markus Sauer Lehrstuhl für Biotechnologie und Biophysik, Julius-Maximilians-Universität Würzburg
Primary Supervisor:	Prof. Dr. Markus Engstler Lehrstuhl für Zell- und Entwicklungsbiologie, Julius-Maximilians-Universität Würzburg
Supervisor (second):	Prof. Dr. Heike Walles Forschungszentrum Dynamische Systeme (CDS), Otto von Guericke Universität Magdeburg
Supervisor (third):	Dr. Florian Groeber-Becker Translationszentrum Regenerative Therapien (TLC-RT), Fraunhofer ISC Würzburg

Date of Public Defense:

Date of Receipt of Certificate:

Affidavit/Eidesstattliche Erklärung

I hereby confirm that my thesis entitled “Development of a tissue-engineered primary human skin infection model to study the pathogenesis of tsetse fly-transmitted African trypanosomes in mammalian skin” is the result of my own work. I did not receive any help or support from commercial consultants. All sources and/or materials applied are listed and specified in the thesis.

Furthermore, I confirm that this thesis has not yet been submitted as part of another examination process neither in identical nor in similar form.

Würzburg, _____

Christian Reuter

Ich erkläre hiermit an Eides statt, dass ich die vorliegende Dissertation „Entwicklung eines primären humanen Hautinfektionsmodells basierend auf Gewebezüchtung zur Erforschung der Pathogenese von Tsetsefliegen-übertragenen Afrikanischen Trypanosomen in der Säugetierhaut“ eigenständig, d.h. insbesondere ohne die Hilfe oder Unterstützung von kommerziellen Promotionsberatern, angefertigt habe. Ergänzend bestätige ich, dass ich keine anderen als die von mir angegebenen Quellen oder Hilfsmittel verwendet habe.

Ich erkläre außerdem, dass diese Dissertation weder in gleicher noch in ähnlicher Form bereits in einem Prüfungsverfahren vorgelegen hat.

Würzburg, _____

Christian Reuter

Summary

Many arthropods such as mosquitoes, ticks, bugs, and flies are vectors for the transmission of pathogenic parasites, bacteria, and viruses. Among these, the unicellular parasite *Trypanosoma brucei* (*T. brucei*) causes human and animal African trypanosomiases and is transmitted to the vertebrate host by the tsetse fly. In the fly, the parasite goes through a complex developmental cycle in the alimentary tract and salivary glands ending with the cellular differentiation into the metacyclic life cycle stage. An infection in the mammalian host begins when the fly takes a bloodmeal, thereby depositing the metacyclic form into the dermal skin layer. Within the dermis, the cell cycle-arrested metacyclic forms are activated, re-enter the cell cycle, and differentiate into proliferative trypanosomes, prior to dissemination throughout the host.

Although *T. brucei* has been studied for decades, very little is known about the early events in the skin prior to systemic dissemination. The precise timing and the mechanisms controlling differentiation of the parasite in the skin continue to be elusive, as does the characterization of the proliferative skin-residing trypanosomes. Understanding the first steps of an infection is crucial for developing novel strategies to prevent disease establishment and its progression.

A major shortcoming in the study of human African trypanosomiasis is the lack of suitable infection models that authentically mimic disease progression. In addition, the production of infectious metacyclic parasites requires tsetse flies, which are challenging to keep. Thus, although animal models - typically murine - have produced many insights into the pathogenicity of trypanosomes in the mammalian host, they were usually infected by needle injection into the peritoneal cavity or tail vein, bypassing the skin as the first entry point. Furthermore, animal models are not always predictive for the infection outcome in human patients. In addition, the relatively small number of metacyclic parasites deposited by the tsetse flies makes them difficult to trace, isolate, and study in animal hosts.

The focus of this thesis was to develop and validate a reconstructed human skin equivalent as an infection model to study the development of naturally-transmitted metacyclic parasites of *T. brucei* in mammalian skin. The first part of this work describes the development and characterization of a primary human skin equivalent with improved mechanical properties. To achieve this, a computer-assisted compression system was

designed and established. This system allowed the improvement of the mechanical stability of twelve collagen-based dermal equivalents in parallel through plastic compression, as evaluated by rheology. The improved dermal equivalents provided the basis for the generation of the skin equivalents and reduced their contraction and weight loss during tissue formation, achieving a high degree of standardization and reproducibility. The skin equivalents were characterized using immunohistochemical and histological techniques and recapitulated key anatomical, cellular, and functional aspects of native human skin. Furthermore, their cellular heterogeneity was examined using single-cell RNA sequencing - an approach which led to the identification of a remarkable repertoire of extracellular matrix-associated genes expressed by different cell subpopulations in the artificial skin. In addition, experimental conditions were established to allow tsetse flies to naturally infect the skin equivalents with trypanosomes.

In the second part of the project, the development of the trypanosomes in the artificial skin was investigated in detail. This included the establishment of methods to successfully isolate skin-dwelling trypanosomes to determine their protein synthesis rate, cell cycle and metabolic status, morphology, and transcriptome. Microscopy techniques to study trypanosome motility and migration in the skin were also optimized. Upon deposition in the artificial skin by feeding tsetse, the metacyclic parasites were rapidly activated and established a proliferative population within one day. This process was accompanied by: (I) reactivation of protein synthesis; (II) re-entry into the cell cycle; (III) change in morphology; (IV) increased motility. Furthermore, these observations were linked to potentially underlying developmental mechanisms by applying single-cell parasite RNA sequencing at five different timepoints post-infection.

After the initial proliferative phase, the tsetse-transmitted trypanosomes appeared to enter a reversible quiescence program in the skin. These quiescent skin-residing trypanosomes were characterized by very slow replication, a strongly reduced metabolism, and a transcriptome markedly different from that of the deposited metacyclic forms and the early proliferative trypanosomes. By mimicking the migration from the skin to the bloodstream, the quiescent phenotype could be reversed and the parasites returned to an active proliferating state. Given that previous work has identified the skin as an anatomical reservoir for *T. brucei* during disease, it is reasonable to assume that the quiescence program is an authentic facet of the parasite's behavior in an infected host.

In summary, this work demonstrates that primary human skin equivalents offer a new and promising way to study vector-borne parasites under close-to-natural conditions as an alternative to animal experimentation. By choosing the natural transmission route - the bite of an infected tsetse fly - the early events of trypanosome infection have been detailed with unprecedented resolution. In addition, the evidence here for a quiescent, skin-residing trypanosome population may explain the persistence of *T. brucei* in the skin of aparasitemic and asymptomatic individuals. This could play an important role in maintaining an infection over long time periods.

Zusammenfassung

Zahlreiche Arthropoden wie Stechmücken, Zecken, Wanzen und Fliegen sind Überträger für krankheitserregende Parasiten, Bakterien und Viren. Hierzu gehört der einzellige Parasit *Trypanosoma brucei* (*T. brucei*), welcher durch Tsetsefliegen übertragen wird und die Afrikanische Trypanosomiasis bei Menschen und Tieren verursacht. Der Entwicklungszyklus des Parasiten in der Fliege ist komplex und endet in der Speicheldrüse mit der Differenzierung in das metazyklische Lebensstadium. Diese metazyklischen Formen werden durch den Biss der blutsaugenden Tsetsefliege in die dermale Hautschicht des Säugetierwirts injiziert. Die zellzyklusarretierten metazyklischen Formen werden in der Dermis aktiviert und der Widereintritt in den Zellzyklus sowie die Differenzierung zu proliferativen Trypanosomen eingeleitet. Anschließend breitet sich der Parasit systemisch im Säugetierwirt aus.

Obwohl *T. brucei* bereits seit Jahrzehnten erforscht wird, ist nur sehr wenig über das frühe Infektionsgeschehen in der Haut bekannt. Der genaue Zeitpunkt und die Mechanismen, die der Differenzierung des Parasiten in der Haut zugrunde liegen, sind unbekannt. Ebenso wurden die proliferativen Trypanosomen in der Haut bisher nur unzureichend charakterisiert. Das Verständnis über die ersten Schritte einer Infektion ist jedoch von entscheidender Bedeutung für die Entwicklung von neuen Strategien, die die Krankheitsentstehung und deren Fortschreiten verhindern sollen.

Ein großes Hindernis bei der Erforschung der humanen Afrikanischen Trypanosomiasis ist der Mangel an geeigneten Infektionsmodellen, die den Krankheitsverlauf authentisch nachbilden. Außerdem werden für die Erzeugung der infektiösen metazyklischen Parasiten Tsetsefliegen benötigt, die aufwändig zu züchten sind. Tiermodelle haben es ermöglicht - hauptsächlich Mäuse -, viele Erkenntnisse über die Pathogenese von Trypanosomen im Säugetierwirt zu erlangen. Allerdings wurden diese überwiegend durch Nadelinjektion in den Bauchraum oder die Kaudalvene infiziert, wodurch die Haut als erste Eintrittspforte umgangen wurde. Darüber hinaus lassen Tiermodelle nicht immer Rückschlüsse auf den Infektionsverlauf beim Menschen zu. Zusätzlich erschwert die geringe Anzahl von metazyklischen Parasiten, die von Tsetsefliegen injiziert werden, die Isolation, Nachweis und Untersuchung im tierischen Wirt.

Das Ziel der vorliegenden Arbeit war es, ein rekonstruiertes menschliches Hautäquivalent zu entwickeln und als Infektionsmodell zu validieren, um die Entwicklung von natürlich übertragenen metazyklischen Parasiten von *T. brucei* in der Säugetierhaut zu untersuchen. Der erste Teil dieser Arbeit beschreibt die Entwicklung und Charakterisierung eines primären menschlichen Hautäquivalents mit verbesserten mechanischen Eigenschaften. Zu diesem Zweck wurde ein computergesteuertes Kompressionssystem entworfen und hergestellt. Dieses System ermöglichte die gleichzeitige Verbesserung der mechanischen Stabilität von zwölf kollagenbasierten dermalen Äquivalenten durch plastische Kompression, die mittels Rheologie evaluiert wurden. Die verbesserten dermalen Äquivalente dienten als Fundament für die Erzeugung der Hautäquivalente und reduzierten deren Kontraktion und Gewichtsverlust während der Gewebebildung. Dadurch wurde ein hohes Maß an Standardisierung und Reproduzierbarkeit erreicht. Die Hautäquivalente wurden durch immunhistochemische und histologische Techniken charakterisiert und bildeten wichtige anatomische, zelluläre und funktionelle Aspekte der nativen menschlichen Haut nach. Des Weiteren wurde die zelluläre Heterogenität durch Einzelzell-RNA-Sequenzierung untersucht. Mit dieser Technik wurde ein umfangreiches Spektrum an extrazellulären Matrix-assoziierten Genen identifiziert, die von verschiedenen Zellsubpopulationen in der künstlichen Haut exprimiert werden. Zusätzlich wurden experimentelle Bedingungen etabliert, damit Tsetsefliegen eingesetzt werden konnten, um die Hautäquivalente auf natürlichem Weg mit Trypanosomen zu infizieren.

Im zweiten Teil dieser Arbeit wurde die Entwicklung der Trypanosomen in der künstlichen Haut im Detail untersucht. Dies umfasste die Etablierung von Methoden zur erfolgreichen Isolierung der Trypanosomen aus der Haut, um deren Proteinsyntheserate, Zellzyklus- und Stoffwechselstatus, sowie Morphologie und Transkriptom zu bestimmen. Zusätzlich wurden Mikroskopietechniken zur Untersuchung der Trypanosomenmotilität und -migration in der Haut optimiert. Nach der Injektion in die künstliche Haut durch Tsetsefliegen wurden die metazyklischen Parasiten schnell aktiviert und etablierten innerhalb eines Tages eine proliferative Population. Dieser Entwicklungsprozess wurde begleitet von (I) einer Reaktivierung der Proteinsynthese, (II) einem Wiedereintritt in den Zellzyklus, (III) einer Veränderung der Morphologie und (IV) einer erhöhten Motilität. Des Weiteren wurden diese Beobachtungen mit potentiell zugrundeliegenden entwicklungsbiologischen Mechanismen in Verbindung gebracht, indem eine

Einzelzell-RNA-Sequenzierung der Trypanosomen zu fünf verschiedenen Zeitpunkten nach der Infektion durchgeführt wurde.

Nach der ersten proliferativen Phase traten die Tsetse-übertragenen Trypanosomen in der Haut in ein reversibles Ruhestadium ein. Diese ruhenden Trypanosomen waren durch eine sehr langsame Zellteilung, einen stark reduzierten Stoffwechsel und ein Transkriptom gekennzeichnet, dass sich deutlich von dem der injizierten metazyklischen Formen und der ersten proliferativen Trypanosomen unterschied. Durch Nachahmung der Migration von der Haut in den Blutkreislauf konnte dieser Phänotyp reaktiviert werden und die Parasiten kehrten in einen aktiven, proliferierenden Zustand zurück. Unter Berücksichtigung, dass vorangegangene Forschungsarbeiten die Haut als anatomisches Reservoir für *T. brucei* während des Krankheitsverlaufs identifiziert haben, ist anzunehmen, dass das Ruheprogramm eine authentische Facette im Verhalten des Parasiten in einem infizierten Wirt darstellt.

Zusammenfassend zeigt diese Arbeit, das primäre menschliche Hautäquivalente eine neue und vielversprechende Möglichkeit bieten, vektorübertragene Parasiten unter naturnahen Bedingungen als Alternative zu Tierversuchen zu untersuchen. Durch die Verwendung des natürlichen Infektionsweges - dem Biss einer infizierten Tsetsefliege -, konnten die frühen Prozesse einer Trypanosomen-Infektion mit noch nie dagewesener Detailtiefe nachvollzogen werden. Des Weiteren könnte der hier erbrachte Nachweis einer ruhenden, hautresidenten Trypanosomen-Population die Persistenz von *T. brucei* in der Haut von aparasitämischen und asymptomatischen Personen erklären. Dies könnte eine wichtige Rolle bei der Aufrechterhaltung einer Infektion über lange Zeiträume spielen.

Table of contents

Affidavit/Eidesstattliche Erklärung ..... **v**

Summary ..... **vii**

Zusammenfassung ..... **x**

Abbreviation index ..... **xvi**

Contribution by others ..... **xix**

I. Biological background **1**

1.1 Anatomy and organization of human skin 1

1.1.1 Epidermis 2

1.1.2 Dermis 5

1.1.3 Hypodermis 6

1.2 Arthropod-borne parasitic infections and the skin interface 7

1.3 African trypanosomes and diseases 9

1.3.1 Cell architecture and cell cycle 10

1.3.2 Genome organization and regulation of gene expression 12

1.3.3 The life cycle of *T. brucei* 14

1.3.3.1 Development in the insect vector 14

1.3.3.2 Development in the mammalian host 17

1.4 The role of mammalian skin in trypanosomiasis 19

1.4.1 Early parasitological features in the mammalian host 20

1.4.2 Early host response in the skin 21

1.4.3 The skin as a reservoir tissue for trypanosomes 23

1.5 Skin tissue engineering 24

1.6 Aim of the study 27

II. Development and adaptation of a standardized primary human skin equivalent with increased mechanical properties to study the pathogenesis of *Trypanosoma brucei* **29**

2.1 Development of a computer-assisted compression system 30

2.2 Plastic compression improves mechanical properties and reduces dermal contraction and weight loss in high-density skin equivalents 33

2.3 Set-up of infection parameters for co-cultivation of *T. brucei* parasites and high-density skin equivalents 36

2.4 High-density primary human skin equivalents resemble native human skin in its histological architecture as well as in the development of distinctive physiological parameters 39

2.4.1 Histological comparison between the high-density skin equivalent and native human skin 39

2.4.2 Single-cell RNA sequencing details the cellular heterogeneity of the high-density skin equivalent 41

2.4.3 Integration of endothelial cells allows endothelialization of the high-density skin equivalent 47

2.5 Elaboration of an optimized protocol for the generation of high-density skin equivalents and subsequent infection with trypanosomes by tsetse flies 48

III. Development of tsetse fly-transmitted *T. brucei* parasites in the high-density primary human skin equivalent 51

3.1 Simulation of natural vector transmission by using tsetse flies to infect skin equivalents with *T. brucei* 51

3.2 Tsetse-borne *T. brucei* parasites infect the skin equivalent 58

3.3 Metacyclic parasites rapidly differentiate into proliferative trypanosomes in the skin equivalent 61

3.4 Single-parasite RNA sequencing reveals the programmed activation of metacyclic forms in the skin equivalent 64

3.5 Analysis of trypanosome migration and motility in the dermis 73

3.6 Skin-dwelling parasites successfully infect tsetse flies and complete their natural mammalian developmental program in the skin equivalent 75

3.7 *T. brucei* enters a reversible quiescence program in the skin equivalent 77

3.7.1 Skin-dwelling parasites reduce their protein synthesis and metabolism 78

3.7.2 The quiescent state in the skin is characterized by a unique gene expression profile 82

3.7.3 The skin microenvironment influences the behavior of trypanosomes 86

IV. Discussion and outlook 91

4.1 The high-density primary human skin equivalent is a versatile and accessible model to study the pathogenesis of *T. brucei* in mammalian skin 92

4.2 Early parasitological features of tsetse-transmitted *T. brucei* parasites in the high-density skin equivalent 97
4.3 Tsetse-transmitted *T. brucei* parasites adapt to the tissue-engineered skin environment as quiescent skin tissue forms 106
4.4 Outlook and perspectives 113
V. Materials and methods 115
5.1 Materials 115
5.1.1 Media, buffers, and solutions 115
5.1.3 Enzymes and enzyme buffers 118
5.1.4 Instruments and devices 119
5.1.5 Labware and consumables 121
5.1.6 Antibodies and dyes 122
5.1.7 Oligonucleotides 123
5.1.8 Commercial kits 124
5.1.9 Organisms 124
5.1.10 Software 126
5.2 Methods 128
5.2.1 Working with *Trypanosoma brucei* 128
5.2.2 Working with tsetse flies 130
5.2.3 Working with primary human cells 132
5.2.4 Working with the high-density skin equivalent 136
5.2.5 Working with *E. coli* 153
5.2.6 Molecular biological methods 154
VI. References 157
VII. Annex 175
7.1 List of Figures 175
7.2 List of tables 177
7.3 List of movies 178
7.4 List of supplementary spreadsheets 178
VIII. Curriculum vitae 179
IX. List of Publications 181
X. Acknowledgment 183

Abbreviation index

3D	three-dimensional
AAT	animal African trypanosomiasis
AnTat	Antwerp Institut Trypanozoon Antigen Typ
BABB	benzyl alcohol/benzyl benzoate
Blas	blasticidin
BSA	bovine serum albumin
BSF	bloodstream form
B-VSG	bloodstream form VSG
$CaCl_2$	calcium chloride
CDS	coding sequence
$CHCl_3$	chloroform
CO_2	carbon dioxide
DAPI	4',6-Diamidine-2'-phenylindole dihydrochloride
ddH_2O	double-distilled water
DMEM	Dulbecco's Modified Eagle Medium
DMSO	dimethyl sulfoxide
DNA	deoxyribonucleic acid
dNTPs	deoxynucleoside triphosphates
DPBS	Dulbecco's Phosphate-Buffered Saline
dpi	days post-infection
ECM	extracellular matrix
E. coli	*Escherichia coli*
EDTA	ethylenediaminetetraacetic acid
e.g.	exempli gratia (engl. for example)
EtOH	ethanol
FACS	fluorescence-activated cell sorting
FCS	fetal calf serum
fps	frames per second
gDNA	genomic DNA
GFP	green fluorescent protein
H_2O	water

HAT	human African trypanosomiasis
H&E	hematoxylin and eosin
HEPES	4-(2-hydroxyethyl)-1-piperazineethanesulfonic acid
HMI9	Hirumi's modified Iscove's medium 9
HMI9-MC	HMI9-methylcellulose
hpi	hours post-infection
Hygro	hygromycin
IHC	immunohistochemical
KCl	potassium chloride
KRT	cytokeratin
LB	Luria-Bertani
LSFM	light sheet fluorescence microscopy
MCF	metacyclic form
MEM	Minimal Essential Medium
MeOH	methanol
$MgCl_2$	magnesium chloride
M-VSG	metacyclic VSG
N_2	nitrogen
NaCl	sodium chloride
NaOH	sodium hydroxide
NEAA	non-essential amino acids
NLS	nuclear localization signal
O_2	oxygen
ORF	open reading frame
PAD1	protein associated with differentiation 1
PBS	phosphate-buffered saline
PCF	procyclic form
PCR	polymerase chain reaction
PFA	paraformaldehyde
Puro	puromycin
RNA	ribonucleic acid
RT	room temperature
SD	standard deviation
SG	salivary glands

SIF	stumpy induction factor
T. brucei	*Trypanosoma brucei*
TDB	trypanosome dilution buffer
tdT	tandem-dimer Tomato
UTR	untranslated region
vs.	versus
VSG	variant surface glycoprotein
WT	wildtype

Units

%	percent
°C	degree Celsius
bp	base pair
g	gram / g-force
h	hour
l	liter
M	molar
m	meter
min	minute
nt	nucleotide
pH	minus the decimal logarithm of the hydrogen concentration
rpm	rounds per minute
s/sec	second

Multiples

M	mega (10^6)
k	kilo (10^3)
m	milli (10^{-3})
µ	micro (10^{-6})
n	nano (10^{-9})
p	pico (10^{-12})

Contribution by others

The work described in this PhD thesis was conducted under supervision of Prof. Dr. Markus Engstler, Chair of Cell and Developmental Biology, Julius-Maximilians-University of Würzburg, Germany. Parts of the here described work that have been conducted in collaboration with others, are indicated below.

- The computer-assisted compression system for the generation of high-density skin equivalents was developed under the supervision of Dr. Florian Groeber-Becker at the Translational Center for Regenerative Therapies (TLC-RT), Fraunhofer ISC, Würzburg, Germany.

- Single-cell RNA sequencing libraries of high-density skin equivalents and trypanosomes were prepared with the support of Fabian Imdahl under the supervision of Dr. Antoine-Emmanuel Saliba at the Helmholtz Institute for RNA-based Infection Research (HIRI), Würzburg, Germany.

- Bioinformatic processing and analysis of single-cell RNA sequencing data of high-density skin equivalents and trypanosomes was performed with the support of Ehsan Vafadarnejad under the supervision of Dr. Antoine-Emmanuel Saliba at the Helmholtz Institute for RNA-based Infection Research (HIRI), Würzburg, Germany.

- Lightsheet fluorescence microscopy images were taken with the support of Sina Thusek under the supervision of Prof. Dr. Andreas Beilhack, Department of Medicine II, University Hospital Würzburg, Würzburg, Germany.

I. Biological background

The skin is the largest organ of the human body and serves as a protective barrier at the interface between the body and its environment. Due to its exposed position, the skin is the first site of contact for potentially harmful biological, physical, and chemical threats. Thus, the skin has developed multiple mechanisms to protect itself against pathogens, radiation, heat, and many other stress factors every day.

For the vast majority of pathogenic microorganisms, such as viruses, bacteria or unicellular parasites, it is virtually impossible to overcome the barrier formed by healthy and intact human skin. Therefore, pathogens must find another way into the human body, for example via the respiratory or digestive tract. For many diseases, the pathogens make also use of blood-sucking arthropods to overcome the skin barrier and enter the human body. This applies to several unicellular parasites of the genus *Plasmodium*, *Leishmania*, and *Trypanosoma*.

These pathogens use a variety of virulence strategies to interact with their host, survive, and cause disease. Very often, *e.g.* in the case of *Trypanosoma brucei*, the underlying molecular mechanisms remain largely unknown, not the least due to the lack of suitable infection models.

The following chapter is intended to provide a general overview of the anatomy and physiology of human skin and the strategies of protozoan parasites to colonize a new host via the skin route, with special emphasis on *Trypanosoma brucei*.

1.1 Anatomy and organization of human skin

The skin has a surface area of approximate 2 m^2 and accounts for about 16 % of the body weight (Hadgraft, 2001, Bensouilah and Buck, 2006). Including all skin appendages such as hair follicles and sweat glands the total size is considered to be 25 - 26 m^2 (Gallo, 2017). Depending on the body region the skin can reach a thickness of 1 - 4 mm (Tur, 1997). Due to its direct exposure to the surrounding environment, it is one of the most strained organs and has developed multiple mechanisms to protect itself and the human body. This is reflected in the unique architecture of the skin with many different specialized skin layers and cell types. Together, they create a robust and protective barrier against harmful substances or microbes, while still providing great elasticity. The human

skin consists of three distinct layers: the epidermis, the dermis, and the hypodermis (Figure 1).

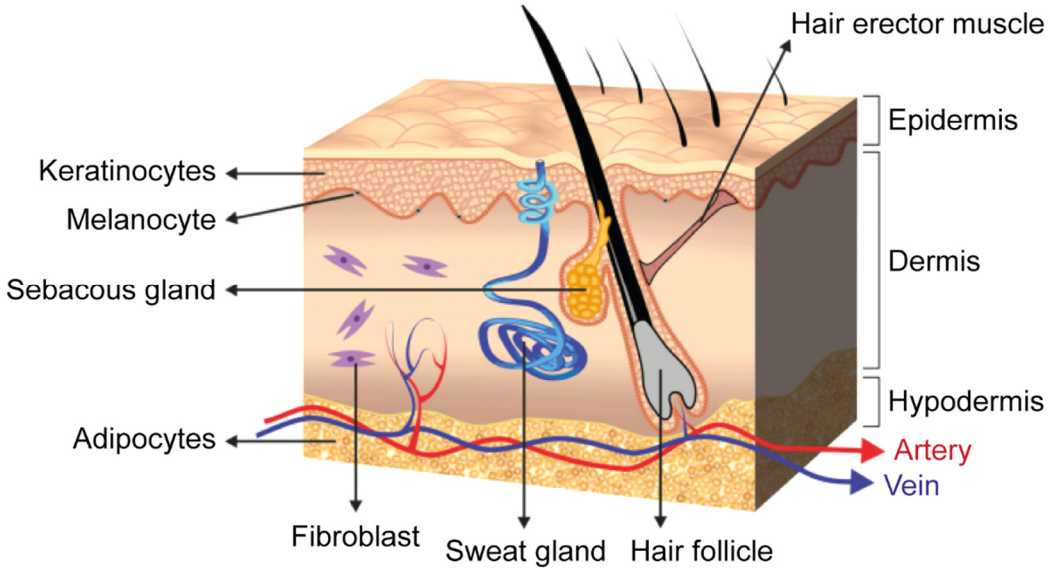

Figure 1: Anatomical properties of the human skin. Schematic representation illustrating the main cell types and structures of human skin, which is composed of three primary layers: the epidermis, the dermis, and the hypodermis. The epidermis consists mainly of keratinocytes and provides most of the barrier function of the skin. The dermis is mainly populated by fibroblasts and consists mainly of collagen, elastic, and reticular fibers embedded in an amorphous ground substance. Many skin appendages such as hair follicles, sweat glands, and sebaceous glands are located in the dermis. The hypodermis is characterized by a thick layer of white adipocytes, also known as dermal white adipose tissue. Adapted from (Goodarzi et al., 2018).

1.1.1 Epidermis

The epidermis is the outer layer of the skin and contains a complex, three-dimensional epithelium that has evolved to perform several essential protective functions. These include preventing water loss, defending against toxins, resisting mechanical stress, and participating in immune responses. This barrier consists mainly of epidermal keratinocytes, but melanocytes, lymphocytes, Langerhans cells, and Merkel cells are also present. The dominating keratinocytes are organized in multiple layers ("strata"), building an adhesive interconnected system to establish a functional barrier: the *stratum basale*, *stratum spinosum*, *stratum granulosum*, and the *stratum corneum* (Figure 2). These layers contain specific cytoskeletal and cell-cell connections such as tight junctions, gap junctions, actin-associated adherens junctions, desmosomes, and the junctional components (mainly keratin, desmogleins, and cadherins) essential for immune surveillance and epidermal barrier function (Simpson et al., 2011).

Keratinocytes in the *stratum basale* undergo a terminal differentiation and migrate outwards to replace cells that are shed from the body surface (Fuchs and Raghavan, 2002). While basal cells of the *stratum basale* remain attached to the basement membrane and proliferate, some of their daughter cells enter the *stratum spinosum* through asymmetric division. In the *stratum spinosum* they exit the cell cycle, grow larger, and establish robust intercellular connections. Keratinocytes in the *stratum granulosum* flatten and assemble a water-impermeable cornified envelope. Finally, keratinocytes of the *stratum corneum* release lysosomal enzymes to degrade major cell organelles. They become metabolically inactive and completely squamous, and are tightly crosslinked together to complete the cutaneous barrier (Candi et al., 2005). In an average adult, the epidermis is continually renewed every 52 - 75 days from keratinocytes in the *stratum basale* (Halprin, 1972).

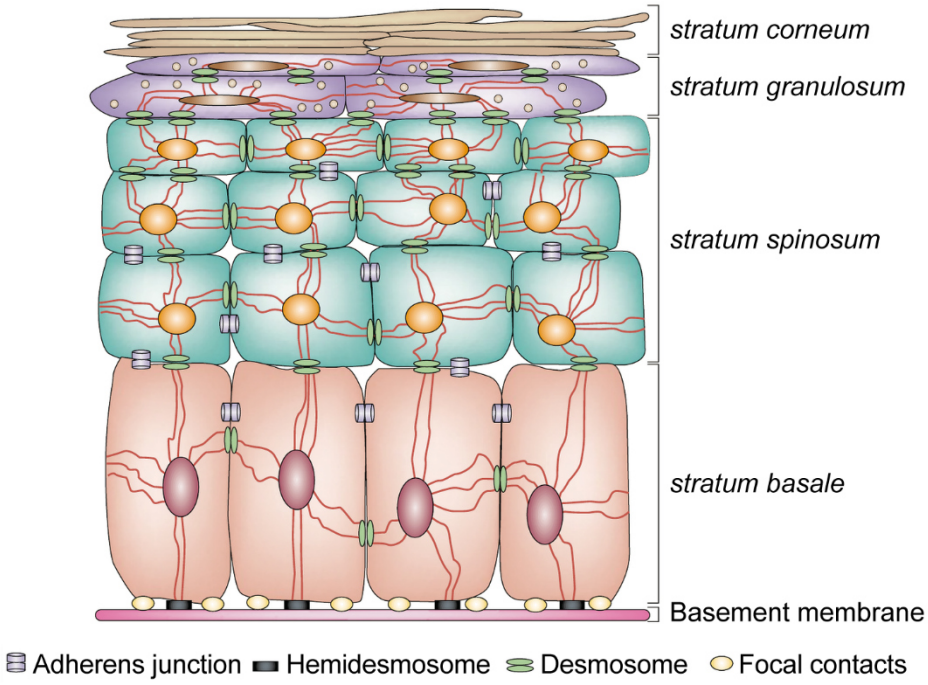

Figure 2: Microarchitecture of the human epidermis. The epidermis is a self-renewing tissue composed mainly of keratinocytes in various stages of terminal differentiation. The basic layers from the basement membrane outward are the *stratum basale*, *stratum spinosum*, *stratum granulosum*, and the *stratum corneum*. Keratinocyte stem cells in the *stratum basale* are attached to the basement membrane by hemidesmosomes and focal adhesions. Through asymmetric division, their daughter cells move outwards through the epidermis and undergo terminal differentiation involving enucleation and the accumulation of keratins, desmosomes, and adherens junctions. Adapted from (Fuchs and Raghavan, 2002).

During terminal differentiation, adherens junctions and desmosomes are first assembled between basal keratinocytes. Throughout the epidermis, the assembly and organization of the cortical actin cytoskeleton is coordinated by adherens junctions by coupling intercellular adhesion to the cytoskeleton. This transcellular network functions as a signal platform to coordinate cell behavior, polarity, division, growth, apoptosis, and barrier function (Niessen and Gottardi, 2008). Desmosomes strengthen the epidermis by connecting the keratin intermediate filaments of neighboring keratinocytes and are important for regulating adhesion and signaling in healthy skin. In the *stratum corneum*, desmosomes are modified into structures called corneodesmosomes, which are crucial for proper barrier formation (Johnson et al., 2014). The expression of different keratin intermediate filaments is thought to fulfil specific and essential cytoskeletal functions during epidermal differentiation. In humans the keratin gene family consists of 54 distinct functional genes and their expression is highly cell type-specific. In the undifferentiated basal cell layer containing the keratinocyte stem cells, the keratins 5 and 14 are strongly expressed and are downregulated in the differentiating suprabasal cell layers. The keratins 1 and 10, however, are highly expressed in spinous and granular layers. The importance of these keratin pairs for epidermal integrity is underscored by the recognition that mutations in these keratin genes cause the blistering skin diseases epidermolysis bullosa simplex and epidermolytic hyperkeratosis, also known as bullous congenital ichthyosiform erythroderma (Moll et al., 2008).

The epidermis is anchored to the underlying dermis via the basement membrane mainly by hemidesmosomes and focal contacts, which are strongly expressed in keratinocytes of the *stratum basale*. Hemidesmosomes are highly specialized integrin-mediated epithelial attachment structures that make keratinocytes firmly adhere to the extracellular matrix by establishing a link between the underlying basement membrane and the intracellular keratin intermediate filament network. Each hemidesmosome consists of five core proteins, namely COL17A1, DST, ITGA6, ITGB4, and PLEC. COL17A1 and the two integrins ITGA6 and ITGB4 interact with Laminin-332, a heterotrimer composed of LAMA3, LAMB3, and LAMC2, in the basement membrane. The indirect linkage with the keratin network is mediated via PLEC and DST. In contrast, focal contacts are integrin-based adhesions that mediate a link between actin filaments and various matrix ligands including fibronectin, collagen, and laminins of the basement membrane. Moreover, different integrin heterodimers, such as ITGA3 and ITGB1, have been

identified. Keratinocytes of the *stratum basale* can secrete components, including collagen IV and laminin-332, to help establish and organize the basement membrane and are inherently polarized as their lower surface is anchored to the basement membrane (Tsuruta et al., 2011).

1.1.2 Dermis

The dermis is a network of dense irregular connective tissues and extends from the basement membrane to the hypodermis (Figure 3). The matrix of this connective tissue consists of collagen, elastic, and reticular fibers embedded in an amorphous ground substance of mucopolysaccharides. The collagen and elastic fibers are highly entangled and form a viscoelastic, three-dimensional scaffold that provides physical support for nerves, vascular structures, and lymphatics. Collagens are the most abundant proteins of the skin dermis, accounting for 70 - 80 % of the dry weight, and are synthesized by the main cell type of the dermis, the fibroblasts (Brinckmann et al., 1994).

Based on its architecture and function, the dermis can be divided into the papillary layer, which is closest to the epidermis, and the underlying reticular layer. Fibroblasts located in the papillary or reticular layer exhibit different functions. It has been shown that papillary fibroblasts are necessary for the formation of hair follicles (Rognoni et al., 2016). The majority of extracellular matrix proteins are produced by reticular fibroblasts, which also constitute the first wave of migration to the wound bed after skin injury (Driskell et al., 2013). Single-cell RNA sequencing revealed at least four distinct subpopulations of dermal fibroblasts (Philippeos et al., 2018), however, the functional relevance of these subtypes is not fully understood.

The upper papillary layer is thin and consists of a loose connective tissue network of collagen and elastic fibers surrounding a large number of nerves, capillaries, water, and cells. The papillary dermis can protrude into the epidermis to form the finger-like projections called dermal papillae that create unique fingerprints in humans. The reticular layer is much thicker and constitutes an irregular, dense connective tissue with fewer cells and more fibers, which is the main source of skin strength and flexibility (Watt, 2014).

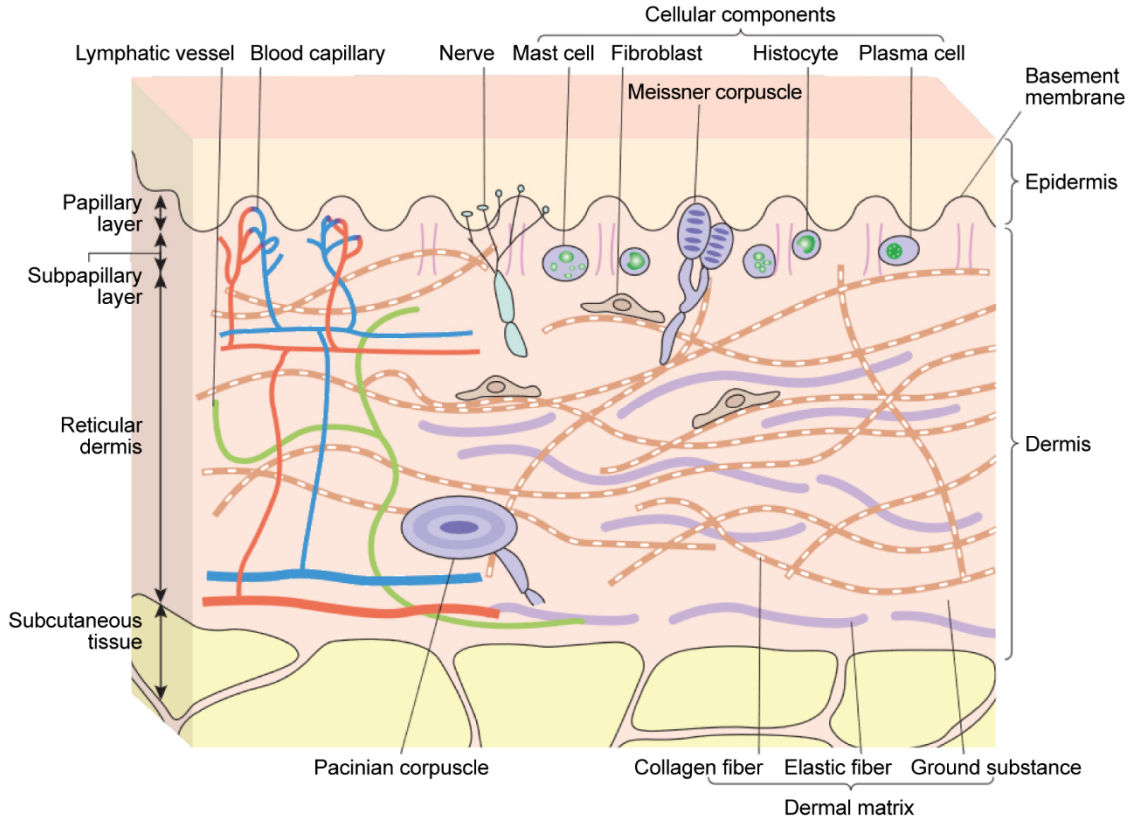

Figure 3: Architecture of the human dermis. The dermis primarily consists of dense irregular connective tissue and extends from the basement membrane to the hypodermis. It is mainly populated by fibroblasts that synthesize collagens, elastic, and reticular fibers, and the amorphous ground substance that forms the extracellular matrix. The dermis incorporates hair follicles, different types of glands, small blood vessels, lymphatics, and nerves. It is divided into two layers, the superficial area adjacent to the epidermis called the papillary layer and a deep thicker area known as the reticular dermis. Fibroblast density is higher in papillary dermis, and the reticular dermis is characterized by an abundance of fibrillar collagen. Adapted from (http://www.derm-hokudai.jp/shimizu-dermatology/pdf/01-05.pdf) (access in Mar 2021).

1.1.3 Hypodermis

The deepest dermal layer, historically termed the hypodermis, is characterized by a thick layer of white adipocytes, also known as dermal white adipose tissue. The adipocytes in the hypodermis are separated by a rich network of vasculature and collagen type I fibers (Driskell et al., 2014). Its thickness varies greatly and depends on body site, age, and gender. The function of the hypodermis is to prevent heat loss, store energy, provide a physical barrier, and to support growth and repair of the skin (Alexander et al., 2015). Dermal white adipose tissue was also recognized to support innate immunity of the skin and an increase in proliferation of adipocytes has been found in response to bacterial infection (Chen et al., 2019, Zhang et al., 2015).

1.2 Arthropod-borne parasitic infections and the skin interface

Many arthropods such as mosquitoes, ticks, bugs, sandflies, and blackflies are vectors for the transmission of parasites, bacteria, and viruses that are pathogenic in mammals but are not harmful to the vector. Among arthropod-borne diseases, infections induced by protozoan parasites have a devastating socio-economic impact in endemic countries and occupy a significant place in public health. The unicellular eukaryotic parasites depend on their vector for transmission and consequently their prevalence is limited to the distribution of their arthropod vector (Table 1). Most parasitic diseases caused by protozoans are neglected, particularly those associated with poverty and tropical countries. Thus, it is not surprising that drugs, vaccines, surveillance, and control measurements are lacking for most of these diseases and disease control remains problematic (Ghorbani and Farhoudi, 2018, Wilson et al., 2019, De Koning, 2020).

Table 1: Human diseases caused by arthropod-borne protozoan parasites. The most important parasitic protozoa, their insect vectors for disease transmission, and their geographical distribution are shown.

Disease	Protozoan parasite	Insect vector	Distribution
Malaria	*Plasmodium falciparum* *Plasmodium vivax* *Plasmodium ovale* *Plasmodium malariae*	Female mosquito (*Anopheles*)	Worldwide in tropics and subtropics
Leishmaniasis, visceral	*Leishmania donovani*	Sand fly (*Phlebotomus*)	India, China, Africa
Leishmaniasis, cutaneous	*Leishmania major*	Sand fly (*Phlebotomus*)	Africa, Middle East, Central Asia
	Leishmania tropica	Sand fly (*Phlebotomus*)	Africa, Middle East, Central Asia, India
	Leishmania mexicana	Sand fly (*Lutzomyia*)	USA, Ecuador, Peru, Venezuela
	Leishmania braziliensis	Sand fly (*Lutzomyia*)	Latin America
Sleeping sickness	*Trypanosoma brucei gambiense* *Trypanosoma brucei rhodesiense*	Tsetse fly (*Glossina*)	Sub-Saharan Africa
Chagas' disease	*Trypanosoma cruzi*	Reduviid bug (*Triatoma*)	Latin America

All arthropod-borne protozoan parasite infections have in common that specialized infectious parasites are inoculated by the vector into the dermis of the mammalian skin during a bloodmeal. With the exception of *Trypanosoma cruzi* (*T. cruzi*), which is introduced into the skin when infectious parasites in the bug feces contaminate the bug bite wound. To avoid immune elimination in the skin the parasites have evolved different strategies. The most studied parasites and their first steps in the skin are parasites of the genus *Leishmania* and *Plasmodium*.

The transmitted infective stage of *Plasmodium* species is called sporozoite and resides in the salivary glands of *Anopheles* mosquitos. It has long been thought that sporozoites are deposited directly into the bloodstream by the mosquito during feeding. However, experiments using bite site removal, interruption of mosquito feeding, and intravital fluorescence microscopy confirmed that most sporozoites are injected into the skin when the mosquito proboscis probes the skin for blood and ejects saliva. To avoid immune elimination by the host sporozoites move at high speed in the dermis by gliding motility. The parasites leave the bite site via the bloodstream or lymphatics to infect erythrocytes and hepatocytes. However, studies have also shown that some sporozoites remain in the skin and can invade cells in the epidermis, dermis or cells associated with hair follicles (Menard et al., 2013).

Infective metacyclic promastigotes of *Leishmania* species are regurgitated into the skin of a mammalian host by the bite of hematophagous sand flies. The bite causes significant damage of the skin, leading to rupture of the dermis and its capillaries, creating a wound milieu that attracts neutrophils and macrophages. Macrophages are the main host cell type of *Leishmania*. However, it has been shown that the first target cell for the parasite is the neutrophil, which appears at the bite site within 30 minutes (Laskay et al., 2003, van Zandbergen et al., 2004). After activation, neutrophils become apoptotic and eventually are internalized by macrophages to be degraded (Nauseef, 2007). *Leishmania* parasites have successfully adapted to life in the macrophage, an ideal way to escape the immune system, obtain nutrients, and proliferate (Arango Duque and Descoteaux, 2015, de Menezes et al., 2016).

Introduced infective metacyclic trypomastigotes of *T. cruzi* evade immune elimination by rapid invasion of a wide range of non-phagocytic cells. Several surface molecules participate in the invasion process, which induces an increase of intracellular Ca^{2+} in host

cells and triggers lysosome recruitment and fusion at the parasite entry site (Cardoso et al., 2015, Cestari et al., 2012).

The interaction of the infective metacyclic stage of *Trypanosoma brucei* species, which contrary to the other protozoa have an exclusively extracellular lifestyle, with the host skin has been much less explored. The following subchapters are dedicated to provide a general overview of African trypanosomiasis with a particular focus on the mammalian skin as interface in the transmission and skin-residing trypanosomes.

1.3 African trypanosomes and diseases

African trypanosomes are flagellated unicellular eukaryotes that have branched from the eukaryotic lineage early in evolution and belong to the order of Trypanosomatida in the class of Kinetoplastea (Fernandes et al., 1993). The class is characterized by the presence of a kinetoplast, which is easily identifiable as a large mass of mitochondrial DNA (kDNA) (d'Avila-Levy et al., 2015). African trypanosomes are exclusively extracellular pathogens transmitted by the bite of the tsetse fly vector and infect a variety of vertebrate hosts. In 1857, it was first reported by David Livingstone that the animal disease nagana is caused by the bite of a tsetse fly (Livingstone, 1857). 40 years later, David Bruce identified trypanosomes in the blood of infected animals as the causative agent of the disease (Bruce, 1895). Shortly afterwards trypanosomes and tsetse flies were also linked to sleeping sickness in humans (Dutton, 1902, Kleine, 1909).

Among African trypanosomes, the *brucei*-group is the most prominent and its representatives are responsible for both sleeping sickness (or human African trypanosomiasis, HAT) and nagana (or animal African trypanosomiasis, AAT). The two subspecies *Trypanosoma brucei rhodesiense* (*T.b.r.*) and *Trypanosoma brucei gambiense* (*T.b.g.*) are able to survive in human blood and cause HAT. They are resistant to the human trypanolytic factor (TLF), a combination of apolipoprotein L1 (APOL1) and a haptoglobin-related protein (HPR). In the circulation, hemoglobin (Hb) binds to HPR, hence to TLF1. In turn the TLF1-HPR-Hb complex binds to the trypanosome haptoglobin-Hb receptor. This binding triggers the uptake of TLF1 and subsequent trypanosome lysis (Wheeler, 2010, Perez-Morga et al., 2005). As both species can also infect livestock and wild animals, these animals play an important epidemiological role

as carriers or reservoirs from which tsetse flies can acquire HAT trypanosomes (Brun and Balmer, 2006).

The most prevalent species causing AAT in wildlife, livestock, and other domesticated animals, besides *Trypanosoma brucei brucei*, are *Trypanosoma vivax* and *Trypanosoma congolense* (Rotureau and Van Den Abbeele, 2013). As AAT is fatal for numerous domesticated animals it is a $4.5 billion annual burden on the African economy, livestock, and agricultural production (Kimaro, 2021). In contrast, infected wild animals have acquired a kind of tolerance to the parasites and therefore serve as an important reservoir for the disease (Anderson et al., 2011, Auty et al., 2012).

In general, African trypanosomiasis occurs in two stages, an initial hemolymphatic stage followed by a meningoencephalitic stage after the trypanosomes have invaded the central nervous system. In the first stage, the parasites develop in blood, lymph, and various tissue-spaces causing non-specific symptoms such as fever, headache, joint pains, and shivering attacks. The second stage is initiated when the parasites cross the blood-brain barrier (BBB) to infect the brain and central nervous system (CNS). More obvious signs and symptoms such as disturbance of the sleep cycle, which has given the disease its name, appear at this stage and patients eventually fall into a coma and die (Kennedy, 2013). Infection with *T.b.r.* produces an acute and severe condition in which the CNS is infected within weeks, leading to death after a few months, whereas *T.b.g.* causes a more chronic form that can last for several years (Brun et al., 2010).

Fly control, combined with surveillance and treatment, has reduced the number of annual cases of sleeping sickness from 25,000 reported cases in 2000 to less than 1,000 reported cases in 2018 and sleeping sickness is now approaching elimination in many countries (Franco et al., 2020). However, the disease was similarly close to elimination during the 1960s and the role of asymptomatic human carriers and animal reservoirs remains unclear and needs further investigation (Informal Expert Group on Gambiense et al., 2018).

1.3.1 Cell architecture and cell cycle

Trypanosoma brucei brucei (*T.b.b.*) is closely related to the human infectious trypanosomes and has been established as a model organism for molecular cell biology, genetics, and parasitology. *T.b.b.* is a highly structured, polarized eukaryotic cell in which most organelles are present as a single copy and have a specific location (Figure 4 A).

Cell shape is defined by a highly polarized microtubule cytoskeleton, with the minus ends at the anterior pole and the plus ends at the posterior pole. This cytoskeleton remains intact throughout the cell cycle and the single-copy organelles, such as the flagellar pocket, flagellum, kinetoplast, mitochondrion, and nucleus, are precisely positioned within the cytoskeletal corset (Robinson et al., 1995). The most posterior structure is the flagellar pocket, which is an invagination of the plasma membrane and the only site of endo- and exocytosis (Overath and Engstler, 2004). In addition, the flagellar pocket is the exit point for the flagellum. It is attached along the exterior length of the parasite via the flagellum attachment zone and has a free distal tip at the anterior pole (Taylor and Godfrey, 1968). The kinetoplast is located next to the flagellar pocket and physically connected to the flagellum via the basal body, which plays a crucial role in mitochondrial genome segregation during the cell cycle (Robinson and Gull, 1991). Trypanosomes possess a single Golgi stack with a restricted position between the flagellar pocket and the nucleus. The endoplasmic reticulum (ER) and mitochondrion span the whole cell, with the ER always adjacent to the flagellum. The parasite is propelled by the single flagellum in posterior to anterior direction (Rodriguez et al., 2009). Parasite motility is crucial for survival, morphogenesis, cell division, and infection in the mammalian host (Broadhead et al., 2006, Ralston et al., 2006, Kohl et al., 2003), and also for the life cycle in the tsetse vector (Rotureau et al., 2014).

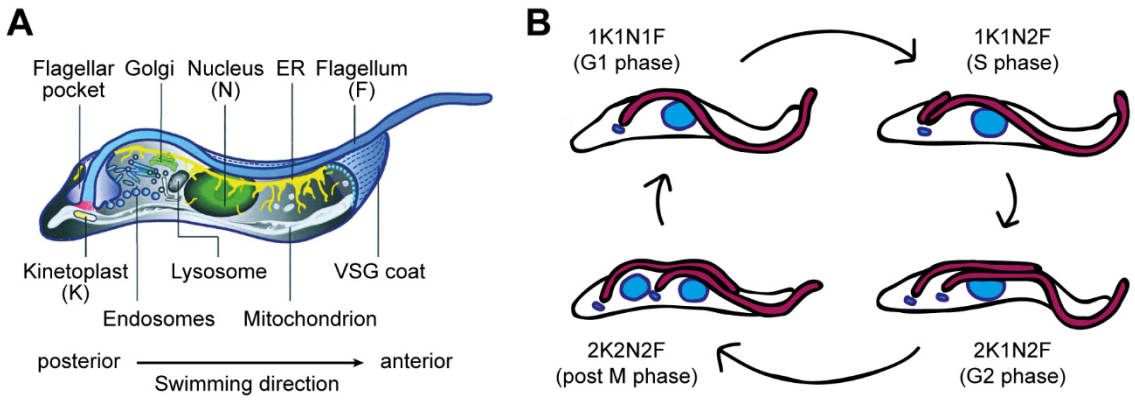

Figure 4: Cell architecture and cell cycle of *Trypanosoma brucei brucei*. (A) Schematic representation of the trypanosome cell architecture with the major organelles and their location. The kinetoplast (K) is associated with the basal body of the flagellum (F) and its division precedes that of the nucleus (N). Adapted from (Grunfelder et al., 2003). **(B)** The key cell cycle stages of *T.b.b.*, showing the order of duplication of the kinetoplast (K), nucleus (N) and flagellum (F) and their morphology. 2K2N2F cells divide by binary fission along the cell's longitudinal axis, resulting in two 1K1N1F cells.

The cell cycle of *T. brucei* is a precisely timed program of coordinated processes that mediate the replication of key cellular structures and their subsequent distribution to daughter cells (Figure 4 B). One example is that the growing daughter flagellum precisely follows the old flagellum during cell division, transferring structural information from the old to the new flagellum (Moreira-Leite et al., 2001). Several proteins are important for the correct progression of the parasite through the cell cycle and are often expressed at specific timepoints. For example, the RNA-binding protein PUF9 is responsible for the accumulation of several RNA molecules after DNA replication. The proteins encoded by these RNAs appear to function in the division of various cellular structures at this timepoint (Archer et al., 2009).

The first structure to be duplicated is the basal body, which serves as the nucleation site for the newly synthesized flagellum (Sherwin and Gull, 1989, Lacomble et al., 2010). The replicated mitochondrial DNA of the kinetoplast is segregated during the S phase of the cell cycle, resulting in an elongated kinetoplast, and its division precedes that of the nucleus. The nuclear DNA is replicated in the S phase and separated in the G2 phase without disassembly of the nuclear envelope (closed mitosis) (Ogbadoyi et al., 2000). After complete segregation, the cell enters the post-M phase and has two kinetoplasts and two nuclei (2K2N). Cytokinesis is initiated at the anterior pole of the cell after complete duplication of all cell organelles. This is achieved by longitudinal binary fission, in which a cleavage furrow towards the posterior pole between the two flagella is formed and separates the two daughter cells.

1.3.2 Genome organization and regulation of gene expression

The *T. brucei* strains most commonly used in molecular and cell biology research are TREU 927 and Lister 427. The pleomorphic strain TREU 927 is competent for the progression through all life cycle stages of the parasite, in contrast to the monomorphic strain Lister 427 (van Deursen et al., 2001). The genome of the TREU 927 strain was published in 2005 and is ~ 26 megabases (Mb) in size (haploid) and contains 9,068 genes that are distributed among 11 megabase-size chromosomes (Berriman et al., 2005). The nuclear genome also contains 5 intermediate-size chromosomes (200 - 900 kb) and ~ 100 minichromosomes (30 - 150 kb) (Daniels et al., 2010). For comparison, the human genome is > 3,000 Mb in size and contains ~ 30,000 genes that are located on

22 chromosomes and two sex chromosomes (Guo et al., 2017). The minichromosomes harbor a repertoire of variable surface glycoprotein (VSG) genes and their proposed function is to increase the pool for antigenic variation. Among the 9,068 predicted genes, ~ 900 are pseudogenes and ~ 1,700 are *T. brucei*-specific genes. The genes located on the 11 megabase chromosomes are organized as long, non-overlapping polycistronic transcription units (PTUs), which can consist of > 100 genes (Berriman et al., 2005, Siegel et al., 2009).

The majority of protein-coding genes are organized in PTUs, although they are generally not functionally related. Genes in PTUs are constitutively transcribed by RNA polymerase II, with the exception of the telomeric VSG expression sites, which are transcribed by RNA polymerase I. Contiguous PTUs are transcribed from the same DNA strand, whereas the direction of neighboring PTUs can be oriented in the same (convergent) or opposite direction (divergent) (Siegel et al., 2011). Individual mRNAs are matured by co-transcriptional *trans*-splicing and polyadenylation (Matthews et al., 1994). In *trans*-splicing, mRNAs of a PTU are separated by a splicing reaction in which a 39-nt spliced leader RNA (SL RNA) sequence is attached to the 5′ end of all mRNAs and provides the 5′ cap structure for the mRNA (Perry et al., 1987). This process is crucial for the maturation of primary transcripts into mature mRNAs in *T. brucei* and provides a mechanism for post-transcriptional regulation of gene expression (Nilsson et al., 2010).

Trypanosomes lack promotor motifs upstream of the PTUs and initiation of transcription by RNA polymerase II is not controlled at the level of individual genes. Therefore, PTUs are thought to be constitutively transcribed and regulation of gene expression occurs post-transcriptional. Such post-transcriptional control can occur at various steps of mRNA processing, translation, and decay (Clayton, 2019). A crucial role in expression regulation in trypanosomes play RNA-binding proteins (RBPs) (Kolev et al., 2014). By now, there are many examples of the importance of RBPs in *T. brucei*. About 150 RBPs are annotated in the genome and they have been shown to regulate the cell cycle, life cycle, and stress response of the parasite (Kolev et al., 2014, Clayton, 2019). Their mode of action is not fully understood, yet in most cases they control expression by stabilizing or de-stabilizing specific mRNAs, thereby mediating their translation or degradation (Erben, 2018).

1.3.3 The life cycle of *T. brucei*

During its life cycle, *T. brucei* alternates between a vertebrate host and the tsetse fly vector. On this journey, the parasite encounters a wide variety of environmental conditions with changing temperatures, pH values, and nutrients. To survive, *T. brucei* must quickly adapt to these changing environments and has evolved several strategies (Figure 5). In addition to adaptations in metabolism and surface coat composition, they have also developed multifunctional morphological modifications (Smith et al., 2017, MacGregor et al., 2012, Rotureau and Van Den Abbeele, 2013). Five different life cycle stages have been described for *T. brucei* in the tsetse vector and at least two different stages exist in the mammalian host. Besides the circulatory system, the parasites accumulate in the interstitial spaces of various tissues, especially the brain, skin, and visceral adipose tissue. By adapting to these tissues, more life cycle stages could exist in the mammalian host (Trindade et al., 2016, Capewell et al., 2016).

The best characterized parasite stages are those that can be cultured *in vitro*, namely the bloodstream form (BSF) and the stumpy form, which live in the mammalian host, and the procyclic form (PCF), which colonizes the tsetse midgut. Knowledge about the other life cycle stages in the fly is mostly limited to basic morphological features and some known surface proteins (Sharma et al., 2009). However, the discovery that overexpression of the RNA-binding protein 6 (RBP6) in PCFs induces differentiation into the further developmental stages of the fly *in vitro* (Kolev et al., 2012) has greatly facilitated the study of the other fly stages.

1.3.3.1 Development in the insect vector

During a bloodmeal on an infected mammalian host, the tsetse fly takes up trypanosomes, which are transported to the posterior midgut of the fly. From there, the parasites migrate to the salivary glands and acquisition of mammalian infectivity takes about 20 to 30 days (Rotureau and Van Den Abbeele, 2013). In order to survive the drop in temperature, the change in nutrients, and the higher pH, the ingested parasites quickly adapt to the fly's gut environment and differentiate to PCFs. The VSG surface coat is replaced by the procyclin proteins GPEET (early PCF) and EP (late PCF) which are suggested to

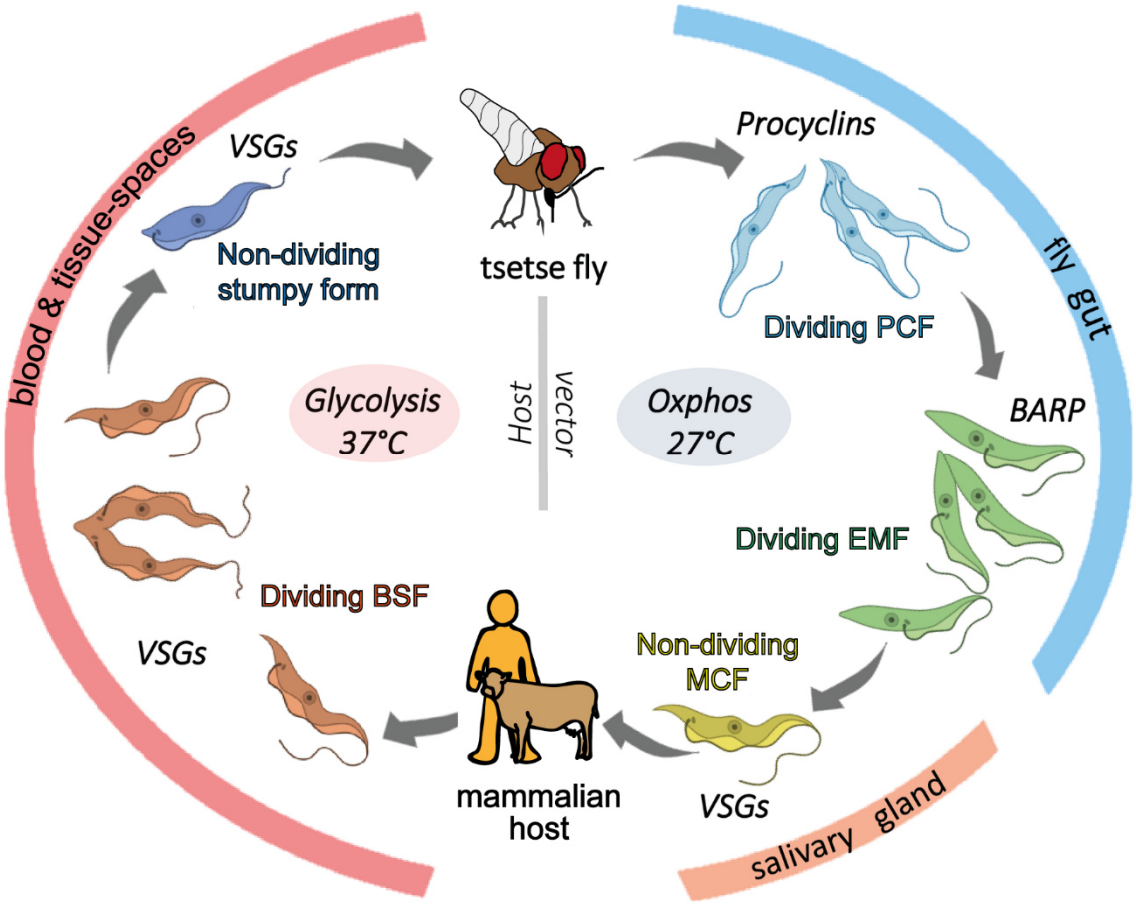

Figure 5: The life cycle of *T. brucei*. The major mammalian and tsetse vector life cycle stages of *T. brucei* are illustrated. As *T. brucei* cycles between its mammalian and arthropod host, it is exposed to drastic environmental changes and has evolved various adaption strategies, including changes in metabolism, surface proteins, and morphology. After a tsetse bite, the transmitted infectious, non-dividing metacyclic form (MCF) quickly adapts to the mammalian host and differentiates to the dividing bloodstream form (BSF). As parasitemia increases BSFs are capable of sensing population density. This triggers differentiation to the non-dividing stumpy form, which is pre-adapted to life in the tsetse fly. Once taken-up during a bloodmeal, the stumpy form differentiates into the dividing procyclic form (PCF) in the fly gut. During migration to the salivary glands of the fly, the PCF differentiates into the epimastigote form (EMF), which divides asymmetrically in the glands resulting in a short and long EMF. The short EMF attaches to the gland epithelium and gives rise by asymmetric division to the mammalian-infective, non-dividing metacyclic form (MCF). In general, the parasite stages in the fly vector use oxidative phosphorylation (Oxphos), while the mammalian stages rely on glycolysis for energy production. During the parasites' journey through the different hosts, *T. brucei* expresses different sets of surface coat proteins: variable surface glycoproteins (VSGs) in the mammalian and procyclins, BARPs, and metacyclic VSGs in the fly host. Adapted and modified from (Cestari and Stuart, 2020).

protect the parasites from digestive enzymes and are essential for infection (Roditi et al., 1989, Acosta-Serrano et al., 2001). In the mammalian host, *T. brucei* relies on glycolysis for energy production, however, the fly's midgut contains hardly any glucose, but is rich in amino acids, such as proline. Thus, ingested parasites activate their mitochondrion and respiratory chain to produce energy by oxidative phosphorylation (Oxphos) (Smith et al., 2017). Furthermore, the PCFs re-enter the cell cycle and begin to multiply in the midgut. However, the fly's innate immune system is activated and many trypanosomes are eliminated or in some cases the infection is completely cleared (Maudlin et al., 1998).

The remaining PCFs are able to cross the peritrophic matrix, which separates the lumen of the midgut from the epithelium, and hide from the fly's immune system inside the ectoperitrophic space (Gibson and Bailey, 2003). Here, the PCFs differentiate into long mesocyclic cells and migrate towards the anterior end of the fly's alimentary tract to reach the proventriculus. The mesocyclic stage is characterized by cell cycle arrest in the G2 phase and the replicated nucleus and kinetoplast have not yet segregated (Sharma et al., 2008). In the proventriculus, the parasites differentiate into the next stage, the epimastigote form (EMF). The cells become thinner and the nucleus migrates towards the posterior end of the cell so that the nucleus is located posterior to the kinetoplast. The EMF re-enters the cell cycle and divides asymmetrically, which produces a long and a short daughter cell (Sharma et al., 2008). The function of the long epimastigote is not fully understood, but it is thought that the long form acts as a transporter for the short form to the salivary glands (Rotureau et al., 2011). This step seems to be a major bottleneck, as many flies can suffer from a severe midgut infection that does not progress to the salivary glands (Oberle et al., 2010).

The short EMF attaches with its flagellum to the glandular epithelium and colonizes the salivary glands (Sharma et al., 2008, Van Den Abbeele et al., 1999). In addition, their procyclin surface coat is replaced by *brucei* alanine-rich proteins (BARPs) (Urwyler et al., 2007). To colonize the glands, they undergo symmetrical division and the two identical daughter cells stay attached to the glandular epithelium and continue to proliferate. Furthermore, the attached EMF can divide asymmetrically to produce an epimastigote and a trypomastigote cell (Rotureau et al., 2012).

The trypomastigote cell is called a pre-metacyclic cell and the nucleus is again located anterior to the kinetoplast. Finally, the pre-metacyclic cell differentiates to the cell cycle-arrested, mammalian-infective stage, called metacyclic form (MCF). During this process,

the parasites detach from the epithelium, are released into the duct of the gland, and acquire a metacyclic VSG surface coat (Tetley et al., 1987). This VSG coat prepares the MCFs for transmission to the mammalian host (Barry et al., 1998). Once established, the attached EMF population sustains the entire life span of the vector and can produce hundreds of MCFs per day (Otieno and Darji, 1979).

1.3.3.2 Development in the mammalian host

During the bite of a tsetse fly, the fly probes the mammalian skin for blood and secretes saliva, thereby depositing the infectious MCFs in the skin. By still unknown factors, the cell cycle-arrested MCFs are activated in the skin, re-enter the cell cycle, and differentiate into proliferative trypanosomes, which morphologically resemble the proliferative mammalian life cycle stage known as the bloodstream form (BSF) (Dwinger et al., 1988). It has been shown that a subpopulation of the injected trypanosomes persists in the skin around the bite (Caljon et al., 2016), which can cause the typical trypanosome chancre. A local inflammatory response of the skin associated with swelling and an influx of immune cells (Naessens et al., 2003). After ~ 2 days trypanosomes are detectable in the central lymph and after 4 - 5 days they appear in the bloodstream (Barry and Emery, 1984). From the bloodstream, the parasites spread throughout the host and accumulate in various host tissues (Silva Pereira et al., 2019).

As *T. brucei* is an exclusively extracellular parasite it is continuously exposed to the host immune system. The metacyclic VSG surface coat represents an initial immune evasion strategy, as only one variable antigen type is expressed per cell, yielding an antigenically mixed MCF population (Tetley et al., 1987). However, the metacyclic VSG repertoire is relatively small (≤ 27) (Turner et al., 1988) compared to the huge VSG repertoire of the bloodstream form of more than 2,000 VSG genes (Cross et al., 2014). Therefore, the metacyclic VSG coat is replaced with VSG isoforms of the bloodstream form ~ 4 - 6 days post-infection (Esser and Schoenbechler, 1985, Barry et al., 1998).

The VSG surface coat is a dense monolayer of ~ 10^7 identical VSG molecules, which are the major parasite antigens that are targeted by the host's immune system (Jackson et al., 1985, Schwede et al., 2011). The VSG homodimers can freely diffuse on the plasma membrane and are highly immunogenic, which provokes a fast production of IgM and IgG antibodies (Reinitz and Mansfield, 1990). However, at low antibody titers, *T. brucei*

can actively remove antibodies bound to the VSGs by endocytosis. This is achieved by hydrodynamic forces generated by the forward movement of the parasite pushing the VSG-bound antibody to the posterior pole of the cell, where it can be internalized via the flagellar pocket (Engstler et al., 2007). While the endocytosed antibody is degraded in the lysosome, the VSG is recycled and transported back to the cell surface. With this system, the parasite is able to clear and recycle its entire VSG surface coat within 12 minutes (Engstler et al., 2004).

At high antibody titers, however, this system reaches its limit and the parasites are cleared by the host's immune system (Dempsey and Mansfield, 1983). However, *T. brucei* is infamous for its ability to evade the adaptive immune response by periodically switching the expression to an immunologically distinct VSG gene, a phenomenon called antigenic variation (Cross, 1977). Due to stochastic VSG switching, this process leads to an antigenically mixed trypanosome population that causes the typical waves of parasitemia in infected individuals (Deitsch et al., 2009, Mugnier et al., 2015). Antigenic variation and the vast VSG repertoire are the main reasons why there is no vaccine against sleeping sickness.

To control their virulence, the parasites limit their proliferation, as a constant high parasitemia damages the host and accelerates its death (Seed and Wenck, 2003). On the other hand, low parasitemia may lead to reduced transmission capacity to the tsetse vector. Therefore, *T. brucei* has evolved an elegant mechanism to balance the parasite load in the host with the transmissibility of the parasite to the vector. As parasitemia increases, BSFs are able to detect population density by quorum sensing, and this triggers differentiation to the non-dividing stumpy form, which is pre-adapted to life in the tsetse fly (Vassella et al., 1997). Stumpy cells have a higher tolerance for changes in pH and proteolytic stress (Nolan et al., 2000) and have a limited life span of 2 - 3 days in the mammalian host (MacGregor et al., 2011). In addition, stumpy forms cannot undergo antigenic variation (Amiguet-Vercher et al., 2004). The quorum sensing signal, termed stumpy induction factor (SIF), accumulates over time in the host. It has been shown that trypanosome-secreted oligopeptidases create a pool of peptide breakdown products from surrounding host proteins of which specific oligopeptide compounds can be detected by the parasite (Rojas et al., 2019). As this signal accumulates, some parasites arrest in the cell cycle and prepare for transfer to the tsetse vector by differentiating into the stumpy form. This differentiation is accompanied by morphological changes, such as a shorter,

stout cell shape with a reduced flagellum length, and an elaborated mitochondrion (Brown et al., 1973). In order to recognize the entry into the fly, the proteins associated with differentiation (PAD) 1 and 2, which are surface-localized carboxylate transporters, play an important role. PAD1 and PAD2 are highly expressed in stumpy forms and serve as marker proteins for the stumpy stage (Dean et al., 2009). In addition, a second density independent stumpy development pathway has been described, in which an unsuccessful VSG switch is the key to the differentiation process (Zimmermann et al., 2017). As not all BSFs differentiate into stumpy forms, infection continues in the host, while transmission with fly-adapted stumpy forms and completion of the parasite cycle are ensured. However, there is also strong evidence that the non-adapted BSFs can successfully complete the life cycle of the parasite in the fly after being ingested during a bloodmeal (Schuster et al., 2020). Until now, it was assumed that these cells, unlike the stumpy forms, die in the fly's midgut.

1.4 The role of mammalian skin in trypanosomiasis

In a number of historical studies, it has already been observed that trypanosomes accumulate in various tissue spaces, including the skin matrix (Yorke, 1911, Willett and Gordon, 1957, Ormerod, 1970, Goodwin, 1970, Goodwin, 1971). However, the above-mentioned studies and their findings have largely disappeared from the field of trypanosome research, which may have several reasons. First, the production of infectious MCFs requires tsetse flies, which are challenging to keep. Therefore, experimental murine hosts were usually infected by needle injection of BSFs in the peritoneal cavity or tail vein, bypassing the skin as the first entry point for MCFs. However, recent studies have shown that the intradermal route differs considerably from the experimental tail vein or peritoneal route. The dermis has been revealed as a strict bottleneck for BSFs to establish infection, while MCFs are somehow pre-adapted to survive in the dermis and establish infection (Wei et al., 2011, Caljon et al., 2016, Ndungu et al., 2019). Furthermore, tracing trypanosomes in living tissue, especially at high spatiotemporal resolution, is very challenging even with state-of-the-art technology. For example, only recent technical advances in intravital microscopy have allowed a more systematic analysis and quantification of trypanosome tissue tropisms (De Niz et al., 2019, Silva Pereira et al., 2019). Nowadays, we known that *T. brucei*, as well as *T. congolense*,

T. vivax, and *T. cruzi*, accumulate in various tissues of the host, including the skin, adipose tissue, brain, liver, and heart (Silva Pereira et al., 2019).

1.4.1 Early parasitological features in the mammalian host

To date, only few studies have addressed the early parasitological features of a naturally transmitted trypanosome infection in mammalian skin and the timing and the mechanisms controlling the differentiation from the injected cell cycle-arrested MFCs to proliferative trypanosomes remain largely unknown.

The infectious dose of transmitted MCFs required to establish infection in the mammalian host has been investigated in a few studies. It has been shown that five intradermally injected metacyclic trypanosomes are sufficient to develop systemic infection in mice (Caljon et al., 2016), while a historical study in humans found that a subcutaneous dose of 300 to 450 metacyclic parasites are required (Fairbairn and Burtt, 1946). In contrast, 200 intradermally injected BSFs were unable to establish an infection in mice (Caljon et al., 2016) and even 20,000 subcutaneously injected BSFs failed to infect humans (Willett, 1956). This strongly suggests, that MCFs are pre-adapted to survive in the mammalian skin and establish infection. However, it is not clear what could be the basis for the higher infectivity of metacyclic trypanosomes. To date, there has been no study comparing the transcriptome of MCFs with that of BSFs. Only one study compared the transcriptional profile of parasitized salivary glands with BSFs, but the glandular trypanosome population is complex and does not contain only MCFs (Telleria et al., 2014). Nevertheless, the authors found differences in gene expression associated with glycolysis, cytoskeleton, protein kinase activity, transport, and translation.

After the bite of a tsetse fly, trypanosomes were rapidly detected in the draining lymph nodes of mice within 18 hours (Caljon et al., 2016) and after ~ 2 days in the central lymph of goats (Barry and Emery, 1984). In the skin tissue, the parasites were found proliferative ~ 3 - 4 days post-infection (Gordon and Willett, 1958, Caljon et al., 2016). A successful culture of *T. b. rhodesiense* MCFs was even described where the authors claimed that trypanosomes were present at each division stage 17 hours post-inoculation (Gordon and Willett, 1958). After 4 - 5 days post-infection, the first parasites are detectable in the host's bloodstream and the metacyclic VSG coat is replaced with VSG isoforms of the

bloodstream form (Barry and Emery, 1984, Dwinger et al., 1988, Esser and Schoenbechler, 1985, Barry et al., 1998).

The MCFs experience a drastic change in their environment when injected into mammalian skin. These include physical (*e.g.* changes in temperature and oxygen pressure), mechanical (*e.g.* transition from fly saliva to solid skin tissue), biochemical (*e.g.* changes in glucose abundance), and immunological changes (*e.g.* activation of immune cells upon infection). However, it is unclear which environmental stimuli act as drivers for parasite activation and differentiation. Moreover, the exact timing and molecular sequences of differentiation remain to be elucidated. Although it has been reported that a subpopulation of the injected trypanosomes persists in the skin around the bite (Caljon et al., 2016), it is not clear whether this initial population remains in the skin throughout the entire course of the disease and whether it is distinct from the parasites found in the bloodstream.

1.4.2 Early host response in the skin

The saliva of the tsetse fly not only serves as a transmission vehicle, but is also known to affect the hemostatic and immunological response of the host (Alfituri et al., 2020). It contains several proteins to suppress vasoconstriction, platelet aggregation, and blood coagulation to enable successful blood feeding. In addition, tsetse saliva induces a distinct Th2 immune response in mouse models and suppresses T- and B-cell responses, resulting in increased levels of IL-4 and IL-10, and decreased INF-γ titers (Caljon et al., 2006a). This favors an alternative activation of macrophages, a more anti-inflammatory state. Moreover, bites from parasitized flies have a reduced anti-coagulation capacity compared to bites from naïve flies, resulting in a prolonged feeding time and thus, an increased likelihood of parasite transmission. Hence, tsetse saliva increases the transmission-efficiency of *T. brucei* to the mammalian host (Caljon et al., 2006b) and induces a skin microenvironment more suitable for the MCFs. However, the saliva is also dispensable, as washed, intradermally injected MCFs can also successfully establish infection in mice (Caljon et al., 2016).

The first cellular responders against the injected trypanosomes in the skin are neutrophils, natural killer (NK) cells, and NK T-cells (Stijlemans et al., 2016, Caljon et al., 2018). This first immune response is directed against the metacyclic VSG coat and can lead to a

local skin reaction, called chancre, a few days after infection. The immune response and size of the chancre correlates with the number of MCFs that are deposited in the skin (Barry and Emery, 1984). In addition, $CD4^+$ T-cells were shown to play a key role in chancre formation (Naessens et al., 2003).

Neutrophils are involved in the killing of various pathogens, including protozoa, not only by phagocytosis but also by the release of reactive oxygen species and neutrophil extracellular traps (NETs) (Guimaraes-Costa et al., 2009, Silva et al., 2016). In the case of *T. brucei*, they have been shown to be recruited to the dermal bite site within 4.5 h, but surprisingly, these early neutrophils do not appear to contribute to the elimination of trypanosomes in the skin. Instead, they appear to support the establishment of the parasite infection for reasons that are still unknown (Caljon et al., 2018). Neutrophils also contribute to wound healing after skin injury and are recruited in high numbers after tissue damage. A variety of genes known to be important for wound healing have been shown to be transcriptionally upregulated when neutrophils leave the bloodstream and reach the site of injury (Wilgus et al., 2013).

Macrophages are the most abundant immune cell type in the skin and monitor the skin microenvironment for signals that indicate cell stress, tissue injury or infection (Murray and Wynn, 2011). The knowledge about the role of macrophages in African trypanosomiasis comes from studies with experimental intraperitoneal or intravenous infections of mice. Therefore, the role of macrophages in the skin during trypanosome infection is still poorly understood. Trypanosomes activate skin-resident macrophages through pathogen-associated molecular patterns (PAMPs), such as released soluble VSG, and induce the expression of the inducible nitric oxide synthase (iNOS) enzyme, which produces toxic nitric oxide (NO). NO has been shown to contribute to the innate resistance of intradermally injected BSFs of *T. congolense* (Wei et al., 2011, Lu et al., 2011).

Skin-residing dendritic cells (DCs) include epidermal Langerhans cells, which sample and present antigens from the epidermis to promote the adaptive immune response, and dermal DCs (Haniffa et al., 2015, Kaplan, 2017). They have been shown to suppress *Leishmania* infections by modifying the behavior of regulatory T-cells but their role in African trypanosomiasis remains to be elucidated (Kautz-Neu et al., 2011).

1.4.3 The skin as a reservoir tissue for trypanosomes

It has long been known that trypanosomes accumulate in various host tissues during disease progression (Yorke, 1911, Willett and Gordon, 1957, Ormerod, 1970, Goodwin, 1970, Goodwin, 1971, Kruger et al., 2018, Silva Pereira et al., 2019). However, these tissue-inhabiting parasites have been little investigated, mainly due to the technical challenges associated with isolating and studying the tissue-dwelling trypanosomes. In 2016, two elegant studies shed some more light on trypanosomes hiding in tissue spaces.

The first study reported that *T. brucei* parasites occupy and functionally adapt to the adipose tissue in mice (Trindade et al., 2016). The parasites were consistently detected in the interstitial space of adipose tissue already 6 days after infection and the authors termed these parasites adipose tissue forms (ATFs). ATFs have been shown to be proliferative in adipose tissue, as parasites have been found in the S and G2 phases of the cell cycle. The total number of ATFs in fat remained almost constant during the course of infection and increased only very slowly. However, the doubling time of ATFs was not determined, and the dynamics of parasite entry and exit into adipose tissue were not examined. Therefore, no conclusions about the growth behavior of ATFs could be drawn in the study. The authors found that ATFs resemble BSFs in their morphology and are competent to differentiate into stumpy forms. ATFs have been shown to be transcriptionally distinct from BSFs and to upregulate genes for fatty acid metabolism. By upregulating these transcripts, it has been shown that ATFs adapt metabolically to adipose tissue by using fatty acid-β oxidation for energy production. This was supported by evidence that ATFs can actively take up exogenous myristate and form β-oxidation intermediates.

The second publication identified the mammalian skin as an overlooked tissue reservoir for *T. brucei* parasites (Capewell et al., 2016) and trypanosomes have been frequently found in the skin of infected animals and humans, even in aparasitemic and asymptomatic individuals (Capewell et al., 2016, Casas-Sanchez and Acosta-Serrano, 2016, Capewell et al., 2019, Camara et al., 2020). The skin-resident parasites were found motile and replicative. However, the replicative capacity of skin parasites has only been demonstrated by an increase in the total number of parasites dwelling in the skin during the course of infection. The dynamics of entry and exit of the parasites into the skin have not been studied. The parasites were observed in the skin with a dynamic distribution with

changing localizations and variable density. It has also been shown that skin-dwelling parasites can successfully develop into stumpy forms, and skin-dwelling parasites from laboratory mice can be transmitted to tsetse flies, even in the absence of detectable blood parasitemia (Capewell et al., 2016). This strongly suggests a contribution to disease transmission. The extent to which these skin-dwelling parasites differ from ATFs or BSFs, or whether adaptation to skin tissue occurs as observed with ATFs, is not yet known. Hence, a more detailed characterization of skin-resident trypanosomes is needed.

The detection of potentially transmissible trypanosomes in several human skin biopsies from individuals without a history of trypanosomiasis and in aparasitemic and asymptomatic individuals (Capewell et al., 2016, Camara et al., 2020) could explain why sleeping sickness has persisted in some areas, despite treatment and active surveillance. Residing in tissue spaces may provide a selective advantage. For example, if parasites become latent or slow growing in tissues, it may reduce disease burden, which then prolongs host survival and ultimately promotes disease transmission and completion of the life cycle. However, whether the trypanosomes, which are found in the skin or fatty tissue, become latent or slow growing remains elusive.

Slow growing persister cells have been described for few other protozoan parasites, such as *Leishmania* or *T. cruzi*, but not for African trypanosomes (Barrett et al., 2019). In the related protist, *Leishmania mexicana*, quiescent amastigotes in murine lesions show very slow growth with a doubling time of 12 days and low rates of RNA, protein, and membrane turnover (Kloehn et al., 2015). Furthermore, slow-growing intracellular amastigotes of *Leishmania major* with a doubling time of 60 hours have also been reported (Mandell and Beverley, 2017). In *T. cruzi*, chronic infections are associated with a reduced replication rate of the parasite in the colon (Ward et al., 2020).

1.5 Skin tissue engineering

The field of tissue engineering was originally established by Langer and Vacanti with the aim to develop functional substitutes by combining biological and engineering principles to replace or regenerate damaged tissue (Langer and Vacanti, 1993). Since then, tissue engineering has evolved into a multi- and interdisciplinary combination of engineering, materials science, medicine, chemistry, physics, and biology. The generation of complex *in vitro* tissue substitutes with essential morphological, chemical, and mechanical

properties requires knowledge from all disciplines to develop scaffolds and bioreactors, as well as to integrate signals important for proper tissue formation.

Tissue-engineered substitutes recapitulate the microenvironment of human organs. Thus, consideration of the "3R" principle (Reduction, Refinement, Replacement; (Russell and Burch, 1959)) and animal welfare has led to regulations that encourage the use of tissue equivalents as alternative *in vitro* testing strategies, avoiding animal testing whenever possible. In particular, an entire animal testing ban for cosmetic ingredients has been in force since 2013 in European countries (Cosmetic Regulation No 1223/2009), making human skin equivalents increasingly important as an alternative to animal testing.

Fundamental to tissue engineering has been the principle that successful tissue formation depends on the synergistic activity of many cell types, not just the isolated effects of a single population. Moreover, these cells communicate with each other in a three-dimensional (3D) system through living and non-living components (Gerdes and Pepperkok, 2013, Rubashkin et al., 2014). This overarching theme of combining cells, 3D scaffolds, and environmental signals represents a promising strategy for tissue formation (Figure 6).

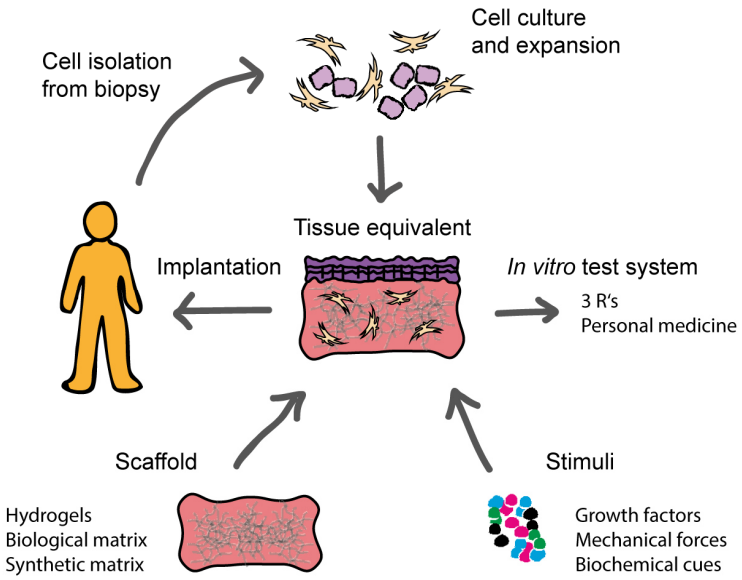

Figure 6: Basic concept of tissue engineering. In general, primary cells isolated from human biopsies are cultured and expanded *in vitro*. Alternatively, cells isolated from animals or cell lines can be used. Next, cells are incorporated into a three-dimensional (3D) scaffold, which may consist either of a hydrogel, biological, or synthetic matrix. During culture, tissue maturation is supported by the integration of appropriate environmental signals, such as growth factors or mechanical and biochemical cues. Integration of environmental signals often requires culturing the tissue in sophisticated bioreactor systems. The mature tissue equivalents can be implanted in patients to replace or regenerate damaged tissue, or they can be used as test systems or models as an alternative to animal testing.

Of particular importance is the 3D scaffold. Most cells require cues from a 3D environment that mimics real tissue to form relevant physiological tissue structures *in vitro.* This also applies to many pathogens and ultimately affects the outcome of an infection (Tomlin and Piccinini, 2018). In the field of skin tissue engineering various techniques and materials have evolved to incorporate appropriate cells into 3D matrices. Such auxiliary structures can for example be produced by hydrogels. The starting materials can vary widely and include collagen (Antoine et al., 2014), cellulose (Loh et al., 2018), polymers (Jeong et al., 2017), or decellularized small intestinal submucosa (Shi et al., 2019). As versatile as the starting material are the techniques used to fabricate the 3D scaffold (Yun et al., 2018). 3D hydrogels can for example be produced by 3D bioprinting. Hydrogels have high print resolution and easily modifiable chemical structures and are therefore commonly used bio-inks (Gopinathan and Noh, 2018). Artificial human skin produced by bioprinting has also been reported (Lee et al., 2014). In general, hydrogels have low mechanical stability, which makes them susceptible to fibroblast-mediated contraction during culture (Feng et al., 2003). To overcome contraction, additional techniques have been developed, such as freeze-drying of the hydrogel prior to cell integration (Lu et al., 2013), crosslinked hydrogels (Lotz et al., 2017), or hydrogel compression (Brown et al., 2005). Electrospinning represents a further technique to fabricate 3D scaffolds. Electrospun polymer nanofiber meshes have high morphological similarity to the natural extracellular matrix and are therefore attractive for generating skin equivalents. The meshes are characterized by a fibrous structure, high surface-to-volume ratio, and high porosity (Li et al., 2006). Compared to other structures, the high surface area of electrospun nanofiber meshes provides a large area for cell adhesion and proliferation. However, electrospun 3D scaffolds have some limitations, such as poor cellular infiltration into the inner region of the structure, possible toxicity of solvents or crosslinkers, and insufficient mechanical strength (Khorshidi et al., 2016). Skin-on-a-chip technologies combine tissue-engineering methodologies with bioinspired microfluidic systems. Skin-on-a-chip devices have the potential to mimic the complex architecture of skin tissue and create a microenvironment that mimics the mechanical forces in living tissue, for example, by applying cyclic strain in addition to continuous perfusion (Lee et al., 2017).

A major challenge in tissue engineering is the vascularization of large tissues, as sufficient vascularization is critical for cell survival and the promotion of metabolism and function

(Yang et al., 2020). This can be achieved, for example, by using a Biological Vascularized Scaffold (BioVaSc) based on a decellularized segment of a porcine jejunum that is supplied by a single artery-vein-pair (Mertsching et al., 2005, Schanz et al., 2010). The scaffold comprises structures of the former native vascular network that can be reseeded with human endothelial cells. However, a sophisticated bioreactor is required for tissue maturation and perfusion. In 2016, a first vascularized skin equivalent has been described (Groeber et al., 2016) based on a bioreactor system that supports the culture of the BioVaSc (Groeber et al., 2013).

1.6 Aim of the study

Infection with African trypanosomes begins when tsetse flies with a mature salivary gland infection take a bloodmeal, thereby depositing the infectious MCF of the parasite into the dermal skin layer of the mammalian host. Within the dermis, the cell cycle-arrested MCFs are activated by yet unknown factors, re-enter the cell cycle, and differentiate into proliferative trypanosomes (Dwinger et al., 1988, Caljon et al., 2016). However, the timing and the mechanisms controlling differentiation remain elusive, as does the characterization of the proliferative skin-residing trypanosomes. From skin tissue, parasites migrate via afferent lymphatic vessels to the local draining lymph nodes before they appear in the bloodstream and systemically infect the host (Barry and Emery, 1984, Alfituri et al., 2020). In addition, the skin acts as a reservoir tissue during disease, as trypanosomes have been frequently found in the skin of infected animals and humans, even in aparasitemic and asymptomatic individuals (Capewell et al., 2016, Capewell et al., 2019, Camara et al., 2020). The skin-dwelling parasites of laboratory mice can be transmitted to tsetse flies (Capewell et al., 2016, Caljon et al., 2016), strongly suggesting a contribution to disease transmission.

Current *in vitro* and *in vivo* infection models granted many insights into the pathogenicity of trypanosomes in the mammalian host. However, these studies were mainly focused on the BSF living in the circulation. Hence, skin-resident trypanosomes have been little investigated both shortly after injection into the skin and during the course of infection. One reason is that the production of infectious MCFs requires tsetse flies, which are challenging to keep. As a consequence, experimental murine hosts were usually infected by needle injection of BSFs in the peritoneal cavity or tail vein, bypassing the skin as the

first entry point for MCFs. In addition, the relatively small number of tsetse-transmitted metacyclic parasites makes them challenging to isolate and study in animal models.

This thesis aims to employ, advance, and validate an *in vitro* tissue-engineered primary human skin equivalent as an infection model to study the pathogenesis of tsetse fly-transmitted African trypanosomes in mammalian skin. This includes the establishment of infection-relevant conditions and readouts as well as the exploration of factors involved in host-pathogen interactions. In addition, this work aims to elucidate the timing and programmed changes in gene expression that occur during the developmental differentiation of the tsetse-borne trypanosomes in the skin. The ultimate goal is to evaluate and verify the primary human skin equivalent to establish it as a new tool for studying skin-resident trypanosomes as an alternative to animal experimentation. The skin infection model would facilitate the culture and access to skin-inhabiting parasites, allowing them to be studied more effectively.

II. Development and adaptation of a standardized primary human skin equivalent with increased mechanical properties to study the pathogenesis of *Trypanosoma brucei*

A key factor in research on infectious diseases is the ability to recreate the virulence-determining processes elicited by pathogens using suitable model systems. However, limitations of current infection models limit the understanding of such intricate mechanisms. This includes the study of tsetse-transmitted trypanosomes in the early stages of infection in mammalian skin. To date, not much is known about the processes, factors, and interactions of host, parasite, and vector that play a role in the skin at the beginning of an infection and contribute to a successful infection of a new host. Substantial progress leading to a better understanding has been achieved by Capewell et. al. and Caljon et. al. (Capewell et al., 2016, Caljon et al., 2016). However, these are limited by the use of mice as animal models that confront *T. brucei* with a non-natural host environment. As an alternative to overcoming not only ethical but also technical limitations in animal experimentation, a standardized primary human skin equivalent was developed in this thesis with the aim to recreate and investigate the early events of an infection caused by tsetse-transmitted trypanosomes in mammalian skin.

Skin equivalents were already successfully used as model systems in infection research, *e.g.* with *C. albicans* (Kuhbacher et al., 2017), *S. aureus* (Reddersen et al., 2019), and helminths (Jannasch et al., 2015). However, a major problem with collagen-based skin equivalents is their susceptibility to fibroblast-mediated contraction during culture. The poor mechanical stability of the dermal component (Feng et al., 2003) makes standardization difficult. Thus, skin equivalents with improved mechanical properties are needed to counteract contraction and weight loss during culture.

In this work, an advanced primary human skin equivalent (hereinafter referred to as high-density skin equivalent) was developed and validated as a model for vector-borne trypanosome skin infection. For this, an established skin equivalent (Reuter et al., 2017) was further refined by improving the mechanical stability of the dermal component to reach a high level of standardization and reproducibility.

2.1 Development of a computer-assisted compression system

Collagen is the major structural protein of the skin and comprises 70 - 80 % of its dry weight. Skin collagen is synthesized by fibroblasts and is composed of 80 - 85 % type I collagen (Shoulders and Raines, 2009). Therefore, collagen hydrogels are the first biological material of choice to remodel the dermal component of human skin. However, due to the high viscosity of dissolved collagen, only a concentration of up to approximately 10 mg/ml can be conveniently processed. Thus, after reconstitution conventionally used reconstructed dermal equivalents have a collagen concentration of about 6.66 mg/ml, usually even less (Antoine et al., 2014). The low collagen concentration and high-water content result in poor mechanical stability and these low-density dermal equivalents experience massive weight and area loss during culture.

In order to reduce contraction and weight loss of collagen gels without affecting their biocompatibility, the technique of plastic compression was applied. Collagen gels are poroelastic/biphasic systems consisting of a hyperhydrated fibrillar loose lattice structure. In the technique originally developed by Brown et al., the fluid from reconstituted hyperhydrated collagen gels is displaced by plastic compression. This produces scaffolds that are relatively dense, cellular and mechanically strong, and have a controllable structure (Brown et al., 2005).

The implementation of the technique was realized by a specifically developed computer-assisted compression system consisting of a custom-made compression reactor (Figure 7 A and 7 B) and a linear motor (Figure 7 C). The computer-aided design (CAD) of the reactor was created by Tamara Finger during her bachelor thesis (Finger, 2016) and the reactor was manufactured at GT Labortechnik. As material for the reactor, the semi-crystalline, high-performance engineering thermoplastic PEEK (polyether ether ketone) was used. This material meets all requirements that are important for the development of bioreactors in the field of tissue engineering. It can be processed by mechanical production processes and is chemically resistant to common solvents such as ethanol, dimethyl sulfoxide or acetone. In addition, it does not change in physiological solutions, which have a relatively high salt content and thus a greatly increased oxidation capacity. It can be sterilized by steam pressure sterilization, which places high demands on the material with regard to temperature and pressure. Furthermore, PEEK is permanently biocompatible and does not damage living tissue.

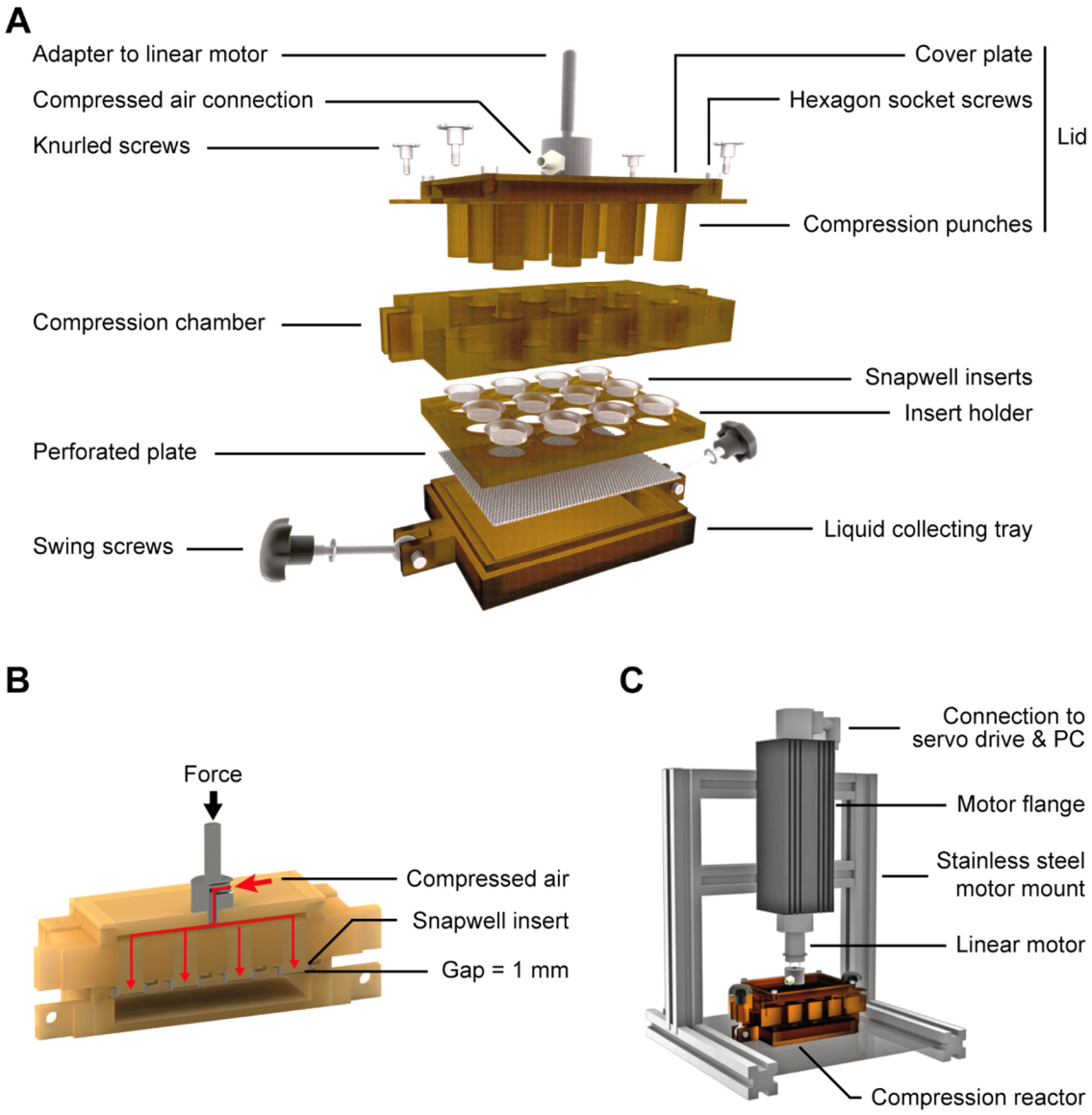

Figure 7: Computer-assisted compression system. (A) Representation of the computer-aided design (CAD) of the compression reactor with all individual parts. **(B)** Cross section through the closed reactor after complete compression. The red arrows mark the route of the compressed air through the reactor. The compressed air is introduced through the compressed air connection, which can then exit through the channels in the individual compression punches to release the dermal equivalents. **(C)** Representation of the compression system. Shown is the configuration of the linear motor, which is attached to a stainless-steel motor mount via the motor flange. The motor can be controlled with the LinMot®-Talk software by connecting it to a computer. Images were rendered based on the CAD files created by Tamara Finger.

The reactor was designed to allow the compression of 12 collagen gels in parallel (Figure 7 A). The reconstituted collagen gels were compressed in Snapwell inserts, as these were the only commercially available cell culture inserts with perpendicular walls. An insert holder was designed for the 12 Snapwell inserts, and a perforated plate underneath prevented the insert membranes from rupturing during compression. A liquid

collecting tray below collected the displaced liquid from the gels. Given that the Snapwell inserts with a wall height of 5 mm and a diameter of 12 mm would only provide a compression volume of 566 µl, an attachable compression chamber with a height of 20 mm was designed to increase the compression volume per insert up to 2,800 µl. All these parts can be firmly connected to each other by tightening the swing screws, which are located on both sides of the liquid collecting tray, on the compression chamber.

The lid of the compression reactor consists of two components, the compression punches and the cover plate, which are connected with 4 hexagon socket screws and a sealing O-ring. The 12 cylindrical compression punches were designed to fit exactly into the 12 openings of the compression chamber with a minimum of friction. Due to their defined length of 24 mm, the distance between the insert membranes and the lower edge of the compression punches was always exactly 1 mm after complete compression (Figure 7 B). Consequently, the compressed collagen gels had a standardized height of 1 mm and a diameter of 12 mm based on the diameter of the Snapwell inserts.

In addition, an adapter with compressed air connection for the attachment to the linear motor can be mounted centrally on the lid via a screw thread. Via the compressed air connection, compressed air can be introduced into the reactor. The compressed air is evenly distributed through the sealed cavity in the lid into the 0.5 mm diameter channels, which pass centrally through each of the 12 compression punches (Figure 7 B). The compressed air was used to release the compressed collagen gels from the compression punches residue-free and without damage, as these, including the Snapwell inserts, adhered to the compression punches after compression.

The compression was performed with a linear motor from the company NTI AG LinMot (Figure 7 C). This consisted of the actual linear motor, a motor flange, a servo drive, and a power supply unit. The linear motor was connected to a computer via the servo drive with a motor cable. The motor was controlled using the LinMot®-Talk software. The electrical wiring of the components was done by the electrical workshop of the Biocenter and the production of the stainless-steel motor mount and the installation of the motor was done by the central workshop of the Biocenter. A detailed protocol for the generation of high-density primary human skin equivalents is described in 5.2.4.1.

2.2 Plastic compression improves mechanical properties and reduces dermal contraction and weight loss in high-density skin equivalents

In this work, the dermal component of each high-density skin equivalent was generated using 4.52×10^4 primary normal human dermal fibroblasts (NHDFs) and 800 µl reconstituted collagen gel. The ideal number of NHDFs was previously determined by Tamara Finger during her bachelor thesis (Finger, 2016). The 800 µl of reconstituted collagen gel were compressed by a factor of 7.1 and the final volume of each compressed high-density dermal equivalent (hdDE) was 113 µl by default (h = 1 mm, Ø = 12 mm). Thus, the initial concentration of NHDFs per hdDE was 4×10^5 cells/ml. The in-house isolated rat tail collagen type I used for the dermal component had a final concentration of 10 mg/ml and after reconstitution a concentration of 6.66 mg/ml. Consequently, the calculated final collagen concentration of compressed hdDEs was 47.2 mg/ml, in contrast to the non-compressed low-density dermal equivalents (ldDEs) with a 7-fold lower concentration.

A long-term comparison over 3 weeks between ldDEs ($c_{collagen}$ = 6.66 mg/ml) and hdDEs ($c_{collagen}$ = 47.2 mg/ml) revealed that hdDEs showed significantly less contraction and weight loss (Figure 8 A and 8 B). Whereas hdDEs lost only 6.7 ± 10.5 % of weight and 15.7 ± 4.4 % of area in 3 weeks of culture, ldDEs lost more than 82.7 ± 3.7 % and 71.8 ± 2.3 %, respectively. In both dermal equivalents the proliferation of dermal fibroblasts was comparable with no significant difference in cell count at day 21 (hdDE: $2.3 \pm 0.48 \times 10^5$ versus ldDE: $2.13 \pm 0.65 \times 10^5$, Figure 8 B). Furthermore, viability staining performed with fluorescein diacetate (FDA, which is hydrolyzed to fluorescent fluorescein in live cells) and propidium iodide (PI, which intercalates in the DNA of dead cells) showed that dermal fibroblasts survived compression (Figure 8 C).

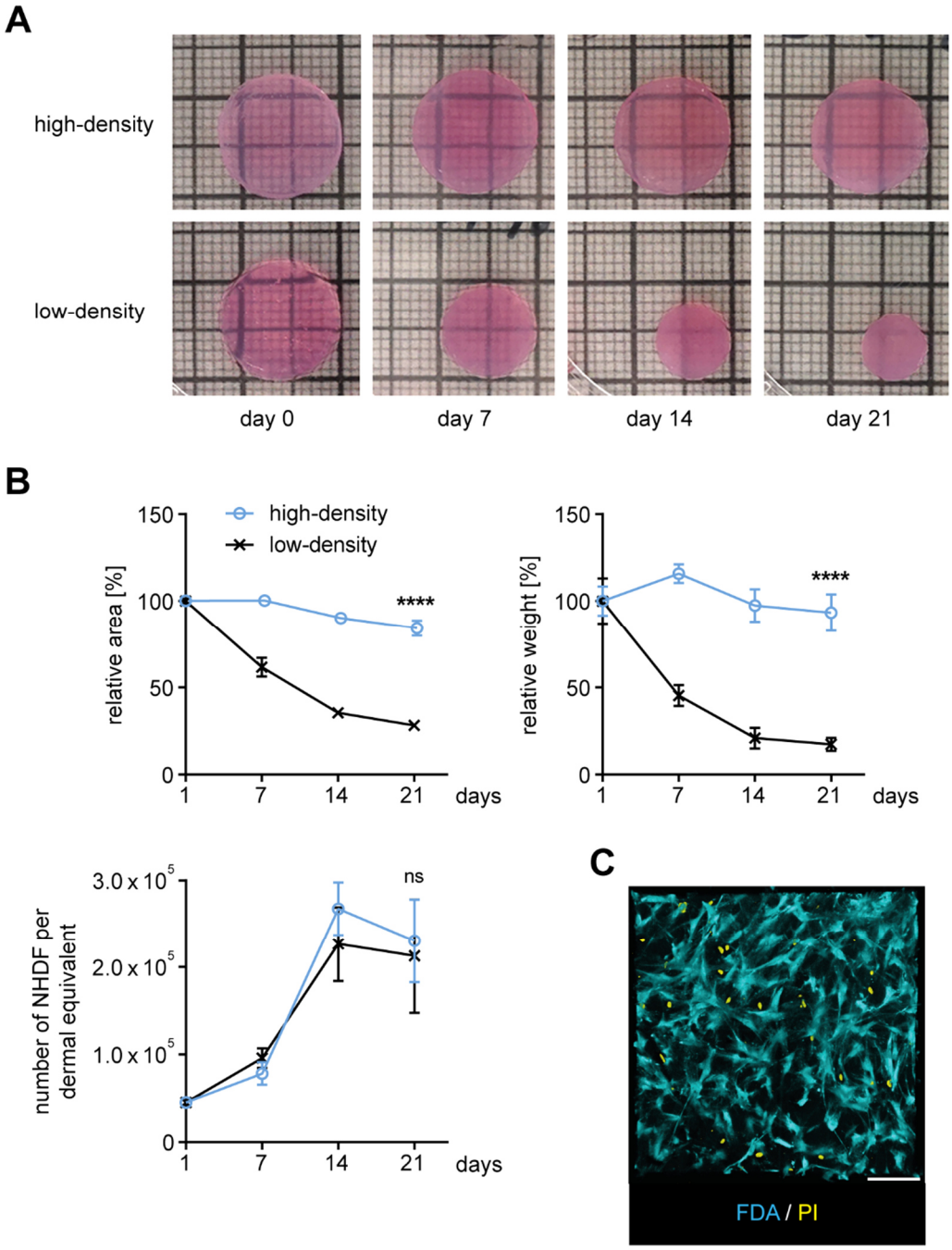

Figure 8: Plastic compression of dermal equivalents reduces dermal shrinkage and weight loss. (A) Images of high-density ($c_{collagen}$ = 47.2 mg/ml) and low-density ($c_{collagen}$ = 6.66 mg/ml) dermal equivalents at various culture times show massive shrinkage of low-density dermal equivalents. Dermal equivalents were cultured for up to 3 weeks and their area and weight were determined each week using graph paper and a precision balance. **(B)** Quantification of the relative dermal area and weight, and the total number of fibroblasts (NHDF) in high- and low-density dermal equivalents. Experiments were conducted three times in triplicates. Graphs represent the mean value with corresponding SDs. ****: $p < 0.0001$, ns: not significant. Statistical analyses were performed with the Student's *t*-test. **(C)** Assessment of fibroblast viability in a high-density dermal equivalent 3 weeks after compression. Fibroblasts were stained with fluorescein diacetate (FDA, cyan) and propidium iodide (PI, yellow) for live/dead discrimination. Scale bar, 100 µm.

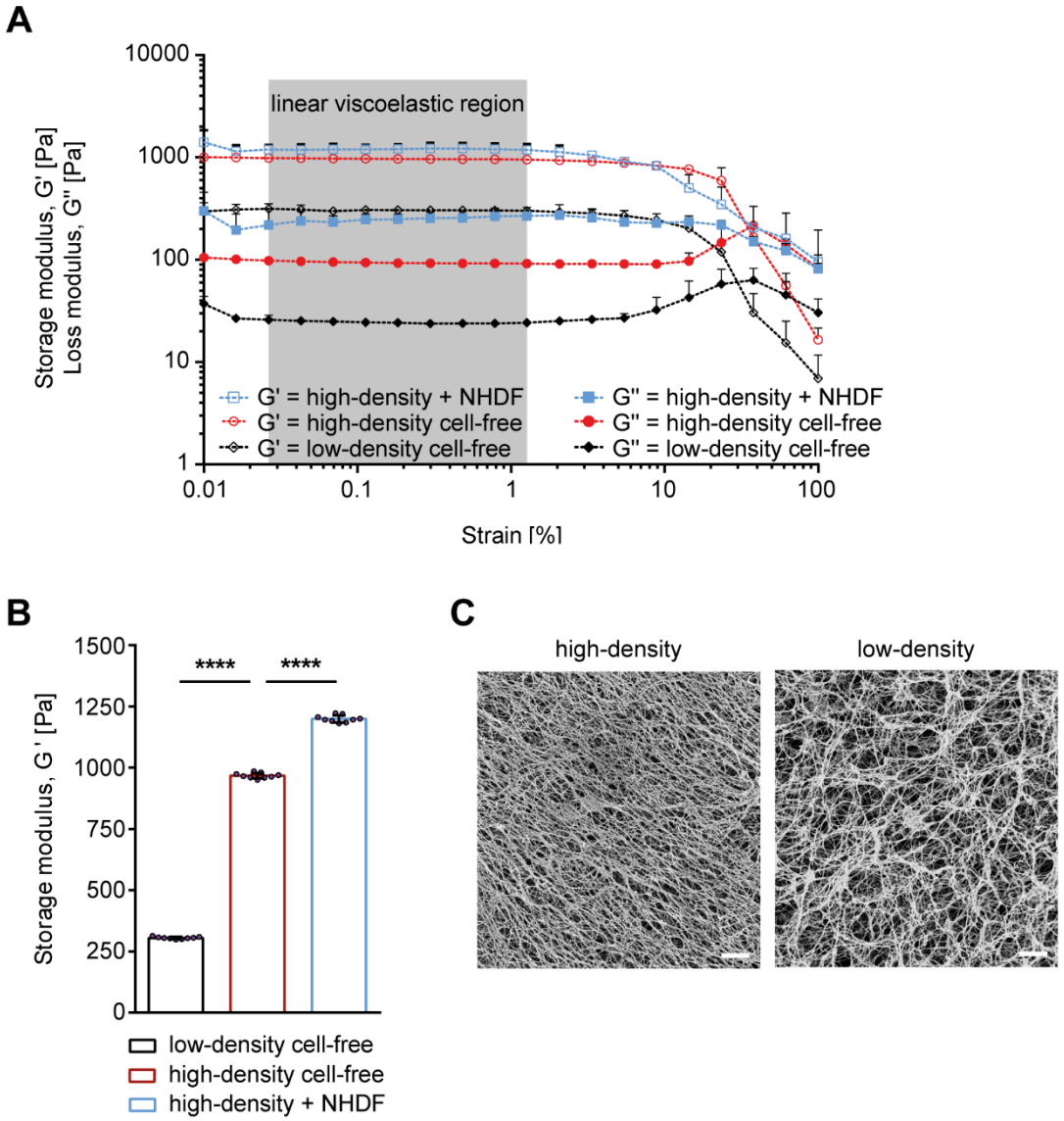

Figure 9: High-density dermal equivalents have improved mechanical properties. (A) Data plot of oscillatory rheological measurements. Storage, G′ (open circles/squares), and loss moduli, G″ (filled circles/squares), of cell-free and NHDF-populated high- and low-density dermal equivalents were determined in dependency on the strain deformation measured at ω = 6.28 rad/s and T = 22 °C. The linear viscoelastic region (gray box) was determined according to DIN 53019-4. **(B)** The storage moduli G′ of NHDF-populated and cell-free, high- and low-density dermal equivalents indicate improved mechanical properties of high-density dermal equivalents. One to two experiments were conducted in triplicates. Graphs represent the mean value with corresponding SDs. The mean ± SD of G′ was calculated from values in the linear viscoelastic region. ****: $p < 0.0001$. For statistical analysis, the Student's *t*-test was employed. **(C)** Scanning electron microscopy of the fibrillar collagen ultrastructure of high- and low-density dermal equivalents show a denser collagen network in high-density dermal equivalents. Scale bar, 2 µm.

As a consequence of the increased collagen concentration, the mechanical properties of the hydrogels were improved, as demonstrated by rheology. The rheological measurements were performed by Philipp Fey during his master thesis (Fey, 2017). For characterization, hdDEs and ldDEs were prepared and storage modulus G′ was used as a measure of hydrogel strength. All dermal equivalents showed linear behavior of G′ between 0.0264 and 1.27 % strain (Figure 9 A, gray box). However, ldDEs showed an earlier flow point (G′ = G″) than hdDEs, correlating with a lower structural resistance against shear forces. Furthermore, hdDEs had an approximately three times higher G′ compared to ldDEs in the linear viscoelastic region, indicating stronger viscoelastic strength of the cell-free hdDEs (Figure 9 B). The viscoelastic strength was even more pronounced in hdDEs colonized with NHDFs for 23 days. Thus, plastic compression of the dermal equivalents resulted in increased strength, as G′ was tripled and the flow point was extended. In addition to the rheological analysis, scanning electron microscopy was performed to confirm proper assembly of collagen fibers (Figure 9 C). Both, ldDEs and hdDEs, showed proper polymerization of collagen fibers, however, in contrast to ldDEs, the collagen fibers in hdDEs showed a denser and more uniform distribution.

2.3 Set-up of infection parameters for co-cultivation of *T. brucei* parasites and high-density skin equivalents

An infection model must not only reflect the natural environment of the tissue as accurately as possible, but also provide a suitable habitat for the pathogen. In addition, for long-term studies, the infected model should continue to be as close to nature as possible and respond only to factors that are actually attributable to the pathogen and not to external factors independent of the pathogen, such as media change, nutrient supply, or change in pH.

In order to find optimal conditions that support both growth of parasites and skin equivalents different media compositions were tested. For this, the monomorphic *T. brucei* strain MITat 1.2 was grown in different media and monitored for 3 weeks (Figure 10 A). Parasites grown in the skin-specific medium E3 died after 9 days in culture, regardless of whether the medium was supplemented with 10 % FCS or not. In contrast, trypanosomes cultured in the trypanosome-specific medium HMI9 or a 1:1 mixture of HMI9 and E3 (= infection medium; INF) exhibited exponential growth

and long-term survival. Moreover, the parasites showed a comparable growth and population doubling time (PDT) in both media (PDT_{HMI9} = 6.2 h, PDT_{INF} = 6.4 h).

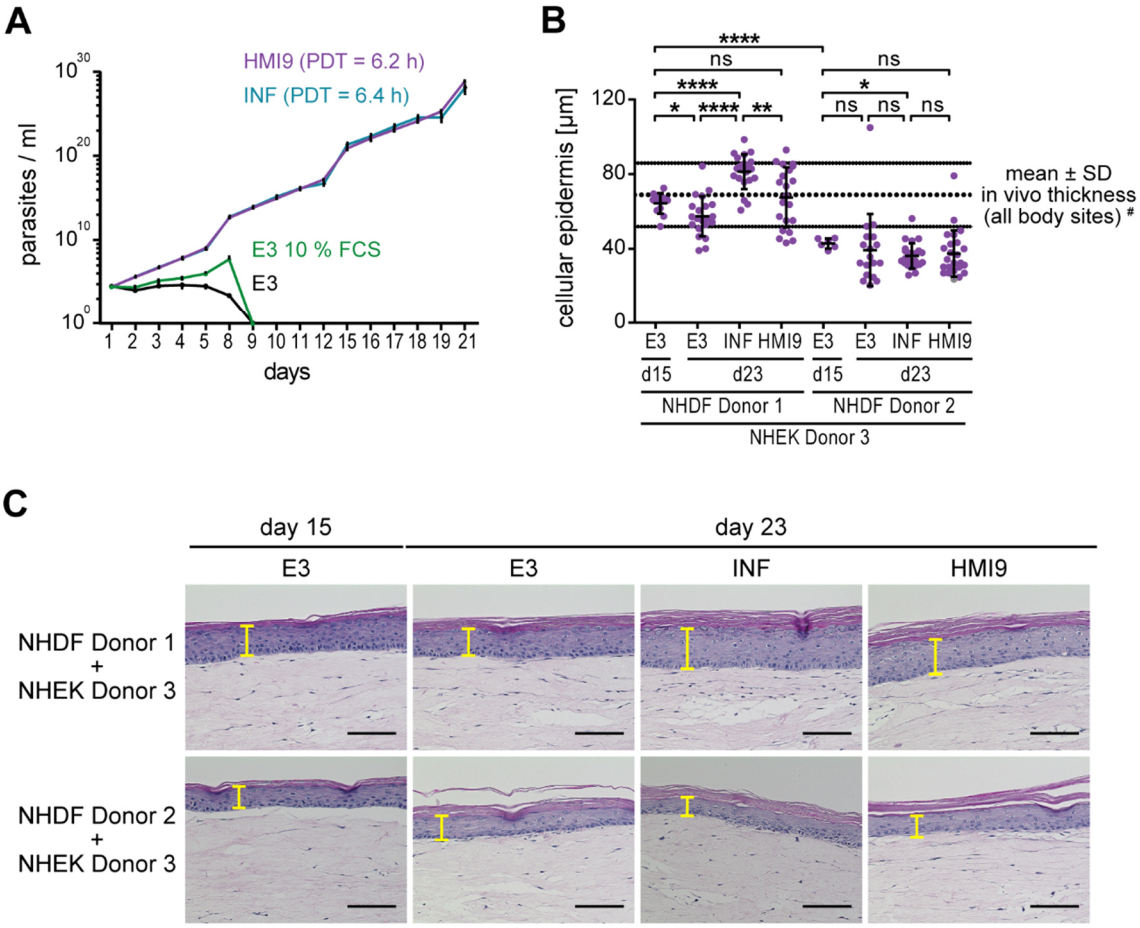

Figure 10: Trypanosomes and skin equivalents can be cultured with the same medium without detrimental effects. (A) Growth curves of the *T. brucei* strain MITat 1.2 grown in HMI9 (purple), INF (cyan), and E3 (suppl. with 10 % FCS, green; w/o FCS, black) medium. The mean ± SD of three replicates is shown for each condition. **(B)** Analysis of the thickness of the cellular epidermis of high-density skin equivalents generated with NHDFs from two different donors and NHEKs from a third donor. In addition, skin equivalents were cultured with E3 medium until day 15. On day 15, the medium was changed to E3, INF, or HMI9 until day 23. Image J was used to measure the thickness of the cellular epidermis in hematoxylin and eosin-stained cross sections of skin equivalents. Each approach was performed in triplicates and measurements were taken at the thickest and thinnest region of the cellular epidermis. Data represent mean ± SD. # (Sandby-Moller et al., 2003). ****: $p < 0.0001$, **: $p < 0.01$, *: $p < 0.05$, ns: not significant. Statistical analyses were performed with the Student's *t*-test. **(C)** Representative images of hematoxylin and eosin-stained cross sections of skin equivalents cultured with E3, INF, or HMI9 media at day 23 compared with day 15. The yellow markings indicate the thickness of the cellular epidermis. Tissue samples were fixed with 4 % PFA, embedded in paraffin and sectioned into 5 µm thick slices for subsequent hematoxylin and eosin staining. Scale bar, 100 µm.

On the other hand, it had to be ensured that the skin equivalents could be cultured with INF medium without negative effects. In addition, primary cells show a great variety regarding donor compatibility and quality. Therefore, in addition to the different media, NHDFs from two different donors were tested for compatibility with normal primary human epidermal keratinocytes (NHEKs) from a third donor (Figure 10 B and 10 C). For this purpose, high-density skin equivalents (hdSEs) were generated with NHDFs from one of the two NHDF donors and the NHEKs of the third donor. In addition, different culture media were tested and compared from day 15 to 23. To investigate whether a medium switch from E3 to INF or HMI9 had a negative effect on epidermal tissue maintenance, skin equivalents were fixed with 4 % PFA, processed for paraffin sectioning, and stained with hematoxylin and eosin (Figure 10 C). The histological staining highlights cell nuclei in blue, followed by counterstaining of eosinophilic structures in shades of red and pink. Subsequently, the thickness of the cellular epidermis was measured both immediately before the medium switch (d15) and 8 days after the switch (d23) at the thickest and thinnest region with Image J (Figure 10 B).

In case of good donor compatibility (NHDF donor 1 + NHEK donor 3) the cellular epidermis on day 15 was with 64.4 ± 5.6 µm one-third thicker than in case of poor compatibility with 43.0 ± 2.7 µm (NHDF donor 2 + NHEK donor 3). In case of poor compatibility, a subsequent switch to a different medium had no positive influence. In fact, continuous culture in E3 medium resulted in a decrease by 8.4 % in the mean thickness of the cellular epidermis and a further decrease by 15.6 % and 12.8 % when switching to INF or HMI9 medium, respectively. Furthermore, under all conditions, the mean thickness of the cellular epidermis was outside the lower deviation of the *in vivo* epidermal thickness of native human skin (Sandby-Moller et al., 2003).

By contrast, in case of good compatibility, switching to INF medium increased the mean epidermal thickness by 26.2 %, whereas continuous culture in E3 medium led to a decrease by 10.7 %. Furthermore, a slight increase in the mean epidermal thickness by 4.8 % could be observed after switching to HMI9 medium. Under all conditions, the mean thickness of the cellular epidermis was in the range of the *in vivo* thickness.

In summary, these results demonstrate that trypanosomes cultured with INF medium showed no growth deficits in comparison to the trypanosome-specific medium HMI9. Likewise, the hdSEs showed no detrimental effects when cultured with INF medium. In fact, in case of good donor compatibility, a switch from E3 to INF medium on day 15

significantly increased the mean thickness of the cellular epidermis by 29.3 % on day 23 compared to a continued culture with E3 medium. Compared to human skin, the hdSEs cultured with INF medium had a thickness of 81.3 ± 9.4 µm, which is in the upper range of the mean *in vivo* thickness of the cellular epidermis. Overall, these results indicate that trypanosomes and hdSEs can be co-cultured with INF medium without detrimental effects.

2.4 High-density primary human skin equivalents resemble native human skin in its histological architecture as well as in the development of distinctive physiological parameters

2.4.1 Histological comparison between the high-density skin equivalent and native human skin

To investigate whether the morphology of hdSEs is comparable to native human skin, hdSEs were fixed with 4 % PFA at different maturity stages and paraffin-embedded sections were prepared and stained with hematoxylin and eosin. As a control, prepuce biopsies from juvenile donors were processed in the same way to consider the effects on native tissue during embedding, dissection, and staining (Figure 11 A).

Nine days after preparation the hdSE still showed an immature epidermis. Although a first cornified layer had already formed, the overall structure was still unorganized and the individual layers were not yet distinguishable. In contrast, the four characteristic layers of the human skin could be distinguished on day 15. The *stratum corneum* had increased in thickness (Figure 11 A - a) and the *stratum basale* had formed a palisade-like structure with polarized, elongated cells (Figure 11 A - d). Furthermore, the layers *stratum spinosum* (Figure 11 A - b), in which the gradual cornification of the keratinocytes is initiated, and *stratum granulosum* (Figure 11 A - c), in which the cells gradually flatten and the cytoplasm appears granular, could be identified. On day 23, the four different layers were even more pronounced and clearly distinguishable. On days 15 and 23, the overall morphology of the hdSEs was reminiscent of native human skin in direct comparison. Thus, in a time window of minimally 9 days, the tissue architecture of the hdSE resembled native human skin. Both the structure of the epidermis with the four characteristic layers and the architecture of the dermis with the fibroblasts

(Figure 11 A - blue arrows) were comparable. However, the hdSEs lacked vascular structures that were naturally present in the native skin (Figure 11 A - red arrows).

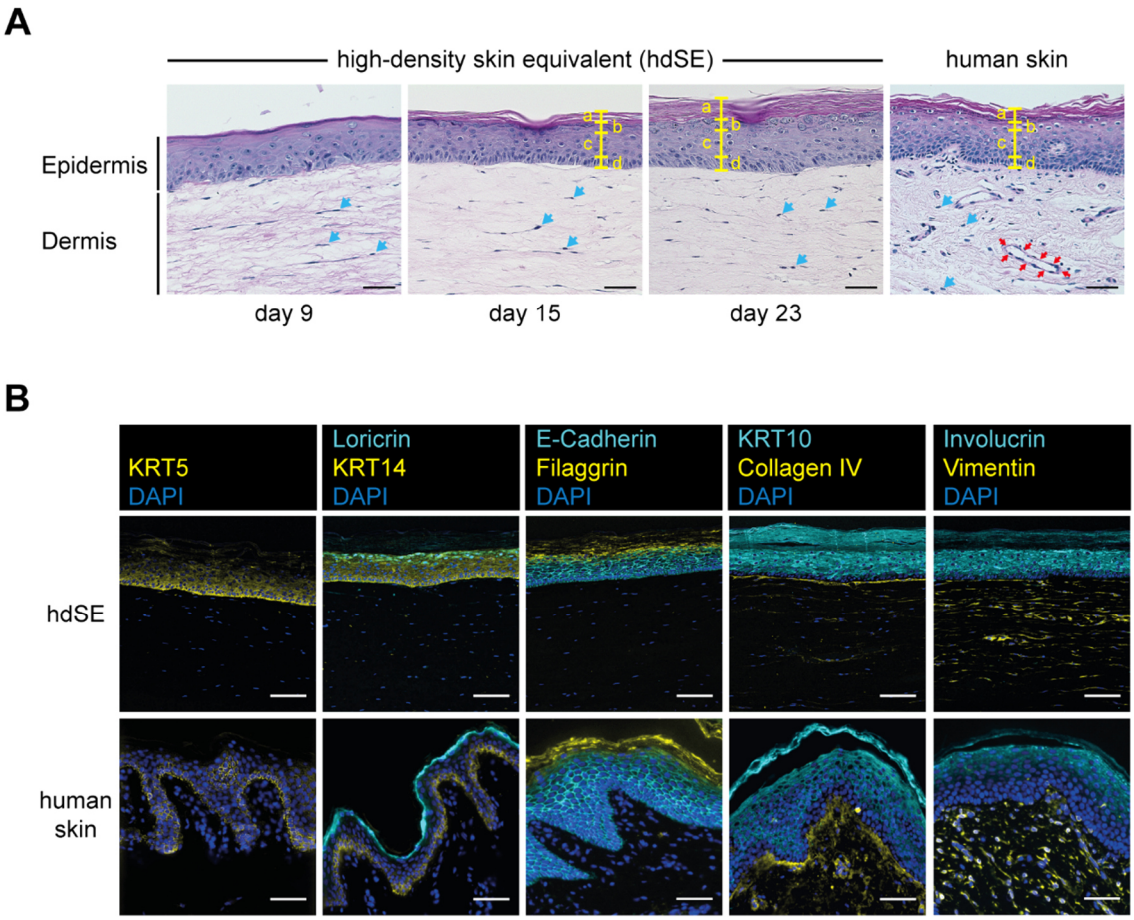

Figure 11: The high-density skin equivalent resembles native human skin. (A) Histological analysis of the morphology of hdSEs in comparison to native human skin. Representative images of hdSEs cultured for 9, 15, and 23 days and native human skin from prepuce biopsies are shown. The yellow markings refer to the individual layers of the epidermis: a = *stratum corneum*, b = *stratum granulosum*, c = *stratum spinosum*, d = *stratum basale*. The blue arrows mark NHDFs present in the dermis and the red arrows mark a vascular structure. Tissue samples were fixed with 4 % PFA, embedded in paraffin, and sectioned into 5 µm thick slices for subsequent hematoxylin and eosin staining. Scale bar, 40 µm. **(B)** Immunohistochemical analysis of distinctive physiological markers expressed in hdSEs and native human skin. Representative images of hdSEs cultured for 23 days and prepuce biopsies are shown. Tissue samples were fixed with 4 % PFA, embedded in paraffin, and sectioned into 5 µm thick slices for subsequent staining with DAPI (nuclei, blue) and antibodies against Loricrin, E-Cadherin, Cytokeratin 10 (KRT10), Involucrin (all cyan), and Cytokeratin 5 (KRT5) and 14 (KRT14), Filaggrin, Collagen IV, and Vimentin (all yellow). Scale bar, 75 µm.

In addition, immunohistochemical staining of distinctive physiological markers was performed. For this, hdSEs cultured for 23 days and prepuce biopsies from juvenile donors were stained with specific antibodies to detect various marker proteins (Figure 11 B). A comparative analysis revealed that important physiological skin markers were expressed in the hdSEs. The presence of epidermal differentiation markers such as KRT5 and KRT14 in the basal layer, KRT10 in the suprabasal layers, and loricrin, filaggrin, and involucrin in the *stratum granulosum* and *stratum corneum* verified an anatomically correct differentiation of the epidermis. Additionally, positive staining for E-cadherin indicates fully developed cell-cell junctions, which are important for the epidermal barrier function (Tunggal et al., 2005). The detection of collagen IV demonstrated the presence of basement membrane proteins at the structurally and biochemically complex dermal-epidermal junction. Moreover, the homogenous distribution of vimentin-positive cells in the dermis indicated the presence of NHDFs.

In conclusion, the hdSE resembles native human skin in its histological architecture as well as in the development of distinctive physiological parameters from day 15 to at least day 23.

2.4.2 Single-cell RNA sequencing details the cellular heterogeneity of the high-density skin equivalent

To define the cellular heterogeneity of the hdSE in more detail single-cell RNA sequencing (scRNAseq) was performed using the droplet based 10x Genomics platform (Figure 12 A, (Macosko et al., 2015)). For this purpose, the epidermis and dermis of two hdSEs were separated and dissociated by trypsin- and liberase-treatment, respectively. Subsequently, the obtained cell suspensions were sorted by fluorescence activated cell sorting (FACS) and single, viable cells were collected. The single cell suspension was processed on a microfluidic chip to form reaction vesicles called “Gel Beads in Emulsion” (GEMs). Each GEM contained a single cell, a single gel bead, and reverse transcription reagents. Each gel bead contained oligonucleotides with a unique barcode specific to the gel bead for later identification of transcripts originating from the single cell in the GEM.

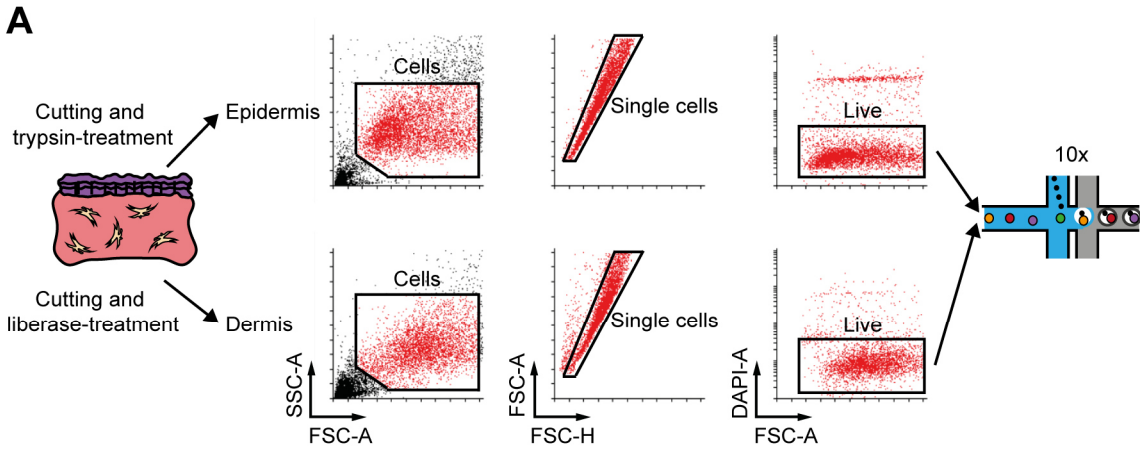

B

Sequencing statistics		Mapping statistics		Cells statistics	
Number of reads	815,786,691	Reads mapped to genome	97.3 %	Estimated number of cells	8,125
Valid barcodes	98.5 %	Reads mapped confidently to genome	94.2 %	Fraction reads in cells	92.0 %
Valid UMIs	100.0 %	Reads mapped confidently to intergenic regions	3.2 %	Mean reads per cell	100,405
Sequencing saturation	46.1 %	Reads mapped confidently to intronic regions	13.5 %	Median genes per cell	5,019
Q30 bases in barcode	96.7 %	Reads mapped confidently to exonic regions	77.5 %	Total genes detected	24,821
Q30 bases in RNA read	94.9 %	Reads mapped confidently to transcriptome	73.5 %	Median UMI counts per cell	34,970
Q30 bases in sample index	95.4 %	Reads mapped antisense to gene	1.1 %		
Q30 bases in UMI	96.5 %				

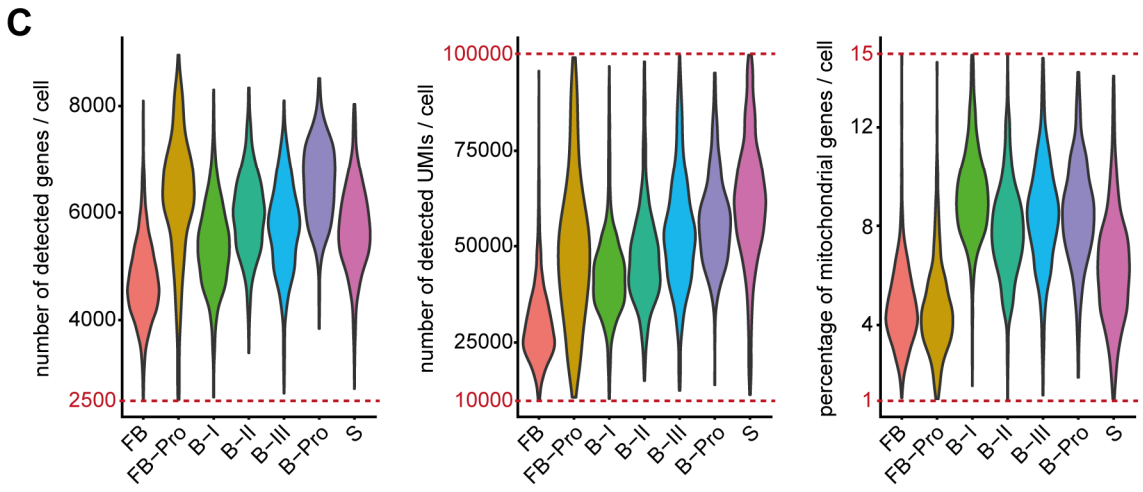

Figure 12: Workflow, statistics, and quality control of the single-cell RNA sequencing experiment of high-density skin equivalents. (A) Schematic representation of the experimental pipeline of the single-cell RNA sequencing of high-density skin equivalents. The epidermis and dermis of two skin equivalents were separated, cut, and dissociated by trypsin- or liberase-treatment. Cell suspensions were subjected to FACS and single, live cells were sorted. Subsequently, 10,000 single cells were loaded on the droplet-based 10x platform according to the manufacturers' instructions and sequenced. **(B)** Statistics of the demultiplexed and aligned sequencing reads with CellRanger software. Reads were mapped to the human reference genome GRCh38. 8,125 single cells were recovered. A total of 815,786,691 reads were obtained and 92 % originated from identified cells. An average of 100,405 reads per cell were observed and 24,821 different genes across the profiled cells were detected, with a median of 5,019 expressed genes detected per cell. **(C)** Quality control of mapped sequencing reads showing the number of detected genes, UMIs (unique molecular identifier), and the percentage of mitochondrial genes per cell in each of the 7 subclusters shown in Figure 13 A. The red lines in each graph represent quality control thresholds and cells above or below these thresholds were excluded from analysis.

In the subsequent reaction, within each GEM reaction vesicle, the single cell was lysed, the polyadenylated mRNAs bound to the oligonucleotides of the dissolved gel bead, and reverse transcription was performed. As a result, all cDNAs from a single cell had the same barcode, allowing the sequencing reads to be mapped back to their original single cells of origin. The preparation of libraries from these barcoded cDNAs was then carried out in a bulk reaction. The GEMs were dissociated, cDNAs were amplified and cleaned-up, and Illumina sequencing adaptors were added.

After sequencing, all reads were demultiplexed and mapped to the human reference genome GRCh38 with the CellRanger software (Figure 12 B). The aim was to sequence 10,000 single cells, of which 8,125 cells were recovered. A total of 815,786,691 reads were obtained, of which 98.5 % had valid barcodes and 100 % had valid unique molecular identifier (UMI) sequences. The nucleotides of all obtained reads had a high quality as ≥ 94.9 % of the RNA reads had a quality score of Q30. The quality score Q30 is a measure to predict the accuracy of nucleotide identity and is defined such that one base call in 1,000 is predicted to be incorrect. Of all reads 94.2 % were confidentially mapped to the human genome and 92 % originated from the 8,125 identified cells. On average, 100,405 reads per cell were observed, with a median of 5,019 expressed genes detected per cell. Across the profiled cells, a total of 24,821 different genes were detected. The gene expression analysis was based on unique molecular identifier (UMI) counts. In addition to the unique barcode that allows the transcripts to be traced back to their original single cell, each oligonucleotide contained an additional UMI sequence that allows accurate quantification of the mRNA molecules that were present in the cell. A median of 34,970 UMI counts per cell were observed (Table S1).

The obtained digital gene expression matrix was subsequently analyzed with the Seurat software package (Butler et al., 2018). Quality control was performed and only cells with > 2,500 genes, 10^4 to 10^5 UMIs, and 1 % to 15 % mitochondrial genes were considered for downstream analyses (Figure 12 C). Cells with < 2,500 genes, less than 10^4 UMIs, and < 1 % mitochondrial genes were most likely empty GEMs containing no cell. Cells with > 15 % mitochondrial genes were considered as apoptotic or broken cells (Ilicic et al., 2016).

Data analysis of 5,958 cells that passed quality control resulted in a t-distributed stochastic neighbor embedding (t-SNE) plot displaying 7 clusters with distinct expression profiles (Figure 13 A and Table S1). All clusters were confirmed by the expression of

known marker genes (Figure 13 B). Fibroblasts were identified in two clusters (clusters FB and FB-Pro) by their archetypal markers DCN and LUM (Philippeos et al., 2018). Keratinocytes were detected in 5 clusters and their diversity was mainly due to their degree of differentiation. Basal keratinocytes (clusters B-I, B-II, B-III, and B-Pro) highly

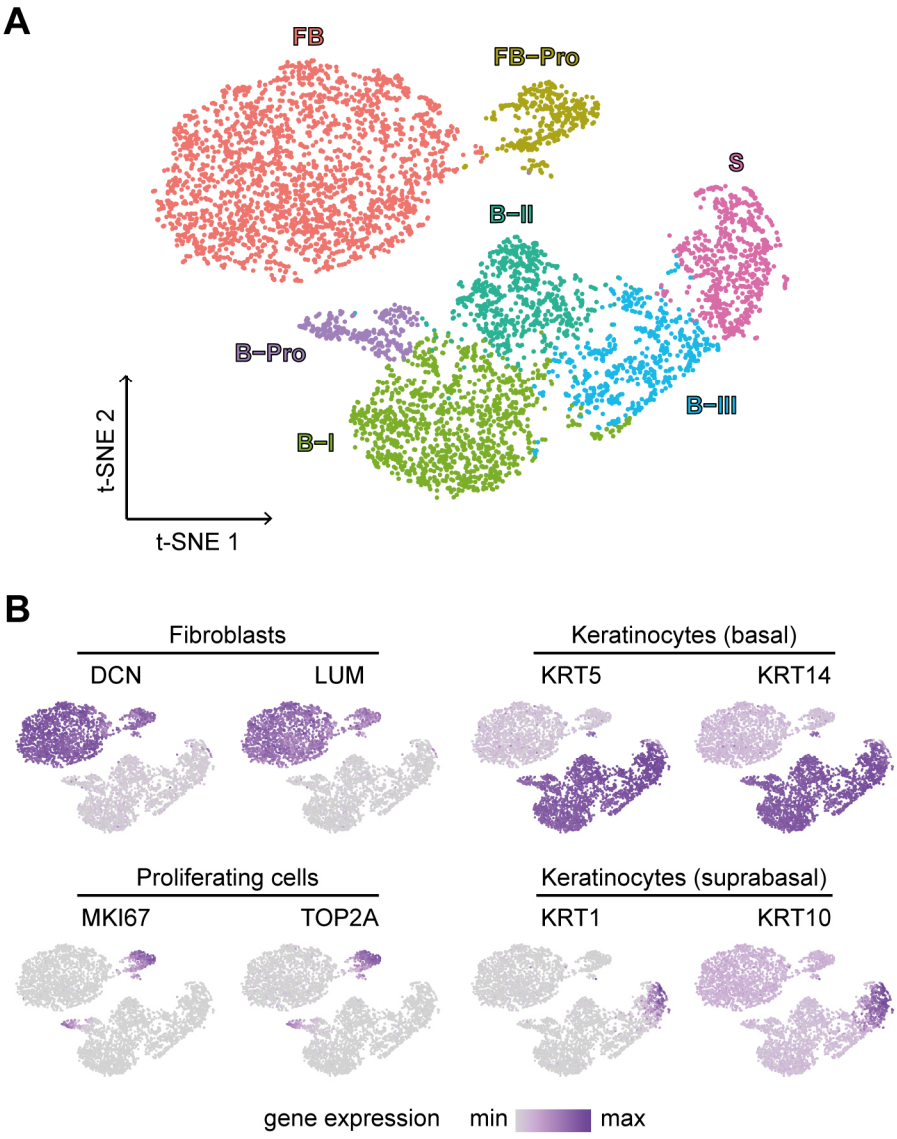

Figure 13: Defining cell populations in the high-density skin equivalent using single-cell RNA sequencing. (A) t-Distributed stochastic neighbor embedding (t-SNE) plot of 5,958 cells that passed quality control derived from two hdSEs at day 23. Skin cells were grouped in 7 clusters including fibroblasts (FB), proliferating fibroblasts (FB-Pro), basal (B-I - III), spinous (S), and proliferating keratinocytes (B-Pro). **(B)** Feature plots show the expression of fibroblast and keratinocyte markers from basal, suprabasal, and proliferating cells. Normalized gene expression levels for each cell are color-coded from gray to purple and overlaid onto the t-SNE plot. Fibroblasts were identified using the marker genes decorin (DCN) and lumican (LUM). Basal keratinocytes were recognized based on cytokeratin 5 (KRT5) and cytokeratin 14 (KRT14), whereas suprabasal keratinocytes were identified based on the marker genes cytokeratin 1 (KRT1) and cytokeratin 10 (KRT10). The marker genes MKI67 (Marker of Proliferation Ki-67) and TOP2A (DNA Topoisomerase II Alpha) were used to detect proliferating fibroblasts and keratinocytes.

expressed KRT5 and KRT14, whereas suprabasal keratinocytes (S) specifically expressed KRT1 and KRT10. Proliferating cells were present in both cell type populations. They were identified by their expression of mitotic markers such as MKI67 and TOP2A (clusters FB-Pro and B-Pro).

Differential gene expression analysis of the 5 keratinocyte subclusters revealed 3 clusters of basal keratinocytes (B-I, B-II, and B-III), which is in good agreement with native human skin (Wang et al., 2020). In addition to KRT5 and KRT14, the B-I cluster was also characterized by KRT15, DAPL1, and CXCL14. CXCL14 is constitutively expressed in skin and produced by keratinocytes (Meuter and Moser, 2008). Cluster B-II contained mainly genes that are important for the formation of hemidesmosomes and the attachment of the epidermis to the dermis via the basement membrane such as LAMA3, LAMB3, LAMC2, ITGA6, ITGB4, DST, PLEC, COL7A1, and COL17A1 (Figure 14 and 15, and Table S1). Cluster B-III was defined by RHCG, KRT6A, and KRT16. This is in line with the results of a previous study using native human skin and it was assumed that these cells could directly differentiate into spinous cells (Wang et al., 2020). Spinous cells in cluster S expressed known markers for epidermal differentiation such as SBSN or KRTDAP. Cluster B-Pro was enriched for cell cycle marker genes (UBE2C, PCNA).

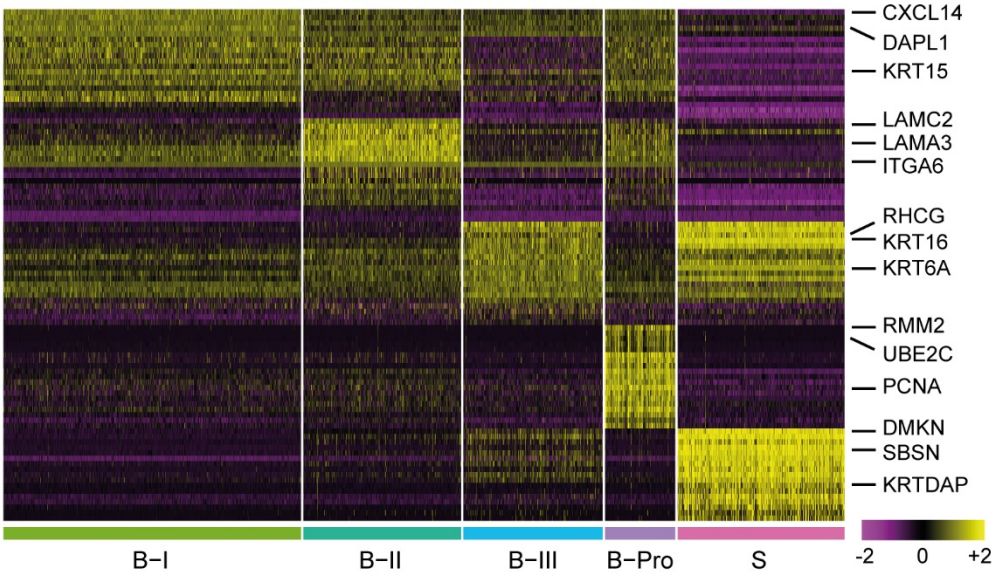

Figure 14: Differential gene expression analysis of the keratinocyte subclusters. Heatmap showing the scaled expression levels of the 20 most differentially expressed genes in each of the five clusters of epidermal keratinocytes (basal (B-I - III), spinous (S), and proliferating keratinocytes (B-Pro)). Each column in the respective cluster assignment represents a single cell, and each row represents an individual gene. The color key from pink to yellow indicates low to high gene expression levels. Cell-type-specific representative genes are listed to the right.

Furthermore, a detailed analysis of extracellular matrix (ECM)-associated genes revealed a remarkable repertoire of expressed ECM genes in the hdSE (Figure 15). Many components of the ECM, including the collagens COL1A1, COL1A2, COL3A1, COL12A1, as well as elastin (ELN), fibronectin (FN1), and fibrillin (FBN1) were expressed in the fibroblast clusters. The same was true for factors involved in matrix assembly, such as MFAP4, SFRP2, LOX, FAP, and ANXA2, as well as for proteins involved in matrix remodeling, such as matrix metallopeptidases (MMP2, MMP14) and TIMP metallopeptidase inhibitors (TIMP1, TIMP3).

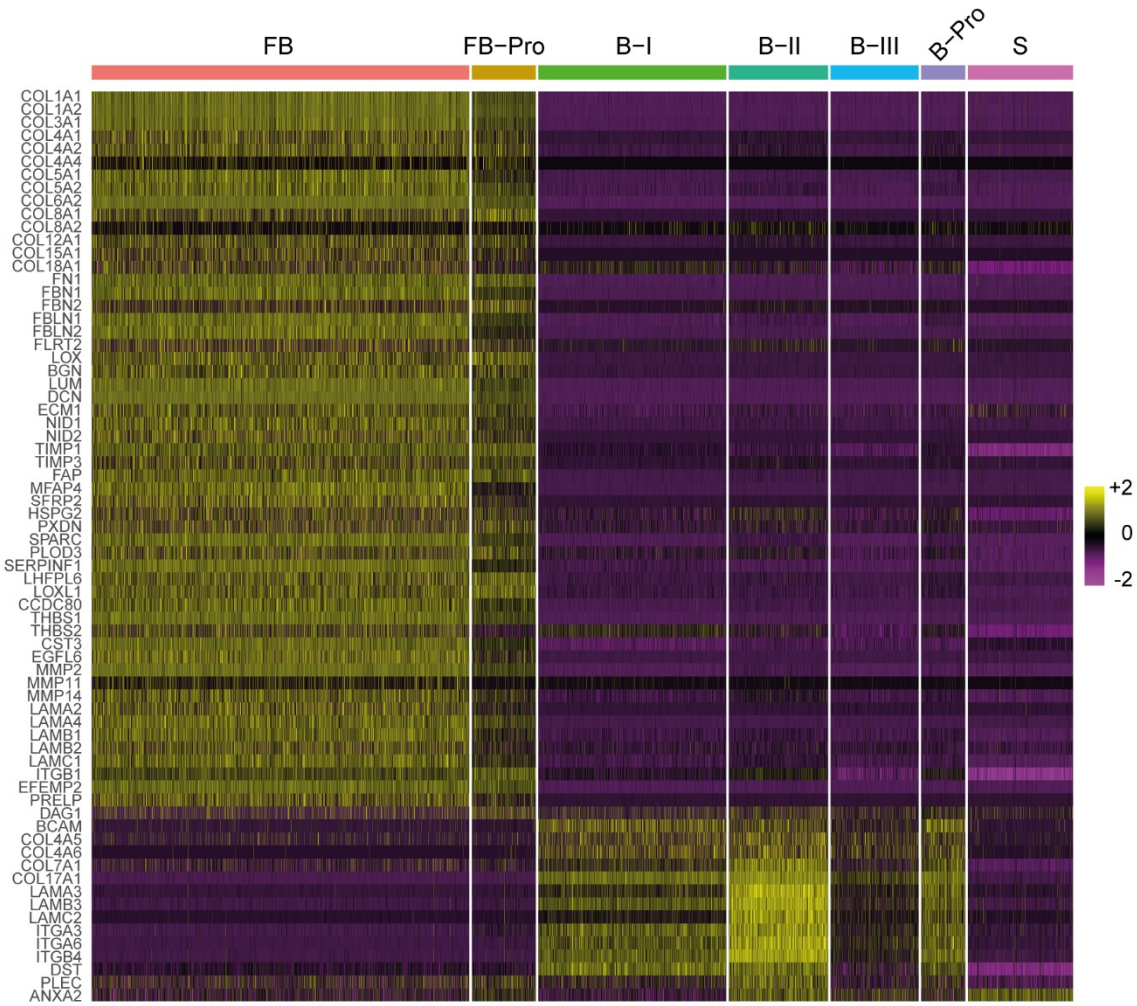

Figure 15: Differential gene expression analysis of extracellular matrix-associated genes in the high-density skin equivalent. Heatmap showing the scaled expression levels of extracellular matrix-associated genes differentially expressed in each of the seven clusters (dermal (FB) and proliferating fibroblasts (FB-Pro), basal (B-I - III), spinous (S), and proliferating keratinocytes (B-Pro)). Each column in the respective cluster assignment represents a single cell, and each row represents an individual gene. The color key from pink to yellow indicates low to high gene expression levels.

In summary, the scRNAseq data demonstrate a high degree of cellular heterogeneity in the hdSE and the expression of genes characteristic of the different cell populations in native human skin.

2.4.3 Integration of endothelial cells allows endothelialization of the high-density skin equivalent

To compensate for the lack of vascular structures in the hdSE, a method was developed to add primary normal human dermal microvascular endothelial cells to the basal side of the skin equivalent. This was achieved by first completely removing the center of the insert membrane in a radius of 4 mm, leaving a hole with a diameter of 8 mm. Since the insert membrane had a diameter of 12 mm, a continuous edge with a width of 2 mm remained, which provided support for the high-density dermal equivalent in the Snapwell insert. Through this opening the basal side of the dermal equivalent was accessible and could be colonized with endothelial cells. A detailed protocol for the generation of endothelialized high-density primary human skin equivalents (endo-hdSEs) is described in 5.2.4.1.4.

Histological analysis of fully developed, chemically fixed, and hematoxylin and eosin-stained endo-hdSEs revealed that the endothelial cells formed a confluent monolayer on the basal side of the skin equivalents (Figure 16 A - orange arrows). This monolayer was consistent over a large area and showed no obvious defects (Figure 16 B - orange arrows; length of the monolayer ~ 750 µm). However, although a cornified layer had formed, the overall morphology of the epidermis seemed to be immature, and not all individual layers could be clearly identified. Moreover, the cellular epidermis appeared to be very thin (Figure 16 A - yellow marking). In addition, the transition of the endothelial cells at the interface between the exposed dermal equivalent and the remaining insert membrane was investigated (Figure 16 C). The analysis of the transition zone indicated that the endothelial cells (Figure 16 C - orange arrows) migrated onto the insert membrane (Figure 16 C - blue arrows) and continued the monolayer without defects.

Overall, the results suggest that the endothelial cells formed a continuous monolayer over the complete basal surface of the skin equivalent. However, with the drawback of a thin and poorly differentiated epidermis.

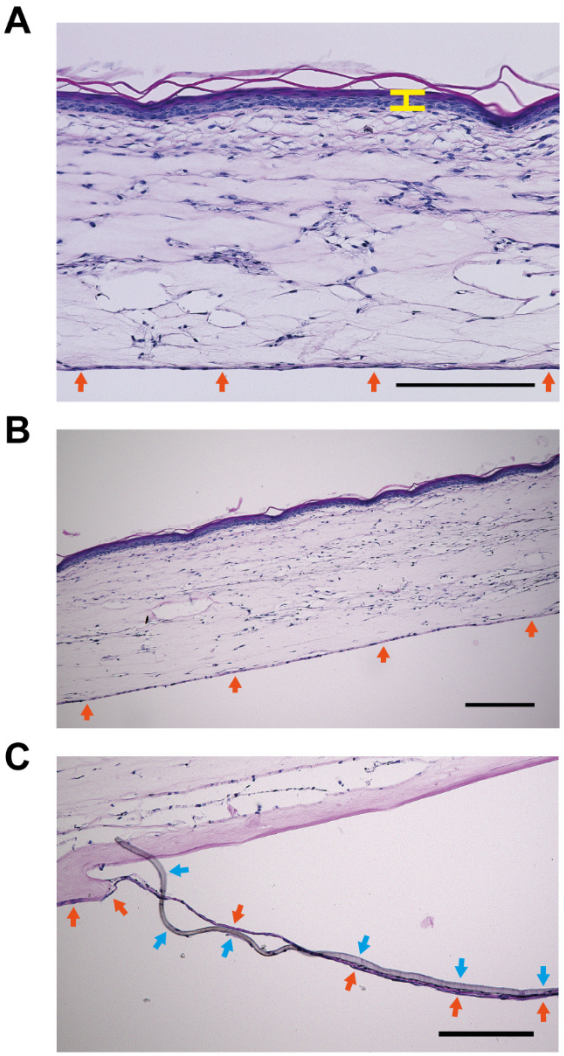

Figure 16: Endothelial cells form a continuous monolayer on the basal side of the high-density skin equivalent. Histological analysis of the morphology of endothelialised hdSEs (endo-hdSEs). Endo-hdSEs were cultured for 23 days, chemically fixed, embedded in paraffin, and sectioned into 5 µm thick slices for subsequent haematoxylin and eosin staining. Scale bars, 100 µm. **(A)** Detailed view of a representative endo-hdSE. The yellow marking indicates the cellular epidermis. **(B)** Large overview of an endothelialised hdSE. The orange arrows mark the confluent monolayer formed by the primary normal human dermal microvascular endothelial cells on the basal side of the skin equivalent. **(C)** Analysis of the transition zone between the exposed dermal equivalent and the remaining insert membrane (blue arrows).

2.5 Elaboration of an optimized protocol for the generation of high-density skin equivalents and subsequent infection with trypanosomes by tsetse flies

The results obtained so far conclude that the compression system developed in this work is suitable for the generation of skin equivalents with improved mechanical properties. The resulting hdSEs have a significantly higher long-term stability and recapitulate key anatomical, cellular, and functional aspects of native human skin. The possibility to culture both *T. brucei* parasites and hdSEs under equal culture conditions without adverse effects suggests that the hdSEs may be a suitable infection model to study the pathogenesis of African trypanosomes in mammalian skin.

However, to implement and standardize this, an optimized protocol for the generation of hdSEs and their subsequent infection with trypanosomes by tsetse flies had to be

elaborated (Figure 17). All subsequent investigations with *T. brucei* described in chapter 3 are based on this protocol.

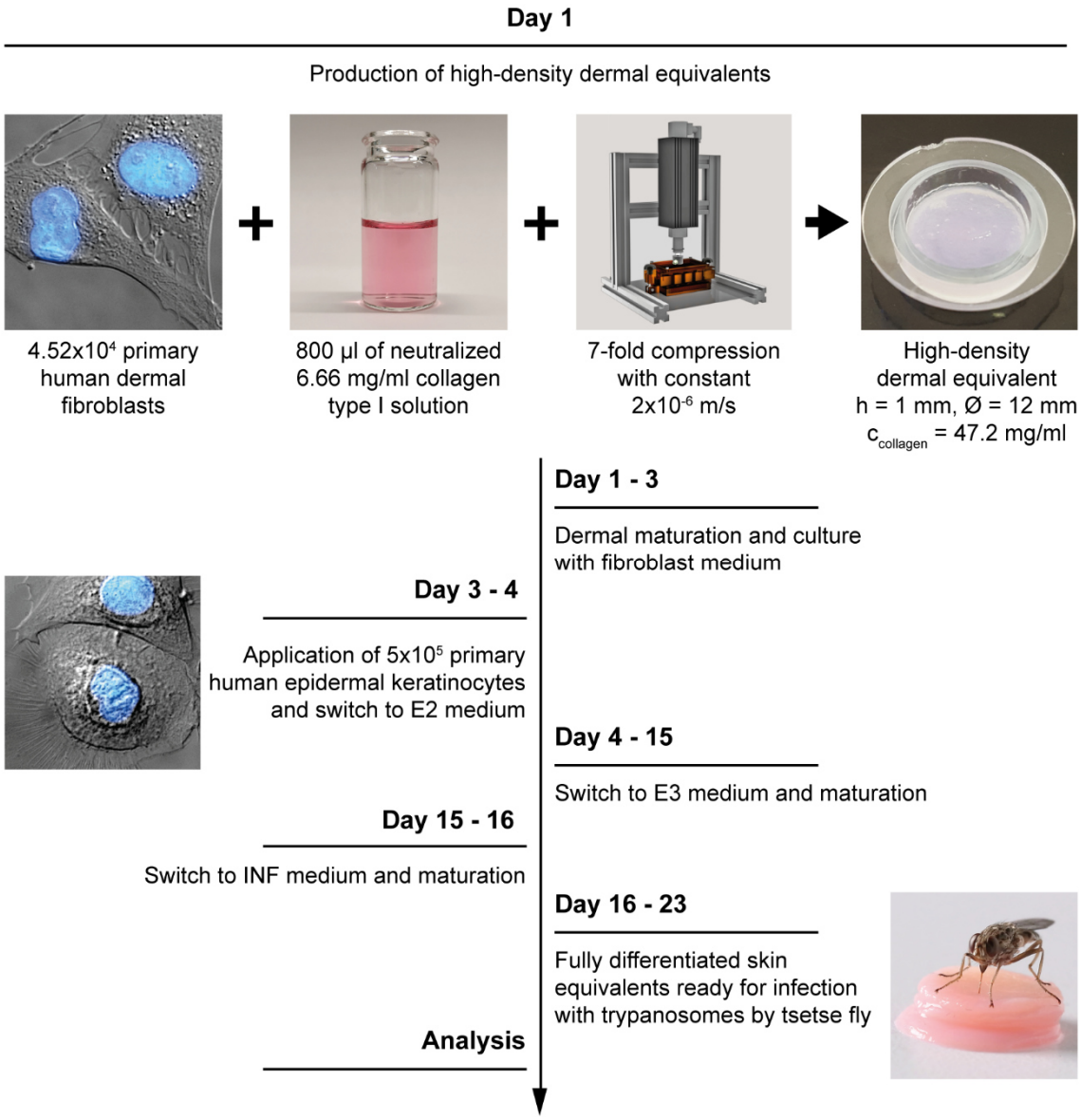

Figure 17: Workflow to implement the high-density skin equivalent as an infection model to study the pathogenesis of African trypanosomes in mammalian skin. An optimized protocol was elaborated for the generation and culture of high-density skin equivalents and their subsequent infection with trypanosomes by tsetse flies. All experiments with *T. brucei* described in chapter 3 are based on this protocol. The protocol can be divided into three main steps: First, on days 1 to 3, the dermal component, consisting of NHDFs and reconstituted collagen, was generated with the compression system and cultured. In the second step from day 3 to 15, the epidermal component was generated by applying NHEKs to the apical side of the dermal component and initiating the culture at the air interface for tissue maturation. In the last step, the mature hdSEs were infected with trypanosomes by tsetse flies. For this purpose, the medium of the hdSEs was changed to INF medium on day 15. From day 16 to 23 the hdSEs were infected with *T. brucei* by salivary gland-positive tsetse flies, depending on further experiments and the duration of culture of the infected skin equivalents.

III. Development of tsetse fly-transmitted *T. brucei* parasites in the high-density primary human skin equivalent

Infection with African trypanosomes starts when metacyclic stage parasites are injected into mammalian skin by a salivary gland-positive tsetse fly. However, knowledge about the early events in the skin after the deposition of the cell cycle-arrested metacyclic forms (MCFs) is currently highly limited. The timing and the mechanisms controlling differentiation remain elusive, as does the characterization of the proliferative skin-residing trypanosomes. The skin equivalent introduced in the previous chapter could act as an infection model. Thus, the aim of the following chapter is to assess whether this *in vitro* engineered tissue is suitable to study the development of tsetse fly-transmitted African trypanosomes in mammalian skin.

3.1 Simulation of natural vector transmission by using tsetse flies to infect skin equivalents with *T. brucei*

Earlier studies clearly indicate that natural transmission of metacyclic trypanosomes by tsetse flies significantly differs from needle injection used routinely in experimental mice (Caljon et al., 2006b, Bai et al., 2015). In order to simulate the infection process in the most natural way, tsetse flies with a mature salivary gland infection were employed to transmit the infective metacyclic stage to the hdSEs (Figure 17). Advantages of vector-borne infection are the natural deposition of the parasites in the skin and the inclusion of potentially infection-modulating factors from fly saliva.

To visualize the injected parasites, the pleomorphic trypanosome strain AnTat 1.1 harboring the two constructs p4231_GFP:PAD1$_{UTR}$ and pTSARib_tdTomato was used. The plasmid p4231 was a courtesy of Mark Carrington and the transgenic strain AnTat 1.1 harboring p4231_GFP:PAD1$_{UTR}$ was generated by Henriette Zimmermann during her doctoral thesis (Zimmermann, 2020). The plasmid pTSARib_tdTomato was a courtesy of Brice Rotureau and the transgenic strain AnTat 1.1 tdTomato + GFP:PAD1$_{UTR}$ was generated by Julia Weingart during her bachelor thesis (Weingart, 2018).

The plasmid p4231 integrates into the tubulin intergenic region and consists of a green fluorescent protein (GFP) open reading frame with a nuclear retention signal, which is coupled to the 3'UTR of the '*protein associated with differentiation 1'* (PAD1). A sequence motif within the 3'UTR mediates the exclusive increase of PAD1 expression upon differentiation from the bloodstream to the stumpy stage (Dean et al., 2009, MacGregor and Matthews, 2012). Consequently, a GFP signal is detectable in the nucleus of stumpy stage parasites. The plasmid pTSARib_tdTomato integrates into the ribosomal DNA locus under control of the rDNA promotor (Xong et al., 1998). Thus, the fluorescent protein tdTomato is constitutively expressed in the cytoplasm of all life cycle stages.

To ensure that the transgene-expressing strain (tdTomato + GFP:PAD1$_{UTR}$) shows no deficits, the growth (Figure 18 A) and the competence to infect tsetse flies (Figure 18 B) were investigated and compared to the wildtype. For tsetse infection, BSFs were differentiated to stumpy forms and fed to teneral tsetse flies. Both, the mutant and the wildtype showed exponential growth over eight observation days with comparable PDTs of 6.8 h for the wildtype and 6.6 h for the mutant. However, in comparison with the wildtype, slightly lower salivary gland infection rates were recorded in flies infected with the transgene-expressing strain. For the wildtype, metacyclic stage parasites could be detected in the saliva of 65 % of the flies, while for the mutant, MCFs were present in the saliva of 52 % of the flies. This could be linked to a slower transition between life cycle stages of the transgenic parasites within the fly. The parasites have five different life cycle stages in the fly, each of which is essential for the passage through several organs to reach and colonize the salivary glands. However, the slight reduction of salivary gland positive flies was not a major concern as only positive flies were used and micrographs of tsetse saliva deposits showed high parasite densities of MCFs in the saliva (Figure 18 C). In addition, the successful colonization of the salivary gland proved that the developmental competence of the transgenic strain was not impaired.

A

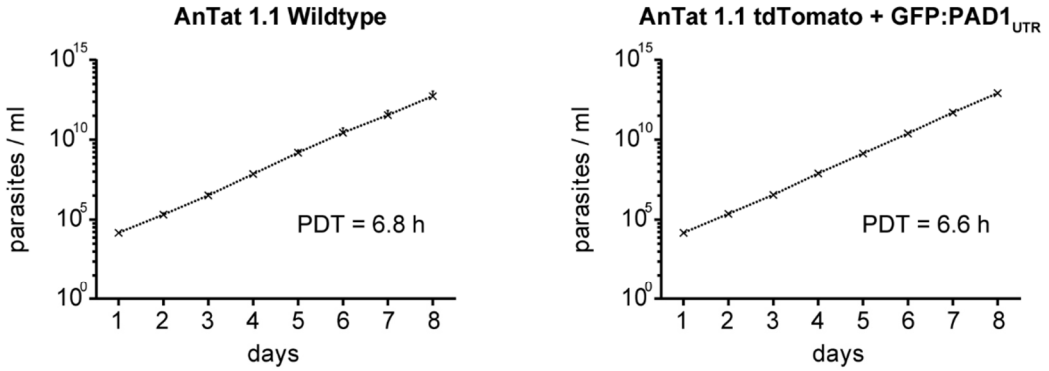

B

AnTat 1.1 wildtype			AnTat 1.1 tdTomato + GFP:PAD1$_{UTR}$		
	Total	[%]		Total	[%]
MCF +	177	65	MCF +	378	52
MCF -	95	35	MCF -	347	48
Total	272	100	Total	725	100

C

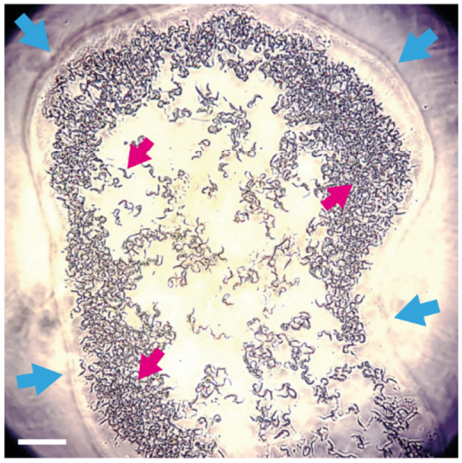

Figure 18: The transgenic strain AnTat 1.1 tdTomato + GFP:PAD1$_{UTR}$ shows similar growth and infection kinetics as the wildtype. (A) Growth curves of the *T. brucei* strains AnTat 1.1 wildtype and tdTomato + GFP:PAD1$_{UTR}$ grown in HMI9 medium for 8 days. Data are shown as mean ± SD of three replicates. **(B)** Transmissibility of *T. brucei* strains AnTat 1.1 wildtype and tdTomato + GFP:PAD1$_{UTR}$ in tsetse flies. Teneral male tsetse flies were infected with stumpy forms of the wildtype or transgenic strain in the presence of 10 mM N-acetyl-glucosamine and 12.5 mM L-glutathione mixed with sheep blood. Flies were tested 35 days after infection by induced probing on pre-warmed microscopy slides. The deposited saliva was examined by microscopy for the presence (MCF +) or absence (MCF -) of metacyclic parasites. **(C)** Tsetse saliva deposits containing metacyclic trypanosomes of the *T. brucei* AnTat 1.1 tdTomato + GFP:PAD1$_{UTR}$ strain. Blue arrows indicate the saliva sample. Red arrows mark the metacyclic trypanosomes in the saliva. Scale bar, 30 µm.

To infect the skin equivalents, three hdSEs were stacked on top of each other to obtain a final height of 3 mm. Subsequently, six salivary gland-positive tsetse flies were allowed to bite into the stack (Figure 19 A). The flies first probed the top skin equivalent with their proboscis (Figure 19 A, left panel, # 1) and then began to bite. The bite was of such depth that the entire proboscis was sunk into the stack (Figure 19 A, right panel). The bite was repeated several times by upward and downward movements. In general, the biting behavior of the flies was similar to that observed under natural conditions with initial probing, biting, and subsequent multiple up and down movements (Movie 1).

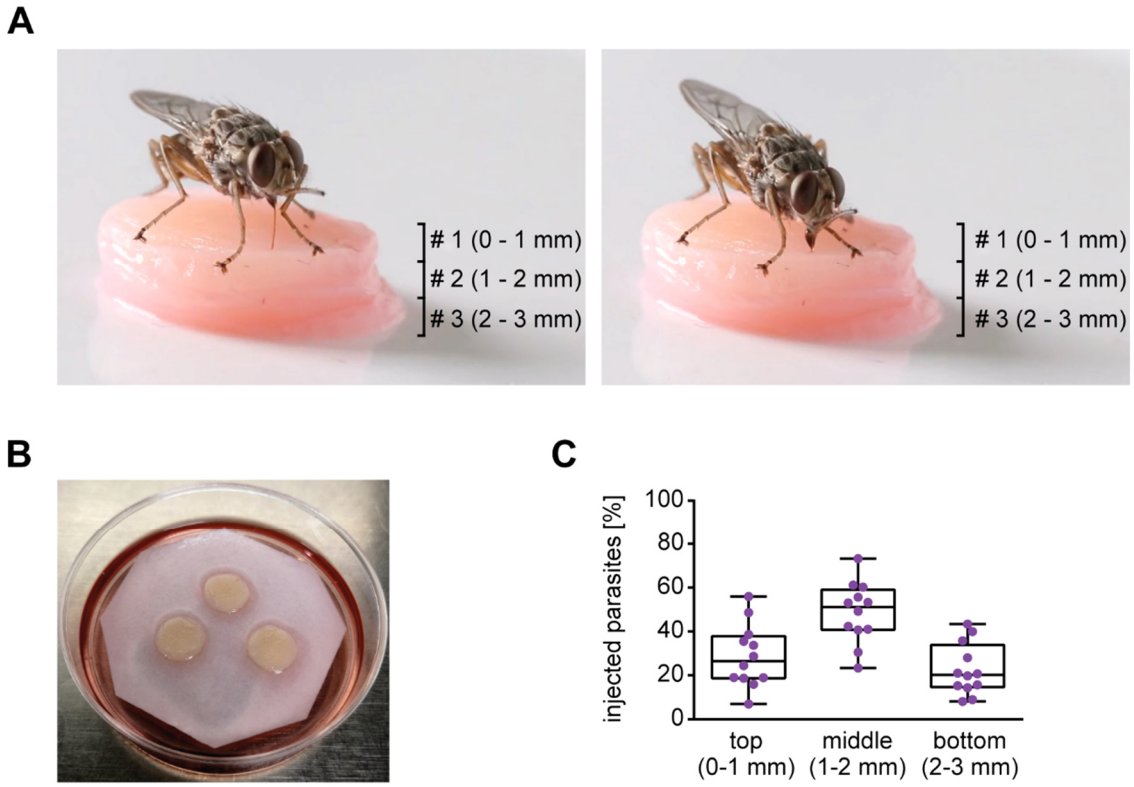

Figure 19: Simulation of natural vector transmission by using tsetse flies to infect high-density skin equivalents with *T. brucei*. (A) Tsetse flies accept and bite into the hdSEs. To infect skin equivalents, three hdSEs were stacked on top of each other (# 1, 2, 3). Subsequently, salivary gland-positive tsetse flies were allowed to bite into the stack. Stacking was necessary because the proboscis of the tsetse fly has a length of 2 mm, whereas the hdSEs only have a standard height of 1 mm. Without stacking, the flies simply bit through the hdSEs and deposited most of the parasites underneath. Movie 1 shows the natural transmission of *T. brucei* parasites to the skin equivalents by a tsetse fly. **(B)** Trypanosome-infected hdSEs were cultured with 7 ml of INF medium at the air-liquid interface by placing three infected hdSEs on a sterile Whatman paper in a petri dish. **(C)** A distribution analysis revealed that half of the injected parasites were deposited at a depth between 1 - 2 mm. The other half of the parasites was injected almost equally into the hdSE at the top (0 - 1 mm) and at the bottom (2 - 3 mm). Results are shown as median ± IQR of four replicates.

In order to have sufficient quantities and equal numbers of parasites for downstream analysis per skin equivalent, the positions of the stacked hdSEs were changed after six fly bites and another round of six flies were allowed to bite into the stack. This was repeated three times, so that each of the three hdSEs was once on each position (top, middle, bottom). Subsequently, the trypanosome-infected hdSEs were cultured at the air-liquid interface by placing them on Whatman paper until analysis (Figure 19 B). Stacking of the hdSEs was necessary because the proboscis of the tsetse fly has a length of ~ 2 mm, whereas the hdSEs only have a standard height of 1 mm. Without stacking, the flies simply bit through the hdSEs and deposited most of the parasites underneath. The

distribution of the deposited MCFs was analyzed without rotation to verify that the parasites were injected in each of the stacked hdSEs. Half of the deposited trypanosomes were detected at a depth between 1 - 2 mm, which corresponds to the hdSE in the middle of the stack. The other half of the parasites was injected almost equally into the hdSE at the top (0 - 1 mm) and at the bottom (2 - 3 mm) (Figure 19 C). Consequently, during an infection process in which the positions of the stacked hdSEs were changed, each of the three hdSEs should contain a similar number of trypanosomes.

Each bite of a fly caused a wound in the skin equivalent that was clearly visible in the epidermis (Figure 20 A). The diameter of the wound corresponded approximately to the diameter of the fly's proboscis with about 80 to 100 µm (Gibson et al., 2017). Below the epidermal wound, the expressed fluorescent protein tdTomato (tdT) enabled rapid identification of the injected parasites in the dermis (Figure 20 B). The parasites were viable as they were moving (Movie 2) and interestingly, the parasites were not injected in a straight path, but formed a pattern with multiple finger-like protrusions (Figure 20 B, white arrows). It can be assumed that these patterns reflect the actual path of the fly’s proboscis in the dermis and that the parasites were deposited predominantly in the channels caused by the bite. Moreover, the deposition of the parasites along the entire injection channel may contribute to the dissemination of the parasites in the dermis.

To visualize the three-dimensional structure of these complex patterns in more detail, multicolor light sheet fluorescence microscopy (LSFM) was applied. With this technique high resolution optical stacks of intact transparent skin tissue can be generated by imaging autofluorescent or fluorescence-labeled structures. For this purpose, infected hdSEs were fixed with 4 % PFA and optical cleared with benzyl alcohol/benzyl benzoate solution (BABB). Intact, translucent, infected hdSEs were scanned at the LSFM for the epidermal wound and subsequently a defined region around the wound was recorded (Figure 20 C).

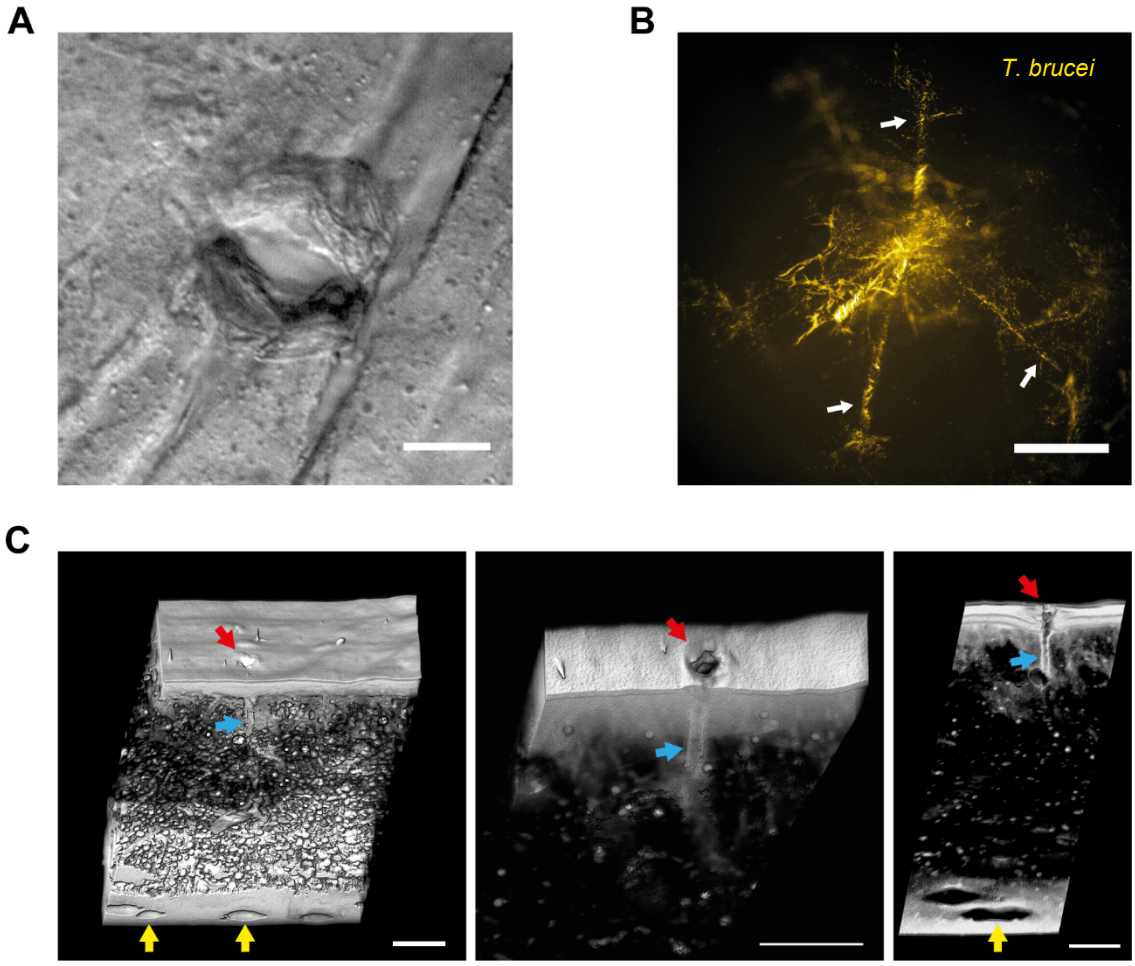

Figure 20: Microscopic analysis of the skin lesion caused by a tsetse bite and the transmitted trypanosome population in the high-density skin equivalent. (A) The epidermal wound caused by the fly bite was clearly visible under the stereomicroscope. Scale bar, 50 µm. **(B)** Below the epidermal wound, the injected trypanosomes (yellow) could be detected in the dermis by their cytoplasmic marker tdTomato. Strikingly, the parasites were deposited within an intricate bite path network in the dermis (white arrows). Scale bar, 500 µm. The panel shows a still image of the corresponding movie 2. **(C)** Representative images of the region around the epidermal wound of infected hdSEs acquired by light sheet fluorescence microscopy. The injected tdTomato-expressing parasites could not be detected, but the epidermal wound (red arrows), a part of the injection channel (blue arrows), and interestingly, cavities in the lower part of the hdSEs could be observed (yellow arrows). Scale bar, 200 µm.

Unfortunately, the injected tdT-expressing trypanosomes could not be detected in the infected hdSEs. Therefore, other clearing protocols were tested additionally, including the usage of other alcohols such as isopropanol or tert-Butanol for tissue dehydration, a basic pH of 9.5 during dehydration, and the usage of other clearing solutions such as ethyl cinnamate (ECi). The usage of isopropanol instead of ethanol during dehydration at 4 °C should reduce the high autofluorescence of collagen in the dermis. By adjusting the pH, the stability of the fluorescent protein tdT should be increased and by using the non-toxic solution ECi, denaturation of tdT should be prevented. Although a weak tdT-fluorescence

signal could be detected with a wide-field fluorescence microscope (Figure 21), which was potentially attributable to trypanosomes in the dermis, the LSFM was still unable to detect a clear trypanosome signal.

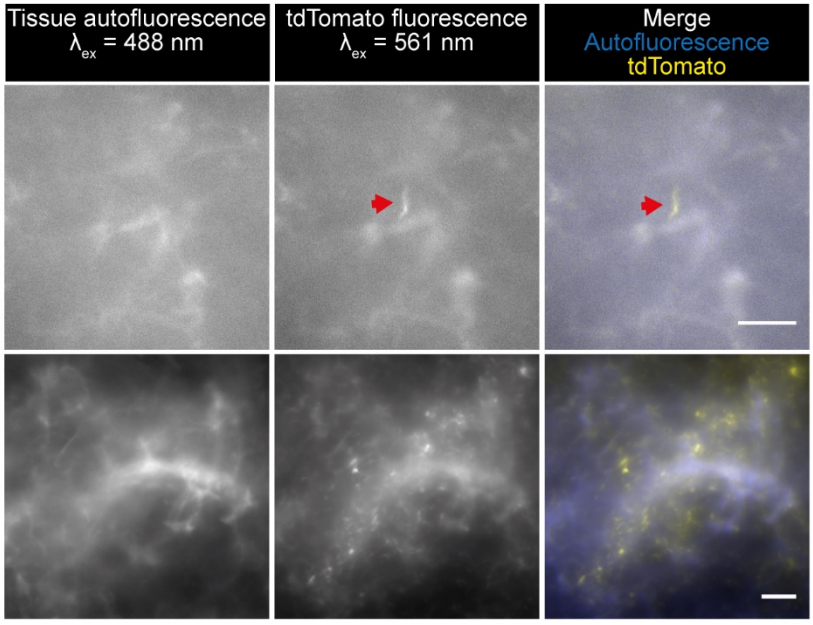

Figure 21: Testing of an alternative clearing protocol for light sheet fluorescence microscopy. A different clearing protocol was tested and images were acquired with a wide-field fluorescence microscope. For tissue dehydration ethanol was replaced by tert-Butanol and the pH was adjusted to 9.5. For tissue clearing, benzyl alcohol/benzyl benzoate solution (BABB) was replaced by ethyl cinnamate (ECi). Although a weak tdT-fluorescence signal, which may be attributable to trypanosomes, could be detected (red arrow), no clear trypanosome signal could be detected by light sheet fluorescence microscopy. Scale bar, 20 µm.

Nevertheless, the epidermal wound (Figure 20 C, red arrows) and a part of the injection channel (Figure 20 C, blue arrows) could be resolved and an overall impression of the tissue structure could be obtained. Similar to stereomicroscopy, the diameter of the wound corresponded to the diameter of the fly's proboscis with about 80 - 100 µm (Gibson et al., 2017). Furthermore, the injection channel could be traced over a length of 200 - 250 µm into the tissue. In deeper tissue the injection channel could not be distinguished from the autofluorescence of the surrounding tissue and the multiple branches of the channel as shown in Figure 20 B could not be visualized. Interestingly, cavities were visible in the lower part of the hdSEs (Figure 20 C, yellow arrows). These structures resemble the recently discovered interstitial space in human skin (Benias et al., 2018). However, whether the cavities in the hdSEs are actually a coherent network or an artifact resulting from compression requires further investigation.

3.2 Tsetse-borne *T. brucei* parasites infect the skin equivalent

To calculate the maximum number of injectable MCFs per fly, salivary gland-positive flies were allowed to spit in pre-warmed HMI9 medium for 10 minutes. The length of the time period should allow complete draining of the salivary glands. Subsequently, the total number of parasites in the medium was determined with a Neubauer chamber and divided by the number of flies used to calculate the mean number of MCFs per fly. As a result, the maximum number of injectable trypanosomes per fly bite was calculated to 3,934 MCFs on average (Figure 22 A). This number agrees with the number obtained by parasite outflows from non-disrupted individually dissected salivary gland pairs analyzed by flow cytometry (Caljon et al., 2016).

Within the observation period of 7 days post-infection (dpi), the tsetse-transmitted cell cycle-arrested MCFs increased their total numbers by around two orders of magnitude in the dermis of the hdSEs (Figure 22 B). Measurement of the mean parasite population density (cells/ml) in the hdSEs showed that it increased from an initial 8.24×10^4 cells/ml to 1.07×10^6 cells/ml on day 7. This results in 3.7 parasite doublings and a total PDT of 45 h.

To test the possibility that the skin-residing trypanosomes escape from the hdSEs into the surrounding culture medium, both the Whatman paper and the supernatant were examined for the presence of parasites. An extensive examination of the Whatman paper under a stereomicroscope showed that only sporadic and very few parasites were entangled in the fibers of the Whatman paper (Figure 22 C, yellow arrow). Furthermore, the culture medium contained on average less than 8,000 parasites on each of the three time intervals tested. In total only 12,283 parasites were counted on average in the supernatant within one week (Figure 22 D). Moreover, it must be taken into account that three infected hdSEs were always cultured on one Whatman paper (Figure 19 B). Thus, the detected trypanosomes in the Whatman paper and supernatant originated from three hdSEs. In relation to the number of trypanosomes in the entire culture system (3 hdSEs + supernatant) the parasite escape from the hdSEs was negligible and amounted to only 3.4 % on average after one week. However, the dynamics of the parasites' exit and re-entry into the hdSEs are not clear.

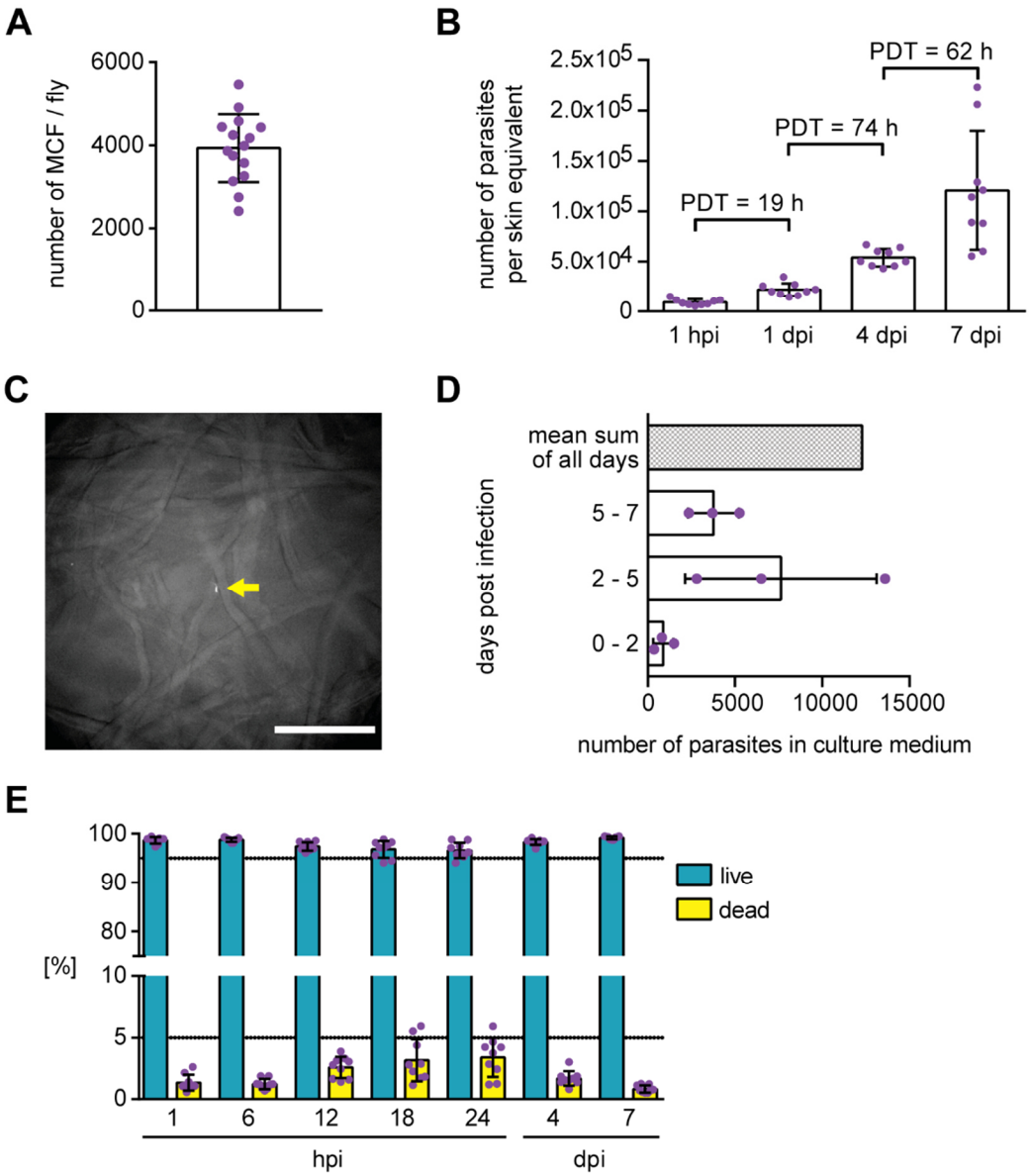

Figure 22: Tsetse borne *T. brucei* parasites infect the high-density skin equivalent. **(A)** Number of MCFs in spit samples from 15 salivary gland-positive flies infected with AnTat 1.1 tdTomato + GFP:PAD1$_{UTR}$. The maximum number of injectable trypanosomes per fly bite was calculated to 3,934 MCFs on average. **(B)** Growth curve and population doubling times (PDTs) of tsetse-transmitted trypanosomes cultured in skin equivalents for 7 days. Data of three replicates are shown. **(C)** Representative image acquired with a fluorescence stereomicroscope showing a single trypanosome entangled in the fibers of a Whatman paper (yellow arrow). Scale bar, 150 µm. **(D)** Quantification of the parasites present in the culture medium during the culture of three infected hdSEs within one week. The culture medium was collected before the medium change on days 2, 5, and 7, centrifuged, and the number of trypanosomes was determined with a Neubauer chamber. Data of three replicates are shown. **(E)** Flow cytometric assessment of parasite viability by Calcein-AM staining in infected hdSEs at various timepoints post-infection. Results of three replicates are shown. All data are shown as mean ± SD.

To test whether the parasites experienced an increased death rate in the hdSE, their viability was assessed by Calcein-AM staining (Figure 22 E). In live cells the non-fluorescent Calcein-AM is converted to a green-fluorescent calcein by intracellular

esterases. In the hours (hpi) and days (dpi) following infection, viability staining detected only low numbers (< 5 %) of dead trypanosomes in the dermis. The highest number of dead parasites was reached after 18 h and 24 h post-infection, with 3.2 % and 3.4 % on average, respectively. The absence of significant numbers of non-viable parasites is consistent with previous findings in mice (Caljon et al., 2016).

Additionally, scanning electron microscopy of infected hdSEs was performed to visualize the interaction of the skin-residing trypanosomes with collagen fibers and dermal fibroblasts. A large overview of infected hdSEs showed an intact epidermal layer with the characteristic skin scales (Figure 23, I) and the presence of trypanosomes in the connective tissue of the dermis (Figure 23, I - yellow arrow). Scanning electron microscopy revealed a high degree of entanglement of skin-dwelling parasites with collagen fibers (Figure 23, I - III), and the trypanosomes were frequently found in close contact with dermal fibroblasts (Figure 23, IV - V). The presence of dividing trypanosomes was indicated by the observation of cells with a second flagellum (Figure 23, V - VI).

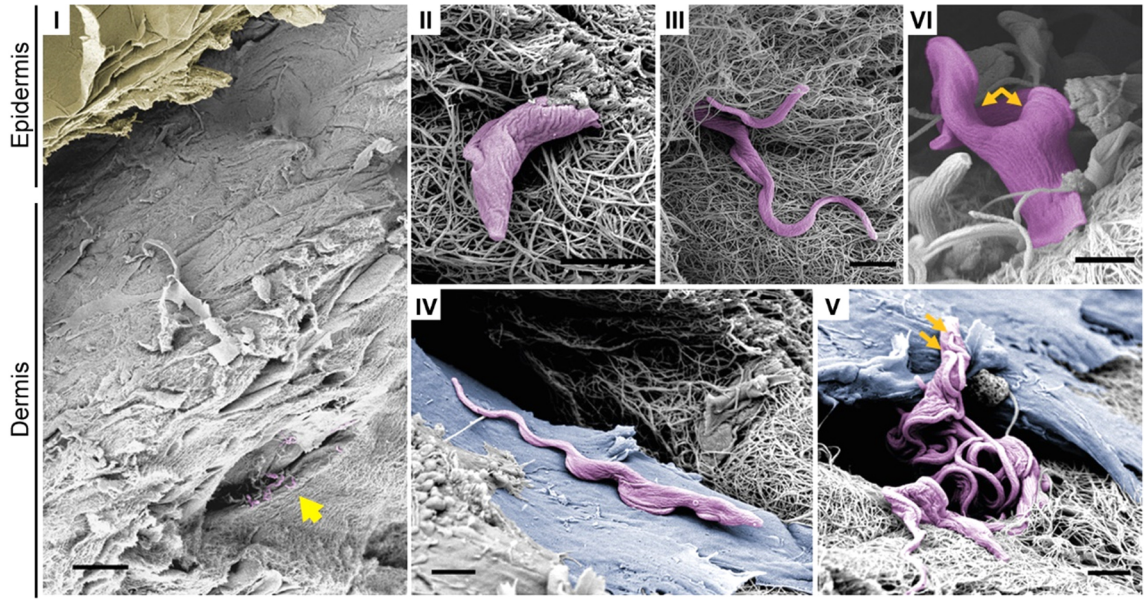

Figure 23: Trypanosomes are entangled by collagen fibers and are in direct contact with dermal fibroblasts. Scanning electron microscopy of hdSEs 4 dpi illustrating the presence of parasites (colored magenta) in the dermal layer. **(I)** Overview showing an intact epidermal layer (colored yellow) and the presence of trypanosomes in the connective tissue of the dermis (yellow arrow). Scale bar, 30 µm. **(II + III)** Intricate interactions and entanglement of trypanosomes with collagen fibers were observed frequently. **(IV + V)** Parasites were found in close contact with dermal fibroblasts (colored blue). **(V + VI)** The presence of proliferating parasites was indicated by the double flagella of trypanosomes (orange arrows). Scale bar, 2 µm (II, III, IV, V, VI).

In conclusion, the results strongly suggest that the tsetse fly-transmitted cell cycle-arrested MCFs established a proliferative population in the dermal tissue of the hdSEs. Furthermore, the findings indicate that the parasites remain in the skin equivalents, as only a few trypanosomes were found in the surrounding culture medium and Whatman paper. In addition, the observed intricate interactions with collagen fibers and dermal fibroblasts had no detrimental effects on the parasites as indicated by a high viability of the skin-dwelling trypanosomes.

3.3 Metacyclic parasites rapidly differentiate into proliferative trypanosomes in the skin equivalent

It has been observed that the tsetse-transmitted MCFs have already doubled in the skin equivalent within the first 24 hours post-infection (hpi) (Figure 22 B). This suggests that the differentiation from the injected cell cycle-arrested MCFs to proliferative trypanosomes occurs very quickly after injection into the skin by the tsetse fly.

To measure the timing of the transition of the injected MCFs to proliferative parasites in the skin equivalent, cell cycle analyses by flow cytometry was performed at various timepoints post-infection (Figure 24 A). More than 90 % of MCFs and parasites isolated form hdSEs at 6 hpi were in the G1 phase of the cell cycle. Besides MCFs, a small amount of long and short epimastigote forms may be present in the saliva of tsetse flies, which are also transmitted during a bite. Since long and small epimastigotes are proliferative parasites, this could explain the small number of parasites in the S and G2 phases at these early timepoints. However, 12 hpi a 3.6-fold increase of parasites in the S and G2 phases (15.0 %) compared to 6 hpi (4.2 %) was observed. The number of dividing parasites further increased after 18 hpi (19.7 %) and 24 hpi (27.1 %).

In addition, when analyzed using flow cytometry, the mean fluorescence intensity of the forward scatter width (FSC-W, a measure of cell size) of the injected parasites resembled that of BSF culture cells within 24 hpi (Figure 24 B). In contrast to BSFs, MCFs and stumpy forms are smaller (Schuster et al., 2017) and therefore have a shorter dwell time in the laser beam of the flow cytometer and thus, a shorter signal width in the forward scatter (FSC-W) (Hoffman, 2009). Furthermore, the change in morphology was supported by microscopy of skin-derived trypanosomes at the same timepoints (Figure 24 C). Analysis of the microscopic images confirmed the presence of cells with

a BSF-like morphology and that both the length of the cell body and the length of the flagellum increased within the first 24 hpi.

To determine the onset of protein synthesis as indication of MCF activation, the incorporation of a methionine analogue into nascent proteins was quantified. The activation must be completed in less than 12 h after the injection, as the first proliferative parasites have already been observed in the skin equivalent at 12 hpi (Figure 24 A). Therefore, at various timepoints post-infection the protein synthesis rate of skin-residing trypanosomes was determined and compared to MCFs and BSFs (Figure 25 A and 25 B).

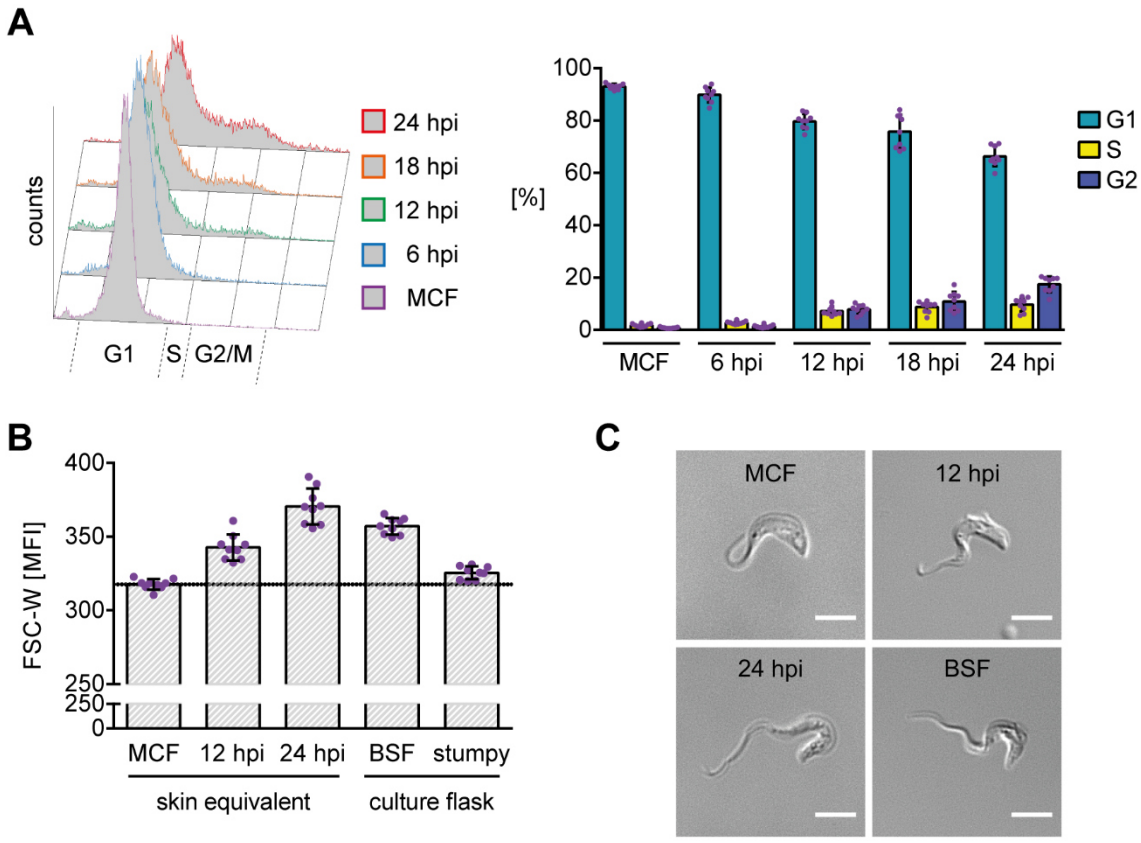

Figure 24: Tsetse-transmitted cell cycle-arrested metacyclic parasites rapidly re-enter the cell cycle and acquire a bloodstream form morphology in the skin equivalent. (A) Flow cytometric assessment of the cell cycle distribution of skin-residing trypanosomes at various timepoints post-infection. The left panel shows representative cell cycle histograms of skin-derived parasites at 6, 12, 18, and 24 hours post-infection (hpi) in comparison to MCFs. The right panel shows the mean ± SD of the cell cycle distribution of three replicates. **(B)** The mean fluorescence intensity (MFI) of the forward scatter width (FSC-W) was analyzed for MCFs and skin-resident parasites at 12 and 24 hpi and compared to bloodstream forms (BSF) and stumpy forms. The FSC-W signal represents the time of flight of the cell through the laser beam and thus, provides information about the cell size. MCFs are smaller compared to stumpy forms and both are smaller than BSFs (Schuster et al., 2017). Results are shown as mean ± SD of three replicates with data representing individual data points. **(C)** Morphology of a MCF trypanosome and parasites isolated from skin equivalents 12 and 24 hpi in comparison to a BSF cell. Scale bar, 5 µm.

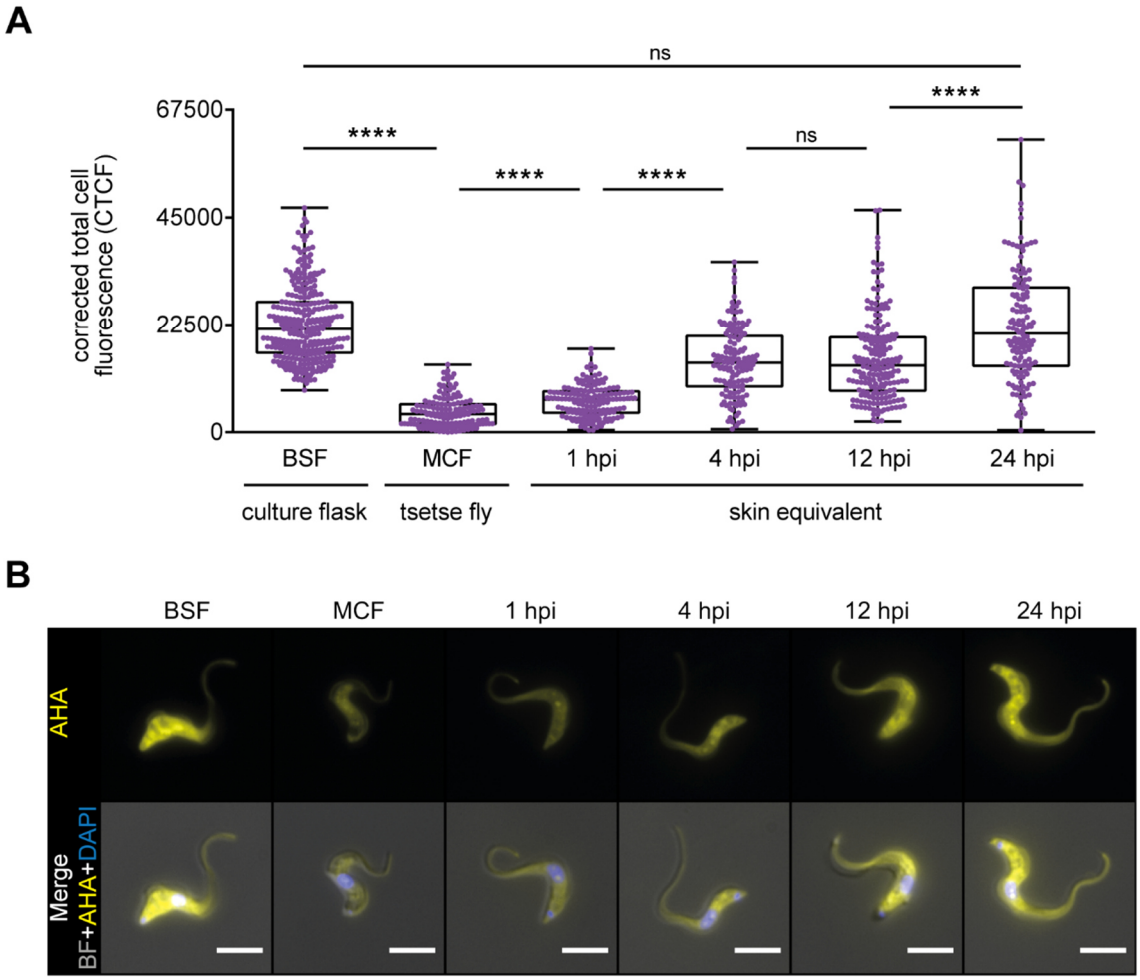

Figure 25: Tsetse-transmitted cell cycle-arrested metacyclic parasites rapidly activate protein synthesis in the skin equivalent. (A) Quantification of protein synthesis rate of skin-dwelling parasites at various timepoints post-infection in comparison to BSFs and MCFs. Trypanosomes were isolated from skin equivalents at the times indicated and incubated with the methionine analogue L-azidohomoalanine (AHA) which is incorporated into newly synthesized proteins. Next, live parasites were sorted on coverslips, chemically fixed, and incorporated AHA was labeled with Alexa Fluor 488. Microscopic images were acquired by focusing in the DAPI channel on the cell nucleus and kinetoplast. Subsequently, images were taken in brightfield, DAPI and AHA channels with same settings for each experiment. Images were analyzed with the ImageJ/Fiji software by measuring the total cell fluorescence of individual trypanosomes in the AHA channel. Furthermore, the corrected total cell fluorescence (CTCF) of individual cells incubated with either AHA or L-methionine was calculated using the following formula: CTCF = integrated density – (area of selected cell x mean fluorescence of background). In addition, to correct for cell autofluorescence, the CTCF values of parasites incubated with L-methionine (negative control) was subtracted from all CTCF values of parasites incubated with AHA. Data are median ± IQR of three replicates. For each approach 136 - 292 individual parasites were analyzed. Statistical analyses were performed with the Mann-Whitney *U*-test, ****: $p < 0.0001$, ns: not significant. **(B)** Fluorescence microscopy of trypanosomes isolated from skin at the times indicated in comparison to BSFs and MCFs. The fluorescence signal intensity of L-azidohomoalanine incorporated into nascent proteins (yellow channel) was measured to assess protein synthesis rate on the single parasite level. Cells were counterstained with DAPI (nuclei, blue channel) and both channels were merged with the phase contrast image in the overlays. Scale bar, 5 µm.

MCFs obtained from tsetse flies showed a low protein synthesis rate compared to BSFs (Figure 25 A and 25 B, MCF - tsetse fly versus BSF - culture flask). However, within the first 24 hpi the protein synthesis rate of the skin-dwelling parasites significantly increased by 5.4-fold. At that timepoint the rate is comparable to *in vitro* cultured BSFs. The increase in protein synthesis was not linear but stepwise. The first step was between 1 and 4 hpi (2.1-fold), and the second between 12 and 24 hpi (1.5-fold). Already after one hour, the injected MCFs exhibited a 1.8-fold increase in the protein synthesis rate compared to the MCFs that were obtained from flies.

It can be concluded, that the tsetse-borne cell cycle-arrested MCFs were activated in the high-density skin equivalent and rapidly differentiated to proliferative skin-residing trypanosomes with a BSF-like morphology. This is indicated by the rapid activation of protein synthesis already 1 hour post-infection and the 5.8-fold increase of parasites in the S and G2 phases of the cell cycle 12 hpi in comparison to MCFs.

3.4 Single-parasite RNA sequencing reveals the programmed activation of metacyclic forms in the skin equivalent

An established developmental hallmark during the differentiation of MCFs is the replacement of the metacyclic VSG coat with VSG isoforms of the bloodstream form. In order to define other programmed changes in gene expression that occur during developmental transition, the transcriptomes of individual trypanosomes were dissected using Smart-seq2 approach (Picelli et al., 2013). The scRNAseq profiles of MCFs collected from flies with a mature salivary gland infection were compared to those of trypanosomes isolated from hdSEs at four different timepoints post-infection (4 hpi, 12 hpi, 24 hpi, and 7 dpi; Figure 26 A).

The parasites were sorted by FACS and single, viable trypanosomes were collected in individual microwells containing lysis buffer and RNase inhibitor. Immediately after sorting, cells were frozen at -80 °C. In contrast to the droplet-based 10x genomics platform, the Smart-seq2 protocol requires each cell to be processed individually. Therefore, a pipetting robot was used to add the required reagents for reverse transcription, cDNA amplification, and adapter ligation step by step into each microwell. The advantage of the Smart-seq2 approach is that the cDNA is sequenced from both ends, 3’ and 5’, which allows the generation of full-length cDNA. In general, this should

improve yield and coverage of cDNA libraries. In the droplet-based approach, the cDNA is sequenced from only one of the two ends. In addition, the droplet-based approach requires pre-known markers to identify different cell types or conditions, as thousands of cells are processed in bulk in one reaction for cost reasons. In the Smart-seq2 approach, each cell can be traced back to its original microwell, from which the contained cell type or condition is known.

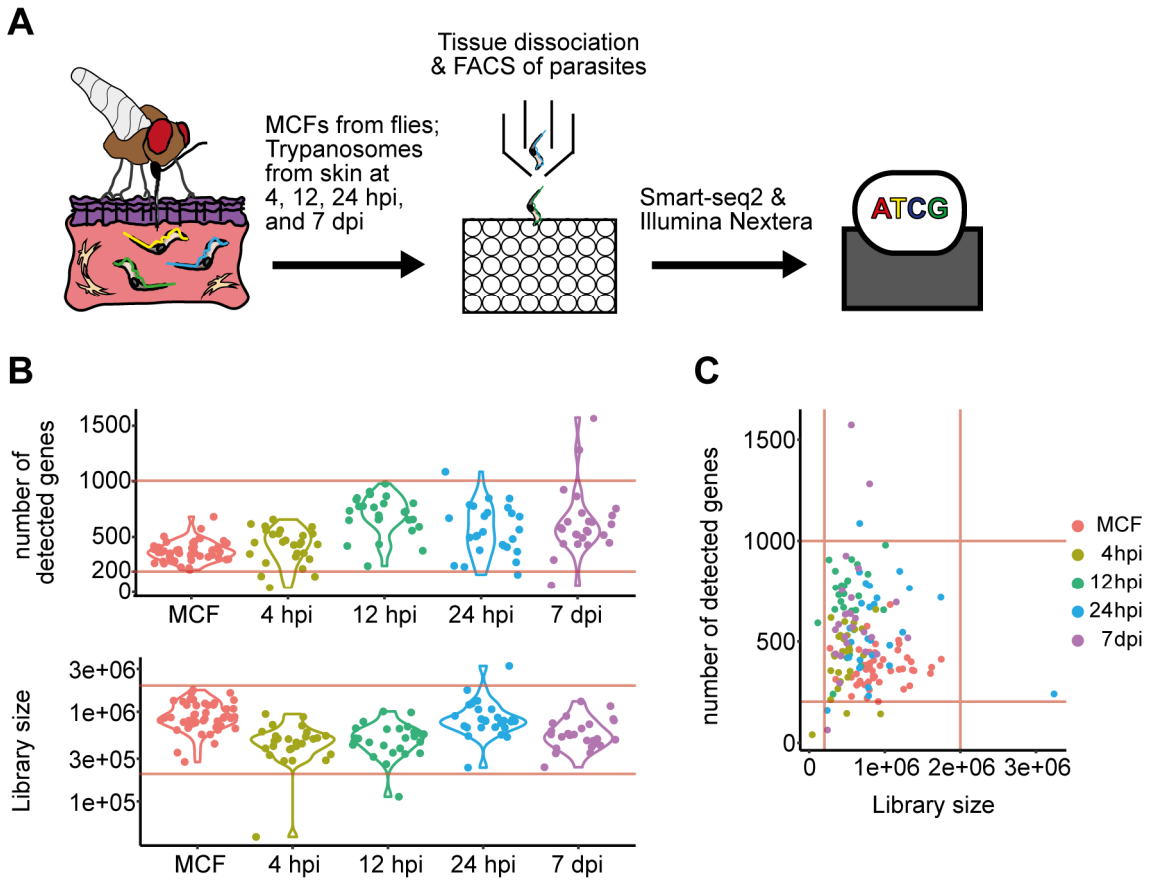

Figure 26: Workflow and quality control of the single-cell RNA sequencing experiment of trypanosomes. (A) Schematic representation of the experimental pipeline of single-parasite RNA sequencing. Tsetse-transmitted trypanosomes were isolated from infected hdSEs at 4, 12, 24 hpi, and 7 dpi. The skin-derived parasites as well as MCFs obtained from salivary gland-positive flies were subjected to FACS and single, viable parasites were sorted into individual microwells, followed by processing with the Smart-seq2 and Nextera protocols, and sequencing. A total of 153 trypanosomes were processed. **(B + C)** Violin and dot plots showing the number of genes detected across all libraries and library size of individual *T. brucei* parasites (MCF, n = 48; 4 hpi, n = 27; 12 hpi, n = 27; 24 hpi, n = 26; 7 dpi, n = 25). The red lines in each graph represent quality control thresholds and only cells with > 200 and < 1,000 detected genes and a library size between 2 x 10^5 and 2 x 10^6 reads were considered for analysis.

The obtained sequencing reads of individual trypanosomes were mapped to the pleomorphic trypanosome reference genome TREU 927 (version 48) with the RNAStar software. The aim was to sequence at least 25 trypanosomes per condition. Therefore, a total of 153 parasites were processed, of which 48 were MCFs, 27 each were parasites isolated from skin at 4 and 12 hpi, and 26 and 25 were parasites isolated at 24 hpi and 7 dpi, respectively. Quality control of the aligned transcriptomes was performed and only trypanosomes with > 200 and < 1,000 detected genes and a library size between 2 x 10^5 and 2 x 10^6 reads were considered for downstream analysis (Figure 26 B and 26 C). Across all profiled trypanosomes, a total of 8,318 different genes were detected. Libraries with less than 200 genes and a size below 2 x 10^5 reads were classified as poor quality, while libraries with more than 1,000 detected genes and a size above 2 x 10^6 reads might have contained more than a single parasite.

After quality control, the remaining 142 single-parasite transcriptomes were examined for the presence of BARP-positive parasites. This was done because different developmental stages may be present in infected tsetse salivary glands. BARP-genes are specifically expressed in epimastigote forms. These parasites give rise to MCFs, but are themselves not infective. Therefore, transcriptomes were visualized using an unbiased principal component analysis (PCA) and the normalized expression levels of the BARP-genes ("Tb927.9.15510", "Tb927.9.15520", "Tb927.9.15530", "Tb927.9.15540", "Tb927.9.15550", "Tb927.9.15560", "Tb927.9.15570", "Tb927.9.15580", "Tb927.9.15590", "Tb927.9.15600", "Tb927.9.15610", "Tb927.9.15620", "Tb927.9.15630", "Tb927.9.15640") were overlaid onto the PCA plot (Figure 27 A). Three parasites were identified expressing high levels of BARP genes and were therefore excluded from downstream analysis.

The remaining 139 transcriptomes were visualized in a recalculated PCA plot (Figure 27 B). Although the transcriptomes collected at different timepoints clustered closely together, the first two principal components could delineate the different timepoints. MCFs are primed for mammalian invasion and in many aspects already resemble BSFs (Christiano et al., 2017). However, based on the first principal component, MCFs (red circles) could be distinguished from parasites isolated at 12 or 24 hpi (green/blue circles). In contrast, parasites isolated from skin at 4 hpi (yellow circles) and 7 dpi (purple circles) clustered between the transcriptomes of MCFs and 12/24 hpi parasites, but could be distinguished based on the second PC.

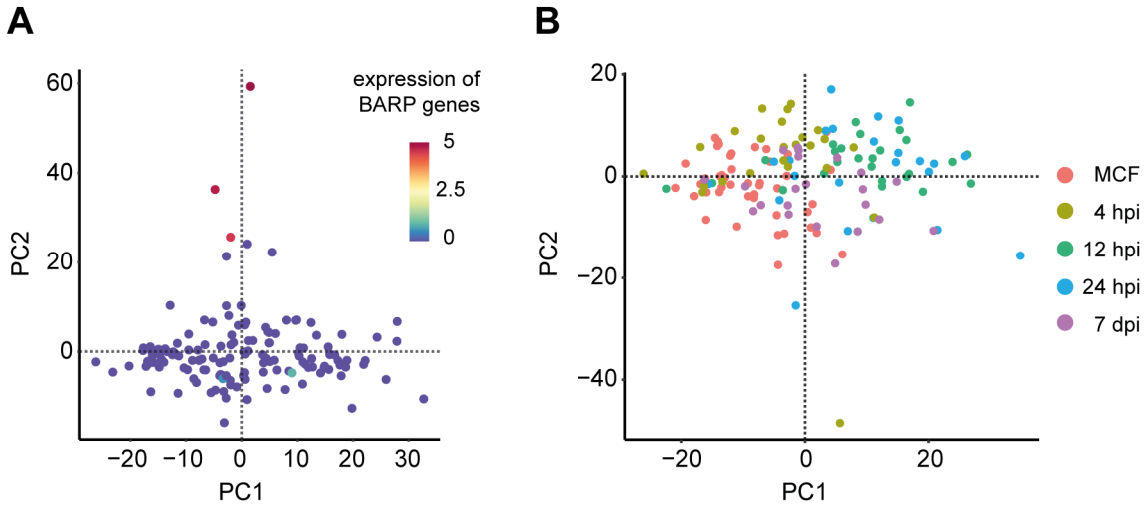

Figure 27: Detection of fly-stage specific BARB-genes and principal component analysis. **(A)** Feature plot of the 142 transcriptomes that passed quality control showing the normalized expression of fly-stage specific BARP-genes ("Tb927.9.15510", "Tb927.9.15520", "Tb927.9.15530", "Tb927.9.15540", "Tb927.9.15550", "Tb927.9.15560", "Tb927.9.15570", "Tb927.9.15580", "Tb927.9.15590", "Tb927.9.15600", "Tb927.9.15610", "Tb927.9.15620", "Tb927.9.15630", "Tb927.9.15640"). Normalized gene expression levels of BARP-genes for each cell are color-coded from blue to red and overlaid onto the principal component analysis (PCA) plot. **(B)** Unbiased projection of the first two principal components (PC) of the 139 transcriptomes used for downstream analysis. Each dot represents a single parasite. Colors indicate the time when the parasites were isolated from the skin equivalents after infection. Principal component analysis was performed selecting the 1,000 genes with the highest variance.

Next, differential gene expression analysis was performed. Two scenarios were tested: (I) The transcriptomes of each timepoint (MCF, 4, 12, 24 hpi, and 7 dpi) were compared with each other. Consequently, only genes specifically up- or downregulated at one of these timepoints were detected (Figure 28 A and Table S2); (II) The transcriptomes of MCFs and parasites isolated at 4 hpi were combined and compared with the combined transcriptomes of parasites isolated from skin at 12 hpi and 24 hpi (Figure 28 B and Table S2). This was done, since parasites isolated at 4 hpi had not yet started cell division (Figure 24 A) and clustered closer to MCFs (Figure 27 B). By contrast, the parasites at 12 hpi and 24 hpi were proliferative and clustered together.

Differential gene expression analysis revealed a number of genes that were specifically enriched at the different timepoints (Figure 28 A). 73 genes were specifically enriched in MCFs and 16 genes by parasites isolated from skin at 4 hpi. 61 and 54 genes were enriched by parasites isolated at 12 and 24 hpi, respectively. Trypanosomes isolated at 7 dpi were specifically enriched in 26 genes (Table S2). The differential gene expression analysis of the second scenario resulted in 24 genes that were significantly upregulated at

early timepoints (MCF + 4 hpi) and 92 genes at late times (12 hpi + 24 hpi) (Figure 28 B and Table S2).

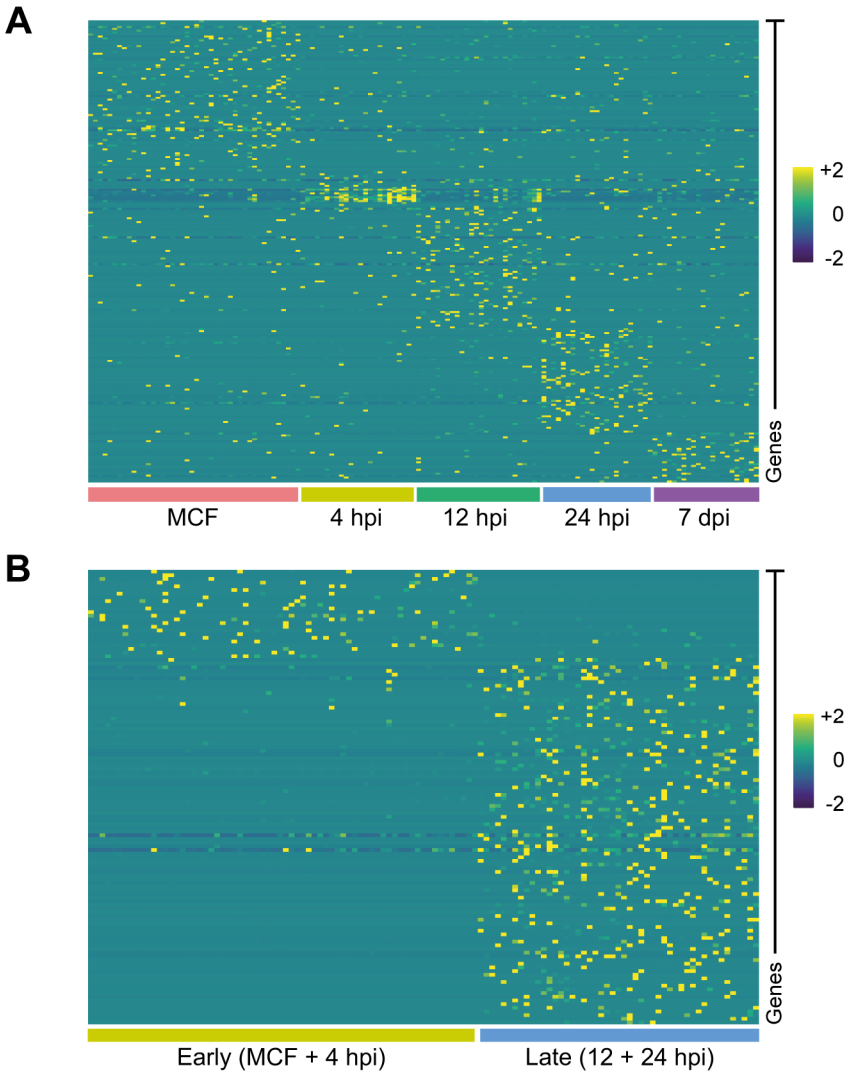

Figure 28: Time-resolved differential gene expression analysis. (A) Heatmap showing the scaled, time-resolved expression levels of significantly upregulated genes of skin-residing trypanosomes isolated at the times indicated in comparison to MCFs. Differential gene expression analysis was performed with DESeq2 software. Genes with an absolute log2-fold change > 2 and adjusted p-value < 0.01 were considered as differentially expressed. **(B)** Heatmap showing the scaled expression levels of upregulated genes of early (MCFs + 4 hpi) and late (12 hpi + 24 hpi) timepoints. In contrast to (A), the transcriptomes of MCFs and parasites isolated at 4 hpi were combined and compared with the combined transcriptomes of parasites isolated from skin at 12 hpi and 24 hpi. Differential gene expression analysis was performed with SCDE software. Genes with an absolute log2-fold change > 2 and a z-score > 1.96 were considered as differentially expressed. Each column represents a single parasite, each row represents an individual gene. The color key from purple to yellow indicates low to high gene expression levels.

Among the differently-expressed genes, many RNA-binding proteins (RBPs) were up- or downregulated at the transcript level for all conditions. In trypanosomes, RBPs play a crucial role in the post-transcriptional regulation of gene expression and adaptation to different environments, simply because transcriptional control of Pol II-transcribed genes does not occur (Clayton, 2013, Kolev et al., 2014).

The RBPs PUF9 (Tb927.1.2600), ZC3H20 (Tb927.7.2660), ZC3H35 (Tb927.10.12740), and ZC3H48 (Tb927.9.10280) were all upregulated during skin infection (Figure 29 A). PUF9 had been previously identified as important for the progression through the cell cycle (Archer et al., 2009). In a number of publications, ZC3H20 was shown to oscillate throughout the life cycle of *T. brucei* (Christiano et al., 2017, Vigneron et al., 2020, Cayla et al., 2020, Liu et al., 2020) and to be implicated in the increase of protein translation or in mRNA stability (Erben et al., 2014, Singh et al., 2014). Thus, upregulation of PUF9 and ZC3H20 is consistent with the above results on cell cycle re-entry and protein synthesis activation. Furthermore, a rapid upregulation of replication-associated transcripts (Figure 29 B) and genes associated with glycolysis (Figure 29 C) was noticed. In contrast to the fly-stages, the mammalian stages of *T. brucei* heavily rely on glycolysis, as glucose is abundant in the mammalian host (Smith et al., 2017). The functions of the two RBPs ZC3H35 and ZC3H48 are not yet known, but both were described to suppress mRNAs containing *boxB* RNA hairpin-motifs in BSFs (Erben et al., 2014, Lueong et al., 2016).

More globally, Gene Ontology (GO) analysis of differentially expressed genes revealed typical signatures associated with each timepoint (Figure 30 and Table S4). While MCFs were preferentially enriched in functions associated with “mRNA processing”, parasites isolated at 4 hpi were additionally associated with GO terms such as “endocytosis”, “import into cell”, and “nucleobase metabolic processes”. Endocytosis is essential to this parasite, not only for nutrient uptake but also for survival in a hostile environment. In fact, BSFs have one of the highest rates of endocytosis of any known eukaryote (Engstler et al., 2004) and activation of endocytosis is suspected as an adaptation to the mammalian host (Natesan et al., 2007). Parasites isolated from skin at 12 hpi were associated with GO terms reflecting reorganization of cellular structures, *e.g.* “anatomical structure development”, “developmental process”, or “cellular component organization or biogenesis”. Skin-derived parasites at 24 hpi were enriched in functions associated with proliferation, while parasites residing in the skin for 7 days were preferentially associated

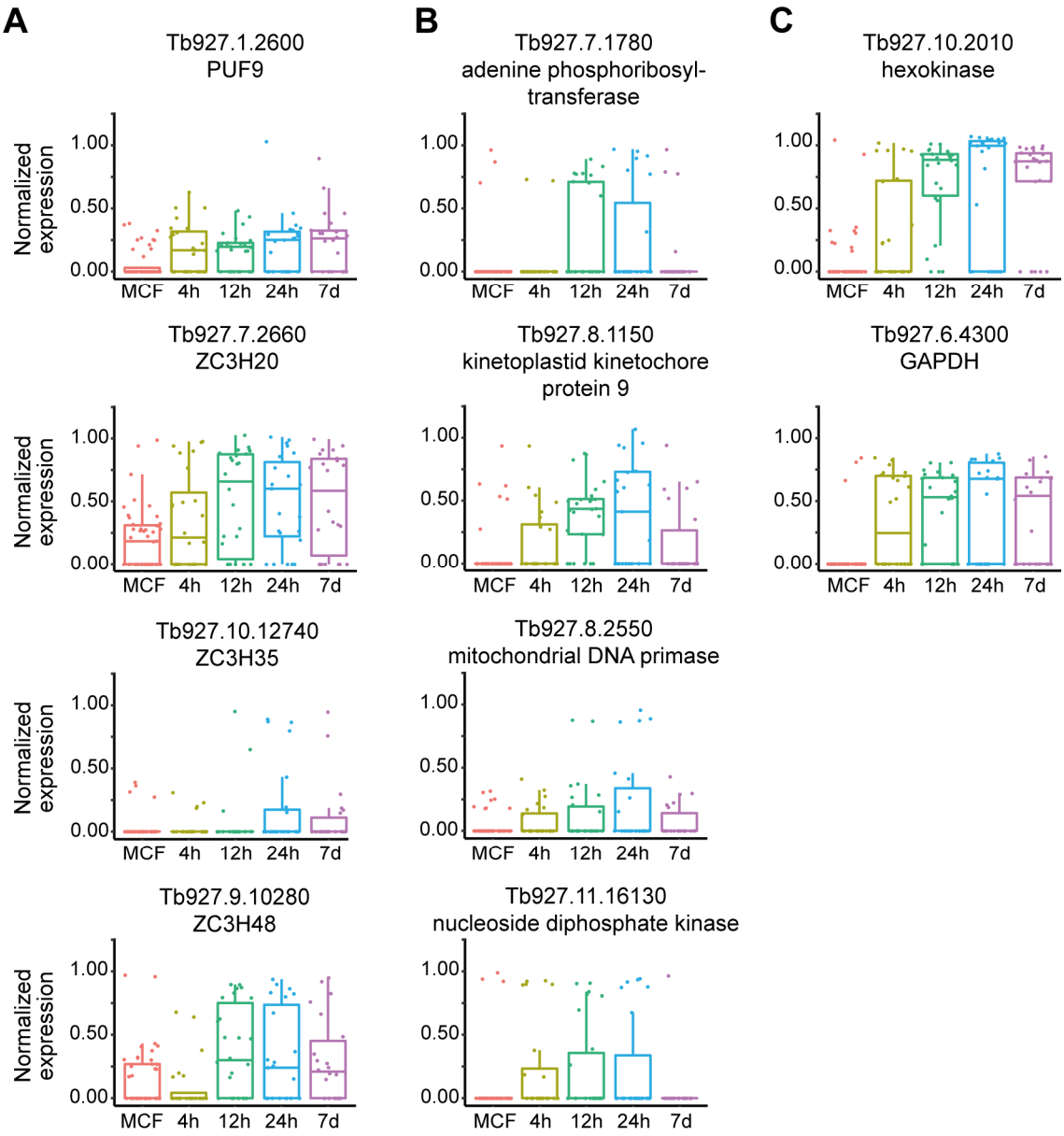

Figure 29: Single-parasite RNA sequencing reveals genes upregulated during skin infection. Boxplots showing the normalized expression of selected **(A)** RNA-binding proteins, **(B)** replication-associated genes, and **(C)** glycolysis-associated genes in MCFs and parasites isolated from skin at 4, 12, 24 hpi, and 7 dpi. Normalization of gene counts is necessary to make accurate comparisons of gene expression between samples. For this, the median of ratios method was used. The gene counts of each cell were divided by sample-specific size factors determined by the median ratio of gene counts relative to the geometric mean per gene.

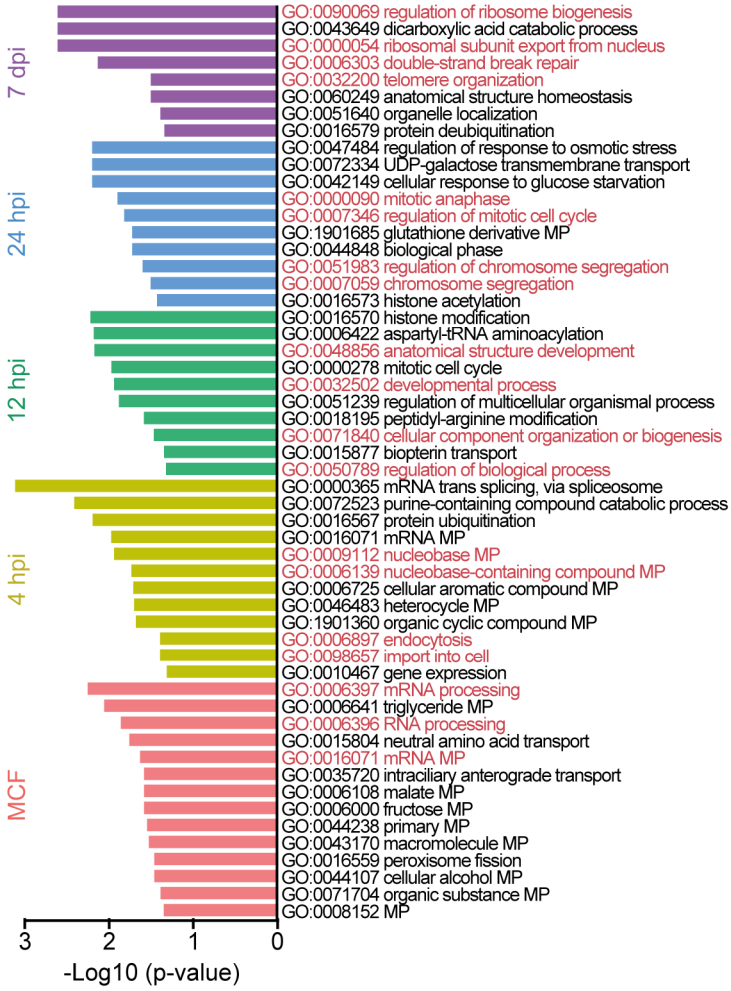

Figure 30: Gene ontology reveals biological processes of trypanosomes during skin infection. Biological process-associated gene ontology (GO) terms significantly enriched in MCFs and parasites isolated from skin at 4, 12, 24 hpi, and 7 dpi. GO term enrichment within the differential expressed genes between the five data sets were determined using the GO enrichment tool on the TriTrypDB webserver. GO terms have been filtered with the Revigo webtool to avoid redundancies. Bars represent the level of significance of the term enrichment.

with "telomere organization", "double-strand break repair", and "regulation of ribosomes". Telomeres and DNA double-strand breaks play important roles in antigenic variation and may be associated with the exchange of the metacyclic VSG coat with VSG isoforms of the bloodstream form (Li, 2015). GO analysis of early (MCF + 4 h) and late (12 h + 24 h) timepoints resulted in a similar picture (Figure 31 and Table S4). However, with some additional early terms such as "regulation of cellular response to heat" and late terms such as "gluconeogenesis".

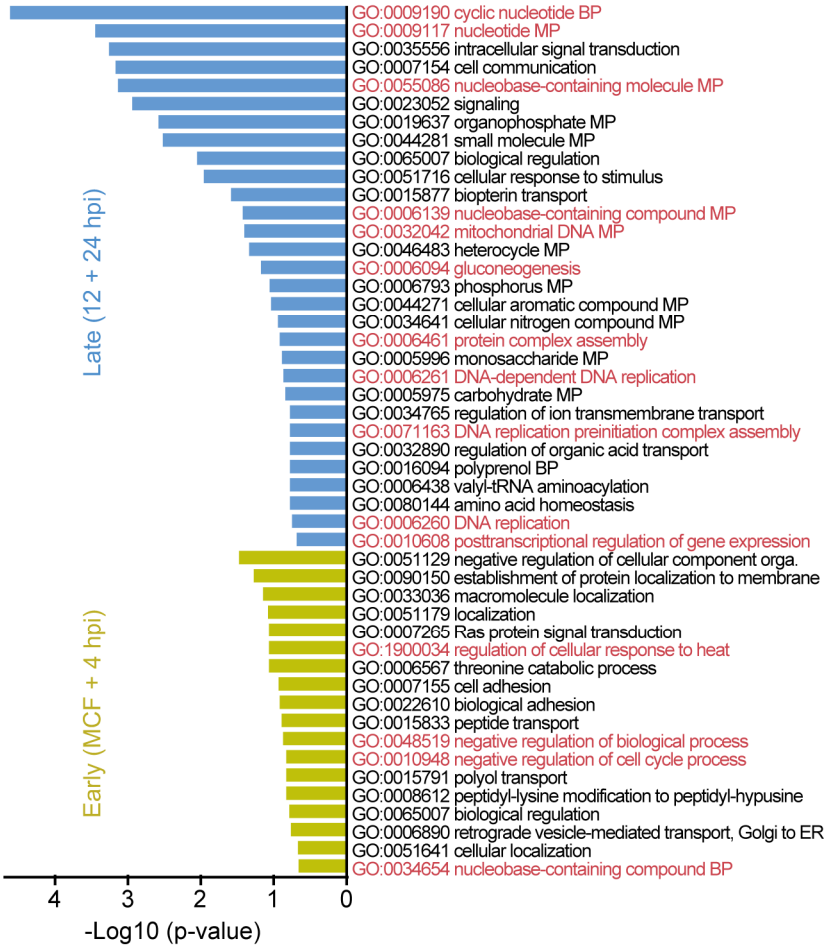

Figure 31: Gene ontology reveals biological processes of trypanosomes during early skin infection. Biological process-associated gene ontology (GO) terms significantly enriched in early (MCFs + 4 hpi) and late (12 hpi + 24 hpi) timepoints. The data sets of MCFs and parasites isolated at 4 hpi were combined and compared with the combined transcriptomes of parasites isolated from skin at 12 hpi and 24 hpi. GO term enrichment within the differential expressed genes between the two data sets were determined using the GO enrichment tool on the TriTrypDB webserver. GO terms have been filtered with the Revigo webtool to avoid redundancies. Bars represent the level of significance of the term enrichment.

Overall, the scRNAseq results confirmed that metacyclic trypanosomes are rapidly activated in the skin equivalents to give rise to a replicating parasite population. Furthermore, a variety of genes potentially involved in cell cycle activation and parasite development were identified, as well as RBPs that might control the differentiation processes.

3.5 Analysis of trypanosome migration and motility in the dermis

Motility is key for trypanosomes to successfully infect a variety of hosts and is critical for virulence. For instance, the parasites show different motility patterns throughout their life cycle, as adaptive responses to the changing microenvironments in the mammalian host and the tsetse vector (Bargul et al., 2016, Schuster et al., 2017). In addition, trypanosomes can sense their environment with the free tip of their flagellum and respond to it by adapting their swimming behavior (Maric et al., 2010, Heddergott et al., 2012). During bloodstream infection motility is crucial for the evasion of the host immune response by hydrodynamic flow-mediated redistribution of VSG-bound antibodies to the posterior end of the cell enabling their uptake and clearing through the flagellar pocket (Engstler et al., 2007). However, little is known about how the parasites move and orient themselves in the compact tissues of the mammalian host, such as the skin.

A two-day observation of the tsetse-transmitted MCFs in the hdSE showed that the parasites spread from the injection site into the surrounding tissue (Figure 32 A). However, a subpopulation remained at the inoculation site. Interestingly, the trypanosomes formed complex patterns in the dermal equivalent at the periphery of the parasite population. However, whether these structures are actively formed by the trypanosomes, for example by collective migration, or are based on existing structures in the dermis in which the parasites preferentially invade is not clear (Finger 32 B).

A more detailed investigation of the parasite motility in the dermis of the hdSEs on a single cell level was done by Laura Hauf during her master thesis (Hauf, 2019). During her thesis the trypanosome motion in the skin was analyzed at different timepoints post-infection. The mean and maximum parasite speed in the dermis was determined directly after injection into the skin equivalent by the tsetse fly (= 1 hpi) and compared to the parasite motion at 24 hpi and 72 hpi. The analysis revealed that the median of the mean parasite speed of all individual parasites increased within 24 h significantly from 2.2 µm/s to 2.9 µm/s. Whereas no further significant increase was detected between 24 and 72 hpi (2.9 µm/s versus 3.0 µm/s) (Figure 33 A and Movie 3). Likewise, the median of the maximum parasite speed increased significantly within 24 h from 10.4 µm/s to 15.5 µm/s. Again, no significant difference was observed between 24 and 72 hpi (15.5 µm/s versus 16.3 µm/s) (Figure 33 B).

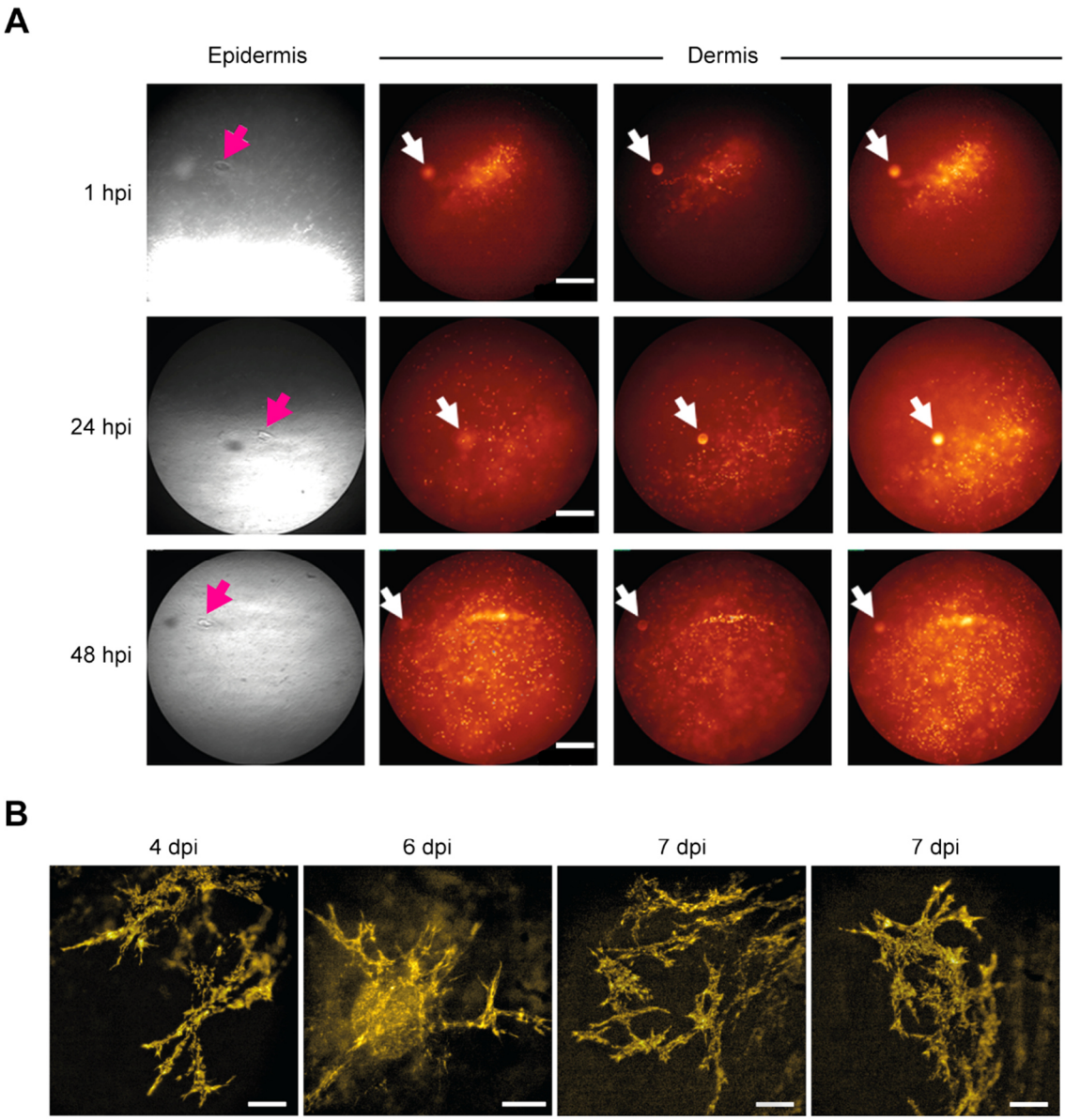

Figure 32: Tsetse-transmitted parasites remain at and migrate from the dermal inoculation site. (A) Two-day observation of the dermal inoculation site by stereomicroscopy. The red arrows mark the epidermal wound caused by the tsetse bite and the white arrows mark an air bubble in the dermis which served as a fiducial. The parasite population in the dermis was imaged at three different depths. Scale bar, 250 µm. **(B)** Stereomicroscopic images of trypanosomes at the periphery of the parasite population in the dermis at late timepoints during infection. Here, the parasites were found in complex patterns. However, whether these structures are actively formed by the trypanosomes or are based on existing structures in the dermis is not clear. Scale bar, 150 µm.

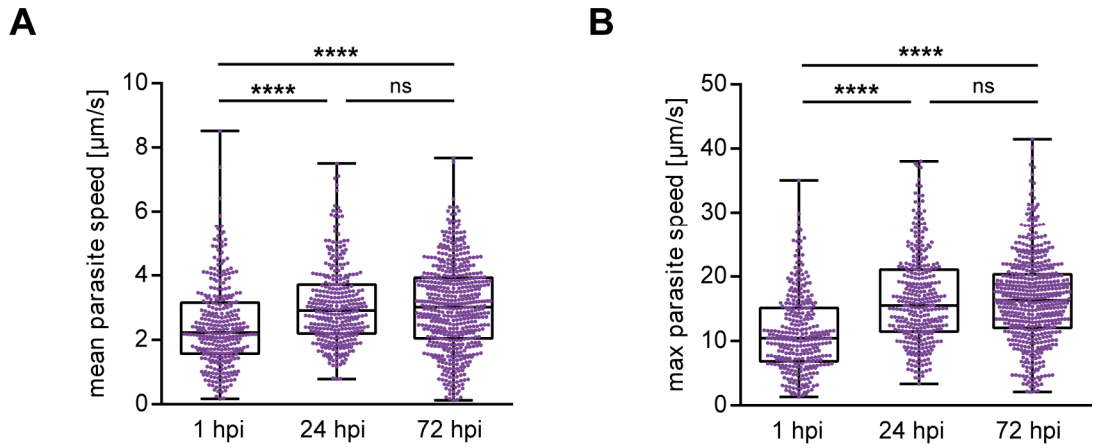

Figure 33: Tsetse-transmitted parasites increase their movement speed in the skin equivalent. The parasite motility in the dermis was analyzed by Laura Hauf during her master thesis. Therefore, skin-dwelling trypanosomes were recorded over a period of 5 min 20 sec and videos were analyzed with Imaris software. **(A + B)** Quantification of the mean (A) and maximum (B) swimming speed of individual skin-dwelling trypanosomes at 1, 24, and 72 hpi. Results are shown as median ± IQR with data representing individual data points. $n \geq 319$ cells for each timepoint. ****: $p < 0.0001$, ns: not significant. Statistical analyses were performed with the two-tailed Mann-Whitney *U*-test. Movie 3 shows exemplary tracks of individual trypanosomes in the skin equivalent for all three timepoints.

In conclusion, although the range of mean and maximum parasite speeds of all timepoints was comparable (minimum and maximum values), the trypanosomes appear to swim faster in the skin equivalent after 24 hpi. This could potentially be attributed to the observed morphological changes, as the parasites at 24 hpi resemble the morphology of BSFs (Figure 24 B and 24 C).

3.6 Skin-dwelling parasites successfully infect tsetse flies and complete their natural mammalian developmental program in the skin equivalent

In the past, it was assumed that tsetse flies could only become infected with trypanosomes by ingesting fly-transmissible stumpy forms present in the blood of infected animals during a bloodmeal. However, recent observations changed this dogma. In 2016, two independent studies found that skin-dwelling parasites contribute to the transmission of the parasites. It has been demonstrated that skin-residing trypanosomes can successfully develop into stumpy forms and that tsetse flies fed on mice with trypanosomes in their skin but without detectable parasites in their blood, became infected (Capewell et al., 2016). Moreover, it has been shown that skin trypanosomes transmitted by tsetse flies can

be reacquired by other tsetse flies as early as 18 hours after infection by a bite in close proximity to the first infectious bite. However, no infection could be detected in the flies, as it was assumed that no stumpy forms could develop in the skin at such an early stage of infection (Caljon et al., 2016).

To test if the trypanosomes in the hdSE are competent to differentiate into stumpy forms, infected hdSEs were screened for the presence of parasites expressing the "Protein Associated with Differentiation 1" (PAD1), which is a stumpy-specific cell marker (Dean et al., 2009). Therefore, a trypanosome line was used harboring a GFP reporter which is fused to a nuclear localization signal at the 5'-end, and to the 3'UTR of the *PAD1* gene at the 3'-end. A sequence motif in the 3'UTR controls the expression of the *PAD1* gene and thus, when the *PAD1* gene is active, the parasites will have a GFP-positive nucleus, (Batram et al., 2014, Zimmermann et al., 2017, Schuster et al., 2020). On days 4 and 7 after infection, PAD1-positive parasites were detected in the skin equivalents, albeit with very low abundance (< 0.1 %; Figure 34 A and Movie 4).

To investigate whether hdSE-derived trypanosomes are competent to infect tsetse flies, hdSEs were infected with trypanosomes by tsetse flies and cultured for 1, 4, and 7 days. Subsequently, trypanosomes were isolated from skin equivalents by protease digestion and sorted by flow cytometry to remove dermal fibroblasts and extracellular matrix proteins from the suspension. Next, trypanosomes were transferred to pre-warmed sheep blood supplemented with 60 mM N-acetyl-D-glucosamine to a final concentration of 5×10^4 cells/ml and fed to teneral tsetse flies. With an uptake volume of 20 µl of blood, this corresponds to the uptake of 1,000 trypanosomes per fly. After 35 days flies were dissected and screened for parasites present in the midgut (MG), proventriculus (PV), and salivary glands (SG) (Figure 34 B). Flies infected with trypanosomes cultured in skin equivalents for 1 day contained no trypanosomes in all relevant organs. In contrast, trypanosomes were found in the organs of flies infected with parasites cultured in hdSEs for 4 and 7 days. In the experiment with parasites isolated from skin at 4 dpi, a completely infected male fly with trypanosomes present in the MG, PV, and SG was found. This corresponded to a prevalence of 0.8 %. The prevalence of infected flies fed with parasites isolated from skin at 7 dpi increased by 3.4-fold to 2.7 %. Although no SG-positive flies were found at this timepoint, flies of both sexes were infected. It has been shown that male flies are more susceptible to infections compared to female flies. Tsetse flies have

robust immune defenses against trypanosome infections, and most flies do not develop transmissible infections (Peacock et al., 2012).

A

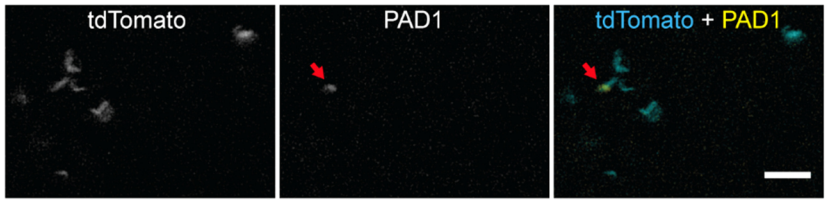

B

Days post infection	♂ dissected	♂ MG+	♂ PV+	♂ SG+	♀ dissected	♀ MG+	♀ PV+	♀ SG+
1	53	-	-	-	56	-	-	-
4	62	1	1	1	70	-	-	-
7	76	1	1	-	73	3	2	-

Figure 34: Skin-residing parasites can develop into stumpy forms and are infectious to tsetse flies. (A) Stereo-fluorescence microscopy of tdTomato-expressing trypanosomes in a hdSE infected for 7 days. The parasites also harbored an endogenous GFP-tagged PAD1 marker as proxy for development to the stumpy stage. PAD1-positive parasites (red arrow) were found in the hdSE with low incidence. Scale bar, 20 µm. The panels show still images of the corresponding movie 4. **(B)** Trypanosomes were isolated from skin equivalents at 1, 4, and 7 days post-infection and sorted by flow cytometry to remove fibroblasts and extracellular matrix proteins. Subsequently, parasites were mixed with sheep blood supplemented with 60 mM N-acetyl-D-glucosamine at 5 x 10^4 cells/ml and fed to teneral tsetse flies. After 35 days flies were dissected and relevant organs were analyzed for the presence of trypanosomes. MG+, midgut positive; PV+, proventriculus positive; SG+, salivary glands positive.

Even though PAD1-positive trypanosomes have been observed rarely in the skin equivalents, infection of tsetse flies with trypanosomes isolated from hdSEs at 4 and 7 dpi resulted in infections in both fly sexes. Detection of trypanosomes in all relevant organs of the flies indicated that the skin-residing parasites possess, in principle, full developmental competence and can complete their entire life cycle.

3.7 *T. brucei* enters a reversible quiescence program in the skin equivalent

In the second phase of skin infection (4 and 7 dpi), the trypanosomes continued to multiply, however, albeit slowly: the population doubling time was measured at 19 h within the first 24 hpi, then slowed to 74 h within the following 3 days (day 1 to day 4) and was at 62 h in the last 3 days (day 4 to day 7), respectively (Figure 22 B). In addition, the parasites remained in the skin equivalent, as very few parasites were found in the surrounding culture medium (Figure 22 D) and no significant increase in cell death was

observed (Figure 22 E), which could explain the high doubling times. Furthermore, the single-parasite RNA sequencing data showed that parasites isolated at 7 dpi from skin differed from the proliferative parasites isolated at 12 or 24 hpi. The 7 dpi parasites did not cluster with the 12/24 hpi parasites (Figure 27 B), were enriched for specific genes (Figure 28 A and Table S2), and replication-associated genes were downregulated at 7 dpi (Figure 29 B). Thus, in the following subchapters, the skin-dwelling parasites at 4 and 7 dpi are investigated in more detail.

3.7.1 Skin-dwelling parasites reduce their protein synthesis and metabolism

In a first step, the cell cycle distribution of the skin-dwelling parasites at 4 and 7 dpi was determined by flow cytometry and compared to MCFs and skin-resident trypanosomes at 6, 12, 18, and 24 hpi (Figure 35 A). As assumed from the growth curve (Figure 22 B), the skin-dwelling parasites continued to be proliferative at 4 and 7 dpi. With a proportion of 25.9 % and 24.6 % of parasites in the S and G2 phases of the cell cycle, the proportion of proliferative trypanosomes decreased only slightly compared to parasites at 24 hpi with 27.1 %.

Furthermore, the protein synthesis rate of skin parasites at 4 and 7 dpi was investigated and compared to skin-residing parasites at earlier timepoints, MCFs, and BSFs (Figure 35 B and 35 C). Interestingly, after an initial 5.4-fold increase in the synthesis rate within the first 24 hpi, at 4 and 7 dpi the skin-dwelling parasites significantly reduced their protein synthesis rate by more than 3.7-fold compared to parasites cultured for 24 hours in the hdSE. The rate of protein synthesis of the parasites on day 7 is comparable to the rate observed in parasites at 1 hpi.

Taken together, at 4 and 7 dpi the skin-residing trypanosomes continued to proliferate, however, with a high doubling time. In addition, the trypanosomes reduced their protein synthesis rate to a basal level and no significant increase in cell death was observed. Furthermore, the transcriptomes of 7 dpi parasites differed from those of proliferative parasites at 12 and 24 hpi. All these findings are characteristic of quiescent cells (Rittershaus et al., 2013, Barrett et al., 2019). Thus, the parasites appeared to have launched a quiescence program. This possibility was further tested by a second independent measure of metabolic activity. The fluorescent reporter tdTomato was integrated within the rDNA locus. Expression of the fluorescent tdTomato protein

therefore reported on the activity of the rDNA locus as a proxy for metabolic activity (Figure 36 A). This approach has previously been used to track quiescence in Leishmania (Jara et al., 2019). In agreement with the protein synthesis measurements (Figure 35 B and 35 C), MCFs showed a significantly lower tdTomato mean fluorescence intensity (MFI) compared to cultured BSFs. After injection, the tdTomato MFI of the skin-residing parasites initially increased within the first day, but then decreased by 2.6- and 4-fold on days 4 and 7 post-infection, respectively (Figure 36 A).

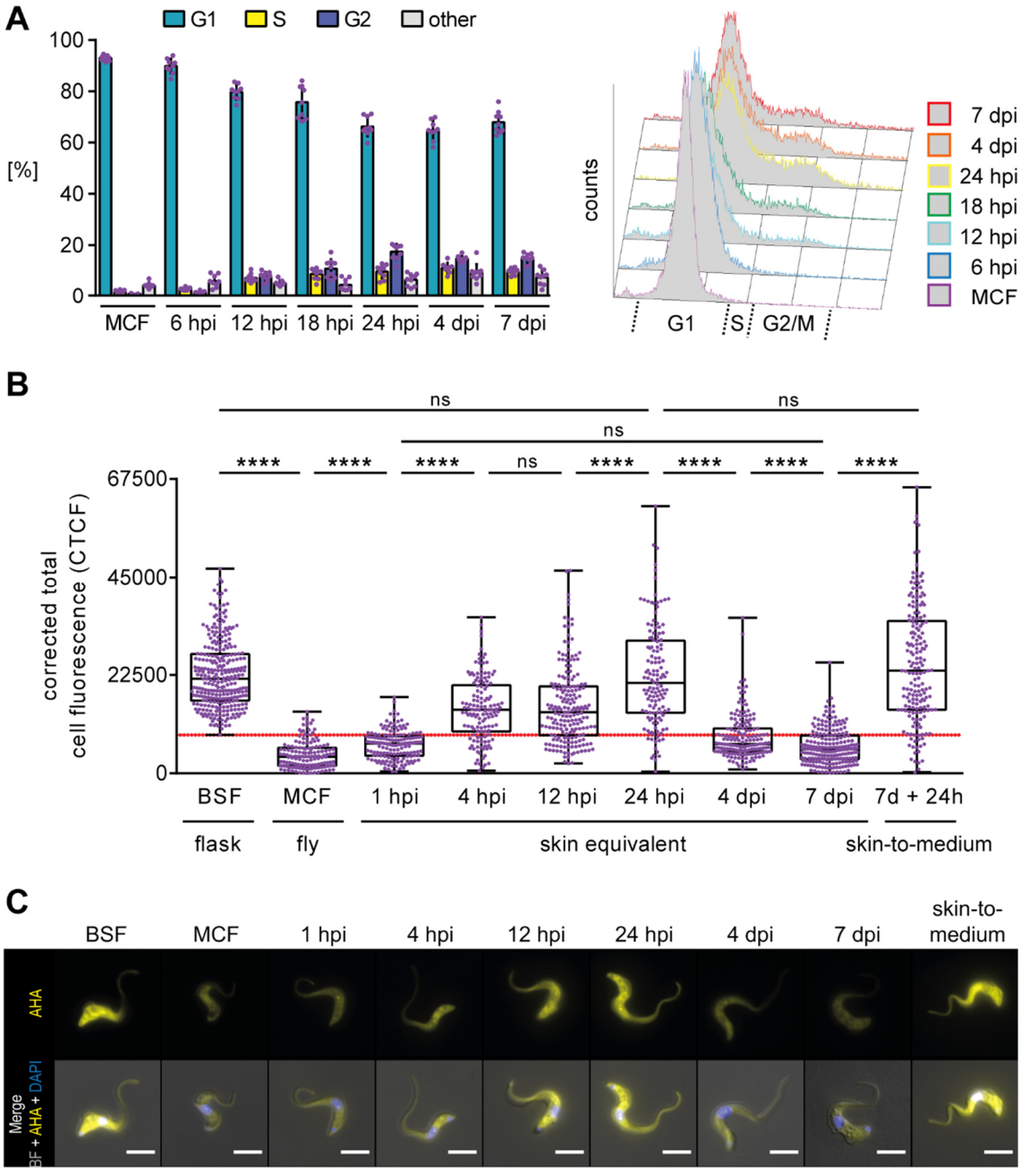

Figure legend on next page

Figure 35: Skin-dwelling parasites reversible reduce their protein synthesis during infection. (A) Flow cytometric assessment of the cell cycle distribution of skin-residing trypanosomes at various timepoints post-infection. The left panel shows the mean ± SD of parasites in the G1, S, or G2 phase of the cell cycle of MCFs and skin-resident trypanosomes at 6, 12, 18, and 24 hpi in comparison to parasites at 4 and 7 dpi. Results of three replicates are shown. The right panel shows representative cell cycle histograms for each timepoint with the three cell cycle phases indicated. **(B)** Quantification of protein synthesis rates of skin-resident parasites isolated at the times indicated post-infection in comparison to BSFs and MCFs. Skin-resident parasites were additionally transferred to HMI9 culture medium supplemented with 1.1 % methylcellulose for 24 h after 7 dpi (skin-to-medium). Trypanosomes were isolated and processed as described in Figure 25. Data are median ± IQR of three replicates. For each approach 136 - 292 individual parasites were analyzed. Statistical analyses were performed with the Mann-Whitney *U*-test, ****: $p < 0.0001$, ns: not significant. The red line defines the threshold for classification as "parasites with low protein synthesis". The lowest synthesis rate measured in cultured BSFs was used as the threshold value. **(C)** Fluorescence microscopy of trypanosomes isolated at the times indicated post-infection from skin equivalents in comparison to BSFs, MCFs, and skin-parasites at 7 dpi, which were transferred to culture medium for 24 h (skin-to-medium). The fluorescence signal intensity of L-azidohomoalanine incorporated into nascent proteins (yellow channel) was measured to assess protein synthesis rate on the single parasite level. Cells were counterstained with DAPI (nuclei, blue channel) and both channels were merged with the phase contrast image in the overlays. Scale bar, 5 µm.

To test whether this phenotype can be reversed, the migration from the skin to the bloodstream was mimicked by extracting skin-residing parasites on day 7 and transferring them into HMI9 culture medium supplemented with 1.1 % methylcellulose to mimic blood viscosity. After skin-to-medium transfer the protein synthesis rate of the parasites significantly increased by 4.2-fold within 24 hours (Figure 35 B and 35 C). Likewise, the tdTomato MFI of the parasites significantly increased by 5.7-fold (Figure 36 A). Moreover, the tdTomato MFI was stable for at least 3 days after transfer. The population doubling time dropped to 7.2 h (Figure 36 B), a value comparable to the 6.8 h of the BSF wildtype strain (Figure 18 A). Since protein synthesis is the most energy-consuming cellular process, it is downregulated to a minimal level during quiescence (Hofmann and Hand, 1994). Thus, the percentage of skin-residing parasites with a low protein synthesis rate was quantified for each timepoint. The lowest synthesis rate measured in cultured BSFs was used as a threshold value (Figure 35 B, red line). After injection into the skin equivalent by the fly, the MCFs reactivated and the number of parasites with a low protein synthesis rate decreased from 89.2 % to 9.6 % within 1 day. However, after 4 and 7 dpi, the skin-resident trypanosomes reduced their protein synthesis rate (Figure 35 B), and 67 % and 76 %, respectively, had a strongly reduced synthesis rate (Figure 36 C). Transfer to culture medium reversed this phenotype and the number of parasites with low protein synthesis decreased to 10.5 % within 24 hours (Figure 36 C). Moreover, the

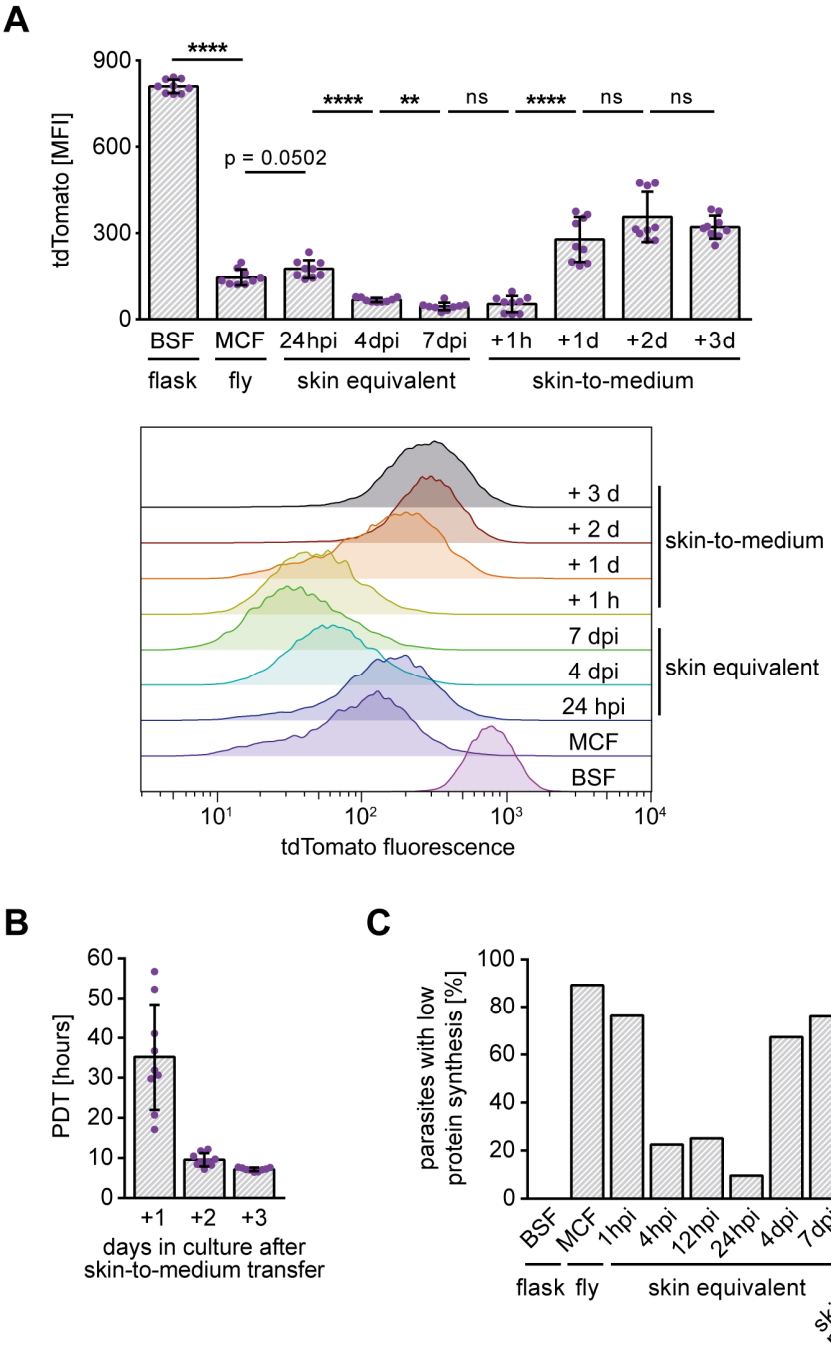

Figure 36: Skin-dwelling parasites reversible reduce their metabolism during infection. **(A)** The upper graph shows the flow cytometric quantification of the tdTomato mean fluorescence intensity (MFI) of skin-resident trypanosomes at various timepoints post-infection compared to BSFs, MCFs, and skin-parasites at 7 dpi, which were transferred to HMI9 culture medium supplemented with 1.1 % methylcellulose to mimic blood viscosity for up to 3 days (skin-to-medium). The reporter tdTomato is located in the rDNA locus, thus control is a proxy for the metabolic state of the parasite. Results are shown as mean ± SD of three replicates. Statistical analyses were performed with the unpaired *t*-test, ****: $p < 0.0001$, **: $p < 0.01$, ns: not significant. The lower graph shows representative histograms of the tdTomato fluorescence for each timepoint. **(B)** Parasites were isolated from hdSEs at 7 dpi and transferred to HMI9 culture medium supplemented with 1.1 % methylcellulose. The population doubling times (PDTs) were recorded for up to 3 days. Data represent mean ± SD of three replicates. **(C)** Quantification of skin-residing trypanosomes classified as "parasites with low protein synthesis", indicated by the red line in Figure 18 B, in comparison to BSFs, MCFs, and skin-parasites at 7 dpi, which were transferred to culture medium for 1 day (skin-to-medium).

protein synthesis rate of the transferred parasites was comparable to cultured BSFs (Figure 35 B).

It can be noted that 4 days after infection, the skin-resident trypanosomes considerably slowed down their growth and reduced their protein synthesis and metabolism to a basal level. This condition was maintained for at least three more days. However, this phenotype could be reversed by mimicking the migration from the skin to the bloodstream. The parasites returned to an active state comparable to BSFs cultured in flasks. Quiescence is defined by a reversible slowdown or arrest of proliferation, and a downregulation of energy metabolism, as well as protein and DNA synthesis is often associated with quiescence (Daignan-Fornier and Sagot, 2011, Coller, 2011, Laporte et al., 2011, Rittershaus et al., 2013, Van den Bergh et al., 2017). Thus, the data strongly suggest that the skin-dwelling trypanosomes entered a quiescent state in the skin equivalent.

3.7.2 The quiescent state in the skin is characterized by a unique gene expression profile

To investigate the skin-dwelling quiescent trypanosomes in more detail, differential gene expression analysis between parasites isolated from infected skin at 7 dpi and 24 hpi was performed (Figure 37 A). The comparative scRNAseq analysis of inactive (7 dpi) and highly active (24 hpi) parasites resulted in 99 genes that were significantly upregulated at 7 dpi and 226 genes specifically upregulated at 24 hpi (Table S3). In addition, the transcriptomes of MCFs were compared with parasites isolated at 7 dpi, as both forms possess a reduced metabolism (Figure 37 B). Here, 127 genes enriched in MCFs and 115 genes specific for 7 dpi-parasites were retrieved (Table S3). With the settings used to detect differentially expressed genes, log2-fold change > 2 and adjusted p-value < 0.01, it has been found that 3 - 4 % of all genes were differentially expressed between skin parasites at 7 dpi and 24 hpi or MCFs. Among the differently-expressed genes, the RNA-binding protein ZFP2 (Tb927.11.14950) was downregulated at 7 dpi (Figure 37 C) and could be one factor that regulates the development of a quiescent trypanosome form in the skin. The *T. cruzi* ortholog TcZFP2 was found to promote the differentiation to the human infectious metacyclic form (Morking et al., 2012). However, if there is a potential role for ZFP2 in quiescence, further functional validation would be required.

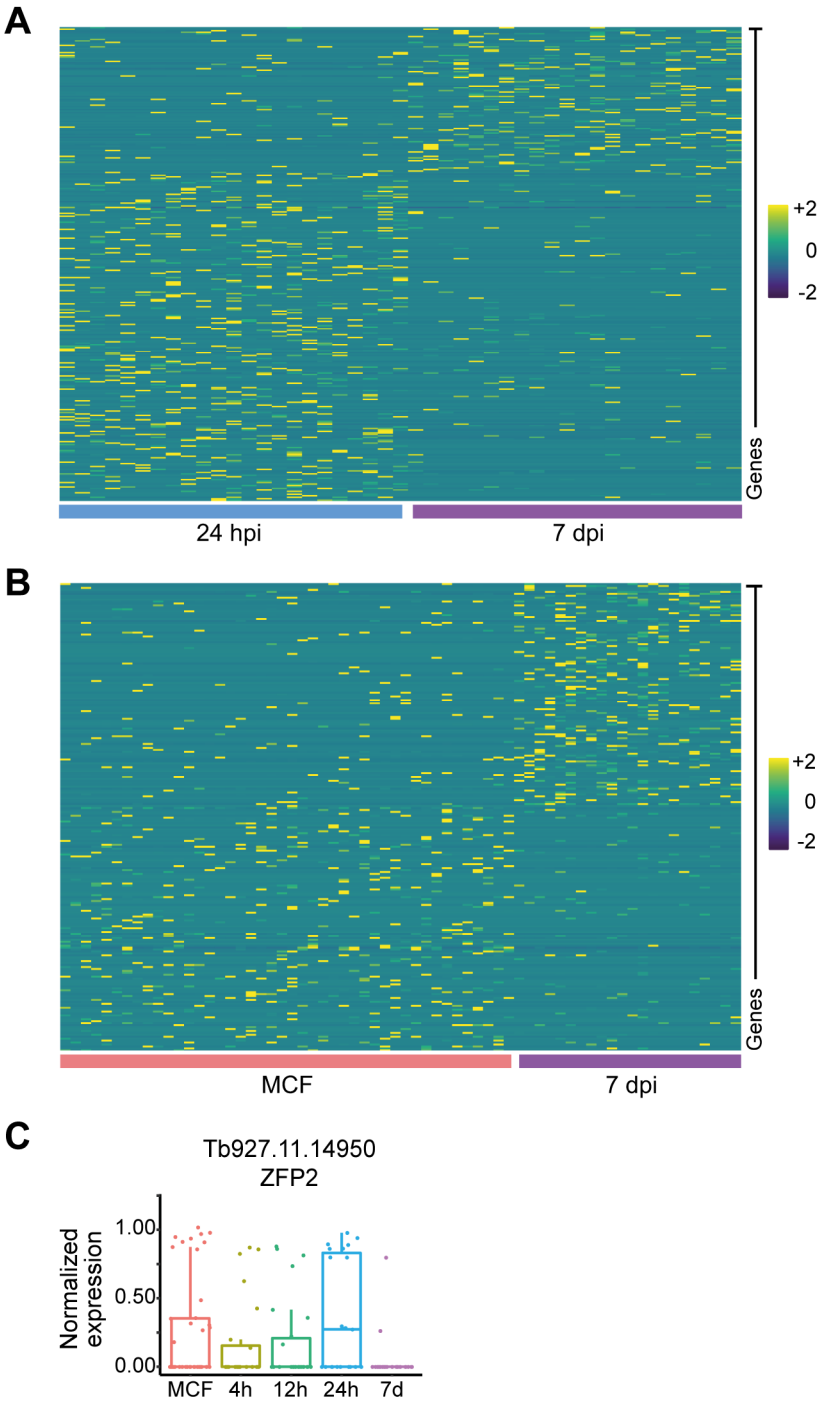

Figure 37: The transcriptome of the quiescent forms in the skin differs from those of skin-resident parasites at 24 hpi and metacyclic forms. (A) Heatmap showing the scaled expression levels of significantly upregulated genes of skin-residing trypanosomes at 24 hpi and 7 dpi. **(B)** Heatmap showing the scaled expression levels of upregulated genes of MCFs in comparison to skin parasites at 7 dpi. Differential gene expression analysis was performed with DESeq2 software. Genes with an absolute log2-fold change > 2 and adjusted p-value < 0.01 were considered as differentially expressed. Each column represents a single parasite, each row represents an individual gene. The color key from purple to yellow indicates low to high gene expression levels. **(C)** Boxplot showing the normalized expression of the RNA-binding protein ZFP2 in MCFs and parasites isolated from skin at 4, 12, 24 hpi, and 7 dpi. In contrast to the other timepoints, ZFP2 is downregulated in skin parasites at 7 dpi.

GO enrichment analysis revealed several metabolic and catabolic processes that were regulated differentially between parasites isolated at 7 dpi and 24 hpi, particularly with regard to arabinose (Figure 38). The underlying gene of the GO terms associated with arabinose is a prostaglandin f synthase (Tb927.11.4700, Table S4). During infection with African trypanosomes, mammals have elevated prostaglandin levels in plasma and cerebrospinal fluid. The elevated prostaglandin level could in part be responsible for symptoms such as fever, headache, immunosuppression, and drowsiness in patients with chronic trypanosomiasis. In addition, *T. brucei* parasites have been shown to be involved in prostaglandin production via a prostaglandin synthase (Kubata et al., 2000).

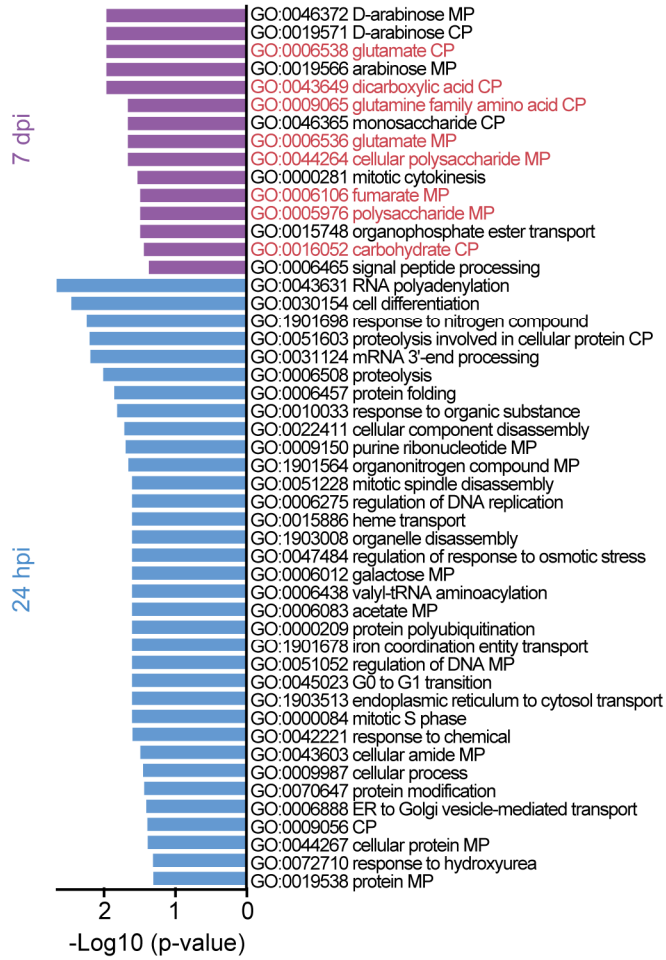

Figure 38: Gene ontology reveals differences in several biological processes of skin-residing trypanosomes at 24 hpi and 7 dpi. Biological process-associated gene ontology (GO) terms significantly enriched in parasites isolated from skin at 24 hpi and 7 dpi. GO term enrichment within the differential expressed genes between the two data sets were determined using the GO enrichment tool on the TriTrypDB webserver. GO terms have been filtered with the Revigo webtool to avoid redundancies. Bars represent the level of significance of the term enrichment. Terms specific to skin parasites at 7 dpi that occurred in both, the comparative analysis with skin parasites at 24 hpi and MCFs (see Figure 39) are highlighted in red.

Compared to MCFs, skin parasites at 7 dpi were enriched in functions associated with "pyruvate metabolic process", "glucose homeostasis", or "protein folding" (Figure 39). Pyruvate is a key product of glycolysis and mainly excreted by BSFs. By contrast, in the tsetse fly, the parasite metabolizes pyruvate in the mitochondria, producing additional ATP molecules.

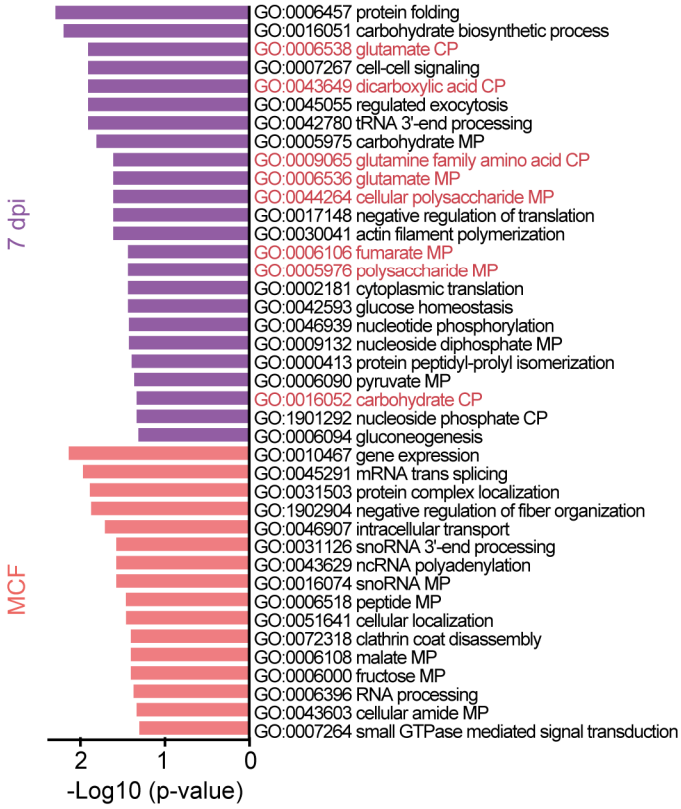

Figure 39: Gene ontology reveals differences in several biological processes of metacyclic forms and skin-residing trypanosomes at 7 dpi. Biological process-associated gene ontology (GO) terms significantly enriched in MCFs and parasites isolated from skin at 7 dpi. GO term enrichment within the differential expressed genes between the two data sets were determined using the GO enrichment tool on the TriTrypDB webserver. GO terms have been filtered with the Revigo webtool to avoid redundancies. Bars represent the level of significance of the term enrichment. Terms specific to skin parasites at 7 dpi that occurred in both, the comparative analysis with MCFs and skin parasites at 24 hpi (see Figure 38) are highlighted in red.

GO terms that occurred in both analyses were functions associated with amino acid (glutamate, glutamine), polysaccharide, and dicarboxylic acid metabolism (fumarate). The underlying gene of the GO terms associated with glutamate is a glutamate dehydrogenase (Tb927.9.5900). It has been shown that glutamate dehydrogenase is induced in quiescent yeast and epithelial cells (Brauer et al., 2005, Murphy et al., 2015, Coloff et al., 2016).

In summary, the skin-resident trypanosomes at 7 dpi replicated 10-times slower and had a protein synthesis rate 3.5-times lower than cultured BSFs. Furthermore, based on the metabolic reporter, their metabolism was reduced 4-fold in comparison to skin parasites at 24 hpi. In addition, the scRNAseq data showed that the transcriptome of the quiescent skin parasites differed from those of MCFs and skin parasites at 24 hpi. Thus, to address these changes and adaptations, the quiescent skin-dwelling trypanosomes will be referred to hereafter as skin tissue forms (STFs).

3.7.3 The skin microenvironment influences the behavior of trypanosomes

To test whether the induction of quiescence can be attributed to the skin microenvironment, metacyclic trypanosomes harvested from tsetse flies were inoculated directly into culture medium. The HMI9 culture medium was supplemented with 1.1 % methylcellulose to mimic blood viscosity. The growth of the parasites was recorded for ten days and the population doubling time was calculated to 6.8 hours (Figure 40 A). This is comparable to the 7.2 h of the extracted STF parasites that were transferred into culture medium (Figure 36 B). No reduction in parasite growth was observed over the 10-day period, which would indicate an entry into quiescence. In contrast, the skin environment does not appear to affect MCF activation and cell cycle re-entry. Similar to the tsetse transmitted MCFs in the skin equivalent, MCFs cultured in suspension started to multiply between 6 and 12 hpi (Figure 40 B) and the cell cycle distribution was similar to that of skin-dwelling parasites (Figure 24 A).

It has been observed that trypanosomes residing in adipose tissue have 3-fold downregulated transcript levels of the active VSG AnTat 1.1 in comparison to trypanosomes living in the bloodstream (Trindade et al., 2016). However, the parasites had an electron-dense coat on their surface, indicating the presence of a VSG coat. This suggests that the active VSG was downregulated or a different VSG was expressed in the adipose tissue parasites. Thus, the influence of the skin environment on VSG expression was tested.

Immunostaining of BSFs of the AnTat 1.1 serodeme with an antibody against AnTat 1.1 and quantification by flow cytometry showed that ~ 95 % of the parasites expressed the VSG AnTat 1.1 on their surface (Figure 40 C). BSFs of the MITat 1.2 serodeme were used as negative control and > 99 % of the parasites were negative for VSG AnTat 1.1.

Since the serodeme AnTat 1.1 is a pleomorphic trypanosome strain, a VSG switch by a small subpopulation (~ 5 %) is reasonable. The trypanosome population obtained from MCFs cultured in suspension for 7 days showed a proportion of AnTat 1.1-positive parasites of ~ 15 %.

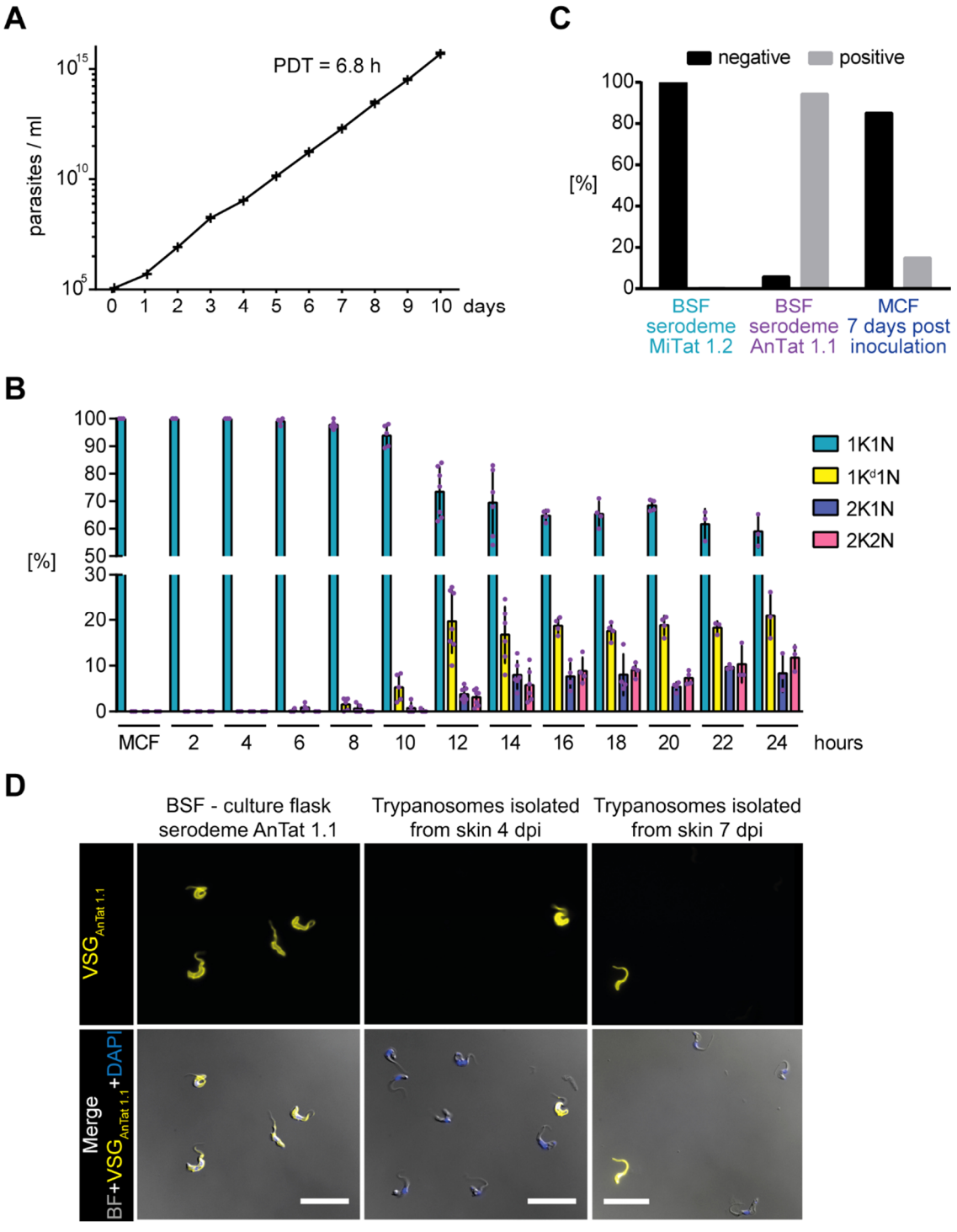

Figure legend on next page

Figure 40: Metacyclic forms re-enter the cell cycle and re-acquire an AnTat 1.1 VSG coat in suspension culture. (A) Growth curve and PDT of MCFs obtained from spit samples of salivary gland-positive tsetse flies incubated in HMI9 medium supplemented with 1.1 % methylcellulose to mimic blood viscosity. The growth was recorded for ten days and the PDT was calculated. Results are shown as mean ± SD of three replicates. **(B)** The cell cycle position of DAPI-stained trypanosomes was analyzed every 2 hours after inoculation of MCFs into HMI9 medium supplemented with 1.1 % methylcellulose. The configuration of the kinetoplast (K) and nucleus (N) was microscopically analyzed. Cells with a non-dividing kinetoplast and a single nucleus are in the G1 phase (1K1N). Parasites with a dividing kinetoplast ($1K^d1N$) are in the mitochondrial S phase. Trypanosomes with two kinetoplasts (2K1N) are in G2 phase, while parasites with two kinetoplasts and nuclei (2K2N) are mitotic. Data represent mean ± SD of three to seven replicates. 507 - 1,150 parasites were analyzed per timepoint. **(C)** Immunocytological quantification of VSG AnTat 1.1 expression of monomorphic BSFs of the serodeme MITat 1.2 (negative control) compared with BSFs of the serodeme AnTat 1.1 (positive control) and MCFs inoculated for 7 days into HMI9 medium supplemented with 1.1 % methylcellulose. MCFs were obtained from tsetse flies infected with stumpy forms of the serodeme AnTat 1.1. The percentage of parasites stained negative or positive for AnTat 1.1 are shown of one replicate. 30,000 parasites were analyzed per condition. **(D)** Immunofluorescence microscopy of skin-derived trypanosomes at 4 and 7 dpi, stained with an antibody against the VSG AnTat 1.1 (yellow channel) and compared to BSFs of the serodeme AnTat 1.1. The phase contrast image was merged with the blue channel (nuclei, DAPI) and the yellow channel in the overlay images. Scale bar, 20 µm.

In comparison, trypanosomes were isolated from skin at 4 and 7 dpi and stained with an antibody against AnTat 1.1. At both timepoints the parasites have been found to express the VSG AnTat 1.1 only with low incidence. Since the background noise was already higher than the low percentage of AnTat 1.1-positive skin parasites, quantification by flow cytometry was excluded and parasites were analyzed by microscopy (Figure 40 D). On both days, only few AnTat 1.1-positive parasites were observed; however, due to the experimental methodology used, a certain number of trypanosomes were applied onto the microscope slides and the percentage of AnTat 1.1-positive stained parasites could be estimated to be < 0.1 %. This is in stark contrast to the 15 % of AnTat 1.1-positive parasites observed in the suspension culture at day 7 (Figure 40 C).

Furthermore, it was tested whether the proliferative trypanosomes obtained from MCFs cultured in suspension are developmentally competent to progress further through the life cycle. For this purpose, MCFs inoculated into HMI9 medium supplemented with 1.1 % methylcellulose were induced by quorum sensing at different timepoints post-inoculation to differentiate into stumpy forms (Figure 41 A). For this, parasites were grown to a density of 5×10^5 cells/ml and cultured for two additional days, which induces differentiation to the stumpy form by quorum sensing (Vassella et al., 1997). Subsequently, the expression of the stumpy reporter GFP:$PAD1_{UTR}$ was quantified. Two days post-inoculation, only a small proportion of 5 % expressed the stumpy reporter. In strong contrast, from day 3 onwards, > 92 % of the parasites were positive for the

reporter. Next, it was tested whether these stumpy forms are developmentally competent to progress through the tsetse fly. For this purpose, flies were infected with stumpy forms derived from MCFs cultured in suspension for 7 days and induced to differentiate into stumpy forms by quorum sensing. Stumpy forms were mixed with sheep blood and fed to flies at a concentration of 4 x 10^6 cells/ml. After 35 days, the saliva of the flies was examined microscopically for the presence of metacyclic trypanosomes (Figure 41 B). On average, 52 % of flies developed a mature salivary gland infection and the results demonstrate that stumpy forms derived from MCFs cultured in suspension for 7 days were competent to infect the fly up to the mammalian-infective stage in the salivary glands. Thus, these stumpy forms possessed full developmental competence.

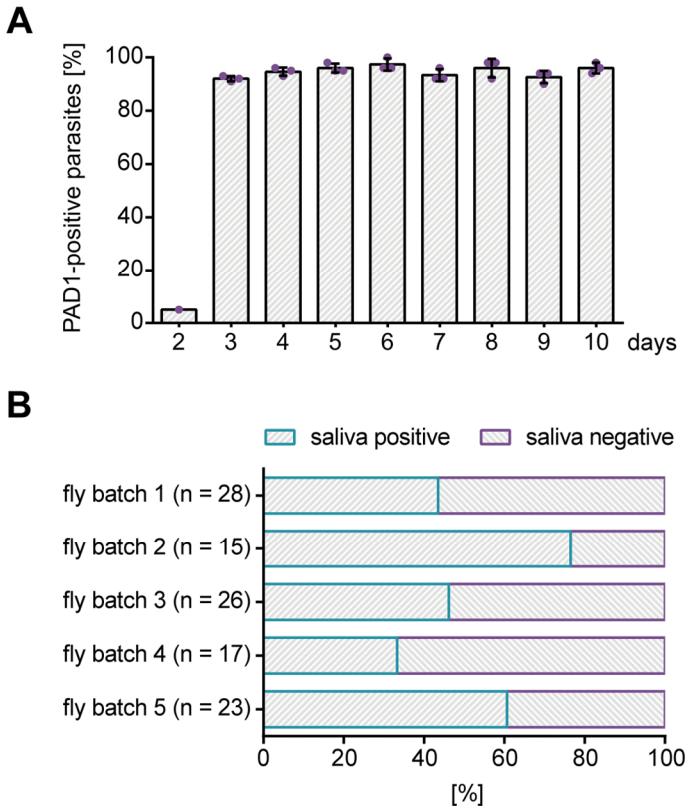

Figure 41: The trypanosome population recovered from metacyclic forms cultured in suspension is developmentally competent to differentiate into stumpy forms and to re-infect tsetse flies. (A) Quantification of parasites expressing the GFP:PAD1$_{UTR}$ reporter. MCFs were harvested from spit samples of salivary gland-positive tsetse flies and inoculated into HMI9 medium supplemented with 1.1 % methylcellulose. At the times indicated the parasites reached a density of 5 x 10^5 cells/ml and were cultured for two additional days, which induces differentiation to the stumpy form by quorum sensing (Vassella et al., 1997). Data represent mean ± SD of three replicates, except day 2 (total n = 2,260 cells). **(B)** MCFs were inoculated into HMI9 medium supplemented with 1.1 % methylcellulose and differentiated to stumpy forms on day 7 post-inoculation. Stumpy forms were mixed with sheep blood at 4 x 10^6 cells/ml and fed to teneral tsetse flies. After 35 days, the saliva of the flies was examined microscopically for the presence of metacyclic trypanosomes. Shown is the percentage of flies with (saliva positive) and without (saliva negative) MCFs in the saliva of five replicates (total flies = 109).

In summary, MCFs were harvested from tsetse flies by induced spitting and inoculated into HMI9 medium. These MCFs re-entered the cell cycle ~ 10 - 12 hours post-inoculation. A timing comparable to naturally-transmitted MCFs in the skin equivalent. However, the inoculated MCFs showed exponential growth over a 10-day period with a doubling time of 6.8 h, whereas naturally-transmitted MCFs entered a quiescent state in the skin ~ 4 dpi. In addition, the percentage of VSG AnTat 1.1-positive parasites was 150-fold increased in MCFs cultured in suspension. These observations suggest that the skin microenvironment strongly influences the behavior of the parasite.

IV. Discussion and outlook

Most pathogenic microorganisms would fail to penetrate the first layer of mammalian defense, the skin. This is overcome by pathogens transmitted by blood-sucking arthropods. These pathogens hijack an arthropod and rely on its capacity to puncture a hole into the skin, which either directly deposits the pathogen within the dermis or opens up a gate of entry into the body. Although vector-borne diseases have been documented throughout history, in many cases the underlying molecular mechanisms by which different pathogens establish infection upon injection into the vertebrate host remain elusive. Therefore, it is important to study the molecular interactions of pathogens with their respective hosts to prevent infections and design vaccines or treatment strategies.

The parasitic life cycle of African trypanosomes within the mammalian host begins in the skin after the injection of metacyclic parasites by the tsetse fly. Studies of trypanosome pathogenesis often employ murine animal models to monitor disease development or virulence phenotypes of certain mutant strains. Although animal models have greatly contributed, and continue to contribute, to our understanding of host-pathogen interactions, the widely experimentally used intraperitoneal infection route may not be representative of natural intradermal infections (Wei et al., 2011, Caljon et al., 2016, Ndungu et al., 2019). Furthermore, considering the relatively small number of tsetse-transmitted metacyclic parasites, they are of limited use for studying the early parasitological features of a naturally transmitted trypanosome infection in the mammalian host. *In vivo* imaging at high spatiotemporal resolution is challenging, and especially achieving optical access to tissues at single cell resolution (Jelicks et al., 2013, De Niz et al., 2019). In addition, they are commonly not the natural hosts of the parasites and can be limited in their ability to reflect the natural host environment (Masopust et al., 2017). This drives the need to establish new versatile and accessible model systems to study the virulence strategies of naturally transmitted trypanosomes.

The aim of this dissertation work was to establish and validate a human skin infection model to study vector-borne *T. brucei* parasites under close-to-natural conditions in mammalian skin. The human skin equivalent developed in this study recapitulated key anatomical, cellular, and functional aspects of native human skin and allowed for the natural infection with trypanosomes by the tsetse fly. Moreover, this work provided a detailed description of the development of the injected cell cycle-arrested metacyclic

trypanosomes and revealed an almost immediate activation and differentiation to proliferative parasites. In the second phase of skin residence, the trypanosome population shared common features described for quiescent cells, namely slow growth, reduced DNA synthesis, and downregulation of protein translation. The skin equivalent was permissive for dual single-cell RNA sequencing of skin cells and trypanosomes and constitutes a step forward in understanding which molecular mechanisms and environmental stimuli could potentially act as drivers for parasite activation, differentiation, and adaptation in mammalian skin. Overall, this work demonstrated that artificial human skin offers a new and promising way to study vector-borne *T. brucei* parasites under close-to-natural conditions as an alternative to animal experimentation. This may also be relevant for other vector-borne parasites such as *Leishmania*, *Plasmodium*, or *Trypanosoma cruzi* to enable infection studies in a highly standardized and tractable model system.

4.1 The high-density primary human skin equivalent is a versatile and accessible model to study the pathogenesis of *T. brucei* in mammalian skin

The mammalian skin plays a major role as the first interface in the transmission of arthropod-borne parasites. The interaction of *Leishmania* or *Plasmodium* parasites with host skin are the best studied and have revealed intriguing strategies for disease establishment (Menard et al., 2013, de Menezes et al., 2016). In stark contrast, our knowledge on the interaction of African trypanosomes with mammalian skin is currently highly limited. Thus, the first aim of this thesis was to develop and validate an advanced primary human skin equivalent as an infection model that mimics key features of native human skin in order to study the tripartite connection of vector, host, and parasite at the skin interface.

Collagen is the primary structural component of the connective tissue of human skin and its biocompatibility makes it an ideal candidate as a scaffold for skin tissue engineering. However, collagen-based skin equivalents usually have low mechanical stability, which makes them susceptible to fibroblast-mediated contraction during culture (Feng et al., 2003). Dissolved collagen has a high viscosity and therefore only low concentrations can

be processed (Antoine et al., 2014). Consequently, the prepared collagen hydrogels have a high water content, which is the reason for their low structural integrity.

In this work the technique of plastic compression (Brown et al., 2005) was applied and validated to compress fibroblast-populated collagen hydrogels to generate high-density dermal equivalents (hdDEs). The working hypothesis was that compression of the hydrogels should displace excess water, thereby reducing their water content and consequently increasing their collagen concentration due to the reduced volume of the gels. The increased collagen concentration should improve the mechanical stability of the dermal equivalents and ultimately increase the structural integrity of the human skin equivalents.

Previous studies have already shown that increasing the collagen concentration significantly reduces the shrinkage and weight loss of collagen gels during culture (Helary et al., 2010, Braziulis et al., 2012). However, Helary et al. did not compress the collagen gels and tested only collagen concentrations between 0.5 and 3 mg/ml. In contrast, Brazilius et al. used a compression system based on cell culture inserts with non-perpendicular walls (*e.g.* with an angle $> 90°$). However, this cannot produce a standardized dermal equivalent because the collagen is forced into the space between the compression punch and the insert wall during compression, resulting in a non-uniform dermal equivalent. Thus, in this dissertation work Snapwell inserts with perpendicular walls were used. Furthermore, for the technical implementation of compression, a computer-assisted compression system was developed, consisting of a custom-made compression reactor and a linear motor. This system allowed a fast and reproducible production of 12 highly standardized hdDEs in parallel. In direct comparison with non-compressed dermal equivalents, hdDEs possessed improved structural integrity and significantly increased long-term stability.

The skin equivalents developed in this work used the hdDEs as dermal components, which prevented the skin equivalents from shrinking. As a consequence, the skin equivalents in the Snapwell inserts could only be supplied with culture medium from the basal side. In the case of shrinking skin equivalents, the culture medium could distribute in the space between the equivalent and the insert wall, providing the skin equivalents with additional nutrients from the lateral side. To ensure sufficient nutrient supply to the high-density skin equivalents (hdSEs), the membrane of the Snapwell inserts had to be perforated with 42 microneedles to improve permeability. This has significantly

improved the quality of the hdSEs. An additional challenge was that the dermal equivalents stuck to the compression punches after the compression process, and damage-free detachment of the hdDEs, for example with forceps, was not possible. Therefore, the compression reactor was designed in such a way that compressed air could be introduced into the compression punches via a connection in the adapter to the linear motor. The compressed air enabled the residue-free detachment of the hdDEs from the compression punches without damaging the dermal equivalents.

The hdSE established in this study recapitulated key aspects of native human skin and the use of a mixture of skin medium and trypanosome medium provided optimal conditions that supported both growth of parasites and skin equivalents. This was of particular importance in order to provide a suitable and stable habitat for the pathogen. In addition to the characteristic morphology visualized by histological hematoxylin and eosin staining of hdSEs when compared with native human skin, natural epidermal differentiation was assessed by immunohistochemical (IHC) staining. Therefore, the intermediate filaments KRT5 and KRT14 were used as markers to detect undifferentiated keratinocytes in the basal layer of the epidermis (Fuchs, 1990). As evidenced by both IHC staining and scRNAseq data, both keratins were expressed in the hdSEs, but not restricted to the basal layer. This is partially inconsistent with the IHC staining of native human skin where KRT5 and KRT14 were restricted to the basal layer and with published scRNAseq data on human skin (Wang et al., 2020). Thus, the results suggest that some of the KRT5 and KRT14 filaments were present in keratinocytes even as differentiation progressed and were only partially replaced by KRT1 and KRT10. A possible explanation could be that the keratinocytes in hdSE differentiate faster than in native human skin and thus the exchange of filaments was not yet complete. In contrast to native skin with a renewal turnover of 52 - 75 days (Halprin, 1972), the turnover in the hdSE was only 20 days. Keratinocytes in the basal layer were mitotic, as evidenced by scRNAseq and consistent with previous findings (Fuchs, 1990, Wang et al., 2020). Furthermore, according to the postulated localizations (Fuchs, 1990), KRT1 and KRT10 was located only in suprabasal cells in both native human skin and hdSEs. Both keratin pairs (KRT5/14 and KRT1/10) are particularly important for epidermal integrity as mutations in these keratin genes cause the blistering skin diseases epidermolysis bullosa simplex and epidermolytic hyperkeratosis (Moll et al., 2008).

In addition to intermediate filaments, other proteins are important for the formation of a functional *stratum corneum*. Involucrin has a central role in this process and is crosslinked with loricrin and trichohyalin by various transglutaminases (Sevilla et al., 2007). Although this crosslinking does not occur until the *stratum granulosum* has formed, synthesis of involucrin begins in the first suprabasal layers (Murphy et al., 1984). Accordingly, involucrin can be detected from the first suprabasal layer, as was the case in the hdSE. Another important protein in the development of the *stratum corneum* is filaggrin. It is formed by dephosphorylation and proteolysis of profilaggrin, the main component of the keratohyalin granules of the *stratum granulosum* that contribute to cornification (Fleckman et al., 1985). The postulated function of filaggrin is to support the aggregation of intermediate filaments. This results in the flattening of keratinocytes and the formation of a corneocyte-specific morphology (Dale et al., 1997). The localization of filaggrin in the hdSE was consistent with that of native human skin. Overall, the hdSE showed a characteristic distribution of several epidermal markers, suggesting natural differentiation and proper synthesis of the *stratum corneum*.

Another structure that determines the quality of a skin equivalent is the basement membrane. In native skin, the basement membrane has important functions. It plays a fundamental role in keratinocyte migration and adhesion, anchors the epidermis to the dermis, and provides a critical barrier against various substances and microorganisms (Breitkreutz et al., 2009). Furthermore, components of the basement membrane play an important role in the maintenance of the epidermal stem cell niche (Lavker and Sun, 2000). The basement membrane contains five main components, which are laminin-332 (LAMA3, LAMB3, and LAMC2) and laminin-411 (LAMA4, LAMB1, and LAMC1), type IV collagen (COL4), nidogen (NID1), and the proteoglycan perlecan (HSPG2) (Breitkreutz et al., 2009). Based on the scRNAseq data, all these components were expressed in the hdSE. In addition, IHC staining confirmed the presence and correct localization of COL4 in the hdSE. COL4 is particularly important for the mechanical stability of the basement membrane (Poschl et al., 2004). The components HSPG2 and NID1 do not form polymers, but are integrated into the laminin/collagen IV-scaffold through their multiple binding sites (Breitkreutz et al., 2009). The anchoring of the epidermis to the dermis is mainly achieved by hemidesmosomes. The intracellular plaque proteins PLEC and DST link the keratin filaments to the transmembrane proteins ITGA6/ITGB4 and COL17A1. The extracellular part of these proteins binds laminin-332

present in the basement membrane which ensures a strong and stable adhesion. The basement membrane is connected to the underlying dermis by anchoring fibrils (loop structures of COL7) interwoven with lattices of COL1 and COL3 fibrils. These adhesion complexes are critical to the overall structural and functional integrity of the skin (Breitkreutz et al., 2009, Tsuruta et al., 2011). The expression of all these proteins, as detected by scRNAseq, strongly suggests that the cells present in the hdSE produced a mature and chemically complex basement membrane.

In order to use the hdSE as an infection model, it was necessary to allow infection of the hdSEs with trypanosomes by tsetse flies. To achieve this, the hdSEs had to be removed from their Snapwell inserts, because it was not possible to navigate the tsetse flies to the skin equivalent while it was still in the insert. Furthermore, the proboscis of the tsetse fly has a length of ~ 2 mm, whereas the hdSEs only had a standard height of 1 mm. Thus, the removed hdSEs had to be stacked until three of them were on top of each other. Otherwise, the flies simply bit through the hdSEs and deposited most of the parasites underneath. Biting in blood-sucking arthropods is a multi-sensory response involving a range of physical and chemical stimuli. It has been shown that the bite of a tsetse fly is mainly triggered by high relative humidity and a rise in temperature close to mammalian temperature (Chappuis et al., 2013). Therefore, the stacked hdSEs were additionally placed on a heating plate at 37 °C. Overall, the consideration of these factors enabled the successful natural transmission of *T. brucei* parasites by tsetse flies into the skin equivalents.

The use of tsetse flies allowed a natural injection of the trypanosomes into the skin and analysis of the skin lesion revealed a complex deposition of the parasites within an intricate bite path network in the dermis. This large-scale injection of parasites possibly supports their spread in the skin and entry into the lymphatic system. Furthermore, the analysis of the injection depth showed that the parasites can be deposited to a depth of 2 - 3 mm and thus can also be deposited in subcutaneous fat tissue. However, whether this affects the development of the parasites in the mammalian host remains unknown.

In conclusion, the skin infection model developed in this work recapitulates native human skin in key anatomical, cellular, and functional aspects and can be infected with trypanosomes through the bite of the tsetse fly. In the following chapters, the development of the injected metacyclic forms in the skin equivalent will be discussed in detail.

4.2 Early parasitological features of tsetse-transmitted *T. brucei* parasites in the high-density skin equivalent

During the life cycle of *T. brucei* the parasite alternates between a warm-blooded vertebrate host and a cold-blooded invertebrate vector. Consequently, when trypanosomes change hosts, they experience a drastic change in their environment. Transmission from the mammalian host to the tsetse fly is far better understood, in contrast to transmission from the fly to the warm-blooded host (Szoor et al., 2020). In general, both transmissions require pre-adapted parasite forms, the stumpy form for transmission back to the fly and the metacyclic form (MCF) to establish infection in the vertebrate host. The fact that the differentiation process from the stumpy form to the procyclic midgut stage in the fly can be accomplished *in vitro* has contributed significantly to the elucidation of this process. However, very recent data strongly suggest that non-adapted bloodstream forms (BSFs) can also establish infection in tsetse flies (Schuster et al., 2020).

In stark contrast, our knowledge on the interaction of metacyclic trypanosomes with mammalian skin and their differentiation into proliferative parasites is currently highly limited. This has been for both, technical and biological reasons. Not only does the bite of a tsetse fly transmit only a few hundred to thousand MCFs into the skin dermis, the injected parasites are also difficult to trace and study in animal hosts. Since only a few parasites can be isolated from animal skin, the low cell number does not allow for many experimental techniques. Most importantly, the natural vector transmission involves tsetse flies, as the infectious metacyclic life cycle stage cannot be cultured *in vitro* and animal models are afflicted with ethical drawbacks. These technical and biological issues have been the major roadblocks for studying the trypanosome skin interaction.

Although the first observations that trypanosomes accumulate and multiply in the skin matrix were made more than 100 years ago (Yorke, 1911, Willett and Gordon, 1957, Gordon and Willett, 1958, Ormerod, 1970, Goodwin, 1970, Goodwin, 1971), a more detailed description was not made until 2016 for the reasons mentioned above (Caljon et al., 2016). Caljon et al. used tsetse flies to naturally infect mice with *T. brucei* parasites and observed that the injected MCFs started multiplying in the skin within 18 hours of transmission. The data presented in this thesis support this observation and narrowed the

onset of replication to 6 - 12 hours post-infection. However, the underlying molecular processes also remained unexplored in the 2016 study.

Further experiments in this thesis showed that re-entry into the cell cycle is preceded by several molecular processes that occur almost immediately after the parasites enter the skin. Cell division is a complex process with high energy and nutrient demands (Salazar-Roa and Malumbres, 2017). Since MCFs are cell cycle-arrested, quiescent cells, they have to be globally activated to synthesize energy and the machinery required for DNA replication and mitosis. Thus, the biosynthesis of new proteins was monitored by following the incorporation of a methionine-analogue into nascent proteins at various timepoints post-infection (Ma and Yates, 2018). This revealed an almost immediate upregulation of protein synthesis after just 1 hour upon arrival into the skin. The synthesis rate peaked after 1 day. At this time, the percentage of proliferative parasites in the hdSEs was highest and the rate of synthesis was comparable to proliferative BSFs in axenic culture. The population doubling time was measured at 19 h within the first 24 hpi. However, cell cycle re-entry occurred only after approximately 12 hpi. If this initial lag phase is subtracted, the doubling time would be 9.7 h. This value is close to the observed doubling time of 6.6 h of axenically cultured BSFs of the same strain and could explain the equally high protein synthesis rates.

The first 12 hpi were also characterized by morphological changes of the injected trypanosomes. During this period, an elongation of the cell body and the free distal tip of the flagellum could be observed. The morphological restructuring of the parasites in the skin appeared to be achieved after 1 day. The morphology at this time strongly resembled that of BSFs. These findings are consistent with the observed timings made during transmission from the mammalian host to the tsetse fly (Schuster et al., 2020). The cell cycle-arrested stumpy forms re-entered the cell cycle between 15 - 17 hours after uptake into the fly and exhibited the morphology of procyclic forms after 24 hours. Hence, it appears that for both host changes, perception of the new environment and transduction of differentiation signals occurs very rapidly to allow for fast adaptation to the new host.

Along with the altered morphology, a significant increase in the swimming speed of the parasites in the skin could be measured. This is consistent with observations that BSFs have a higher maximum velocity and flagellar beat frequency compared to MCFs (Bargul et al., 2016, Schuster et al., 2017, Kruger et al., 2018). An increased swimming speed could influence the spread of the parasites in the dermis and entry into the draining lymph,

where parasites can be detected 1 - 2 days after infection (Barry and Emery, 1984). It can be speculated whether MCFs can remove antibodies bound to VSGs as efficiently as BSFs. This is achieved by hydrodynamic forces generated by the forward movement of the parasite pushing the VSG-antibody complex to the posterior pole. Here, it can be internalized via the flagellar pocket, the only side of endo- and exocytosis (Engstler et al., 2007). However, BSFs have a mean swimming velocity of 20 µm/s while the highest velocity measured for MCFs was only 15 µm/s (Schuster et al., 2017). It remains unclear whether the lower velocity is sufficient to generate enough hydrodynamic force to eliminate bound antibodies. It can be hypothesized that only after the acquisition of a BSF-like morphology after 24 hpi this immune evasion mechanism is functional due to the increased swimming speed. However, these high velocities cannot be achieved constantly in native tissue (Alfituri et al., 2019), suggesting that this immune evasion mechanism plays only a minor role in skin. Furthermore, the primary antibody response of the host does not occur prior to 1 week after antigen exposure (Ademokun and Dunn-Walters, 2010), raising the question of why MCFs have a VSG coat in the first place? Recent studies have shown that the intradermal route differs considerably from the experimental tail vein or peritoneal route. It has been shown that the dermis is a strict bottleneck for BSFs to establish infection, while MCFs are somehow pre-adapted to survive in the dermis and establish infection (Wei et al., 2011, Caljon et al., 2016, Ndungu et al., 2019). Caljon et al. have shown that MCFs require a 10-fold lower intradermal infection dose in contrast to BSFs. However, it is not clear what could be the basis for the higher infectivity of MCFs. Therefore, it is reasonable to hypothesize that the metacyclic VSG coat plays an important role in the evasion of the innate immune response to which the parasites are exposed almost immediately upon injection into the skin. For example, it has been shown that exposure of mononuclear phagocytes, which include monocytes, macrophages, and dendritic cells, to released VSG prior to an IFN-γ trigger downregulates inducible nitric oxide synthase (iNOS) and secretion of toxic nitric oxide (NO) (Cnops et al., 2015). Very early upon injection into the skin, this is a situation that could occur before NK and NK T-cells are recruited to the bite site and release IFN-γ to activate macrophages. As a consequence, lower NO levels at the bite site contribute to a more favorable host environment for parasite outgrowth and persistence. Furthermore, it has been shown that the parasites inhibit through their VSGs the progression of the alternative complement activation pathway beyond the C3 convertase. The VSG coat protects the parasite by masking other surface molecules present on the plasma membrane

which are capable of promoting alternative pathway activation (Ferrante and Allison, 1983, Devine et al., 1986). Otherwise, the complement system would induce trypanolysis, which in the absence of specific antibodies could play a potential role in parasite clearance in the early stages of infection (Stijlemans et al., 2016). Thus, the metacyclic VSG coat plays a key role in modulating the host's cellular response. As metacyclic VSGs are limited in their variability (~ 27 isoforms (Turner et al., 1988)), these are exchanged during infection between day 4 and 6 with VSG isoforms characteristic of the BSF (~ 2,000 isoforms (Cross et al., 2014)). This VSG switch is essential for immune evasion and occurs at the time when the first antibodies are produced by the host's adaptive immune system (Gong and Ruprecht, 2020). However, whether metacyclic VSGs interact differently with the host's innate immune response in comparison to bloodstream VGSs remains elusive. There is evidence that metacyclic VSGs are modified by salivary glycoproteins of the tsetse fly which bind strongly to the surface of MCFs. These MCF-bound glycoproteins may influence the parasite transmission into the vertebrate host (Kozak et al., 2021) and may be the basis for better adaptation of MCFs to the mammalian skin. For example, the Salp15 salivary glycoprotein of *Ixodes* ticks binds to the outer surface protein C of *Borrelia burgdorferi* and creates a protective coat against complement-mediated killing (Ramamoorthi et al., 2005).

To link the early parasitological features observed in the skin equivalent to potentially underlying developmental mechanisms, the transcriptomes of MCFs collected from flies with a mature salivary gland infection were compared to those of trypanosomes isolated from hdSEs at four different timepoints post-infection (4 hpi, 12 hpi, 24 hpi, and 7 dpi). Notably, RNA sequencing has not yet been applied to study the development of MCFs in the vertebrate host and, therefore, direct comparative data are not available. Thus, the Smart-seq2 approach was used in this work to dissect the transcriptomes of individual trypanosomes. In contrast to the droplet-based 10x genomics platform, the Smart-seq2 approach allows identification of different cell types without pre-known marker genes, as each cell can be traced back to its original microwell, from which it is known what cell type or condition it contained.

In contrast to the fly-stages, which use proline to feed their tricarboxylic acid (TCA) cycle, glucose is the only carbon source for ATP production described for replicative BSFs (Smith et al., 2017). MCFs pre-adapt by downregulation of mRNAs for components of the TCA cycle, but retain their protein counterparts. In addition, enzymes of the

glycolytic pathway are upregulated at the protein level, but not at the transcript level (Christiano et al., 2017). Supporting this, the scRNAseq data collected in this work demonstrated a rapid upregulation of genes associated with glycolysis. Among those, HK1 (Tb927.10.2010) and GAPDH (Tb927.6.4300) were the most prominent. However, PGI (Tb927.1.3830), PFK (Tb927.3.3270), TIM (Tb927.11.5520), and PGKC (Tb927.1.700) were also upregulated upon entry into the skin during the first 24 hpi (Table S2). All of these enzymes are part of the glycolysis pathway in *T. brucei* (Coley et al., 2011). In another very recent scRNAseq study GAPDH was used as a marker gene to discriminate between BSFs and stumpy forms (Briggs et al., 2020). Here, the scRNAseq data showed that GAPDH can also be used as a marker to discriminate between MCFs and BSFs.

Furthermore, transcripts associated with replication were rapidly upregulated upon arrival in the skin. This is consistent with the finding that the injected cell cycle-arrested MCFs re-entered the cell cycle between 6 - 12 hpi. These genes include KKT9 (Tb927.8.1150), PRI1 (Tb927.8.2550), NDPK (Tb927.11.16130), and adenine phosphoribosyltransferase (Tb927.7.1780). KKT9 is essential for the segregation of both megabase chromosomes and minichromosomes (Akiyoshi and Gull, 2014). PRI1 is a mitochondrial DNA primase essential for cell growth and kinetoplast DNA replication (Hines and Ray, 2010). NDPK catalyzes the reaction of ATP + nucleoside diphosphate to ADP + nucleoside triphosphate (Lacombe et al., 2018), and adenine phosphoribosyltransferase is part of the purine metabolism pathway.

Trypanosomes depend on post-transcriptional mechanisms to regulate gene expression because of the absence of regulatable RNA polymerase (pol) II promoters. However, gene regulation is particularly important in trypanosomes due to their complex life cycle and the need to adapt to different environments or to pre-adapt in preparation for differentiation. Such post-transcriptional control can occur at various steps of mRNA processing, translation, and decay (Clayton, 2019). A crucial role in expression regulation in trypanosomes play RNA-binding proteins (RBPs) (Kolev et al., 2014). The genome of the parasite contains large numbers of genes encoding predicted RBPs. It has been shown that they are involved in the regulation of the cell cycle, life cycle, and stress response of the parasite (Kolev et al., 2014, Clayton, 2019). In general, RBPs can be subdivided into three groups: Alba and pumilio-domain proteins, RNA recognition motif (RRM) domain proteins, and zinc-finger domain proteins (Clayton, 2013). The scRNAseq data collected

in this work identified RBPs from all three groups that could be involved in the differentiation and adaptation processes of the parasites observed in the skin equivalents (Table S2 and S3).

Transcript levels of the pumilio/PUF RNA binding protein 9 (PUF9, Tb927.1.2600) were already elevated at 4 hpi. PUF9 had been previously identified as important for the progression through the cell cycle by stabilizing target transcripts (Archer et al., 2009). One of these target transcripts is H4V (Tb927.2.2670), a histone variant enriched at probable pol II transcription termination sites (Siegel et al., 2009). The scRNAseq data show that H4V transcripts were elevated in parasites at 12 hpi and 7 dpi. Moreover, the PUF9 target PNT1 (Tb927.11.6550) was enriched in parasites at late timepoints (12 + 24 hpi) in the skin. These results confirm the findings of Archer et. al. and support the previously made observation that the trypanosomes re-enter the cell cycle after deposition into the skin equivalent.

Transcripts of the zinc-finger protein ZC3H20 (Tb927.7.2660) were rapidly upregulated upon arrival in the skin and remained at high levels between 12 hpi and 7 dpi. ZC3H20 is of particular importance as it has been shown in a number of publications to oscillate during the life cycle of *T. brucei*. Vigneron et. al. dissected the transcriptomes of individual trypanosomes residing in parasitized salivary glands of tsetse flies with the droplet-based 10x genomics approach (Vigneron et al., 2020). The authors found that ZC3H20 is downregulated in epimastigote forms and mature MCFs, whereas it is upregulated in pre-mature MCFs. In a second study, bulk RNAseq was used to compare the transcriptome of mature MCFs with procyclic forms (PCFs) (Christiano et al., 2017). Here, it has been shown that ZC3H20 is upregulated in PCFs. In the vertebrate host, ZC3H20 is expressed in both parasite stages, albeit with transient elevated expression at the key BSF to stumpy form transition point (Liu et al., 2020, Briggs et al., 2020). Furthermore, ZC3H20 activity is required for differentiation into the stumpy form (Cayla et al., 2020). It has also been shown that ZC3H20 is associated to the RBP10 protein, to interact with MKT1, and to be implicated in the increase of protein translation or in mRNA stability (Erben et al., 2014, Singh et al., 2014). RBP10 is essential to maintain the BSF stage and is therefore highly expressed in BSFs (Mugo and Clayton, 2017). Although RBP10 (Tb927.8.2780) was detected in the scRNAseq data set, no major changes in RBP10 transcript abundance were observed between the five timepoints. Most likely because RBP10 is already expressed in mature MCFs (Vigneron et al., 2020). In

conclusion, the observed upregulation of ZC3H20 during the development of MCFs in skin is consistent with the results of previous studies and may play a potential role during parasite differentiation. Moreover, it is consistent with the observed increase in the rate of protein synthesis after skin entry and, since ZC3H20 is required for stumpy development, indicates that the skin-resident trypanosomes are not deficient in this important regulator.

In addition, an upregulation of transcripts of two previously undescribed RBPs, ZC3H35 (Tb927.10.12740) and ZC3H48 (Tb927.9.10280), was observed, which may have a function during parasite differentiation in the skin. The precise functions of these two RBPs are not yet known, but both were described to suppress mRNAs containing *boxB* RNA hairpin-motifs in BSFs (Erben et al., 2014, Lueong et al., 2016). The *boxB* RNA motif forms a hairpin structure and has important functions in the antitermination events that allow RNA polymerase II to read through a series of transcription terminators (Vieu and Rahmouni, 2004). Consequently, it could be that binding of either RBPs to the *boxB* hairpin motif terminates transcription and suppresses target transcripts. Furthermore, the mRNA of ZC3H48 was found to be bound by RBP10 in BSFs (Mugo and Clayton, 2017).

One bulk RNAseq study compared the transcriptional profile of parasitized salivary glands with BSFs (Telleria et al., 2014). Although the glandular trypanosome population in the fly is complex, containing not only mature MCFs but also pre-mature MCFs and epimastigote forms, some comparisons can be made. For example, Telleria et. al. observed that the RBP3 (Tb927.11.530) is enriched in BSFs. The scRNAseq data collected in this work demonstrated an upregulation of RBP3 at 24 hpi in the skin compared to skin-residing parasites at 7 dpi. An RNAi screen has found that RNAi of RBP3 in BSFs slowed down growth but had no effect on PCFs (Wurst et al., 2009). Thus, the observed downregulation of RBP3 in parasites at 7 dpi in the skin equivalent could be one factor explaining the higher population doubling time in comparison to parasites at 24 hpi. However, the RBPs DRBD13 (Tb927.8.6650) and RBP9 (Tb927.11.12120) were also upregulated in BSFs in the study by Telleria et. al. and contrast with our data showing an upregulation in MCFs and a downregulation in parasites at 24 hpi and 7 dpi (Table S2 and S3). DRBD13 stabilizes transcripts containing conserved AU-rich elements (Najafabadi et al., 2013) and RNAi of DRBD13 slows growth in BSFs (Wurst et al., 2009), whereas RBP9 is a post-transcriptional repressor (Lueong et al., 2016).

However, it is possible that DRBD13 and RBP9 are not expressed by skin-resident trypanosomes, but only by BSFs living in the circulation.

To better understand the biological differences between the different timepoints and to identify functional differences, the differently-expressed genes identified in this work were used to apply a gene ontology (GO) enrichment analysis. MCFs were preferentially enriched in functions associated with “RNA processing”, and among the underlying genes of these GO terms is RBP6 (Tb927.3.2930). RBP6 overexpression in monomorphic Lister 427 PCFs resulted in differentiation to long and short epimastigote forms as well as to mammalian infective MCFs (Kolev et al., 2012). However, further differentiation to BSFs required infection of mice, and it remains unclear as to how they differ from pleomorphic wildtype MCFs. Nevertheless, RBP6 plays an important role in metacyclogenesis (Christiano et al., 2017, Vigneron et al., 2020) and our scRNAseq analysis showed downregulation of RBP6 transcripts during the course of skin infection (Table S2).

Parasites isolated at 4 hpi from skin were associated with GO terms such as “endocytosis” and “import into cell”, and in the early (MCF + 4 hpi) vs. late (12 hpi + 24 hpi) comparison, additionally with “regulation of cellular response to heat”. The expression of VSG isoforms characteristic of BSFs requires the activation of BSF VSG expression sites and it has been shown that a temperature shift from 28 to 37 °C activates BSF VSG expression site promotors (Kolev et al., 2018). This temperature shift may also act as a general trigger for MCF activation upon inoculation into the skin. However, expression of BSF VSGs occurs relatively late in the infection after day 4 (Esser and Schoenbechler, 1985, Barry et al., 1998), which was also found in this work. Furthermore, skin temperature is usually below 37 °C (van Marken Lichtenbelt et al., 2006, Krauchi and Wirz-Justice, 1994). Thus, other triggers, such as the detection of a high glucose level as a result of an increased endocytosis rate, the dilution of differentiation inhibitors in the skin, which may be present in the fly's saliva, or the interaction with ECM proteins, are also conceivable ideas. In fact, it was demonstrated that the ECM proteins LAMC1 and THBS1 (which are also expressed in the high-density skin equivalent), are required for *T. cruzi* infection (Nde et al., 2012). It has been shown that *T. brucei* expresses proteins to interact with the ECM (de Sousa et al., 2010, Bastos et al., 2010) and its flagellum provides a diverse signalling platform to integrate environmental signals (Parsons and Ruben, 2000, Rotureau et al., 2009, Maric et al., 2010, Oberholzer et al., 2011). Very

recently, the flagellar protein FLAM8 was found to modulate the extravascular dissemination of *T. brucei* in the skin (Alvarez et al., 2021). Although this is a fascinating perspective, model systems to systematically study the host-parasite crosstalk are still lacking. This is especially true for human skin, which is physiologically and immunologically very different from mouse skin (Masopust et al., 2017, Zomer and Trentin, 2018).

Supporting the observation that the injected trypanosomes exhibited morphological changes in the skin within the first 12 hpi, parasites isolated from skin at 12 hpi were associated with GO terms reflecting the reorganization of cellular structures, *e.g.* "anatomical structure development" and "developmental process". The morphological restructuring appeared to be achieved after 24 h and the parasites resembled the morphology of BSFs. Trypanosomes isolated from skin at 24 hpi were associated with GO terms consistent with the presence of a proliferative parasite population in the skin, *e.g.* "regulation of mitotic cell cycle". Parasites at 7 dpi were preferentially enriched with GO terms suggestive of an exchange of metacyclic VSGs with bloodstream VSGs, *e.g.* "telomere organization". This was supported by the finding of AnTat 1.1-positive skin-derived trypanosomes on days 4 and 7 post-infection. This is also consistent with findings in infected mice indicating a VSG switch between 4 - 6 dpi (Esser and Schoenbechler, 1985).

Taken together, the results strongly suggest that the tsetse-borne cell cycle-arrested MCFs are activated in the hdSE and rapidly re-enter the cell cycle and acquire the size, morphology, motility, and protein synthesis rate characteristic of BSFs. These findings were confirmed by scRNAseq and further extended by the identification of a variety of genes potentially involved in cell cycle activation and parasite development in the skin. In the next chapter, the behavior of the skin-dwelling trypanosomes after the initial highly proliferative phase will be further discussed.

4.3 Tsetse-transmitted *T. brucei* parasites adapt to the tissue-engineered skin environment as quiescent skin tissue forms

Caljon et al. have reported that tsetse-transmitted parasites persist in the skin of mice around the bite site for at least 7 days post-infection (Caljon et al., 2016). However, it remained unclear whether this initial population remains in the skin throughout the course of the disease and whether it is distinct from the trypanosomes in the bloodstream. Although the reason(s) why trypanosomes accumulate and persist in mammalian skin continue to remain unknown (Caljon et al., 2016, Capewell et al., 2016), the data in this thesis clearly show that the skin environment strongly influences the parasites. After re-entry into the cell cycle and an initial phase of proliferation, the skin-residing trypanosomes slow down growth, reduce DNA synthesis, and downregulate protein translation and metabolism. Concomitantly, they have very low rates of parasite death. All these characteristics are hallmarks of quiescent cells (Coller, 2011, Daignan-Fornier and Sagot, 2011, Laporte et al., 2011, Rittershaus et al., 2013, Barrett et al., 2019).

Among bacteria the formation of quiescent, non- or slowly replicating but viable cells is common (Fisher et al., 2017) and a fundamental and ancient evolutionary adaptive mechanism (Van den Bergh et al., 2017). Quiescence describes cells that are non-replicating or replicating very slowly with associated metabolic alterations such as diminished DNA synthesis, and widespread downregulation of protein translation when compared with replicative cells (Barrett et al., 2019). These cells are less vulnerable to a variety of transient environmental stresses, including drug treatment and immunological attacks (Van den Bergh et al., 2017). Although quiescence enables bacteria to survive stress, it is not necessarily triggered by stress and once those conditions pass, the quiescent population can return to a proliferative state and recolonize the environment (Barrett et al., 2019). This reversibility separates quiescent cells (cells that can return to an active and proliferative state) from senescent cells (cells that will never re-proliferate due to aging or terminal differentiation) (Sagot and Laporte, 2019).

After the initial proliferative phase, the skin-dwelling trypanosomes slowed down growth and replicated 10-times slower and had a protein synthesis rate 3.5-times lower than cultured BSFs. Similar observations were made with *Mycobacterium tuberculosis*, which has a 5-fold higher doubling time during persistence (Munoz-Elias et al., 2005, Gill et al., 2009), and quiescence in *Saccharomyces cerevisiae* is accompanied by a 20-fold decrease

in protein synthesis (Fuge et al., 1994). Slow growing persister cells have been described for a few other protist parasites, such as *Leishmania* or *Trypanosoma cruzi*, but not yet for African trypanosomes (Barrett et al., 2019). In the related protist, *Leishmania mexicana*, quiescent amastigotes in murine lesions show very slow growth with a doubling time of 12 days and low rates of protein turnover (Kloehn et al., 2015). Slow-growing intracellular amastigotes with a doubling time of 60 hours have also been reported for *Leishmania major* (Mandell and Beverley, 2017). *Leishmania infantum* parasites of infected dogs have been shown to persist in lesions at the primary inoculation sites for several months (Aslan et al., 2016) and chronic infections with *Trypanosoma cruzi* are associated with a reduced replication rate of the parasite in the colon (Ward et al., 2020).

Therefore, it can be hypothesized that the initial phase of trypanosome proliferation functions in establishing a robust population in the host skin. Once this is achieved a second adaptation step yields a slow growing, skin-residing trypanosome population, which contributes to parasite persistence. Interestingly, the trypanosomes do not actively leave the skin equivalent, as only 3.4 % of the total parasite population was found in the surrounding culture medium. Furthermore, when the parasites were extracted from the skin and transferred to culture medium, they resumed rapid growth. Differential gene expression analysis on the single cell level revealed that the quiescent parasites clearly differed from the early proliferative trypanosomes after infection. All of this suggests that trypanosomes transmitted by the tsetse fly into skin enter a persister-like state, the quiescent skin tissue form (STF).

The quiescent STFs are distinct from the two other known quiescent life cycle stages of *T. brucei*, the metacyclic and the stumpy stage, and may represent an adaptive response to the skin microenvironment. First, MCFs and stumpy forms are cell cycle-arrested and require a host change for their reactivation (Szoor et al., 2020). In contrast, the STFs described here replicated very slowly and could be reactivated within the same host, namely when they transit from skin via lymphatic vessels to the bloodstream. Second, the STFs did not, or only very rarely, differentiate to the cell cycle-arrested stumpy stage. The quiescent parasite population in the skin did not express the stumpy-specific marker protein PAD1. Third, the transcriptome of STFs clearly differed from MCFs. Fourth, the morphology of STFs resembled that of BSFs, and fifth, STFs swam faster in the skin than MCFs. Theoretically, induction of quiescence by macro- or microenvironmental

conditions can be distinguished from quiescence coupled to differentiation (Sagot and Laporte, 2019). During embryogenesis, the entry and exit into a quiescent state of specific cells at fixed timepoints plays a crucial role. For example, in the *Drosophila* embryo so called histoblasts enter quiescence early during embryogenesis and remain quiescent for several days. However, these cells are preparing for rapid re-entry into the cell cycle and are primed for proliferation. After pre-pupa formation the histoblasts start rapid proliferation and produce a cell population that will form the abdominal epithelium of the adult fly (O'Farrell, 2011). MCFs are in a similar situation. They prepare for entry into the skin and a rapid proliferation phase by differentiating into a developmentally regulated quiescent state. In contrast, entry into a quiescent state in STFs is most likely not coupled to any developmental biological program, but is induced by the microenvironment of the skin. This is supported by the finding that MCFs differentiated in suspension culture showed no signs of growth reduction over a 10-day period, which would indicate an entry into quiescence.

However, it seems unlikely that the STFs are an as yet undiscovered life cycle stage of *T. brucei*, as these forms can be bypassed by direct inoculation of metacyclic parasites into the host's body cavity or blood. It is more likely that the formation of STFs (and probably also the adipose tissue forms (ATFs) residing in fat (Trindade et al., 2016)) are evolutionary examples for the amazing flexibility in parasite life cycles. Trypanosomes are prime examples for this, because they thrive in various host animals and in body fluids with very different physicochemical properties. In adipose tissue, trypanosomes have been shown to metabolically adapt as ATFs (Trindade et al., 2016). ATFs have a BSF-like morphology but, as a functional adaptation to adipose tissue, can utilize fatty acids as a carbon source, unlike BSFs. However, it remains unclear whether ATFs similarly exhibit reduced metabolism and slow growth. The ability to flexibly and specifically respond to environmental cues is an as yet underestimated hallmark of parasitism.

The exchange of the VSG coat is a known hallmark of the MCF to BSF transition (Barry et al., 1998). The switch from expression of metacyclic to bloodstream form VSGs occurs between days 4 and 6 post-infection (Esser and Schoenbechler, 1985). The VSG repertoire of the pleomorphic strain EATRO 1125 used in this study is not known and predicting which BSF VSG isoforms are expressed is not possible. The only VSG known to be expressed in EATRO 1125 is the VSG AnTat 1.1. Interestingly, positive immunostaining for this BSF VSG isoform was only detected in < 0.1 % of the

skin-residing parasites 4 and 7 days post-infection and contrasts with the observation that MCFs differentiated in suspension culture for 7 days had a proportion of 15 % of AnTat 1.1-positive parasites. A similar observation has been made with ATF parasites of the same strain residing in adipose tissue. Here, the active VSG AnTat 1.1 was 3-fold downregulated compared to parasites in the bloodstream (Trindade et al., 2016). These observations suggest that trypanosome populations residing in different niches of the same host (e.g., skin, adipose tissue, blood) express different VSGs. However, it is not known what the molecular basis for the selective VSG expression in tissues might be, as this is a relatively new discovery. The high-density skin equivalent developed in this study could serve as a platform to elucidate this behavior in the future. Furthermore, the fact that STFs are similar to ATFs in terms of VSG expression strongly suggests that both forms are not *bona fide* BSFs.

In 2016, the skin has been recognized as a reservoir tissue during disease, as trypanosomes have frequently been found in the skin of infected mice (Capewell et al., 2016). These skin-residing trypanosomes could develop into stumpy forms and their proportion has been estimated to be 20 % on day 11 post-infection (Capewell et al., 2016). However, it should be noted that these skin-resident trypanosomes did not result from the injected parasites at the bite wound, but from trypanosomes that migrated from the bloodstream into the skin tissue. The skin-dwelling parasites could be ingested by tsetse flies during a bloodmeal and successfully infected the flies (Capewell et al., 2016). These results were supported by a second study showing that injected trypanosomes that remained in the skin at the bite site can also be transmitted to tsetse flies during a bloodmeal (Caljon et al., 2016). However, the parasites were acquired by the flies as early as 18 h after the initial deposition of the parasites in the skin and were unable to establish infection in the fly. From the data of this thesis, it is now known that at that time the parasites in the skin were still in the process of differentiation to proliferative trypanosomes and the first parasites just started to replicate. For this reason, they were probably unable to infect the fly. In order to assess whether the trypanosomes residing in the hdSE are competent to develop into stumpy forms, the expression of a fluorescent reporter was monitored by live cell microscopy. Proteins of the PAD (proteins associated with differentiation) family were the first markers described as being specific for stumpy trypanosomes (Dean et al., 2009). Therefore, a PAD1 reporter construct was used to clearly identify stumpy trypanosomes in the hdSEs. A sequence motif in the 3´UTR

mediates the early increase of the PAD1 transcript abundance during differentiation to the stumpy form (MacGregor and Matthews, 2012). Thus, the fluorescent protein GFP was fused to the 3'UTR of the *PAD1* gene and to a nuclear localization signal. Consequently, when the *PAD1* gene is active, the parasites will have a GFP positive nucleus, which is a direct indication of stumpy development (Batram et al., 2014, Zimmermann et al., 2017, Schuster et al., 2020). Although stumpy forms expressing PAD1 were found in the hdSE, their proportion was very low with < 0.1 % of all parasites on days 4 and 7. On one hand, this shows that the trypanosomes in the skin equivalent were, in principle, capable of stumpy formation at these early timepoints and supports the conclusion that the parasites were not defective in the key regulator ZC3H20. Expression of this regulator in the skin-residing trypanosomes has already been demonstrated by the scRNAseq data. On the other hand, the postulated paracrine induction by oligopeptides of stumpy formation generated by trypanosome excreted oligopeptidases (Rojas et al., 2019) should have yielded a much larger proportion of stumpy parasites in the confined skin environment. In strong contrast, MCFs differentiated in suspension culture were able to differentiate into stumpy forms from day 3 of inoculation. The parasite population was > 90 % PAD1-positive. These stumpy forms were also successful to infect tsetse flies. However, it is possible that the threshold for stumpy induction was not sufficiently reached within the 7 days in the skin equivalent. In the mouse model, stumpy forms were detected in the skin only from day 11 post-infection (Capewell et al., 2016). Therefore, the observed stumpy forms in the hdSE might not have resulted from the classical stumpy induction pathway through quorum sensing, but rather from a quorum sensing-independent path, which is exclusively controlled by the transcriptional status of the VSG expression site (Zimmermann et al., 2017). Depending on the degree of expression site attenuation, an unsuccessful VSG switch allows a synchronous differentiation to stumpy cells at low parasite densities. This would also be consistent with the first occurrences of AnTat 1.1-positive parasites on days 4 and 7. This alternative mechanism might ensure the transmission of parasites to tsetse flies, even at low cell densities, when the stumpy induction factor is not able to accumulate to an effective concentration. An alternative explanation could be that the STFs do not secrete oligopeptidases, as this has only been shown for BSFs (Rojas et al., 2019), or the STFs are resistant to stumpy induction. Similarly, it has been shown that quiescent myoblasts and fibroblasts are resistant to terminal differentiation (Coller et al., 2006). The hypothesis of specific skin tissue forms is further supported by the very low infection rates of tsetse flies that were fed with skin-

derived trypanosomes. It has recently been shown that a single bloodstream stage trypanosome suffices to successfully infect a tsetse fly, and that it does not matter if this is a proliferative BSF or stumpy stage parasite (Schuster et al., 2020). Thus, if the STFs would be BSFs, much higher fly infection rates would be expected. It is important to note that the same pleomorphic trypanosome serodeme AnTat 1.1 was also used in the tsetse infection study. This suggests that STFs are not tsetse-infective.

At the transcriptome level, the STFs considerably differed from MCFs and parasites isolated at 24 hpi. With the settings used for detecting differentially expressed genes, log2 fold change > 2 and adjusted p value < 0.01, 3 - 4 % of all detected genes were differentially expressed between STFs and MCFs or the highly active parasites at 24 hpi. For comparison, a significant change in transcript abundance has been reported for ATF parasites residing in fat when compared to BSFs. The authors found 20 % of the genes differentially expressed between ATFs and BSFs (Trindade et al., 2016). However, in the ATF study, only a log2 fold change > 1 was used to determine a gene as differentially expressed. As a result, considerably more genes were detected as differentially expressed, but some of them might be false positives due to the low threshold. In addition, STFs have not been compared with *bona fide* BSFs in this work so far, which may result in a similarly high number of differentially expressed genes.

Among the differently-expressed genes, the RNA-binding protein ZFP2 (Tb927.11.14950) was downregulated in STFs. ZFP2 has also been found to be downregulated in ATFs (Trindade et al., 2016). It has been shown that ZFP2, when ablated in BSFs by RNA interference, inhibits the differentiation to the procyclic form. In addition, ectopic expression of ZFP2 in BSFs resulted in a procyclic stage-specific remodeling of the trypanosome cytoskeleton similar to the morphogenic events during differentiation. Furthermore, ZFP2 is expressed equally in BSFs and PCFs and exhibits uniform expression throughout differentiation between stumpy forms and PCFs (Hendriks et al., 2001). Thus, ZFP2 is implicated in the control of early differentiation events during the transmission from the vertebrate to the invertebrate host. The observed downregulation of ZFP2 in STFs could therefore be a potential factor explaining the very low infection rates in tsetse flies fed with STFs.

At the global level, STFs were enriched in functions associated with glutamate and glutamine when compared with MCFs and 24 hpi parasites. The underlying gene of these GO terms is a glutamate dehydrogenase (Tb927.9.5900). This gene is also increased in

the quiescent stumpy form when compared with BSFs (Briggs et al., 2020). Proliferating cells catabolize more glutamate via transaminases to couple non-essential amino acid (NEAA) synthesis to α-ketoglutarate generation. During quiescence, NEAA consumption and transaminase expression are reduced, while glutamate dehydrogenase is induced, leading to decreased NEAA synthesis and a decoupling of carbon and nitrogen metabolism (Coloff et al., 2016). Such metabolic adaptations to quiescence are evolutionarily conserved in yeast, where glutamate dehydrogenase is induced as yeast enter stationary phase (Brauer et al., 2005, Murphy et al., 2015). This pathway favors the synthesis of NEAAs from α-ketoglutarate and ammonia over glutamate, thereby limiting the accumulation of toxic ammonia. This provides biosynthetic and survival advantages over proliferative cells (Coloff et al., 2016). Activation of this pathway strongly suggests entry of STFs into quiescence.

In conclusion, the findings of this thesis are compatible with the following scenario. The tsetse fly deposits cell cycle-arrested MCFs into the host skin. The feeding insect ruptures blood vessels. MCF parasites that directly enter the circulation through the pooled blood, develop to the proliferating BSF stage. Parasites that do not enter the bloodstream but stay in the skin start proliferating in tissue spaces, and in this way establishing a viable population of proliferative trypanosomes within 1 day. At this timepoint they adapt to the skin environment as quiescent STFs, which can persist in the host's skin for extended periods. As the skin interstitial fluid is continuous with the lymphatic system, STF parasites will eventually be drained by suction forces into the lymph, where they start proliferating as BSFs. The skin acts as a reservoir for African trypanosomes (Capewell et al., 2016, Camara et al., 2020) and the hidden, quiescent, but motile STFs could act as a source of parasites that can continuously repopulate the blood.

Interestingly, after the initial immune response of the host against the injected metacyclic trypanosomes in the skin, the skin-dwelling parasites appear not to trigger any further major inflammatory cell infiltration (Capewell et al., 2016, Mabille and Caljon, 2020). The underlying host and parasite factors are unknown. The discovery of STFs in a close to nature, tractable tissue model might provide an experimental system for tackling the important question as to how the parasites might be slipping under the radar of the inflammation response. In recent years, there has been increasing evidence that trypanosomes persist in the skin of aparasitemic (*i.e.* no trypanosomes detectable in blood) and asymptomatic individuals (Capewell et al., 2016, Camara et al., 2020). It has

also been suggested that these individuals contribute to the transmission of the disease (Koffi et al., 2006, Kabore et al., 2011, Capewell et al., 2019). In addition, case reports of longstanding infections with little to no symptoms (Ilboudo et al., 2011, Jamonneau et al., 2012, Sudarshi et al., 2014, Berthier et al., 2016) suggest that at least some individuals may develop latent trypanosome infections, in which quiescent, slowly replicating trypanosomes residing in the skin may play an important role. Furthermore, the skin quiescence might explain some of the treatment failures in humans (Richardson et al., 2016). Quiescent cells are usually less susceptible to chemotherapeutic drugs (Witkowski et al., 2010).

In summary, the tsetse-transmitted parasites almost immediately reactivated the cell cycle and established a proliferative population upon injection into the skin. After this initial proliferative phase, the trypanosome population shared common features described for quiescent cells, namely slow growth, reduced DNA synthesis, and downregulation of protein translation. In addition, their metabolism and transcriptome differed from the highly proliferative trypanosomes in the skin, and they could be reactivated and returned to an active state. The results demonstrate the existence of a quiescence program without cell cycle-arrest in trypanosomes, which may well represent an adaptation to the skin as niche for parasite persistence. The in-depth analyses described here revealed the existence of skin tissue forms of *T. brucei* and, at the same time, proved that the skin infection model developed in this thesis delivers all cues required for induction of parasite development.

4.4 Outlook and perspectives

This thesis presents the development of a novel primary human skin equivalent with improved mechanical properties and its successful implementation as an infection model to investigate the early parasitological features of tsetse-transmitted *T. brucei* parasites. The skin equivalent, which recapitulates key anatomical, cellular, and functional aspects of native human skin and expresses several ECM-associated genes, proved to be remarkably effective in studying the complex mechanisms associated with the infection of arthropod-borne trypanosomes. More than that, the skin infection model has considerable potential for advanced development. The introduction of new cell types, such as macrophages will enable infection studies with other important parasites, for

example *Leishmania*. In addition to other immune cells, adipocytes can also be integrated into the skin equivalent to include dermal white adipose tissue and to investigate its role during skin infection (Lago et al., 2018, Chen et al., 2019). Furthermore, this work demonstrated that the hdSEs could be improved with a confluent monolayer of endothelial cells on the basal side of the dermis, potentially allowing the study of transepithelial migration of pathogens in the skin.

Worldwide, arthropod-borne disease transmission represents one of the greatest threats to public and animal health. While most of these diseases are still restricted to the Global South, there is an increasing significance to study arthropod-borne diseases, especially in the wake of the climate crisis. The Asian tiger mosquito (*Aedes albopictus*), for example, is an important vector for the transmission of viral diseases, including Zika, Chikungunya, and Dengue, and is now present in several European countries. Furthermore, sand flies, which can carry parasites of the genus *Leishmania*, have been confirmed in Greece and in the Mediterranean region of Europe (Semenza and Menne, 2009, Folly et al., 2020). These pathogens depend on their vector for transmission and consequently their prevalence is limited to the distribution of their arthropod vector. Among many other factors, such as habitat destruction, land use, pesticide use, and host density, climate is an important factor. It affects the proliferation of the pathogen, the reproduction of the vector, the transmission season, and the migration of the vector. Consequently, due to climate change, the risk of vector-borne diseases originating in the tropics is increasing in Europe as well.

V. Materials and methods

5.1 Materials

5.1.1 Media, buffers, and solutions

Table 2: Media, buffers, and solutions

Medium, buffer, solution

General	Manufacturer
Accutase	Thermo Fisher Scientifc, Waltham (USA)
Agencourt AMPure XP beads	Beckman Coulter
Antibiotic-Antimycotic, 100X (Anti/Anti)	Thermo Fisher Scientifc, Waltham (USA)
Collagenase Type XI	Sigma-Aldrich (St. Louis, USA)
Dispase II, powder	Thermo Fisher Scientifc, Waltham (USA)
DMEM, 2x	Merck, Darmstadt (DE)
DMEM, high glucose, GlutaMAX	Thermo Fisher Scientifc, Waltham (USA)
$DPBS^-$ (w/o Ca^+/Mg^+)	Thermo Fisher Scientifc, Waltham (USA)
$DPBS^+$ (with Ca^+/Mg^+)	Thermo Fisher Scientifc, Waltham (USA)
Epilife	Thermo Fisher Scientifc, Waltham (USA)
ERCC RNA Spike-In Mix	Thermo Fisher Scientifc, Waltham (USA)
Hellmanex III	Hellma, Müllheim (DE)
Human Keratinocyte Growth Supplement HKGS	Thermo Fisher Scientifc, Waltham (USA)
IMDM, powder	Thermo Fisher Scientifc, Waltham (USA)
Keratinocyte Growth Factor KGF	Sigma-Aldrich (St. Louis, USA)
Liberase TL Research Grade	Roche, Basel (CH)
MEM	Thermo Fisher Scientifc, Waltham (USA)
MEM Non-Essential Amino Acids solution, 100X	Thermo Fisher Scientifc, Waltham (USA)
Nuclease-Free Water	Thermo Fisher Scientifc, Waltham (USA)
Penicillin/Streptomycin, 100X (P/S)	Thermo Fisher Scientifc, Waltham (USA)
Poly-L-Lysine Solution, 0.01 %	Merck, Darmstadt (DE)
RPMI, no methionine	Thermo Fisher Scientifc, Waltham (USA)
Trypsin 0.5 %/EDTA, 10X	Thermo Fisher Scientifc, Waltham (USA)

continued on next page

General	**Manufacturer**
VascuLife VEGF-Mv	Lifeline Cell Technology, Vancouver (CA)
Versene Solution	Thermo Fisher Scientifc, Waltham (USA)
Cell culture	**Components**
Collagenase solution	Collagenase Type XI, 500 U in 1 ml DMEM
Dispase solution	Dispase II, 2 U (= 4 mg) in 1 ml PBS^-
E1 medium	Epilife, 500 ml
	Penicillin/Streptomycin, 5 ml
	HKGS, 5 ml
E2 medium	E1 Medium, 100 ml
	300 mM $CaCl_2$ solution, 480 µl
E3 medium	E2 Medium, 100 ml
	KGF, 100 µl
	252 mM L-Ascorbic acid 2-phosphate, 100 µl
Endothelial cell freezing medium	Vasculife, 9 ml
	DMSO, 1 ml
Fibroblast medium	DMEM, 450 ml
	FCS, 50 ml
	MEM Non-Essential Amino Acids 100X, 5 ml
	Penicillin/Streptomycin, 5 ml
Fibroblast freezing medium	Fibroblast Medium, 9 ml
	DMSO, 1 ml
GNL	2x DMEM, 231.5 ml
	3 M HEPES, 7.5 ml
	Chondroitin sulfate (5 mg/ml in PBS), 2.5 ml
	FCS, 7.5 ml

continued on next page

Cell culture	**Components**
HMI9 (1x for 1 l or 1.6x for 0.625 l in ddH_2O)	IMDM powder, 17.6 g
	Sodium bicarbonate, 3 g
	Hypoxanthine, 136 mg
	Bathocuproine sulfonate, 28.2 mg
	β-mercaptoethanol, 14.3 µl
	Thymidine, 39 mg
	L-Cystine, 182 mg
	FCS, 10 %
	Penicillin/Streptomycin, 10 ml
HMI9-MC (HMI9 containing 1.1 % methylcellulose)	ddH_2O, 366 ml
	Methylcellulose, 11 g
	1.6x HMI9, 625 ml
Infection medium (INF)	1x HMI9, 50 ml
	E3 Medium, 50 ml
	Anti/Anti, 1 ml
	300 mM $CaCl_2$ solution, 73.5 µl
Keratinocyte freezing medium	E1 Medium, 9 ml
	DMSO, 1 ml
Liberase-solution	Liberase TL, 250 µg in 1 ml TDB
Trypanosoma dilution buffer (TDB), pH 7.6	Na_2HPO_4, 20 mM
	NaH_2PO_4, 2 mM
	Glucose, 20 mM
	KCl, 5 mM
	NaCl, 80 mM
	$MgSO_4$, 1 mM
Trypanosoma freezing medium, 2x	1x HMI9, 8 ml
	Glycerol, 2 ml
DNA Analyses	**Components**
Tris-acetate-EDTA (TAE) buffer, pH 8	Tris, 40 mM
	Acetic acid, 40 mM
	EDTA, 1 mM

continued on next page

***E. coli* cultivation**	Components
Agar plates	LB Medium, 100 ml
	Agar, 1.5 g
	Ampicillin, 10 mg
LB Medium (for 1 l in ddH_2O), pH 7.4	Bacto-Tryptone, 10 g
	Yeast Extract, 5 g
	NaCl, 10 g
Miscellaneous	Components
BSA-PBS	PBS, 50 ml
	BSA, 1.5 g
BSA-T-PBS	PBS, 50 ml
	Triton X-100, 250 µl
	BSA, 1.5 g
Blocking solution	PBS, 20 ml
	BSA, 1 g
Clearing solution for light sheet microscopy	Benzyl alcohol, 33 ml
	Benzyl benzoate, 66 ml

5.1.2 Chemicals and reagents

The chemicals used for this work were obtained from Carl Roth (Karlsruhe, DE), AppliChem (Darmstadt, DE), Sigma-Aldrich (St. Louis, USA) or Thermo Fisher Scientific (Waltham, USA) if not otherwise stated in the text.

5.1.3 Enzymes and enzyme buffers

All enzymes and corresponding buffers used for this work were obtained from Sigma-Aldrich (St. Louis, USA) or Thermo Fisher Scientific (Waltham, USA).

5.1.4 Instruments and devices

Table 3: Instruments and devices

Instrument/device	Manufacturer
Cell culture	
Airstream Class II BSC	Esco global, Hoyland (UK)
Aspiration device for cell culture	Hartenstein, Würzburg (DE)
Amaxa Nucleofector II	Lonza, Basel (CH)
Bottle top filter unit	Roth, Karlsruhe (DE)
CO_2 Incubators	Binder, Tuttlingen (DE)
Computer-assisted compression system	This work; Components: NTI AG LinMot Spreitenbach (CH)
Compression Bioreactor	This work; Manufactured at GT Labortechnik, Arnstein (DE)
Mr. Frosty Freezing Container	Thermo Fisher Scientific, Waltham (USA)
Multipette M4 (multistepper pipette)	Eppendorf, Hamburg (DE)
Neubauer chamber	Marienfeld, Lauda-Königshofen (DE)
Paraffinized Tissue Floating Bath: Type 1052	Medax, Kiel (DE)
Sliding Microtome RM 2255	Leica, Wetzlar (DE)
Tissue blocking station	Leica, Wetzlar (DE)
Tissue embedding center	Leica, Wetzlar (DE)
Centrifuges, shakers and stirrer	
BioVortex V1	Biosan, Riga (LV)
Centrifuge 6-16 K, rotors: 12169, 12170	SIGMA Laborzentrifugen, Osterode (DE)
Centrifuge SpectrafugeTM Mini	Labnet International Inc., Edison (USA)
Centrifuge Z 216 MK	Hermle Labortechnik GmbH, Wehingen (DE)
Centrifuge Z 383 K	Hermle Labortechnik GmbH, Wehingen (DE)
FastPrep FP120 Cell Disrupter	Thermo Fisher Scientifc, Waltham (USA)
Magnetic stirrer RSM-02HP	Phoenix Instrument, Garbsen (DE)
Shaker Celltron	Infors, Bottmingen (CH)
Shaker Ceromat R	B. Braun Biotech International, Melsungen (DE)

continued on next page

Flow cytometer, microscopes, and cameras	
BZ-9000 BIOREVO System Microscope	KEYENCE GmbH, Neu-Isenburg (GER)
Canon EOS 80D	Canon, Tokyo (JP)
Canon EFS 18-135 mm	Canon, Tokyo (JP)
DMI6000 wide-field microscope	Leica, Wetzlar (DE)
Eclipse TS100 microscope	Nikon, Tokio (JP)
FACS Calibur	BD Biosciences, Franklin Lakes (USA)
FACS Aria III	BD Biosciences, Franklin Lakes (USA)
iMIC	FEI-TILL Photonics, Gräfelfing (DE)
Intensilight C-HGFI	Nikon, Tokyo (JP)
JEOL JSM-7500F	Jeol, Tokyo (JP)
Leica DFC 365 FX	Leica, Wetzlar (DE)
Leica MZ16FA	Leica Microsystems Ltd, Heerbrugg (CH)
Light sheet fluorescence microscope, custom built	Department of Medicine II and Inter-disciplinary Center for Clinical Research, University Hospital Würzburg (DE)
Olympus CX41	Olympus Corporation, Tokyo (JP)
pco.camera, type pco.1600	PCO, Kelheim (DE)
sCMOS pco.edge	PCO, Kelheim (DE)
Wilovert, inverted	Helmut Hund GmbH, Wetzlar (DE)
Fly maintenance and work	
Breeding net	Slovak University of Technology, Bratislava (SK)
Feeding membrane	Slovak University of Technology, Bratislava (SK)
Feeding plates (210x154x20 mm and 580x210x20 mm)	Carl Roth GmbH + Co. KG, Karlsruhe (DE)
Glass petri dish	A. Hartenstein, Würzburg (DE)
Heating plate	VWR International, Nynashamn (SE)
Pupae sieve, self-made	Central workshop Biocenter, Würzburg (DE)
Roubaud cages, self-made	Central workshop Biocenter, Würzburg (DE)
Sheep blood, defibrinated, sterile	Acila, Mörfelden-Walldorf (DE)
Trays for breeding, self-made	Central workshop Biocenter, Würzburg (DE)
Tweezers, Dumont #3C	Dumont, Montignez (CH)

continued on next page

Miscellaneous	
Critical Point Dryer CPD 030	BAL-TEC AG, New York (USA)
Cool Sputter Coater SCD 005	BAL-TEC AG, New York (USA)
iBright™ CL1500 Imaging System	Thermo Fisher Scientifc, Waltham (USA)
Rheometer MCR 102	Anton Paar, Graz (AT)
Spinnerflask, 6 l	Corning Costar, Corning (USA)
T-100 Thermal cycler	Bio-Rad Laboratories, München (DE)
Tecan Infinite M200 NanoQuant	Tecan Group, Männerdorf (CH)

5.1.5 Labware and consumables

Table 4: Glass/plastic ware and consumables

Labware	**Manufacturer**
Centrifuge tubes 15, 50 ml	Sarstedt, Nümbrecht (DE)
Circular filters (Ø 50 mm)	Macherey-Nagel, Düren (DE)
Pleated filters (Ø 185 mm)	Macherey-Nagel, Düren (DE)
Combi-stopper Luer-Lock	B. Braun, Melsungen (DE)
Combitips 10 ml	Eppendorf, Hamburg (DE)
Corning Snapwell Inserts, 12 mm, 0.4 µm pore	Corning Costar, Corning (USA)
Coverslips, Menzel-Gläser	Thermo Fisher Scientific, Waltham (USA)
Cryotubes, 2 ml	Sarstedt, Nümbrecht (DE)
DRS DermaPen 0.20 mm	Edvers e.K., Berlin (DE)
Embedding cassettes	A. Hartenstein, Würzburg (DE)
FACS tubes with cell strainer cap (35 µm)	BD Biosciences, Franklin Lakes (USA)
Filter paper for embedding cassettes	Medite, Burgdorf (DE)
Glass Pasteur pipettes	Sarstedt, Nümbrecht (DE)
Lens paper	Karl Hecht GmbH, Sondheim (DE)
Microscope slides, Polysine™	Thermo Fisher Scientific, Waltham (USA)
Object slides, Menzel-Gläser	Thermo Fisher Scientific, Waltham (USA)
Pasteur pipettes, without cotton stopper	Carl Roth GmbH+Co. KG, Karlsruhe (DE)
Pipette tips 10, 20, 100, 1000 µl	Sarstedt, Nümbrecht (DE)
Plastic petri dish	Sarstedt, Nümbrecht (DE)
Reaction tubes 1.5, 2 ml	A. Hartenstein, Würzburg (DE)
Safeflow needlefree injection port	B. Braun, Melsungen (DE)

continued on next page

Labware	Manufacturer
Serological pipettes 1, 2, 5, 10, 25 ml	Sarstedt, Nümbrecht (DE)
Single-use syringes 20 ml (Luer-Lock)	A. Hartenstein, Würzburg (DE)
Stainless-steel cannulae 13G, 18G	A. Hartenstein, Würzburg (DE)
Sterile syringe filter, 0.2 µm pore	VWR International, Radnor (USA)
Surgical blades No. 19, 23	A. Hartenstein, Würzburg (DE)
Tissue culture plates 6, 12, 24-well	Sarstedt, Nümbrecht (DE)
Tissue punch, 8 mm	Kai Medical, Tokyo (JP)
Three-way valve	Medipolis Intensiv, Jena (DE)
Type F Immersion liquid	Leica Microsystems, Wetzlar (DE)
Vented cell culture flasks	Greiner Bio-One, Frickenhausen (DE)
Welted glasses with snap-on lid, 5 ml	A. Hartenstein, Würzburg (DE)

5.1.6 Antibodies and dyes

Table 5: Antibodies and dyes

Antibody/Dye	Origin	Dilution	Manufacturer
Primary antibodies			
anti-Collagen IV	Rabbit	1:250	Abcam, Cambridge (UK)
anti-Cytokeratin 5	Rabbit	1:250	Abcam, Cambridge (UK)
anti-Cytokeratin 10	Mouse	1:250	DakoCytomation, Santa Clara (USA)
anti-Cytokeratin 14	Mouse	1:250	Santa Cruz, Dallas (USA)
anti-E-Cadherin	Mouse	1:250	BD Biosciences, Franklin Lakes (USA)
anti-Filaggrin	Rabbit	1:250	Abcam, Cambridge (UK)
anti-Involucrin	Mouse	1:250	Thermo Fisher Scientific, Waltham (USA)
anti-Loricrin	Rabbit	1:250	Abcam, Cambridge (UK)
anti-Vimentin	Rabbit	1:250	Abcam, Cambridge (UK)
anti-VSG AnTat 1.1	Rat	1:4000	(Engstler and Boshart, 2004)

continued on next page

Secondary antibodies			
anti-mouse IgG Alexa 555	Donkey	1:400	Thermo Fisher Scientific, Waltham (USA)
anti-rabbit IgG Alexa 647	Donkey	1:400	Thermo Fisher Scientific, Waltham (USA)
anti-rat IgG Alexa 647	Goat	1:250	Thermo Fisher Scientific, Waltham (USA)
Dyes			
Calcein-AM		2 µM	Thermo Fisher Scientific, Waltham (USA)
Calcein-AM Violet		2 µM	Thermo Fisher Scientific, Waltham (USA)
DAPI		5 µM	Thermo Fisher Scientific, Waltham (USA)
Fluorescein Diacetate		20 µM	Thermo Fisher Scientific, Waltham (USA)
Fluoromount-G + DAPI		1 x	Thermo Fisher Scientific, Waltham (USA)
GeneRuler DNA ladder Mix		1 x	Thermo Fisher Scientific, Waltham (USA)
Hoechst 33342		5 µM	Thermo Fisher Scientific, Waltham (USA)
NuclearGreen LCS1		1.5 µM	Abcam, Cambridge (UK)
Propidium Iodide		3 µM	Thermo Fisher Scientific, Waltham (USA)
SYBR Green DNA stain		1 x	Thermo Fisher Scientific, Waltham (USA)

5.1.7 Oligonucleotides

Table 6: Synthetic DNA oligonucleotides

Name	**Sequence 5' → 3'**	**Description**
mNeonGreen-fwd-HindIII	CACAAGCTTATGGTGAGCAAGGGC	Cloning of mNeonGreen in pTSARib
mNeonGreen-rev-BamHI	CACGGATCCTTACTTGTACAGCTCGTCCATG	
Seq1 fwd	GCGGCTTGTGTTTACGC	Sequencing of pTSARib
Seq1 rev	GCATTGCAGTCTCCGCT	

5.1.8 Commercial kits

Table 7: Commercial kits

Kit	Manufacturer
Amaxa Basic Parasite Nucleofector Kit 2	Lonza, Basel (CH)
Chromium Next GEM Chip G Single Cell Kit	10x genomics, Pleasanton (USA)
Chromium Next GEM Single Cell 3′ GEM, Library & Gel Bead Kit v3.1	10x genomics, Pleasanton (USA)
Click-iT™ AHA Protein Synthesis Assay	Thermo Fisher Scientific, Waltham (USA)
High Sensitivity DNA Kit	Agilent Technologies, Santa Clara (USA)
Nextera XT DNA Library Preparation Kit	Illumina, San Diego (USA)
NextSeq 500/550 High Output Kit v2.5 (150 Cycles)	Illumina, San Diego (USA)
NovaSeq 6000 SP Reagent Kit v1.5 (100 cycles)	Illumina, San Diego (USA)
NucleoBond PC 100	Macherey-Nagel, Düren (DE)
NucleoSpin Gel and PCR clean-up Kit	Macherey-Nagel, Düren (DE)
NucleoSpin Plasmid Kit	Macherey-Nagel, Düren (DE)
Qubit dsDNA HS Assay Kit	Thermo Fisher Scientific, Waltham (USA)
RNeasy Fibrous Tissue Mini Kit	QIAGEN, Venlo (NL)
RNase-Free DNase Set	QIAGEN, Venlo (NL)
Single Index Kit T Set A	10x genomics, Pleasanton (USA)
SMART-Seq v.4 Ultra Low Input RNA Kit	Takara, Kusatsu (JP)

5.1.9 Organisms

Bacterial strains

Escherichia coli (*E. coli*) Top 10

Genotype: F-mcrA Δ(mrr-hsdRMS-mcrBC) Φ80lacZΔM15 ΔlacX74 recA1 araD139 Δ(araleu)7697galU galK rpsL(StrR) endA1 nupG

Competent bacteria were generated using the method of Chung and colleagues (Chung et al., 1989).

Primary normal human cells

Primary normal human dermal fibroblasts, keratinocytes, and microvascular endothelial cells were isolated from prepuce biopsies from juvenile donors aged between 1 and 7 years. All donors' legal representative(s) provided full informed consent in writing. The study was approved by the local ethical board of the University of Würzburg (vote 182/10 and 280/18-SC).

Trypanosome strains

Table 8: Trypanosome wildtype strains

Name	Description	Origin
Trypanosoma brucei brucei	EATRO 1125 (serodeme AnTat 1.1)	(Le Ray et al., 1977)
Trypanosoma brucei brucei	Lister 427 (serodeme MITat 1.2)	(Johnson and Cross, 1979)

Table 9: Transgenic trypanosome cell lines

Name	Parental cell line	Construct	Selection	Origin
GFP:PAD1$_{UTR}$	AnTat 1.1	p4231 PAD1:NLS (p4231: Sunter and Carrington, unpublished)	Bla	Ines Subota
mNG	AnTat 1.1	pTSARib(puro)_mNeonGreen	Puro	Christian Reuter, this work
tdT	AnTat 1.1 GFP:PAD1$_{UTR}$	pTSARib(puro)_tdTomato	Bla, Puro	Julia Weingart, Bachelor thesis 2018

Transgenic cell lines were selected with the following antibiotics.

Antibiotic	Abbreviation	Manufacturer	Final concentration
Blasticidin	Bla	Invivogen, San Diego (USA)	5 µg/ml
Puromycin	Puro	AppliChem, Darmstadt (DE)	1 µg/ml

Tsetse flies

For this work tsetse flies of the genus *Glossina morsitans morsitans* were used. Flies were originally obtained from the laboratory of Philippe Bastin and Brice Rotureau in Paris (FR), Pasteur Institute.

5.1.10 Software

Table 10: Software

Name	Manufacturer
Adobe Illustrator Creative Suite 6	Adobe Systems Incorporated, San Jose (USA)
Amira visualization and analysis software	Thermo Fisher Scientific, Waltham (USA)
Andor iQ Software	Andor Technology Ltd, Belfast (UK)
Blender	Blender Institute, Amsterdam (NL)
CellRanger	10x genomics
CellQuest Pro	BD Biosciences, Franklin Lakes (USA)
CLC Main Workbench 6	CLC bio, Venlo (NL)
Cutadapt	(Martin, 2011)
DESeq2	(Love et al., 2014)
EndNote	Clarivate Analytics, Philadelphia (USA)
FACSDiva	BD Biosciences, Franklin Lakes (USA)
featureCounts	(Liao et al., 2014)
FlowJo	https://www.flowjo.com/
Graphpad Prism 5	GraphPad Software, La Jolla (USA)
iControl	Tecan, Männedorf (CH)
ImageJ, Fiji	National Institute of Health, Bethesda (USA)
Imaris image analysis software	Bitplane AG, Zürich (CH)
Keyence BZII Analyzer	KEYENCE GmbH, NeuIsenburg (GER)

continued on next page

Name	Manufacturer
Keyence BZII Viewer	KEYENCE GmbH, NeuIsenburg (GER)
Leica Application suite AF	Leica, Wetzlar (DE)
LinMot®-Talk	NTI AG LinMot, Spreitenbach (CH)
Microsoft office	Microsoft, Redmon (USA)
pco.CamWare	PCO, Kehlheim (DE)
R	https://www.r-project.org/
Revigo	(Supek et al., 2011)
RNAStar	(Dobin et al., 2013)
SCDE	(Kharchenko et al., 2014)
Seurat (R package)	(Butler et al., 2018)
SolidWorks 3D CAD	https://www.solidworks.com/
TriTrypDB	(Aslett et al., 2010)

5.2 Methods

5.2.1 Working with *Trypanosoma brucei*

5.2.1.1 Cultivation of monomorphic trypanosomes

Monomorphic BSFs were cultured in suspension below 1 x 10^6 cells/ml in HMI9 medium at 37 °C and 5 % CO_2 (Hirumi and Hirumi, 1989). Parasite density was regularly determined using a Neubauer chamber to ensure logarithmic growth. The medium was supplemented with the appropriate antibiotics to maintain transgenic cell lines. Harvesting of parasites was performed at 1,400 g for 10 min.

5.2.1.2 Cultivation of pleomorphic trypanosomes

Pleomorphic BSFs were cultured in suspension below 5 x 10^5 cells/ml in HMI9 medium supplemented with 1.1 % methylcellulose (HMI9-MC) at 37 °C and 5 % CO_2 (Vassella et al., 2001). Parasite density was regularly determined using a Neubauer chamber to avoid *in vitro* differentiation to the stumpy stage triggered by density (McCulloch et al., 2004). The medium was supplemented with the appropriate antibiotics to maintain transgenic cell lines.

For harvesting the parasites, the methylcellulose had to be removed from the medium. Therefore, the culture was diluted 1:4 with pre-warmed TDB (37 °C) and filtered using either a sterile pleated filter for small volumes (10 ml) or a sterile bottle top filter with circular filters. The filtrate was collected in 50 ml centrifuge tubes and centrifuged at 1,400 g and 37 °C for 15 min.

5.2.1.3 Cryopreservation of trypanosomes

For long-term storage of trypanosomes, BSFs were cryopreserved. Therefore, parasites were harvested by centrifugation and resuspended in ice-cold HMI9 medium at a density of 6 x 10^6 cells/ml. Subsequently, an equal amount of ice-cold 2x trypanosome freezing medium was added and 1 ml each was transferred into cryotubes. Cryotubes were quickly transferred to -80 °C and after 24 hours to -150 °C.

To resuscitate frozen BSFs, a cryotube was quickly thawed in a water bath at 37 °C and the cells were transferred to 10 ml of ice-cold HMI9 medium and centrifuged at 1,400 g and 4 °C for 10 min. Subsequently, cells were resuspended in 1 ml of pre-warmed HMI9

medium (37 °C) and transferred to 10 ml of either HMI9 or HMI9-MC, respectively. After 1 hour, cell concentration was determined. The culture was diluted to an appropriate cell density, and required antibiotics were added.

5.2.1.4 Generating transgenic trypanosome cell lines

To generate transgenic BSFs, the Amaxa Nucleofector II (Lonza, CH) and the Amaxa Basic Parasite Nucleofector Kit 1 (Lonza, CH) were used. During the entire procedure, excessive cooling of the parasites was avoided and equipment was pre-warmed to 37 °C. For each transfection 3×10^7 parasites were harvested as described above and resuspended in 100 µl of Basic Parasite Solution 1 and mixed with 10 µg of linearized DNA. The suspension was quickly transferred into an electroporation cuvette and the program X-001 of the Amaxa Nucleofector II was used for electroporation. Subsequently, 1 ml of pre-warmed HMI9 was added and the suspension was transferred to 35 ml of pre-warmed HMI9-MC containing parental antibiotics. The suspension was carefully mixed and several dilutions were prepared (1:5, 1:15, 1:25). All dilutions were transferred to the cavities of 24-well plates, each cavity containing 1 ml.

After 6 to 12 hours, 1 ml of HMI9-MC medium was added to each well containing double the concentration of the new selection antibiotic and single the concentration of the parental antibiotic. After 4 to 5 days, the plates were screened for the presence of trypanosomes using an inverted light microscope. Parasite-containing cavities were subsequently transferred into cell culture flasks and cultured as described above (cultivation of pleomorphic trypanosomes).

5.2.1.5 Differentiation of BSF parasites to the stumpy stage

To differentiate pleomorphic BSFs to stumpy stage parasites, a BSF culture was grown to a density of 5×10^5 cells/ml and further incubated for 48 hours at 37 °C and 5 % CO_2. Subsequently, stumpy morphology was verified by eye using an inverted light microscope.

5.2.2 Working with tsetse flies

5.2.2.1 Maintenance of the tsetse fly colony

Tsetse flies were kept in an insectary at 27 °C and a relative humidity of 70 %. Additionally, a circadian rhythm was simulated with 12 hours of day and night. Flies were kept in self-made Roubaud cages at a female/male ratio of 3:1 and a maximum of 40 flies per cage. The flies were fed three times a week through a silicon membrane (Moloo, 1971) with defibrinated sterile sheep blood (Acila, DE). Therefore, a thin layer of blood was spread on a feeding plate, covered by a silicon feeding membrane, and warmed to 37 °C on a heating plate. Cages were placed on the membrane and flies were allowed to feed for at least 10 minutes.

On each workday, fly pupae were collected in a glass petri dish and categorized by size once a week. After categorization, 50 pupae each were divided into new cages for hatching. Newly-hatched flies were characterized by sex, separated, and transferred to new cages. Every Monday, Wednesday, and Friday the newly-hatched flies were either infected with trypanosomes or used for breeding.

5.2.2.2 Infection of tsetse flies with trypanosomes and maintenance of infected flies

Tsetse flies were infected with stumpy stage trypanosomes within 72 hours post-eclosion (Walshe et al., 2011). Therefore, stumpy stage parasites were generated and harvested as described above. After centrifugation, stumpy parasites were resuspended in sheep blood at a concentration of 4 - 8 x 10^6 parasites/ml, supplemented with 60 mM N-acetyl-D-glucosamine (Peacock et al., 2006) and 12.5 mM glutathione (MacLeod et al., 2007). Subsequently, the flies were infected by feeding them the infected bloodmeal through a silicon membrane. Infected tsetse flies were kept in Roubaud cages with a maximum of 50 flies per cage.

5.2.2.3 Test for salivary gland infection

A non-invasive method was used to test whether the flies had developed a salivary gland infection. For this purpose, 5 weeks after infection, individual flies were isolated and transferred into a new cage. The cage was placed over a pre-warmed (37 °C) microscope slide. Starvation of the flies for 24 to 48 hours and the increase in temperature triggered the flies to probe and salivate on the microscope slides. Subsequently, the saliva could be

examined under a light microscope for the presence of metacyclic stage parasites. Salivary-gland negative flies were euthanized with chloroform and autoclaved.

5.2.2.4 Large-scale harvest of viable metacyclic forms from live tsetse flies

For harvesting large quantities of viable metacyclic forms, previously tested salivary gland positive (SG+) tsetse flies were used. Therefore, up to 50 SG+ flies were pooled in a new and clean Roubaud cage and the net was stretched with clamps. Next, a small feeding plate (210x154x20 mm) was placed on a heating plate (37 °C), a stack of 3 microscope slides was placed at each end of the feeding plate and 25 ml of pre-warmed HMI9 medium was distributed between the stacks. Two wires (Ø 1 mm) were placed on top of the two stacks for bridging and the Roubaud cage was hung with its large side on the wires above the HMI9 medium. Triggered by the heat stimulus, the flies started to spit into the HMI9 medium, thereby releasing metacyclic forms into the medium.
After 10 min the cage, wires, and microscope slides were removed and the HMI9 medium was poured into a 50 ml centrifugation tube. After a centrifugation step at 1,400 g and 37 °C for 10 min the parasites were resuspended in fresh, pre-warmed HMI9 medium, counted with a Neubauer chamber and used for further experiments.

5.2.2.5 Dissection of tsetse flies

Tsetse flies were dissected for a more detailed examination of the infected organs. Therefore, flies were euthanized with chloroform, wings and legs were removed, and placed on a microscope slide in a drop of PBS. Dissections were performed using high precision tweezers (Dumont, CH) and a stereomicroscope (Wild Heerbrugg, CH). The complete tsetse alimentary tract and the salivary glands were dissected. The midgut, proventriculus, and glands were examined under the light microscope for the presence of trypanosomes. Dissection and analyses were performed by Sarah Schuster and Laura Hauf.

5.2.3 Working with primary human cells

5.2.3.1 Primary cells from human prepuce biopsies - isolation and expansion

5.2.3.1.1 General

All cells used in the thesis were isolated from human juvenile prepuces supplied by various hospitals and clinics after approval by the ethics committee of the University of Würzburg (vote 182/10 and 280/18-SC). For each biopsy, a declaration of consent was signed by the donors' family. The biopsy was delivered in Epilife medium supplemented with 1 % gentamycin and stored at 4 °C. A sterility control was performed by transferring 5 ml of the transport medium into a T25 cell culture flask and incubation overnight at 37 °C and 5 % CO_2. If the medium showed any signs of contamination the next day, the biopsy was discarded. If the skin showed major signs of inflammation, it was discarded as well.

All suitable biopsies were rinsed three times with PBS^+, excess fat and connective tissue was removed using a sterile scalpel, and the size of each biopsy was determined. Subsequently, the biopsy was cut into 2 - 3 mm wide strips and transferred into a petri dish containing 10 ml of dispase solution, followed by an incubation at 4 °C overnight.

5.2.3.1.2 Isolation of primary human epidermal keratinocytes (NHEKs)

The prepared biopsy strips from the previous day were transferred into a new petri dish containing 6 ml of PBS^+. The epidermis was separated from the dermal strips using sterile tweezers and both were transferred to separate petri dishes filled with 6 ml of PBS^+. The dermal strips were kept for later isolation of human dermal microvascular endothelial cells (hdmvECs) and normal human dermal fibroblasts (NHDFs) (see paragraph 5.2.3.1.3 and 5.2.3.1.4). The epidermal strips were rinsed once with PBS^- and cut into pieces of approximately 3 x 3 mm. The pieces were transferred into a 50 ml centrifuge tube, the petri dish was rinsed with 10 ml of pre-warmed (37 °C) 0.05 % Trypsin/EDTA solution, and the solution was transferred into the same 50 ml centrifuge tube. The solution was incubated in a water bath at 37 °C for 5 min with continuous shaking. After 2 min 30 sec and 5 min the tube was vortexed. The enzymatic reaction was stopped by adding 1 ml of FCS. Subsequently, keratinocytes were isolated by vigorous resuspension of the solution with a 10 ml serological pipette for 5 min. The cell suspension was filtered using a 100 µm cell strainer, followed by centrifugation at 300 g and room temperature (RT) for

5 min. The supernatant was aspirated and the pellet resuspended in 1 - 5 ml of E1 medium depending on the pellet size. Keratinocyte number and viability were determined using trypan blue and a Neubauer chamber. 1.5 - 3.5 x 10^6 cells were transferred into a T175 cell culture flask filled with 20 ml of E1 medium. Keratinocytes were passaged when reaching 70 - 90 % confluency by Accutase-treatment for 15 min at 37 °C (see paragraph 5.2.3.2). Isolated keratinocytes were expanded and cryopreserved (see paragraph 5.2.3.3) after passage 1 and 2. For the generation of high-density skin equivalents keratinocytes in passage 3 to 5 were used.

5.2.3.1.3 Isolation of primary human dermal microvascular endothelial cells

The PBS^+ of the previously prepared dermal strips was aspirated and the strips were washed once with Versene solution. Subsequently, the Versene solution was aspirated, 10 ml of pre-warmed (37 °C) 0.05 % Trypsin/EDTA solution was added, and the strips were incubated at 37 °C for 40 min. The enzymatic reaction was stopped by adding 1 ml of FCS and dermal strips were transferred into a new petri dish containing 6 ml of pre-warmed (37 °C) Vasculife medium. Each dermal strip was fixed at one end with sterile forceps and the endothelial cells were squeezed out by repeated scraping from all sides with a sterile scalpel. The dermal strips could now be used for the further isolation of human dermal fibroblasts (see paragraph 5.2.3.1.4). The cell suspension was filtered using a 100 µm cell strainer, followed by centrifugation at 300 g and RT for 5 min. The supernatant was aspirated and the pellet resuspended in 2 ml of Vasculife medium. Endothelial cell number and viability were determined using trypan blue and a Neubauer chamber. 3 x 10^5 cells were transferred into a T25 cell culture flask filled with 3 ml of Vasculife medium. Endothelial cells were passaged when reaching 70 - 90 % confluency by trypsin-treatment for 5 min at 37 °C (see paragraph 5.2.3.2). Isolated hdmvECs were expanded and cryopreserved (see paragraph 5.2.3.3) after passage 1 and 2. For the generation of endothelialized high-density primary human skin equivalents hdmvECs in passage 3 were used.

5.2.3.1.4 Isolation of primary human dermal fibroblasts

For the previously prepared dermal strips, either PBS^+ (without hdmvEC isolation) or Vasculife medium (with hdmvEC isolation) was aspirated. The dermal strips were cut or chopped into very small pieces with a sterile scalpel until they had a mush-like

consistency. Subsequently, 5 ml of pre-warmed (37 °C) collagenase solution was added and the suspension was transferred into a 50 ml centrifuge tube containing 5 ml of the same collagenase solution. The tube was incubated in a water bath at 37 °C for 45 min and vortexed every 10 min. After centrifugation at 300 g for 5 min the supernatant was aspirated and the pellet resuspended in 10 ml of pre-warmed (37 °C) fibroblast medium, followed by a second centrifugation at 300 g for 5 min. The pellet was resuspended in 2 ml fibroblast medium and the suspension was transferred to a T75 cell culture flask wetted with fibroblast medium. The next day, 6 ml of fibroblast medium was carefully added without detaching the dermal pieces. After five days of incubation the remaining dermal fragments were washed off using PBS^- and an additional 15 ml of fibroblast medium were added. Fibroblasts were passaged when reaching 80 - 90 % confluency by trypsin-treatment for 5 min at 37 °C (see paragraph 5.2.3.2). Isolated NHDFs were expanded and cryopreserved (see paragraph 5.2.3.3) after passage 1 and 2. For the generation of high-density primary human skin equivalents NHDFs in passage 3 to 5 were used.

5.2.3.2 Passaging of cells

Primary cells were passaged when reaching 70 - 90 % confluency by either Accutase-treatment (7 ml) for NHEKs or trypsin-treatment (7 ml) for NHDFs and hdmvECs. Prior to treatment with trypsin, the cells had to be washed once with PBS^-. Accutase could be applied directly to the cells. After a 5 min (0.05 % Trypsin/EDTA) or 15 min (Accutase) incubation under culture conditions, the cells were rinsed from the culture flask with 13 ml of the appropriate medium. For NHEKs E1 medium, for NHDFs fibroblast medium, and for hdmvECs Vasculife medium was used. Subsequently, the cell suspension was transferred into a 50 ml centrifuge tube and centrifuged at 300 g for 5 min at RT. The supernatant was aspirated and the pellet resuspended in 10 ml of culture medium. Cell number and viability were determined using trypan blue and a Neubauer chamber. Depending on the desired growth period, a part of the cells was transferred into new T75 or T175 cell culture flasks containing 15 or 20 ml of culture medium. All cells were cultured in a humidified incubator at 37 °C and 5 % CO_2.

5.2.3.3 Cryopreservation of primary cells

For long-term storage of primary cells, NHEKs, NHDFs, and hdmvECs were cryopreserved. Therefore, primary cells were detached when reaching 70 - 90 % confluency by either Accutase-treatment (7 ml) for NHEKs or trypsin-treatment (7 ml) for NHDFs and hdmvECs. After a 5 min (0.05 % Trypsin/EDTA) or 15 min (Accutase) incubation under culture conditions, the cells were rinsed from the culture flask with 13 ml of the appropriate medium. For NHEKs E1 medium, for NHDFs fibroblast medium, and for hdmvECs Vasculife medium was used. Subsequently, the cell suspension was transferred into a 50 ml centrifuge tube and centrifuged at 300 g and RT for 5 min. The supernatant was aspirated and the pellet resuspended in 10 ml of culture medium. Cell number and viability were determined using trypan blue and a Neubauer chamber. The suspension was centrifuged again at 300 g and RT for 5 min. Meanwhile, the required amount of cell-type-specific freezing medium was calculated and prepared (culture medium + 10 % DMSO). For NHEKs, NHDFs, and hdmvECs, 1 ml of freezing medium was used for 3, 1.5, and 1 x 10^6 cells, respectively. After centrifugation the supernatant was aspirated and the cell pellet resuspended in the calculated amount of freezing medium. Next, 1 ml of the suspension was pipetted into one labeled cryotube each, the cryotubes were transferred to the Mr. Frosty at RT, and frozen at -80 °C overnight. The next day, the tubes were transferred to liquid nitrogen for long-term storage.

To resuscitate cryopreserved cells, a cryotube was quickly thawed in a water bath at 37 °C and 1 ml of pre-warmed culture medium was added. The suspension was carefully mixed by pipetting and distributed to several cell culture flasks. For NHEKs, 500 µl were distributed to each of four T175 cell culture flasks containing 20 ml of E1 medium. For NHDFs, 1 ml was distributed to each of two T75 flasks containing 15 ml of fibroblast medium and for hdmvECs, 1 ml was distributed to each of two T175 flasks containing 20 ml of Vasculife medium.

5.2.4 Working with the high-density skin equivalent

5.2.4.1 Generation of the high-density skin equivalent

5.2.4.1.1 Collagen isolation from rat tails

The collagen used to generate skin equivalents was isolated in-house from rat tails. The animals were 8 - 10 weeks old at the time of preparation and the tails were stored at -20 °C until the tendons were isolated. The tails were thawed in PBS^- at RT and after complete thawing incubated in 70 % EtOH. One tail after the other was taken out of the EtOH bath and the skin was cut open with a scalpel about 2/3 of the length. With two hook tweezers the tails were skinned and transferred to PBS^-. Next, the tails were broken into 1 cm pieces from the tail end using tweezers and clamp scissors, and the tendons were pulled out by twisting and pulling. This process was repeated until the entire tail was processed. During one isolation approximately 100 tails were used. The isolated tendons were cleared from excess fat and blood vessels, and washed three times with sterile PBS^-. Storage of the tendons is possible at -80 °C.

The thawed tendons were then rinsed with 70 % EtOH and incubated in 70 % EtOH for another 10 min, followed by three wash steps in PBS^-. Next, tendons were cut into small pieces with a sterile scalpel and excess liquid was completely aspirated. Fibers were transferred to a bottle-top filter and dried under careful stirring with a spatula. Fibers were weighted, and per 1 g fiber 24 ml of sterile 0.1 % acetic acid was added to yield a final collagen concentration of 10 mg/ml. Since the collagen in the tendons did not dissolve completely, a smaller amount of acetic acid was used. The suspension was transferred into a sterile 6 l Spinnerflask and stirred for 17 days at 4 °C. Finally, the collagen solution was centrifuged at 14,000 g and 4 °C for 1 h. The supernatant was aliquoted in sterile 50 ml centrifuge tubes. The collagen was stored at 4 °C.

5.2.4.1.2 Generation of dermal component

The first step for the generation of the high-density skin equivalents (hdSEs) involves the production of the dermal component. For this purpose, the compression reactor, which is described in detail in chapter 2.1, was prepared first. The autoclaved reactor was completely assembled under a sterile workbench except for the compression chamber and the lid. Next, 12 Snapwell inserts were removed from their carrier, the insert membrane was perforated once with a dermapen, and the inserts were placed in the designated slots

in the reactor. Now the compression chamber was attached and fixed with the swing screws.

In the next step, the 12 compression chambers were filled with reconstituted collagen solution containing fibroblasts. Therefore, 8 ml of 10 mg/ml collagen was taken up in a 20 ml syringe using a sterile 13G cannula. During the uptake of collagen into the syringe, air bubbles were strictly avoided and the collagen was kept cold (4 °C). Next, NHDFs were detached by trypsinization and counted (see paragraph 5.2.3.2). For each dermal component a NHDF concentration of 4 x 10^5 cells/ml was used. The final volume of the compressed dermal equivalents was by standard 113 µl. Thus, 45,200 NHDFs were required per dermal component. For each dermal component 800 µl of reconstituted collagen were used. Consequently, 56,500 NHDF per ml of reconstituted collagen were required. To reconstitute the collagen, it was mixed with gel neutralization solution (GNL) in a 2:1 ratio. Consequently, 169,500 NHDF were needed per ml of GNL. Finally, to reconstitute 8 ml of collagen, 4 ml of GNL containing 678,000 NHDF were needed. Thus, after detaching the NHDFs, 678,000 viable NHDFs were resuspended in 4 ml of cold GNL and the suspension was taken up in a 20 ml syringe using a sterile 18G cannula. Next, both syringes (8 ml collagen + 4 ml GNL/NHDF suspension) were connected to a three-way valve. The valve was ventilated with the GNL suspension to eliminate any air in the system. Starting with the GNL containing syringe, both components were mixed by alternately pressing the two syringes. After 8 - 10 mixing steps, the empty syringe was disconnected and replaced by the safeflow needlefree injection port. This port was also ventilated before use with 100 µl of GNL. Next, a 10 ml Combitip connected to a multistepper pipette was inserted into the injection port and by pressing the syringe the reconstituted NHDF containing collagen solution was transferred into the Combitip. The multistepper pipette was set to 800 µl and with each step 800 µl of the reconstituted NHDF containing collagen solution were pipetted into each of the 12 compression chambers. To ensure complete gelation of the collagen hydrogel, the reactor was incubated 30 min under the sterile workbench and an additional 30 min in the cell culture incubator at 37 °C and 5 % CO_2.

In the following step the solidified collagen hydrogels were compressed to increase their collagen concentration and mechanical properties. For this purpose, the computer-assisted compression system, which is described in detail in chapter 2.1, was assembled. For this, the linear motor was disinfected with a 70 % EtOH-moistened tissue and placed under the sterile workbench. Next, the linear motor was connected to the servo drive and

computer via the motor cable. The software LinMot®-Talk was used to control the motor. The motor was moved to the home position and the lid of the compression reactor was attached to the linear motor via the adapter. Next, the 12 compression punches of the lid were inserted into the 12 compression chambers of the reactor, whereby the motor was moved slowly to 50 mm at 0.001 m/s. Up to this point the hydrogels have not yet been touched by the compression punches and the actual compression process is only now beginning. For this, the motor was driven to 58.5 mm with 2 x 10^{-6} m/s. The compression process took approximately 50 min.

When compression was complete, the 12 dermal equivalents had to be released from the compression reactor for culture. Therefore, the lid was fixed to the compression chamber with four knurled screws and the two swing screws on each side were loosened. Now, the linear motor was moved up to 30 mm with 0.001 m/s, lifting the lid together with the compression chamber. In order to release the 12 dermal equivalents from the compression punches without damage, compressed air (3 - 6 bar) was now introduced via the adapter into the lid and the punches, whereby the dermal equivalents were released residue-free from the punches. The Snapwell inserts containing the dermal equivalents were attached to their carriers using sterile tweezers and placed in the provided 6-well plates. 5 ml of pre-warmed fibroblast medium were added to the lower compartment and 250 µl to the upper compartment. The dermal equivalents were cultured for 48 hours at 37 °C and 5 % CO_2 prior to adding the keratinocytes.

5.2.4.1.3 Generation of epidermal component and culture

In order to generate the epidermal component of the high-density skin equivalent (hdSE), NHEKs were detached by Accutase-treatment and counted (see paragraph 5.2.3.2). Per skin equivalent, 5 x 10^5 NHEKs were required, which corresponds to 3 x 10^6 NHEKs for 12 equivalents. Meanwhile, the entire fibroblast medium of the dermal equivalents was carefully aspirated. The prepared NHEKs were resuspended in 3 ml of pre-warmed E2 medium to obtain a concentration of 2 x 10^6 cells/ml. Next, 250 µl of the E2 cell suspension were added on top of each dermal equivalent and 5 ml of E2 medium was added to the lower compartment. The skin equivalents were incubated at culture conditions overnight.

The next day, the entire E2 medium of each skin equivalent was carefully aspirated. During aspiration, it was important to ensure that the surface with the NHEKs was not

touched, but to aspirate all the liquid in order to obtain a dry surface. The lower compartments were each filled with 1,750 µl of pre-warmed E3 medium and the hdSEs were cultured at culture conditions for up to 19 days. This culture method, by which only the dermal part of the hdSE is in contact with the culture medium and the epidermal part is exposed to air, is called air-liquid interface (ALI). Every 2 - 3 days the medium in the lower compartments was replaced with fresh, pre-warmed E3 medium.

5.2.4.1.4 Endothelialization of the high-density skin equivalent

The first step for the generation of endothelialized high-density skin equivalents (endo-hdSEs) includes the production of the dermal component and the culture of hdmvECs on its basal side. For this purpose, the compression reactor was prepared as described above (see paragraph 5.2.4.1.2). But instead of perforating the insert membrane with a dermapen, the center of the membrane was completely removed with an 8 mm tissue punch, leaving a continuous edge about 2 mm wide. In addition, a sterile Whatman paper was placed between the perforated plate and the inserts before the compression chamber was attached and fixed with the swing screws. The dermal components were now produced as already described in paragraph 5.2.4.1.2. Subsequently, the dermal equivalents were cultured overnight with fibroblast medium at 37 °C and 5 % CO_2 prior to adding the hdmvECs.

The next day, the fibroblast medium was exchanged with Vasculife medium and the dermal equivalents were equilibrated for 4 h at 37 °C. Meanwhile, hdmvECs were harvested by trypsinization and resuspended in pre-warmed Vasculife at 6 x 10^6 cells/ml. Next, the entire Vasculife medium of each dermal equivalent was carefully aspirated and with sterile tweezers the inserts were transferred upside down into sterile Petri dishes (Ø = 120 mm). Subsequently, 75 µl of the hdmvEC suspension (= 4.5 x 10^5 cells) were added to the basal side of each dermal equivalent and incubated for 2 h at 37 °C. After the incubation step, the inserts were returned to their original position in the 6-well plate using sterile forceps. 5 ml of pre-warmed Vasculife medium were added to the lower compartment and 250 µl to the upper compartment. The endothelialized dermal equivalents were cultured for 7 days at 37 °C and 5 % CO_2 prior to adding the keratinocytes. The medium was exchanged every 2 - 3 days.

In the following week, the epidermal component was generated as previously described in paragraph 5.2.4.1.3. But with the exception, that the E2 medium in the lower

compartment was supplemented with 10 % FCS. For air-liquid interface (ALI) culture, the first medium exchange was carried out with E3 medium supplemented with 5 % FCS and the second exchange with E3 medium supplemented with 2 % FCS. All subsequent media changes were performed with E3 medium without supplemented FCS. Endo-hdSEs were cultured for another 14 days and the medium was exchanged every 2 - 3 days.

5.2.4.2 Assessment of fibroblast viability and proliferation, as well as dermal contraction and weight loss

In general, collagen-based skin equivalents exhibit massive contraction and weight loss due to poor mechanical stability of the dermal component and collagen-remodeling matrix-metalloproteinases (MMPs) secreted by dermal fibroblasts. To counteract dermal contraction and weight loss, the mechanical properties were increased by 7-fold compression of the dermal equivalents.

Fibroblast viability after compression was determined by fluorescein diacetate (FDA) or Calcein-AM and propidium iodide (PI) staining. Therefore, high-density and non-compressed dermal equivalents were placed into petri dishes (Ø = 35 mm) and stained with 3 ml PBS^- containing either 20 µM FDA or 2 µM Calcein-AM, and 3 µM PI. Equivalents were incubated for 5 min at 37 °C and subsequently, washed three times with PBS^-. Images were acquired using the fluorescence stereomicroscope Leica MZ16 FA.

For assessing fibroblast proliferation in high-density and non-compressed dermal equivalents, equivalents were dissociated and NHDFs were counted using a Neubauer chamber. For dissociation, dermal equivalents were each placed in one cavity of a 6-well plate and cut into small pieces with a sterile scalpel (No. 19). 1 ml of liberase-solution was now added to each cavity and the suspension was transferred to a 1.5 ml reaction tube using a cut-off 1,000 µl pipette tip. The tubes were incubated in a water bath at 37 °C for 30 - 45 min. After complete dissociation, the tubes were centrifuged at 2,000 g for 2 min 30 sec. The supernatant was aspirated, the pellet resuspended in 1 ml of PBS^-, and NHDFs were counted.

To determine dermal contraction and weight loss, the dermal area and weight were measured regularly. For this, high-density and non-compressed dermal equivalents were cultured in petri dishes (Ø = 35 mm) containing 3 ml of fibroblast medium. For up to 3 weeks, each dermal component was photographed once a week using graph paper and the weight was determined with an analytical balance after the medium was completely

aspirated. After the measurements, fresh medium was added, and the dermal equivalents were further cultured.

5.2.4.3 Histological and immunofluorescence staining and imaging

For histological staining, skin equivalents were fixed with 4 % PFA at 4 °C overnight, processed for paraffin embedding using the Leica embedding center and blocking station, and 5 µm thick sections were prepared using a sliding microtome. After deparaffinization and rehydration, sections were stained with hematoxylin and eosin (H&E; adapted from (Fischer et al., 2008)). After the staining process, light microscopy images were obtained with a BZ-9000 BIOREVO System Microscope. The steps involved for paraffin embedding and H&E staining are described below (Table 11 and 12).

Table 11: Protocol for paraffin embedding

Time	Reagent	Description
2 h	ddH_2O	
1 h	50 % EtOH	
1 h	70 % EtOH	Ascending alcohol sequence
1 h	80 % EtOH	for dehydration of the tissue
1 h	96 % EtOH	
1 h	Isopropanol I	
1 h	Isopropanol II	
1 h	Isopropanol/Xylene (1:1)	
1 h	Xylene I	Alcohol removal
1 h	Xylene II	
1.5 h	Paraffin I	Paraffin embedding
1.5 h	Paraffin II	

For immunofluorescence staining, skin equivalents were processed as described above until the deparaffinization and rehydration of the tissue sections was completed. Subsequently, antigens were retrieved by incubation of the tissue sections in 10 mM sodium citrate, pH = 6, at 90 °C for 20 min. Sections were then permeabilized in PBS^- containing 0.3 % Triton X-100 for 5 min and subsequently blocked with 3 % BSA in PBS^- for 20 min at RT to avoid unspecific binding. Next, sections were incubated overnight at 4 °C in a humidity chamber with the appropriate primary antibody, followed

by washing three times for 5 min with PBS^- containing 0.5 % Tween-20. Tissue sections were incubated with the appropriate secondary antibody for 1 h at RT in the dark. After three washing steps with PBS^- containing 0.5 % Tween-20 for 5 min each at RT, sections were mounted in Fluoromount-G + DAPI and imaged with a BZ-9000 BIOREVO System Microscope.

Table 12: Protocol for H&E staining

Time	Reagent	Description
10 min	Xylene I	
10 min	Xylene II	
3x in and out immersion	96 % EtOH	Descending alcohol sequence for
3x in and out immersion	96 % EtOH	deparaffinization and rehydration of the tissue
3x in and out immersion	70 % EtOH	sections
3x in and out immersion	50 % EtOH	
	ddH_2O	Removal of residual alcohol
6 min	Hematoxylin	Acidic according to Mayer. Staining of nuclei
	ddH_2O	Removal of residual Hematoxylin
5 min	Tap water	Blueing of Hematoxylin
6 min	Eosin	Staining of cytosolic components
	ddH_2O	Removal of residual Eosin
3x in and out immersion	70 % EtOH	
2 min	96 % EtOH	
5 min	Isopropanol I	Ascending alcohol sequence for dehydration
5 min	Isopropanol II	of the tissue sections
5 min	Xylene I	
5 min	Xylene II	
	Entellan	Air tight sealing of the tissue sections between the microscope slide and coverslip

5.2.4.4 Assessment of epidermal thickness

Skin equivalents were fixed and H&E stained according to the beforementioned protocol (see paragraph 5.2.4.3). Images were taken with a BZ-9000 BIOREVO System Microscope and analyzed with ImageJ. For each sample, between 3 and 13 images were taken and the thinnest and thickest area of the cellular epidermis was measured in each image.

5.2.4.5 Establishment of natural trypanosome infections in skin equivalents using tsetse flies and culture of infected skin equivalents

Infection with trypanosomes starts when metacyclic stage parasites are injected into the mammalian skin by a tsetse fly. In order to simulate the natural infection process, tsetse flies with a mature salivary gland infection (SG+) were employed to transmit the parasites into the hdSE. The advantage of this is a natural deposition of the parasites in the skin and the inclusion of factors from fly saliva.

For each infection three hdSEs aged between 16 and 23 days were used, depending on further experiments and the duration of culture of the infected skin equivalents. Prior to infection on day 15 of skin equivalent culture, the E3 medium was exchanged with infection medium (INF). Furthermore, the skin equivalents were removed from the Snapwell inserts with sterile tweezers and a scalpel (No. 23) prior to infection and placed in one cavity of a 6-well plate. Each cavity was filled with pre-warmed 1.5 ml INF medium. Next, the 6-well plate with the three hdSEs was put on a pre-warmed (37 °C) heating plate in the fly room. To infect the skin equivalents, the three hdSEs were stacked on top of each other on an aseptic microscope slide placed on the heating plate using sterile tweezers. Subsequently 6 SG+ tsetse flies were allowed to bite into the stack. In order to have sufficient quantities and equal numbers of parasites for downstream analysis per skin equivalent, the positions of the stacked hdSEs were changed after 6 fly bites and another round of 6 SG+ flies were allowed to bite into the stack. This was repeated three times, so that each of the three hdSEs was once on each position (bottom, middle, top). A total of 18 SG+ flies were used for the infection of three hdSEs.

Trypanosome-infected hdSEs were cultured with INF medium at the air-liquid interface. For this, a hexagonal-shaped sterile Whatman paper was placed in a petri dish (Ø = 60 mm) on a sterile, custom-made U-shaped metal spacer (h = 3 mm). Three infected hdSEs were placed on the Whatman paper. Subsequently, the petri dish was filled with 7 ml of INF medium and the hdSEs were cultured under culture conditions at 37 °C and 5 % CO_2. Every 2 - 3 days the medium was exchanged with fresh INF medium.

5.2.4.6 Live cell imaging of trypanosome-infected skin equivalents

For live cell imaging, the skin equivalents were infected with fluorescent trypanosomes expressing tdTomato in the cytosol by tsetse flies as described above (see paragraph 5.2.4.5). In order to image trypanosomes, the hdSE in the petri dish was turned upside

down with sterile tweezers to avoid imaging through the epidermal layer. Turning the hdSE upside down allowed direct microscopy of trypanosomes in the dermis with the fluorescence stereomicroscope Leica MZ16 FA. Images and videos were acquired depending on the experiment performed. In addition, microscopy was used to verify infection and viability of trypanosomes of each hdSE before each experiment. The hdSEs were flipped back over, the medium was renewed, and the hdSEs were further cultured at the air-liquid interface.

5.2.4.7 Scanning electron microscopy of non-infected and trypanosome-infected skin equivalents

Dermal equivalents or infected hdSEs were fixed in Karnovsky solution (2 % PFA, 2.5 % glutaraldehyde in 0.1 M cacodylate buffer, pH = 7.4) overnight at 4 °C. Specimens were washed three times for 5 min at 4 °C with 0.1 M cacodylate buffer, followed by incubation for 1 hour at 4 °C in post-fixation solution (2.5 % glutaraldehyde in 0.1 M cacodylate buffer, pH = 7.4). Samples were washed, incubated in cacodylate buffer containing 2 % tannic acid and 4.2 % sucrose for 1 hour at 4 °C, and washed three times with water for 5 min at 4 °C. Subsequently, specimens were dehydrated in an ascending acetone sequence, critical point dried, and coated with gold-palladium. Images were acquired with a JEOL JSM-7500F scanning electron microscope using the detector LEI for secondary electrons at 5 kV.

5.2.4.8 Lightsheet fluorescence microscopy

Skin equivalents were infected and cultured as described above (see paragraph 5.2.4.5) and fixed with 4 % PFA at 4 °C overnight. The next day, skin equivalents were transferred into welted glasses, washed in PBS^- for 30 min at RT, and processed for optical clearing of the tissues. The clearing protocol is described below (Table 13).

Cleared skin equivalents were imaged using a non-commercial custom-built scanning lightsheet fluorescence microscope from the Department of Medicine II and Interdisciplinary Center for Clinical Research, University Hospital Würzburg (Brede et al., 2012, Stegner et al., 2017). For imaging, the cleared skin equivalents were fixed on a removable sample holder and positioned in a glass chamber filled with clearing solution. The microscope was operated with the Andor iQ software in consultation with an authorized technician of the Department of Medicine II, Würzburg. Three-dimensional

stacks were generated with 2 or 0.5 µm step size and analyzed in detail using ImageJ/Fiji and Amira for 3D visualization.

Table 13: Tissue clearing protocol for lightsheet microscopy

Time	Reagent	Description
overnight	4 % PFA	Fixation of tissue
30 min	PBS^-	
1 h	30 % EtOH	
1 h	50 % EtOH	
1 h	70 % EtOH	Ascending alcohol sequence for dehydration of the tissue
1 h	80 % EtOH	
1 h	90 % EtOH	
1 h	100 % EtOH	
overnight	100 % EtOH	
2 h	100 % n-hexane	After contact with n-hexane, strictly avoid exposing the tissue to air
2 h	100 % n-hexane	
3 x 30 min	Clearing solution	Mixture consisting of 1 part Benzylalkohol and 2 parts Benzylbenzoat
overnight	Clearing solution	The tissue is now completely transparent and can be stored in the clearing solution at RT for a few weeks.

5.2.4.9 Fluorescence activated cell sorting (FACS)

Skin-residing trypanosomes were analyzed and sorted with a FACSAria III cell sorter (nozzle: 100 µm). For this, hdSEs were infected with tdTomato (tdT) expressing trypanosomes and cultured as described above (see paragraph 5.2.4.5). Infected hdSEs were dissociated with liberase-solution to obtain a single cell suspension (see paragraph 5.2.4.2). After complete dissociation, the suspension was centrifuged at 2,000 g for 2 min 30 sec at RT and further processed depending on the experiment. The different experiments are described below.

5.2.4.9.1 Cell cycle and viability analysis of skin-residing parasites

Following the last centrifugation step the cell pellet was resuspended in 500 µl TDB and transferred into FACS tubes with 35 µm cell strainer caps. 20 min and 5 min before analysis, 2 µM Calcein-AM Violet and 2 µM NuclearGreen were added, respectively, and mixed briefly by rotary shaking. Parasites were analyzed by gating first on the tdT signal to exclude NHDFs, extracellular matrix proteins, and dirt from the analysis. Next, viable parasites were selected by setting a gate on the calcein signal and finally, cell cycle distribution was analyzed.

5.2.4.9.2 Analysis of AnTat 1.1 expression

After the last centrifugation step the cell pellet was resuspended in 500 µl TDB containing 2 µM Calcein-AM Violet and 2 µM NuclearGreen. The suspension was incubated 5 min at RT and 5 min on ice. Meanwhile, the primary antibody anti-VSG AnTat 1.1 was diluted in cold HMI9 (1:4,000). After centrifugation at 2,000 g and 4 °C for 2 min 30 sec the supernatant was aspirated and 100 µl of the diluted primary antibody was added to each sample and carefully mixed. The samples were incubated in the cold room for 1 hour on ice. In the meantime, the appropriate secondary antibody anti-rat AF647 was diluted in cold HMI9 (1:250). After one wash step with 1 ml cold HMI9, the pellet was resuspended in 100 µl of the diluted secondary antibody and incubated 10 min on ice. Subsequently, the cells were washed two times with 1 ml cold TDB, resuspended in 500 µl cold TDB and transferred in pre-cooled FACS tubes with 35 µm cell strainer caps on ice. Parasites were analyzed by gating first on the tdT signal to exclude NHDFs, extracellular matrix proteins, and dirt from the analysis. Next, viable parasites were selected by setting a gate on the calcein signal and finally, cell cycle distribution and VSG expression was analyzed.

5.2.4.9.3 Analysis of injection depth and distribution of tsetse-transmitted trypanosomes

Cell-free high-density dermal equivalents (hdDEs) were used for this experiment since no further culture of the equivalents was carried out. Three hdDEs were stacked on top of each other and 18 SG+ tsetse flies were allowed to bite into the stack as described in paragraph 5.2.4.5 with the exception that the hdDEs were not rotated. Immediately after infection, hdDEs were dissociated (see paragraph 5.2.4.2) and the suspension transferred

into FACS tubes. Trypanosomes were detected by their tdT signal and counted. Per experiment, the percentage of trypanosomes in the three differently positioned hdDEs (top, middle, bottom) was calculated. Since each hdDE had a standardized height of 1 mm, a depth of up to 3 mm could be simulated with a resolution of 1 mm.

5.2.4.9.4 Single parasite sorting for single-cell RNA sequencing

For single-cell RNA sequencing (scRNAseq) of skin-residing trypanosomes five different timepoints post-infection were chosen. After natural infection, the hdSEs were cultured for another 4 h, 12 h, 24 h and 7 d, respectively. In addition, freshly collected MCFs obtained from tsetse flies were used as a control. All experiments were performed in triplicates. Subsequently, hdSEs were dissociated (see paragraph 5.2.4.2) and the suspension transferred into FACS tubes. Single viable parasites were sorted based on their tdT and Calcein-AM signal into 0.2 ml PCR strips containing 2.6 µl of 1x lysis buffer (Takara) supplemented with 0.01 µl of RNase inhibitor (40 U/µl; Takara). Immediately after sorting, cells were placed on ice for 5 min and stored at -80 °C.

5.2.4.10 Assessment of protein synthesis rate of skin-residing parasites

The first step in analyzing the protein synthesis rate of skin-residing parasites was the incorporation of the methionine-analogue L-Azidohomoalanine (AHA) into newly synthesized proteins. For this, hdSEs were infected with tdT-expressing trypanosomes using tsetse flies and cultured for different time periods (see paragraph 5.2.4.5). After each time period, hdSEs were dissociated (see paragraph 5.2.4.2) and the cell pellet was resuspended in 500 µl of pre-warmed methionine-free RPMI containing 10 % FCS, Anti/Anti, P/S, and either 50 µM AHA or 50 µM L-methionine as negative control. As a further quality control, BSFs from cell culture flasks were included in each experiment. All samples were incubated in the cell culture incubator for 1 hour at 37 °C.

In the next step, the parasites had to be sorted based on their tdT signal with the FACSAria III cell sorter to exclude NHDFs, extracellular matrix proteins, and dirt from the analysis. For this, after the incubation step, samples were centrifuged at 2,000 g and RT for 2 min 30 sec and the cell pellets were resuspended in 500 µl TDB supplemented with 2 µM Calcein-AM Violet. Subsequently, 1 - 5 x 10^4 viable parasites were sorted based on their tdT and calcein signal in 24-well plates containing a coverslip pre-coated with poly-L-lysine (Ø 15 mm) and filled with 500 µl 3 % PFA (125 µl TDB + 375 µl

4 % PFA). Parasites were incubated at least 15 min at RT and subsequently, 24-well plates were centrifuged at 1,500 g and RT for 5 min to attach parasites to the coverslips. After a washing step with 500 µl BSA-PBS, the plates could be stored overnight at 4 °C. The next day, the incorporated AHA was labeled with AlexaFluor 488. This is possible by chemoselective ligation between the azide moiety of the AHA and the AlexaFluor 488 alkyne. For this, the BSA-PBS was aspirated and 500 µl of BSA-T-PBS was added to each cavity and incubated for 20 min at RT. After two wash steps with 500 µl BSA-PBS, 300 µl Click-iT reaction cocktail was added to each coverslip and incubated for 30 min at RT protected from light. Following a further washing step with 500 µl BSA-PBS, the coverslips were carefully taken out of the cavities of the 24-well plate with a slightly bent cannula and tweezers, and mounted upside down on a microscope slide with 7.5 µl Fluoromount-G with DAPI. L-Azidohomoalanine and the Click-iT reaction cocktail were included in the commercial kit Click-iT™ AHA Protein Synthesis Assay.
At least 136 trypanosomes from three individual experiments were imaged per timepoint with a DMI6000B wide-field fluorescence microscope (Leica), equipped with a 100x oil objective (NA 1.4) and a DFC365FX camera (pixel size 6.45 µm). Images were taken by focusing in the DAPI channel on the cell nucleus and kinetoplast. Subsequently, images were taken in brightfield, DAPI, and AHA channels. Images were then analyzed with the ImageJ/Fiji software. To quantify the fluorescence intensity of incorporated AHA or L-methionine, a rectangular region of interest (ROI) was drawn around individual parasites. The area, mean fluorescent intensity, and integrated density of the ROI was measured in the AHA channel along with several adjacent background measurements using the built-in measurement program (Analyze > Measure). The corrected total cell fluorescence (CTCF) of individual cells incubated with either AHA or L-methionine was calculated using the following formula: CTCF = integrated density – (area of selected cell x mean fluorescence of background). In addition, to correct for cell autofluorescence, the CTCF values of parasites incubated with L-methionine (negative control) was subtracted from all CTCF values of parasites incubated with AHA.

5.2.4.10.1 Coating coverslips with poly-L-lysine

Coverslips (Ø 15 mm) were cleaned with 2 % Hellmanex in a sonication bath for 2x 10 min. After each sonication step, coverslips were extensively rinsed with ddH_2O. After a third sonication step with ddH_2O for 10 min, coverslips were extensively rinsed

with ddH_2O, and dried under a sterile workbench for approximately 30 min. Subsequently, one coverslip was placed in each cavity of a 24-well plate using sterile tweezers. Next, 333 µl of 0.01 % poly-L-lysine solution was added to each coverslip and incubated at RT overnight. The next day, each coverslip was washed once with 500 µl PBS^- for 1 hour with shaking. Finally, coverslips were dried in a sterile workbench and stored dry for a maximum of 2 weeks.

5.2.4.11 Assessment of parasite burden in infected skin equivalents

To determine the number of parasites in each skin equivalent at different timepoints post-infection, hdSEs were infected with trypanosomes using tsetse flies and cultured for different time periods (see paragraph 5.2.4.5). After each time period, hdSEs were dissociated (see paragraph 5.2.4.2) and the cell pellet was resuspended in 1 ml TDB. The number of parasites per hdSE was counted with a Neubauer chamber and the parasite concentration per ml was calculated with the following formula: number of parasites per hdSE (= 113 µl) x 8.85 = parasites/ml

5.2.4.12 Rheology of skin equivalents

To investigate the mechanical properties of high-density in comparison to non-compressed skin equivalents, oscillatory and rotational rheological analyses were performed using a plate-to-plate setup. For this purpose, high-density dermal equivalents were prepared as described above (see paragraph 5.2.4.1). Non-compressed dermal equivalents were prepared equally, with the exception that 800 µl of reconstituted collagen solution were filled in the cavities of a 24-well plate and without the compression step. Both dermal equivalents were incubated overnight in PBS^- at 37 °C.

Next, pieces with a diameter of 8 mm were punched out of each dermal equivalent using an 8 mm tissue punch. Measurements were performed at 37 °C with an 8 mm measuring plate and a gap size of 1 mm using an Anton Paar MCR 102 rheometer. 30 measurement points with a strain from 0.01 - 100 % at 1 Hz were recorded for the amplitude sweep. Rheological measurements were performed by Philipp Fey (Fraunhofer EZRT, Würzburg, Germany).

5.2.4.13 Tracking of single parasites in skin equivalents

In order to track single parasites in skin equivalents, hdSEs were infected with tdT-expressing trypanosomes using tsetse flies and cultured for different time periods (see paragraph 5.2.4.5). At various timepoints post-infection, videos of trypanosomes moving in the hdSEs were recorded at the fluorescence stereomicroscope Leica MZ16 FA. Therefore, the tdT signal of the trypanosomes was recorded with 35x/5x optical magnification and a rate of 4 frames per second (fps) over a period of 5 min 20 sec (2,150 images).

Subsequently, the videos were analyzed with the software Imaris. For tracking, the 5x35_skin gel algorithm was established. The algorithm is based on an autoregressive motion that models the continuous motion of each parasite as an autoregressive AR1 process. It calculates the position of a point at a given time depending on its movement (including distance and direction) from the previous timepoint. The maximum distance defines how much an object may deviate from the previous position. For the 5x35_skin gel algorithm this distance was set to 20 µm. At a maximum swimming speed of 40 µm/s in the blood, the parasites would move a maximum of 10 µm within one frame (= 250 ms). Thus, objects with a distance of more than 20 µm from the previous position are most likely not trypanosomes of the same track.

Furthermore, only objects with a diameter larger than 6 µm were analyzed, since smaller objects most likely do not represent trypanosomes. In addition, the maximum gap size was set to 20 frames in order to automatically connect track fragments with a gap smaller than or equal to 20 frames even if the observed object could not be tracked continuously (most likely because the object was temporarily out of focus due to the three-dimensional tissue). Moreover, tracks with a length of less than 60 sec were excluded from the analysis. All tracks were validated manually and, if necessary, incorrect tracks or incorrectly assigned objects were corrected. The recording of the videos and their analysis was conducted by the previous master student Laura Hauf under the supervision of Dr. Timothy Krüger and myself.

5.2.4.14 Single-cell RNA sequencing of skin equivalent

The dermis of two individual hdSEs at day 23 was separated from the epidermis with forceps and subsequently cut into small pieces and incubated in 1 ml of TDB containing 250 µg liberase TL for 45 min at 37 °C. To isolate NHEK the epidermis was incubated in 3 ml of PBS^- with gentle agitation. PBS^- was aspirated, the epidermis cut into small pieces and 1 ml of 0.05 % Trypsin/EDTA were added for 15 min at 37 °C. 100 µl of FCS were added and NHEK were released by thorough resuspension. Cells were collected by centrifugation at 300 g and RT for 5 min, resuspended in 500 µl INF medium containing 0.5 µg DAPI and filtered through a 35 µm cell strainer. Viable NHDF and NHEK were sorted based on their negative DAPI signal with a FACSAria III cytometer (BD Biosciences) and collected in a single tube. Cell density was evaluated by microscopy using a hemocytometer and adjusted to 1,000 cells/µl.

Subsequently, the Chromium Next GEM Single Cell 3′ Reagent Kits v3.1 (10x Genomics) were used for reverse transcription, cDNA amplification, and library construction according to the manufacturers' instructions. 16.5 µl of cell suspension were used to recover 10,000 cells and libraries were quantified with a Qubit 3 Fluorometer (Thermo Fisher Scientific). Quality was checked using a 2100 Bioanalyzer with High Sensitivity DNA kit (Agilent). Sequencing was performed in paired-end mode with a SP flow cell (2 x 50 cycles) using NovaSeq 6000 sequencer (Illumina).

5.2.4.15 Analysis of single-cell RNA sequencing data of skin equivalents

CellRanger v3.1.0 (10x Genomics) was used to process scRNAseq data. To generate a digital gene expression (DGE) matrix, reads were mapped to the human reference genome GRCh38 and the number of UMIs for each gene in each cell was recorded.

Seurat R package (version 3.1.4) (Butler et al., 2018) was used for further analysis of scRNAseq data. Only cells with > 2,500 genes, between 10^4 and 10^5 UMIs, and between 1 % and 15 % mitochondrial (mt) genes were considered for downstream analyses. The "NormalizeData" function was used to normalize sequencing reads of each gene to total UMIs in each cell. The "ScaleData" function was used to scale and center expression levels in the data set for dimensional reduction. The top 2,000 features that exhibit high cell-to-cell variation in the dataset were selected with the function "FindVariableFeatures" and used for dimensionality reduction. Total cell clustering was performed by "FindNeighbors" function using the first 20 dimensions and "FindClusters"

function at a resolution of 0.4. Dimensionality reduction was performed with "RunTSNE" function and visualized by t-Distributed Stochastic Neighbor Embedding (t-SNE). Marker genes for each cluster were determined with the Wilcoxon rank-sum test by "FindAllMarkers" function. Only those with |'avg_logFC'| > 0.25 and 'p_val_adj' < 0.05 were considered as marker genes.

5.2.4.16 Single-cell RNA sequencing of *T. brucei*

After natural infection, skin equivalents were cultured for another 4 h, 12 h, 24 h, and 7 d, respectively. In addition, freshly collected MCFs obtained from tsetse flies were used. Skin equivalents were dissociated and single viable parasites were sorted based on their tdTomato and Calcein-AM signal with a FACSAria III cytometer (BD Biosciences) into 48 well plates containing 2.6 µl of 1x lysis buffer (Takara) supplemented with 0.01 µl of RNase inhibitor (40 U/µl; Takara). Immediately after sorting, cells were placed on ice for 5 min and stored at -80 °C.

Library preparation and sequencing was carried out as described previously (Muller et al., 2018). Briefly, 0.2 µl of a 1:20,000,000 dilution of ERCC Spike-in Control Mix 1 (Thermo Fisher Scientific) were added to the lysates of single parasites and libraries were prepared using SMART-Seq v.4 Ultra Low Input RNA Kit (Takara) using a quarter of the reagent volumes recommended by the manufacturer. 27 cycles were used for PCR amplification and cDNA was purified using Agencourt AMPure XP beads (Beckman Coulter) using 15 µl of elution buffer (Takara). Library quantification was performed with a Qubit 3 Fluorometer with dsDNA Hs Assay kit (Life Technologies) and the quality of the libraries was assessed using a 2100 Bioanalyzer with High Sensitivity DNA kit (Agilent). 0.5 ng of cDNA was subjected to a tagmentation-based protocol (Nextera XT, Illumina) using a quarter of the recommended volumes, 10 min for tagmentation at 55 °C and 1 min extension time during PCR amplification. Libraries were pooled and sequencing was performed in paired-end mode for 2 x 75 cycles using Illumina's NextSeq 500.

5.2.4.17 Analysis of single-cell RNA sequencing data of *T. brucei*

After demultiplexing, data quality was examined using FastQC (version 0.11.7). Illumina adaptors were removed using cutadapt (version 3.2 (Martin, 2011)). Trimmed reads were mapped to the TREU 927 (version 48) genome with the ERCC spike-in sequences

included, using RNAStar (version 2.6.1b (Dobin et al., 2013)). Read counts for each gene were determined using featureCounts (version 2.0.1 (Liao et al., 2014)) and genes with ≥ 5 aligned reads were considered detected. Only those scRNAseq datasets with > 200 and < 1,000 detected genes and a library size between 2 x 10^5 and 2 x 10^6 reads were considered for analysis. Principal component analysis (PCA) was performed selecting the 1,000 genes with the highest variance. The following libraries were excluded from the analysis due to BARP gene expression: "0h_1_B5_1", "0h_1_G2", "0h_1_C5_1". Differential gene expression analysis was conducted with DESeq2 (version 1.30.0 (Love et al., 2014)) and SCDE (version 2.18.0; only used in early vs. late analysis (Kharchenko et al., 2014)). Features with an absolute log2 fold change > 2 and adjusted P value < 0.01 (DEseq2) or a z score > 1.96 (SCDE) were considered as differentially expressed, respectively.

5.2.4.18 Gene Ontology (GO) Analysis

GO term enrichment within the differential expressed genes between the five data sets (MCF, 4 h, 12 h, 24 h, and 7 d) were determined by Fisher's exact test using the GO enrichment tool on the TriTrypDB webserver (https://tritrypdb.org/tritrypdb/app) (Aslett et al., 2010) and summarized using the REVIGO webtool (Supek et al., 2011) to avoid redundancies. For early vs. late GO term analysis, genes with a z-score > 1.28 (SCDE) were used for enrichment.

5.2.5 Working with *E. coli*

5.2.5.1 Transformation of chemically competent *E. coli* with plasmid DNA

Chemically competent *E. coli* Top 10 were thawed on ice and 10 ng of plasmid DNA or 5 µl of ligation reaction was added. The suspension was carefully mixed by snapping the tube three times with a finger, followed by a 20 min incubation of the suspension on ice. Subsequently, bacteria were exposed to heat shock at 42 °C for 45 sec and immediately incubated on ice for 3 min. 1 ml of LB-medium was added and bacteria were incubated on a shaker at 150 - 200 rpm for 1 h at 37 °C. Next, 100 µl and 300 µl of the bacterial suspension were spread on ampicillin-containing agar plates (100 µg/ml) and incubated overnight upside down at 37 °C. Until further use, the plates were sealed with parafilm and stored at 4 °C.

5.2.5.2 Liquid bacteria culture

LB medium with ampicillin (100 µg/ml) was inoculated with an *E. coli* colony from an agar plate and incubated overnight at 37 °C on a shaker (150 - 200 rpm) to isolate plasmid DNA from a liquid culture. Different volumes of liquid cultures were used depending on the amount of DNA required.

5.2.6 Molecular biological methods

5.2.6.1 Agarose gel electrophoresis and gel extraction of DNA

Agarose gel electrophoresis was conducted to separate PCR products or DNA fragments after digestion using a 0.8 % agarose gel in TAE buffer. SYBR Green DNA (1x) stain was added to each agarose gel to allow visualization of DNA. Each sample was mixed with 6x loading dye and the GeneRuler DNA Ladder Mix was used as a standard for the size of DNA. DNA was visualized with blue light (λ = 488 nm) using the iBright™ CL1500 Imaging System. For DNA isolation the desired DNA band was cut out of the agarose gel with a scalpel and transferred into a 2 ml reaction tube. Subsequently, the NucleoSpin Gel and PCR clean-up Kits were used to extract the DNA according to the manufacturers' protocol.

5.2.6.2 Preparation of plasmid DNA from *E. coli*

Using the NucleoSpin Plasmid kit, plasmid DNA from *E. coli* was extracted from bacterial cells according to the manufacturer’s instructions. DNA concentration and purity were determined with a Infinite M200 Pro plate reader (Tecan) by measuring absorbance at 260 nm and 280 nm. The plasmid DNA was stored at -20 °C.

5.2.6.3 Restriction digestion and DNA ligation

Digestion of DNA with restriction enzymes was performed in the recommended/supplied buffers from New England Biolabs and Fermentas according to the conditions suggested by the manufacturers. T4 DNA ligase was used to ligate digested DNA inserts and linearized vectors (blunt or sticky-end) either for 1 h at RT or overnight at 16 °C prior to transformation.

5.2.6.4 Isopropanol precipitation of DNA

For the precipitation of DNA from aqueous solutions, an equal volume of isopropanol and 10 % 3 M sodium acetate was added. Subsequently, the suspension was mixed and centrifuged at 20,000 g and 4 °C for 20 min, followed by two wash steps of the DNA pellet with 1 ml of 70 % EtOH (20,000 g, 4 °C, 5 min). After the last wash step, the supernatant was carefully aspirated and the DNA pellet dried under sterile conditions. Finally, dried DNA was reconstituted in an appropriate amount of sterile ddH_2O (*e.g.* 10 µg in 10 µl for transfecting trypanosomes).

5.2.6.5 Polymerase chain reaction (PCR)

DNA fragments of interest were amplified from genomic or plasmid DNA by PCR using the Phusion High-Fidelity DNA Polymerase. The general conditions and programs are described below (Table 14), and all synthetic DNA oligonucleotides used are listed in Table 6. The amplified PCR products were then separated via electrophoresis and cleaned up using the NucleoSpin Gel and PCR clean-up Kit.

Table 14: PCR conditions and program

Reagents for 50 µl			
DNA template	10 - 100 ng		
Reaction buffer	10 µl		
dNTPs	1 µl (10 µM)		
Sense/antisense primer	2.5 µl each (100 µM)		
Polymerase	0.5 µl		
ddH_2O	ad 50 µl		
Program			
Step	**Time**	**Temperature**	**Cycles**
Initialization	30 sec	98 °C	1
Denaturation	30 sec	98 °C	35
Annealing	10 sec	Tm – 1 - 5 °C	
Elongation	30 sec/kbp	72 °C	
Final elongation	10 min	72 °C	1

VI. References

ACOSTA-SERRANO, A., VASSELLA, E., LINIGER, M., KUNZ RENGGLI, C., BRUN, R., RODITI, I. & ENGLUND, P. T. 2001. The surface coat of procyclic Trypanosoma brucei: programmed expression and proteolytic cleavage of procyclin in the tsetse fly. *Proc Natl Acad Sci U S A,* 98**,** 1513-8.

ADEMOKUN, A. A. & DUNN-WALTERS, D. 2010. Immune Responses: Primary and Secondary. *eLS.*

AKIYOSHI, B. & GULL, K. 2014. Discovery of unconventional kinetochores in kinetoplastids. *Cell,* 156**,** 1247-1258.

ALEXANDER, C. M., KASZA, I., YEN, C. L., REEDER, S. B., HERNANDO, D., GALLO, R. L., JAHODA, C. A., HORSLEY, V. & MACDOUGALD, O. A. 2015. Dermal white adipose tissue: a new component of the thermogenic response. *J Lipid Res,* 56**,** 2061-9.

ALFITURI, O. A., AJIBOLA, O., BREWER, J. M., GARSIDE, P., BENSON, R. A., PEEL, T., MORRISON, L. J. & MABBOTT, N. A. 2019. Effects of host-derived chemokines on the motility and viability of Trypanosoma brucei. *Parasite Immunol,* 41**,** e12609.

ALFITURI, O. A., QUINTANA, J. F., MACLEOD, A., GARSIDE, P., BENSON, R. A., BREWER, J. M., MABBOTT, N. A., MORRISON, L. J. & CAPEWELL, P. 2020. To the Skin and Beyond: The Immune Response to African Trypanosomes as They Enter and Exit the Vertebrate Host. *Front Immunol,* 11**,** 1250.

ALVAREZ, E. C., CROUZOLS, A. & ROTUREAU, B. 2021. FLAgellum Member 8 modulates extravascular trypanosome distribution in the mammalian host. *bioRxiv***,** 2021.01.08.425862.

AMIGUET-VERCHER, A., PEREZ-MORGA, D., PAYS, A., POELVOORDE, P., VAN XONG, H., TEBABI, P., VANHAMME, L. & PAYS, E. 2004. Loss of the mono-allelic control of the VSG expression sites during the development of Trypanosoma brucei in the bloodstream. *Mol Microbiol,* 51**,** 1577-88.

ANDERSON, N. E., MUBANGA, J., FEVRE, E. M., PICOZZI, K., EISLER, M. C., THOMAS, R. & WELBURN, S. C. 2011. Characterisation of the wildlife reservoir community for human and animal trypanosomiasis in the Luangwa Valley, Zambia. *PLoS Negl Trop Dis,* 5**,** e1211.

ANTOINE, E. E., VLACHOS, P. P. & RYLANDER, M. N. 2014. Review of collagen I hydrogels for bioengineered tissue microenvironments: characterization of mechanics, structure, and transport. *Tissue Eng Part B Rev,* 20**,** 683-96.

ARANGO DUQUE, G. & DESCOTEAUX, A. 2015. Leishmania survival in the macrophage: where the ends justify the means. *Curr Opin Microbiol,* 26**,** 32-40.

ARCHER, S. K., LUU, V. D., DE QUEIROZ, R. A., BREMS, S. & CLAYTON, C. 2009. Trypanosoma brucei PUF9 regulates mRNAs for proteins involved in replicative processes over the cell cycle. *PLoS Pathog,* 5**,** e1000565.

ASLAN, H., OLIVEIRA, F., MENESES, C., CASTROVINCI, P., GOMES, R., TEIXEIRA, C., DERENGE, C. A., ORANDLE, M., GRADONI, L., OLIVA, G., FISCHER, L., VALENZUELA, J. G. & KAMHAWI, S. 2016. New Insights Into the Transmissibility of Leishmania infantum From Dogs to Sand Flies: Experimental Vector-Transmission Reveals Persistent Parasite Depots at Bite Sites. *J Infect Dis,* 213**,** 1752-61.

ASLETT, M., AURRECOECHEA, C., BERRIMAN, M., BRESTELLI, J., BRUNK, B. P., CARRINGTON, M., DEPLEDGE, D. P., FISCHER, S., GAJRIA, B., GAO, X., GARDNER, M. J., GINGLE, A., GRANT, G., HARB, O. S., HEIGES, M., HERTZ-FOWLER, C., HOUSTON, R., INNAMORATO, F., IODICE, J., KISSINGER, J. C., KRAEMER, E., LI, W., LOGAN, F. J., MILLER, J. A., MITRA, S., MYLER, P. J., NAYAK, V., PENNINGTON, C., PHAN, I., PINNEY, D. F., RAMASAMY, G., ROGERS, M. B., ROOS, D. S., ROSS, C., SIVAM, D., SMITH, D. F., SRINIVASAMOORTHY, G., STOECKERT, C. J., JR., SUBRAMANIAN, S., THIBODEAU, R., TIVEY, A., TREATMAN, C.,

VELARDE, G. & WANG, H. 2010. TriTrypDB: a functional genomic resource for the Trypanosomatidae. *Nucleic Acids Res,* 38**,** D457-62.

AUTY, H., ANDERSON, N. E., PICOZZI, K., LEMBO, T., MUBANGA, J., HOARE, R., FYUMAGWA, R. D., MABLE, B., HAMILL, L., CLEAVELAND, S. & WELBURN, S. C. 2012. Trypanosome diversity in wildlife species from the serengeti and Luangwa Valley ecosystems. *PLoS Negl Trop Dis,* 6**,** e1828.

BAI, X., YAO, H., DU, C., CHEN, Y., LAI, R. & RONG, M. 2015. An immunoregulatory peptide from tsetse fly salivary glands of Glossina morsitans morsitans. *Biochimie,* 118**,** 123-8.

BARGUL, J. L., JUNG, J., MCODIMBA, F. A., OMOGO, C. O., ADUNG'A, V. O., KRUGER, T., MASIGA, D. K. & ENGSTLER, M. 2016. Species-Specific Adaptations of Trypanosome Morphology and Motility to the Mammalian Host. *PLoS Pathog,* 12**,** e1005448.

BARRETT, M. P., KYLE, D. E., SIBLEY, L. D., RADKE, J. B. & TARLETON, R. L. 2019. Protozoan persister-like cells and drug treatment failure. *Nat Rev Microbiol,* 17**,** 607-620.

BARRY, J. D. & EMERY, D. L. 1984. Parasite development and host responses during the establishment of Trypanosoma brucei infection transmitted by tsetse fly. *Parasitology,* 88 (Pt 1)**,** 67-84.

BARRY, J. D., GRAHAM, S. V., FOTHERINGHAM, M., GRAHAM, V. S., KOBRYN, K. & WYMER, B. 1998. VSG gene control and infectivity strategy of metacyclic stage Trypanosoma brucei. *Mol Biochem Parasitol,* 91**,** 93-105.

BASTOS, I. M., MOTTA, F. N., CHARNEAU, S., SANTANA, J. M., DUBOST, L., AUGUSTYNS, K. & GRELLIER, P. 2010. Prolyl oligopeptidase of Trypanosoma brucei hydrolyzes native collagen, peptide hormones and is active in the plasma of infected mice. *Microbes Infect,* 12**,** 457-66.

BATRAM, C., JONES, N. G., JANZEN, C. J., MARKERT, S. M. & ENGSTLER, M. 2014. Expression site attenuation mechanistically links antigenic variation and development in Trypanosoma brucei. *Elife,* 3**,** e02324.

BENIAS, P. C., WELLS, R. G., SACKEY-ABOAGYE, B., KLAVAN, H., REIDY, J., BUONOCORE, D., MIRANDA, M., KORNACKI, S., WAYNE, M., CARR-LOCKE, D. L. & THEISE, N. D. 2018. Structure and Distribution of an Unrecognized Interstitium in Human Tissues. *Sci Rep,* 8**,** 4947.

BENSOUILAH, J. & BUCK, P. 2006. *Aromadermatology: aromatherapy in the treatment and care of common skin conditions*, Radcliffe Publishing.

BERRIMAN, M., GHEDIN, E., HERTZ-FOWLER, C., BLANDIN, G., RENAULD, H., BARTHOLOMEU, D. C., LENNARD, N. J., CALER, E., HAMLIN, N. E., HAAS, B., BOHME, U., HANNICK, L., ASLETT, M. A., SHALLOM, J., MARCELLO, L., HOU, L., WICKSTEAD, B., ALSMARK, U. C., ARROWSMITH, C., ATKIN, R. J., BARRON, A. J., BRINGAUD, F., BROOKS, K., CARRINGTON, M., CHEREVACH, I., CHILLINGWORTH, T. J., CHURCHER, C., CLARK, L. N., CORTON, C. H., CRONIN, A., DAVIES, R. M., DOGGETT, J., DJIKENG, A., FELDBLYUM, T., FIELD, M. C., FRASER, A., GOODHEAD, I., HANCE, Z., HARPER, D., HARRIS, B. R., HAUSER, H., HOSTETLER, J., IVENS, A., JAGELS, K., JOHNSON, D., JOHNSON, J., JONES, K., KERHORNOU, A. X., KOO, H., LARKE, N., LANDFEAR, S., LARKIN, C., LEECH, V., LINE, A., LORD, A., MACLEOD, A., MOONEY, P. J., MOULE, S., MARTIN, D. M., MORGAN, G. W., MUNGALL, K., NORBERTCZAK, H., ORMOND, D., PAI, G., PEACOCK, C. S., PETERSON, J., QUAIL, M. A., RABBINOWITSCH, E., RAJANDREAM, M. A., REITTER, C., SALZBERG, S. L., SANDERS, M., SCHOBEL, S., SHARP, S., SIMMONDS, M., SIMPSON, A. J., TALLON, L., TURNER, C. M., TAIT, A., TIVEY, A. R., VAN AKEN, S., WALKER, D., WANLESS, D., WANG, S., WHITE, B., WHITE, O., WHITEHEAD, S., WOODWARD, J., WORTMAN, J., ADAMS, M. D., EMBLEY, T. M., GULL, K., ULLU, E., BARRY, J. D., FAIRLAMB, A. H., OPPERDOES, F., BARRELL, B. G., DONELSON, J. E., HALL, N., FRASER, C. M., et al. 2005. The genome of the African trypanosome Trypanosoma brucei. *Science,* 309**,** 416-22.

BERTHIER, D., BRENIERE, S. F., BRAS-GONCALVES, R., LEMESRE, J. L., JAMONNEAU, V., SOLANO, P., LEJON, V., THEVENON, S. & BUCHETON, B. 2016. Tolerance to Trypanosomatids: A Threat, or a Key for Disease Elimination? *Trends Parasitol,* 32**,** 157-168.

BRAUER, M. J., SALDANHA, A. J., DOLINSKI, K. & BOTSTEIN, D. 2005. Homeostatic adjustment and metabolic remodeling in glucose-limited yeast cultures. *Mol Biol Cell,* 16**,** 2503-17.

BRAZIULIS, E., DIEZI, M., BIEDERMANN, T., PONTIGGIA, L., SCHMUCKI, M., HARTMANN-FRITSCH, F., LUGINBUHL, J., SCHIESTL, C., MEULI, M. & REICHMANN, E. 2012. Modified plastic compression of collagen hydrogels provides an ideal matrix for clinically applicable skin substitutes. *Tissue Eng Part C Methods,* 18**,** 464-74.

BREDE, C., FRIEDRICH, M., JORDAN-GARROTE, A. L., RIEDEL, S. S., BAUERLEIN, C. A., HEINZE, K. G., BOPP, T., SCHULZ, S., MOTTOK, A., KIESEL, C., MATTENHEIMER, K., RITZ, M., VON KROSIGK, V., ROSENWALD, A., EINSELE, H., NEGRIN, R. S., HARMS, G. S. & BEILHACK, A. 2012. Mapping immune processes in intact tissues at cellular resolution. *J Clin Invest,* 122**,** 4439-46.

BREITKREUTZ, D., MIRANCEA, N. & NISCHT, R. 2009. Basement membranes in skin: unique matrix structures with diverse functions? *Histochem Cell Biol,* 132**,** 1-10.

BRIGGS, E. M., MCCULLOCH, R., MATTHEWS, K. R. & OTTO, T. D. 2020. Single cell transcriptomic analysis of bloodstream form Trypanosoma brucei reconstructs cell cycle progression and differentiation via quorum sensing. *bioRxiv***,** 2020.12.11.420976.

BRINCKMANN, J., BODO, M., BREY, M., WOLFF, H. H. & MULLER, P. K. 1994. Analysis of the age-related composition of human skin collagen and collagens synthesized by fibroblast culture. *Arch Dermatol Res,* 286**,** 391-5.

BROADHEAD, R., DAWE, H. R., FARR, H., GRIFFITHS, S., HART, S. R., PORTMAN, N., SHAW, M. K., GINGER, M. L., GASKELL, S. J., MCKEAN, P. G. & GULL, K. 2006. Flagellar motility is required for the viability of the bloodstream trypanosome. *Nature,* 440**,** 224-7.

BROWN, R. A., WISEMAN, M., CHUO, C.-B., CHEEMA, U. & NAZHAT, S. N. 2005. Ultrarapid Engineering of Biomimetic Materials and Tissues: Fabrication of Nano- and Microstructures by Plastic Compression. *Advanced Functional Materials,* 15**,** 1762-1770.

BROWN, R. C., EVANS, D. A. & VICKERMAN, K. 1973. Changes in oxidative metabolism and ultrastructure accompanying differentiation of the mitochondrion in Trypanosoma brucei. *Int J Parasitol,* 3**,** 691-704.

BRUCE, D. 1895. Preliminary Report on Tsetse Fly Disease or Nagana in Zululand. *Bennett and Davis***,** 18 pp.

BRUN, R. & BALMER, O. 2006. New developments in human African trypanosomiasis. *Curr Opin Infect Dis,* 19**,** 415-20.

BRUN, R., BLUM, J., CHAPPUIS, F. & BURRI, C. 2010. Human African trypanosomiasis. *Lancet,* 375**,** 148-59.

BUTLER, A., HOFFMAN, P., SMIBERT, P., PAPALEXI, E. & SATIJA, R. 2018. Integrating single-cell transcriptomic data across different conditions, technologies, and species. *Nat Biotechnol,* 36**,** 411-420.

CALJON, G., MABILLE, D., STIJLEMANS, B., DE TREZ, C., MAZZONE, M., TACCHINI-COTTIER, F., MALISSEN, M., VAN GINDERACHTER, J. A., MAGEZ, S., DE BAETSELIER, P. & VAN DEN ABBEELE, J. 2018. Neutrophils enhance early Trypanosoma brucei infection onset. *Sci Rep,* 8**,** 11203.

CALJON, G., VAN DEN ABBEELE, J., STERNBERG, J. M., COOSEMANS, M., DE BAETSELIER, P. & MAGEZ, S. 2006a. Tsetse fly saliva biases the immune response to Th2 and induces anti-vector antibodies that are a useful tool for exposure assessment. *Int J Parasitol,* 36**,** 1025-35.

CALJON, G., VAN DEN ABBEELE, J., STIJLEMANS, B., COOSEMANS, M., DE BAETSELIER, P. & MAGEZ, S. 2006b. Tsetse fly saliva accelerates the onset of Trypanosoma brucei infection in a mouse model associated with a reduced host inflammatory response. *Infect Immun,* 74**,** 6324-30.

CALJON, G., VAN REET, N., DE TREZ, C., VERMEERSCH, M., PEREZ-MORGA, D. & VAN DEN ABBEELE, J. 2016. The Dermis as a Delivery Site of Trypanosoma brucei for Tsetse Flies. *PLoS Pathog,* 12**,** e1005744.

CAMARA, M., SOUMAH, A. M., ILBOULDO, H., TRAVAILLE, C., CLUCAS, C., COOPER, A., KUISPOND SWAR, N. R., CAMARA, O., SADISSOU, I., CALVO ALVAREZ, E., CROUZOLS, A., BART, J. M., JAMONNEAU, V., CAMARA, M., MACLEOD, A., BUCHETON, B. & ROTUREAU, B. 2020. Extravascular dermal trypanosomes in suspected and confirmed cases of gambiense Human African Trypanosomiasis. *Clin Infect Dis*.

CANDI, E., SCHMIDT, R. & MELINO, G. 2005. The cornified envelope: a model of cell death in the skin. *Nat Rev Mol Cell Biol,* 6**,** 328-40.

CAPEWELL, P., ATKINS, K., WEIR, W., JAMONNEAU, V., CAMARA, M., CLUCAS, C., SWAR, N. K., NGOYI, D. M., ROTUREAU, B., GARSIDE, P., GALVANI, A. P., BUCHETON, B. & MACLEOD, A. 2019. Resolving the apparent transmission paradox of African sleeping sickness. *PLoS Biol,* 17**,** e3000105.

CAPEWELL, P., CREN-TRAVAILLE, C., MARCHESI, F., JOHNSTON, P., CLUCAS, C., BENSON, R. A., GORMAN, T. A., CALVO-ALVAREZ, E., CROUZOLS, A., JOUVION, G., JAMONNEAU, V., WEIR, W., STEVENSON, M. L., O'NEILL, K., COOPER, A., SWAR, N. K., BUCHETON, B., NGOYI, D. M., GARSIDE, P., ROTUREAU, B. & MACLEOD, A. 2016. The skin is a significant but overlooked anatomical reservoir for vector-borne African trypanosomes. *Elife,* 5.

CARDOSO, M. S., REIS-CUNHA, J. L. & BARTHOLOMEU, D. C. 2015. Evasion of the Immune Response by Trypanosoma cruzi during Acute Infection. *Front Immunol,* 6**,** 659.

CASAS-SANCHEZ, A. & ACOSTA-SERRANO, A. 2016. Skin deep. *Elife,* 5.

CAYLA, M., MCDONALD, L., MACGREGOR, P. & MATTHEWS, K. 2020. An atypical DYRK kinase connects quorum-sensing with posttranscriptional gene regulation in Trypanosoma brucei. *Elife,* 9.

CESTARI, I., ANSA-ADDO, E., DEOLINDO, P., INAL, J. M. & RAMIREZ, M. I. 2012. Trypanosoma cruzi immune evasion mediated by host cell-derived microvesicles. *J Immunol,* 188**,** 1942-52.

CESTARI, I. & STUART, K. 2020. The phosphoinositide regulatory network in Trypanosoma brucei: Implications for cell-wide regulation in eukaryotes. *PLoS Negl Trop Dis,* 14**,** e0008689.

CHAPPUIS, C. J., BEGUIN, S., VLIMANT, M. & GUERIN, P. M. 2013. Water vapour and heat combine to elicit biting and biting persistence in tsetse. *Parasit Vectors,* 6**,** 240.

CHEN, S. X., ZHANG, L. J. & GALLO, R. L. 2019. Dermal White Adipose Tissue: A Newly Recognized Layer of Skin Innate Defense. *J Invest Dermatol,* 139**,** 1002-1009.

CHRISTIANO, R., KOLEV, N. G., SHI, H., ULLU, E., WALTHER, T. C. & TSCHUDI, C. 2017. The proteome and transcriptome of the infectious metacyclic form of Trypanosoma brucei define quiescent cells primed for mammalian invasion. *Mol Microbiol,* 106**,** 74-92.

CHUNG, C. T., NIEMELA, S. L. & MILLER, R. H. 1989. One-step preparation of competent Escherichia coli: transformation and storage of bacterial cells in the same solution. *Proc Natl Acad Sci U S A,* 86**,** 2172-5.

CLAYTON, C. 2013. The regulation of trypanosome gene expression by RNA-binding proteins. *PLoS Pathog,* 9**,** e1003680.

CLAYTON, C. 2019. Regulation of gene expression in trypanosomatids: living with polycistronic transcription. *Open Biol,* 9**,** 190072.

CNOPS, J., DE TREZ, C., STIJLEMANS, B., KEIRSSE, J., KAUFFMANN, F., BARKHUIZEN, M., KEETON, R., BOON, L., BROMBACHER, F. & MAGEZ, S. 2015. NK-, NKT- and CD8-Derived IFNgamma Drives Myeloid Cell Activation and Erythrophagocytosis, Resulting in Trypanosomosis-Associated Acute Anemia. *PLoS Pathog,* 11**,** e1004964.

COLEY, A. F., DODSON, H. C., MORRIS, M. T. & MORRIS, J. C. 2011. Glycolysis in the african trypanosome: targeting enzymes and their subcellular compartments for therapeutic development. *Mol Biol Int,* 2011**,** 123702.

COLLER, H. A. 2011. Cell biology. The essence of quiescence. *Science,* 334**,** 1074-5.

COLLER, H. A., SANG, L. & ROBERTS, J. M. 2006. A new description of cellular quiescence. *PLoS Biol,* 4**,** e83.

COLOFF, J. L., MURPHY, J. P., BRAUN, C. R., HARRIS, I. S., SHELTON, L. M., KAMI, K., GYGI, S. P., SELFORS, L. M. & BRUGGE, J. S. 2016. Differential Glutamate Metabolism in Proliferating and Quiescent Mammary Epithelial Cells. *Cell Metab,* 23**,** 867-80.

CROSS, G. A. 1977. Antigenic variation in trypanosomes. *Am J Trop Med Hyg,* 26**,** 240-4.

CROSS, G. A., KIM, H. S. & WICKSTEAD, B. 2014. Capturing the variant surface glycoprotein repertoire (the VSGnome) of Trypanosoma brucei Lister 427. *Mol Biochem Parasitol,* 195**,** 59-73.

D'AVILA-LEVY, C. M., BOUCINHA, C., KOSTYGOV, A., SANTOS, H. L., MORELLI, K. A., GRYBCHUK-IEREMENKO, A., DUVAL, L., VOTYPKA, J., YURCHENKO, V., GRELLIER, P. & LUKES, J. 2015. Exploring the environmental diversity of kinetoplastid flagellates in the high-throughput DNA sequencing era. *Mem Inst Oswaldo Cruz,* 110**,** 956-65.

DAIGNAN-FORNIER, B. & SAGOT, I. 2011. Proliferation/quiescence: the controversial "aller-retour". *Cell Div,* 6**,** 10.

DALE, B. A., PRESLAND, R. B., LEWIS, S. P., UNDERWOOD, R. A. & FLECKMAN, P. 1997. Transient expression of epidermal filaggrin in cultured cells causes collapse of intermediate filament networks with alteration of cell shape and nuclear integrity. *J Invest Dermatol,* 108**,** 179-87.

DANIELS, J. P., GULL, K. & WICKSTEAD, B. 2010. Cell biology of the trypanosome genome. *Microbiol Mol Biol Rev,* 74**,** 552-69.

DE KONING, H. P. 2020. The Drugs of Sleeping Sickness: Their Mechanisms of Action and Resistance, and a Brief History. *Trop Med Infect Dis,* 5.

DE MENEZES, J. P., SARAIVA, E. M. & DA ROCHA-AZEVEDO, B. 2016. The site of the bite: Leishmania interaction with macrophages, neutrophils and the extracellular matrix in the dermis. *Parasit Vectors,* 9**,** 264.

DE NIZ, M., MEEHAN, G. R., BRANCUCCI, N. M. B., MARTI, M., ROTUREAU, B., FIGUEIREDO, L. M. & FRISCHKNECHT, F. 2019. Intravital imaging of host-parasite interactions in skin and adipose tissues. *Cell Microbiol,* 21**,** e13023.

DE SOUSA, K. P., ATOUGUIA, J. & SILVA, M. S. 2010. Partial biochemical characterization of a metalloproteinase from the bloodstream forms of Trypanosoma brucei brucei parasites. *Protein J,* 29**,** 283-9.

DEAN, S., MARCHETTI, R., KIRK, K. & MATTHEWS, K. R. 2009. A surface transporter family conveys the trypanosome differentiation signal. *Nature,* 459**,** 213-7.

DEITSCH, K. W., LUKEHART, S. A. & STRINGER, J. R. 2009. Common strategies for antigenic variation by bacterial, fungal and protozoan pathogens. *Nat Rev Microbiol,* 7**,** 493-503.

DEMPSEY, W. L. & MANSFIELD, J. M. 1983. Lymphocyte function in experimental African trypanosomiasis. V. Role of antibody and the mononuclear phagocyte system in variant-specific immunity. *J Immunol,* 130**,** 405-11.

DEVINE, D. V., FALK, R. J. & BALBER, A. E. 1986. Restriction of the alternative pathway of human complement by intact Trypanosoma brucei subsp. gambiense. *Infect Immun,* 52**,** 223-9.

DOBIN, A., DAVIS, C. A., SCHLESINGER, F., DRENKOW, J., ZALESKI, C., JHA, S., BATUT, P., CHAISSON, M. & GINGERAS, T. R. 2013. STAR: ultrafast universal RNA-seq aligner. *Bioinformatics,* 29**,** 15-21.

DRISKELL, R. R., JAHODA, C. A., CHUONG, C. M., WATT, F. M. & HORSLEY, V. 2014. Defining dermal adipose tissue. *Exp Dermatol,* 23**,** 629-31.

DRISKELL, R. R., LICHTENBERGER, B. M., HOSTE, E., KRETZSCHMAR, K., SIMONS, B. D., CHARALAMBOUS, M., FERRON, S. R., HERAULT, Y., PAVLOVIC, G., FERGUSON-SMITH, A. C. & WATT, F. M. 2013. Distinct fibroblast lineages determine dermal architecture in skin development and repair. *Nature,* 504**,** 277-281.

DUTTON, J. E. 1902. Preliminary note upon a trypanosome occurring in the blood of man. *Thompson Yates Lab,* Rep 4**,** 455 - 468.

DWINGER, R. H., RUDIN, W., MOLOO, S. K. & MURRAY, M. 1988. Development of Trypanosoma congolense, T vivax and T brucei in the skin reaction induced in goats by infected Glossina morsitans centralis: a light and electron microscopical study. *Res Vet Sci,* 44**,** 154-63.

ENGSTLER, M., PFOHL, T., HERMINGHAUS, S., BOSHART, M., WIEGERTJES, G., HEDDERGOTT, N. & OVERATH, P. 2007. Hydrodynamic flow-mediated protein sorting on the cell surface of trypanosomes. *Cell,* 131**,** 505-15.

ENGSTLER, M., THILO, L., WEISE, F., GRUNFELDER, C. G., SCHWARZ, H., BOSHART, M. & OVERATH, P. 2004. Kinetics of endocytosis and recycling of the GPI-anchored variant surface glycoprotein in Trypanosoma brucei. *J Cell Sci,* 117**,** 1105-15.

ERBEN, E. D. 2018. High-throughput Methods for Dissection of Trypanosome Gene Regulatory Networks. *Curr Genomics,* 19**,** 78-86.

ERBEN, E. D., FADDA, A., LUEONG, S., HOHEISEL, J. D. & CLAYTON, C. 2014. A genome-wide tethering screen reveals novel potential post-transcriptional regulators in Trypanosoma brucei. *PLoS Pathog,* 10**,** e1004178.

ESSER, K. M. & SCHOENBECHLER, M. J. 1985. Expression of two variant surface glycoproteins on individual African trypanosomes during antigen switching. *Science,* 229**,** 190-3.

FAIRBAIRN, H. & BURTT, E. 1946. The infectivity to man of a strain of Trypanosoma rhodesiense transmitted cyclically by Glossina morsitans through sheep and antelope; evidence that man requires a minimum infective dose of metacyclic trypanosomes. *Ann Trop Med Parasitol,* 40**,** 270-313.

FENG, Z., YAMATO, M., AKUTSU, T., NAKAMURA, T., OKANO, T. & UMEZU, M. 2003. Investigation on the mechanical properties of contracted collagen gels as a scaffold for tissue engineering. *Artif Organs,* 27**,** 84-91.

FERNANDES, A. P., NELSON, K. & BEVERLEY, S. M. 1993. Evolution of nuclear ribosomal RNAs in kinetoplastid protozoa: perspectives on the age and origins of parasitism. *Proc Natl Acad Sci U S A,* 90**,** 11608-12.

FERRANTE, A. & ALLISON, A. C. 1983. Alternative pathway activation of complement by African trypanosomes lacking a glycoprotein coat. *Parasite Immunol,* 5**,** 491-8.

FEY, P. 2017. Standardisation and scientific validation of a 3D full-thickness skin equivalent based on a biophysical optimised collagen hydrogel. Co-supervised Master Thesis, Julius-Maximilians-Universität Würzburg.

FINGER, T. 2016. Entwicklung eines technischen Verfahrens zur Herstellung von verdichteten Kollagenhydrogelen für *in-vitro*-Hautmodelle. Supervised Bachelor Thesis, Julius-Maximilians-Universität Würzburg.

FISCHER, A. H., JACOBSON, K. A., ROSE, J. & ZELLER, R. 2008. Hematoxylin and eosin staining of tissue and cell sections. *CSH Protoc,* 2008**,** pdb prot4986.

FISHER, R. A., GOLLAN, B. & HELAINE, S. 2017. Persistent bacterial infections and persister cells. *Nat Rev Microbiol,* 15**,** 453-464.

FLECKMAN, P., DALE, B. A. & HOLBROOK, K. A. 1985. Profilaggrin, a high-molecular-weight precursor of filaggrin in human epidermis and cultured keratinocytes. *J Invest Dermatol,* 85**,** 507-12.

FOLLY, A. J., DOREY-ROBINSON, D., HERNANDEZ-TRIANA, L. M., PHIPPS, L. P. & JOHNSON, N. 2020. Emerging Threats to Animals in the United Kingdom by Arthropod-Borne Diseases. *Front Vet Sci,* 7**,** 20.

FRANCO, J. R., CECCHI, G., PRIOTTO, G., PAONE, M., DIARRA, A., GROUT, L., SIMARRO, P. P., ZHAO, W. & ARGAW, D. 2020. Monitoring the elimination of human African trypanosomiasis at continental and country level: Update to 2018. *PLoS Negl Trop Dis,* 14**,** e0008261.

FUCHS, E. 1990. Epidermal differentiation: the bare essentials. *J Cell Biol,* 111**,** 2807-14.

FUCHS, E. & RAGHAVAN, S. 2002. Getting under the skin of epidermal morphogenesis. *Nat Rev Genet,* 3**,** 199-209.

FUGE, E. K., BRAUN, E. L. & WERNER-WASHBURNE, M. 1994. Protein synthesis in long-term stationary-phase cultures of Saccharomyces cerevisiae. *J Bacteriol,* 176**,** 5802-13.

GALLO, R. L. 2017. Human Skin Is the Largest Epithelial Surface for Interaction with Microbes. *J Invest Dermatol,* 137**,** 1213-1214.

GERDES, H. H. & PEPPERKOK, R. 2013. Cell-to-cell communication: current views and future perspectives. *Cell Tissue Res,* 352**,** 1-3.

GHORBANI, M. & FARHOUDI, R. 2018. Leishmaniasis in humans: drug or vaccine therapy? *Drug Des Devel Ther,* 12**,** 25-40.

GIBSON, W. & BAILEY, M. 2003. The development of Trypanosoma brucei within the tsetse fly midgut observed using green fluorescent trypanosomes. *Kinetoplastid Biol Dis,* 2**,** 1.

GIBSON, W., PEACOCK, L. & HUTCHINSON, R. 2017. Microarchitecture of the tsetse fly proboscis. *Parasit Vectors,* 10**,** 430.

GILL, W. P., HARIK, N. S., WHIDDON, M. R., LIAO, R. P., MITTLER, J. E. & SHERMAN, D. R. 2009. A replication clock for Mycobacterium tuberculosis. *Nat Med,* 15**,** 211-4.

GONG, S. & RUPRECHT, R. M. 2020. Immunoglobulin M: An Ancient Antiviral Weapon - Rediscovered. *Front Immunol,* 11**,** 1943.

GOODARZI, P., FALAHZADEH, K., NEMATIZADEH, M., FARAZANDEH, P., PAYAB, M., LARIJANI, B., TAYANLOO BEIK, A. & ARJMAND, B. 2018. Tissue Engineered Skin Substitutes. *Adv Exp Med Biol,* 1107**,** 143-188.

GOODWIN, L. G. 1970. The pathology of African trypanosomiasis. *Trans R Soc Trop Med Hyg,* 64**,** 797-817.

GOODWIN, L. G. 1971. Pathological effects of Trypanosoma brucei on small blood vessels in rabbit ear-chambers. *Trans R Soc Trop Med Hyg,* 65**,** 82-8.

GOPINATHAN, J. & NOH, I. 2018. Recent trends in bioinks for 3D printing. *Biomater Res,* 22**,** 11.

GORDON, R. M. & WILLETT, K. C. 1958. Studies on the deposition, migration, and development to the blood forms of trypanosomes belonging to the Trypanosoma brucei group. III. The development of Trypanosoma rhodesiense from the metacyclic forms, as observed in mammalian tissue and in culture. *Ann Trop Med Parasitol,* 52**,** 346-65.

GROEBER, F., ENGELHARDT, L., LANGE, J., KURDYN, S., SCHMID, F. F., RUCKER, C., MIELKE, S., WALLES, H. & HANSMANN, J. 2016. A first vascularized skin equivalent as an alternative to animal experimentation. *ALTEX,* 33**,** 415-422.

GROEBER, F., KAHLIG, A., LOFF, S., WALLES, H. & HANSMANN, J. 2013. A bioreactor system for interfacial culture and physiological perfusion of vascularized tissue equivalents. *Biotechnol J,* 8**,** 308-16.

GRUNFELDER, C. G., ENGSTLER, M., WEISE, F., SCHWARZ, H., STIERHOF, Y. D., MORGAN, G. W., FIELD, M. C. & OVERATH, P. 2003. Endocytosis of a glycosylphosphatidylinositol-anchored protein via clathrin-coated vesicles, sorting by default in endosomes, and exocytosis via RAB11-positive carriers. *Mol Biol Cell,* 14**,** 2029-40.

GUIMARAES-COSTA, A. B., NASCIMENTO, M. T., FROMENT, G. S., SOARES, R. P., MORGADO, F. N., CONCEICAO-SILVA, F. & SARAIVA, E. M. 2009. Leishmania amazonensis promastigotes induce and are killed by neutrophil extracellular traps. *Proc Natl Acad Sci U S A,* 106**,** 6748-53.

GUO, Y., DAI, Y., YU, H., ZHAO, S., SAMUELS, D. C. & SHYR, Y. 2017. Improvements and impacts of GRCh38 human reference on high throughput sequencing data analysis. *Genomics,* 109**,** 83-90.

HADGRAFT, J. 2001. Skin, the final frontier. *Int J Pharm,* 224**,** 1-18.

HALPRIN, K. M. 1972. Epidermal "turnover time"--a re-examination. *Br J Dermatol,* 86**,** 14-9.

HANIFFA, M., GUNAWAN, M. & JARDINE, L. 2015. Human skin dendritic cells in health and disease. *J Dermatol Sci,* 77**,** 85-92.

HAUF, L. 2019. The differentiation of metacyclic to bloodstream form trypanosomes in bioartificial human skin. Supervised Master Thesis, Julius-Maximilians-Universität Würzburg.

HEDDERGOTT, N., KRUGER, T., BABU, S. B., WEI, A., STELLAMANNS, E., UPPALURI, S., PFOHL, T., STARK, H. & ENGSTLER, M. 2012. Trypanosome motion represents an adaptation to the crowded environment of the vertebrate bloodstream. *PLoS Pathog,* 8**,** e1003023.

HELARY, C., BATAILLE, I., ABED, A., ILLOUL, C., ANGLO, A., LOUEDEC, L., LETOURNEUR, D., MEDDAHI-PELLE, A. & GIRAUD-GUILLE, M. M. 2010. Concentrated collagen hydrogels as dermal substitutes. *Biomaterials,* 31**,** 481-90.

HENDRIKS, E. F., ROBINSON, D. R., HINKINS, M. & MATTHEWS, K. R. 2001. A novel CCCH protein which modulates differentiation of Trypanosoma brucei to its procyclic form. *EMBO J,* 20**,** 6700-11.

HINES, J. C. & RAY, D. S. 2010. A mitochondrial DNA primase is essential for cell growth and kinetoplast DNA replication in Trypanosoma brucei. *Mol Cell Biol,* 30**,** 1319-28.

HIRUMI, H. & HIRUMI, K. 1989. Continuous cultivation of Trypanosoma brucei blood stream forms in a medium containing a low concentration of serum protein without feeder cell layers. *J Parasitol,* 75**,** 985-9.

HOFFMAN, R. A. 2009. Pulse width for particle sizing. *Curr Protoc Cytom,* Chapter 1**,** Unit 1 23.

HOFMANN, G. E. & HAND, S. C. 1994. Global arrest of translation during invertebrate quiescence. *Proc Natl Acad Sci U S A,* 91**,** 8492-6.

ILBOUDO, H., JAMONNEAU, V., CAMARA, M., CAMARA, O., DAMA, E., LENO, M., OUENDENO, F., COURTIN, F., SAKANDE, H., SANON, R., KABORE, J., COULIBALY, B., N'DRI, L., DIARRA, A., N'GORAN, E. & BUCHETON, B. 2011. Diversity of response to Trypanosoma brucei gambiense infections in the Forecariah mangrove focus (Guinea): perspectives for a better control of sleeping sickness. *Microbes Infect,* 13**,** 943-52.

ILICIC, T., KIM, J. K., KOLODZIEJCZYK, A. A., BAGGER, F. O., MCCARTHY, D. J., MARIONI, J. C. & TEICHMANN, S. A. 2016. Classification of low quality cells from single-cell RNA-seq data. *Genome Biol,* 17**,** 29.

INFORMAL EXPERT GROUP ON GAMBIENSE, H. A. T. R., BUSCHER, P., BART, J. M., BOELAERT, M., BUCHETON, B., CECCHI, G., CHITNIS, N., COURTIN, D., FIGUEIREDO, L. M., FRANCO, J. R., GREBAUT, P., HASKER, E., ILBOUDO, H., JAMONNEAU, V., KOFFI, M., LEJON, V., MACLEOD, A., MASUMU, J., MATOVU, E., MATTIOLI, R., NOYES, H., PICADO, A., ROCK, K. S., ROTUREAU, B., SIMO, G., THEVENON, S., TRINDADE, S., TRUC, P. & VAN REET, N. 2018. Do Cryptic Reservoirs Threaten Gambiense-Sleeping Sickness Elimination? *Trends Parasitol,* 34**,** 197-207.

JACKSON, D. G., OWEN, M. J. & VOORHEIS, H. P. 1985. A new method for the rapid purification of both the membrane-bound and released forms of the variant surface glycoprotein from Trypanosoma brucei. *Biochem J,* 230**,** 195-202.

JAMONNEAU, V., ILBOUDO, H., KABORE, J., KABA, D., KOFFI, M., SOLANO, P., GARCIA, A., COURTIN, D., LAVEISSIERE, C., LINGUE, K., BUSCHER, P. & BUCHETON, B. 2012. Untreated human infections by Trypanosoma brucei gambiense are not 100% fatal. *PLoS Negl Trop Dis,* 6**,** e1691.

JANNASCH, M., GROEBER, F., BRATTIG, N. W., UNGER, C., WALLES, H. & HANSMANN, J. 2015. Development and application of three-dimensional skin equivalents for the investigation of percutaneous worm invasion. *Exp Parasitol,* 150**,** 22-30.

JARA, M., MAES, I., IMAMURA, H., DOMAGALSKA, M. A., DUJARDIN, J. C. & AREVALO, J. 2019. Tracking of quiescence in Leishmania by quantifying the expression of GFP in the ribosomal DNA locus. *Sci Rep,* 9**,** 18951.

JELICKS, L. A., LISANTI, M. P., MACHADO, F. S., WEISS, L. M., TANOWITZ, H. B. & DESRUISSEAUX, M. S. 2013. Imaging of small-animal models of infectious diseases. *Am J Pathol,* 182**,** 296-304.

JEONG, K.-H., PARK, D. & LEE, Y.-C. 2017. Polymer-based hydrogel scaffolds for skin tissue engineering applications: a mini-review. *Journal of Polymer Research,* 24**,** 112.

JOHNSON, J. G. & CROSS, G. A. 1979. Selective cleavage of variant surface glycoproteins from Trypanosoma brucei. *Biochem J,* 178**,** 689-97.

JOHNSON, J. L., NAJOR, N. A. & GREEN, K. J. 2014. Desmosomes: regulators of cellular signaling and adhesion in epidermal health and disease. *Cold Spring Harb Perspect Med,* 4**,** a015297.

KABORE, J., KOFFI, M., BUCHETON, B., MACLEOD, A., DUFFY, C., ILBOUDO, H., CAMARA, M., DE MEEUS, T., BELEM, A. M. & JAMONNEAU, V. 2011. First evidence that parasite infecting apparent aparasitemic serological suspects in human African trypanosomiasis are Trypanosoma brucei gambiense and are similar to those found in patients. *Infect Genet Evol,* 11**,** 1250-5.

KAPLAN, D. H. 2017. Ontogeny and function of murine epidermal Langerhans cells. *Nat Immunol,* 18**,** 1068-1075.

KAUTZ-NEU, K., NOORDEGRAAF, M., DINGES, S., BENNETT, C. L., JOHN, D., CLAUSEN, B. E. & VON STEBUT, E. 2011. Langerhans cells are negative regulators of the anti-Leishmania response. *J Exp Med,* 208**,** 885-91.

KENNEDY, P. G. 2013. Clinical features, diagnosis, and treatment of human African trypanosomiasis (sleeping sickness). *Lancet Neurol,* 12**,** 186-94.

KHARCHENKO, P. V., SILBERSTEIN, L. & SCADDEN, D. T. 2014. Bayesian approach to single-cell differential expression analysis. *Nat Methods,* 11**,** 740-2.

KHORSHIDI, S., SOLOUK, A., MIRZADEH, H., MAZINANI, S., LAGARON, J. M., SHARIFI, S. & RAMAKRISHNA, S. 2016. A review of key challenges of electrospun scaffolds for tissue-engineering applications. *J Tissue Eng Regen Med,* 10**,** 715-38.

KIMARO, E. G., ABIOLA, P. M. 2021. Epidemiology and Economic Importance of African Animal Trypanosomiasis. *Combating and Controlling Nagana and Tick-Borne Diseases in Livestock.***,** 24 - 52.

KLEINE, F. K. 1909. Weitere wissenschaftliche Beobachtungen über die Entwicklung von Trypanosomen in Glossinen. *Dtsch. Medizinische Wochenschrift,* 35**,** 924 - 925.

KLOEHN, J., SAUNDERS, E. C., O'CALLAGHAN, S., DAGLEY, M. J. & MCCONVILLE, M. J. 2015. Characterization of metabolically quiescent Leishmania parasites in murine lesions using heavy water labeling. *PLoS Pathog,* 11**,** e1004683.

KOFFI, M., SOLANO, P., DENIZOT, M., COURTIN, D., GARCIA, A., LEJON, V., BUSCHER, P., CUNY, G. & JAMONNEAU, V. 2006. Aparasitemic serological suspects in Trypanosoma brucei gambiense human African trypanosomiasis: a potential human reservoir of parasites? *Acta Trop,* 98**,** 183-8.

KOHL, L., ROBINSON, D. & BASTIN, P. 2003. Novel roles for the flagellum in cell morphogenesis and cytokinesis of trypanosomes. *EMBO J,* 22**,** 5336-46.

KOLEV, N. G., RAMEY-BUTLER, K., CROSS, G. A., ULLU, E. & TSCHUDI, C. 2012. Developmental progression to infectivity in Trypanosoma brucei triggered by an RNA-binding protein. *Science,* 338**,** 1352-3.

KOLEV, N. G., RAMSDELL, T. K. & TSCHUDI, C. 2018. Temperature shift activates bloodstream VSG expression site promoters in Trypanosoma brucei. *Mol Biochem Parasitol,* 226**,** 20-23.

KOLEV, N. G., ULLU, E. & TSCHUDI, C. 2014. The emerging role of RNA-binding proteins in the life cycle of Trypanosoma brucei. *Cell Microbiol,* 16**,** 482-9.

KOZAK, R. P., MONDRAGON-SHEM, K., WILLIAMS, C., ROSE, C., PERALLY, S., CALJON, G., VAN DEN ABBEELE, J., WONGTRAKUL-KISH, K., GARDNER, R. A., SPENCER, D., LEHANE, M. J. & ACOSTA-SERRANO, A. 2021. Tsetse salivary glycoproteins are modified with paucimannosidic N-glycans, are recognised by C-type lectins and bind to trypanosomes. *PLoS Negl Trop Dis,* 15**,** e0009071.

KRAUCHI, K. & WIRZ-JUSTICE, A. 1994. Circadian rhythm of heat production, heart rate, and skin and core temperature under unmasking conditions in men. *Am J Physiol,* 267**,** R819-29.

KRUGER, T., SCHUSTER, S. & ENGSTLER, M. 2018. Beyond Blood: African Trypanosomes on the Move. *Trends Parasitol,* 34**,** 1056-1067.

KUBATA, B. K., DUSZENKO, M., KABUTUTU, Z., RAWER, M., SZALLIES, A., FUJIMORI, K., INUI, T., NOZAKI, T., YAMASHITA, K., HORII, T., URADE, Y. & HAYAISHI, O. 2000. Identification of a novel prostaglandin f(2alpha) synthase in Trypanosoma brucei. *J Exp Med,* 192**,** 1327-38.

KUHBACHER, A., HENKEL, H., STEVENS, P., GRUMAZ, C., FINKELMEIER, D., BURGER-KENTISCHER, A., SOHN, K. & RUPP, S. 2017. Central Role for Dermal Fibroblasts in Skin Model Protection against Candida albicans. *J Infect Dis,* 215**,** 1742-1752.

LACOMBE, M. L., TOKARSKA-SCHLATTNER, M., BOISSAN, M. & SCHLATTNER, U. 2018. The mitochondrial nucleoside diphosphate kinase (NDPK-D/NME4), a moonlighting protein for cell homeostasis. *Lab Invest,* 98**,** 582-588.

LACOMBLE, S., VAUGHAN, S., GADELHA, C., MORPHEW, M. K., SHAW, M. K., MCINTOSH, J. R. & GULL, K. 2010. Basal body movements orchestrate membrane organelle division and cell morphogenesis in Trypanosoma brucei. *J Cell Sci,* 123**,** 2884-91.

LAGO, M. E. L., CERQUEIRA, M. T., PIRRACO, R. P., REIS, R. L. & MARQUES, A. P. 2018. 14 - Skin in vitro models to study dermal white adipose tissue role in skin healing. *In:* MARQUES, A. P., PIRRACO, R. P., CERQUEIRA, M. T. & REIS, R. L. (eds.) *Skin Tissue Models.* Boston: Academic Press.

LANGER, R. & VACANTI, J. P. 1993. Tissue engineering. *Science,* 260**,** 920-6.

LAPORTE, D., LEBAUDY, A., SAHIN, A., PINSON, B., CESCHIN, J., DAIGNAN-FORNIER, B. & SAGOT, I. 2011. Metabolic status rather than cell cycle signals control quiescence entry and exit. *J Cell Biol,* 192**,** 949-57.

LASKAY, T., VAN ZANDBERGEN, G. & SOLBACH, W. 2003. Neutrophil granulocytes--Trojan horses for Leishmania major and other intracellular microbes? *Trends Microbiol,* 11**,** 210-4.

LAVKER, R. M. & SUN, T. T. 2000. Epidermal stem cells: properties, markers, and location. *Proc Natl Acad Sci U S A,* 97**,** 13473-5.

LE RAY, D., BARRY, J. D., EASTON, C. & VICKERMAN, K. 1977. First tsetse fly transmission of the "AnTat" serodeme of Trypanosoma brucei. *Ann Soc Belg Med Trop,* 57**,** 369-81.

LEE, S., JIN, S. P., KIM, Y. K., SUNG, G. Y., CHUNG, J. H. & SUNG, J. H. 2017. Construction of 3D multicellular microfluidic chip for an in vitro skin model. *Biomed Microdevices,* 19**,** 22.

LEE, V., SINGH, G., TRASATTI, J. P., BJORNSSON, C., XU, X., TRAN, T. N., YOO, S. S., DAI, G. & KARANDE, P. 2014. Design and fabrication of human skin by three-dimensional bioprinting. *Tissue Eng Part C Methods,* 20**,** 473-84.

LI, B. 2015. DNA double-strand breaks and telomeres play important roles in trypanosoma brucei antigenic variation. *Eukaryot Cell,* 14**,** 196-205.

LI, J., HE, A., ZHENG, J. & HAN, C. C. 2006. Gelatin and gelatin-hyaluronic acid nanofibrous membranes produced by electrospinning of their aqueous solutions. *Biomacromolecules,* 7**,** 2243-7.

LIAO, Y., SMYTH, G. K. & SHI, W. 2014. featureCounts: an efficient general purpose program for assigning sequence reads to genomic features. *Bioinformatics,* 30**,** 923-30.

LIU, B., KAMANYI MARUCHA, K. & CLAYTON, C. 2020. The zinc finger proteins ZC3H20 and ZC3H21 stabilise mRNAs encoding membrane proteins and mitochondrial proteins in insect-form Trypanosoma brucei. *Mol Microbiol,* 113**,** 430-451.

LIVINGSTONE, D. 1857. Missionary Travels and Researches in South Africa. *John Murray London,* 548.

LOH, E. Y. X., MOHAMAD, N., FAUZI, M. B., NG, M. H., NG, S. F. & MOHD AMIN, M. C. I. 2018. Development of a bacterial cellulose-based hydrogel cell carrier containing keratinocytes and fibroblasts for full-thickness wound healing. *Sci Rep,* 8**,** 2875.

LOTZ, C., SCHMID, F. F., OECHSLE, E., MONAGHAN, M. G., WALLES, H. & GROEBER-BECKER, F. 2017. Cross-linked Collagen Hydrogel Matrix Resisting Contraction To Facilitate Full-Thickness Skin Equivalents. *ACS Appl Mater Interfaces,* 9**,** 20417-20425.

LOVE, M. I., HUBER, W. & ANDERS, S. 2014. Moderated estimation of fold change and dispersion for RNA-seq data with DESeq2. *Genome Biol,* 15**,** 550.

LU, T., LI, Y. & CHEN, T. 2013. Techniques for fabrication and construction of three-dimensional scaffolds for tissue engineering. *Int J Nanomedicine,* 8**,** 337-50.

LU, W., WEI, G., PAN, W. & TABEL, H. 2011. Trypanosoma congolense Infections: Induced Nitric Oxide Inhibits Parasite Growth In Vivo. *J Parasitol Res,* 2011**,** 316067.

LUEONG, S., MERCE, C., FISCHER, B., HOHEISEL, J. D. & ERBEN, E. D. 2016. Gene expression regulatory networks in Trypanosoma brucei: insights into the role of the mRNA-binding proteome. *Mol Microbiol,* 100**,** 457-71.

MA, Y. & YATES, J. R., 3RD 2018. Proteomics and pulse azidohomoalanine labeling of newly synthesized proteins: what are the potential applications? *Expert Rev Proteomics,* 15**,** 545-554.

MABILLE, D. & CALJON, G. 2020. Inflammation following trypanosome infection and persistence in the skin. *Curr Opin Immunol,* 66**,** 65-73.

MACGREGOR, P. & MATTHEWS, K. R. 2012. Identification of the regulatory elements controlling the transmission stage-specific gene expression of PAD1 in Trypanosoma brucei. *Nucleic Acids Res,* 40**,** 7705-17.

MACGREGOR, P., SAVILL, N. J., HALL, D. & MATTHEWS, K. R. 2011. Transmission stages dominate trypanosome within-host dynamics during chronic infections. *Cell Host Microbe,* 9**,** 310-8.

MACGREGOR, P., SZOOR, B., SAVILL, N. J. & MATTHEWS, K. R. 2012. Trypanosomal immune evasion, chronicity and transmission: an elegant balancing act. *Nat Rev Microbiol,* 10**,** 431-8.

MACLEOD, E. T., MAUDLIN, I., DARBY, A. C. & WELBURN, S. C. 2007. Antioxidants promote establishment of trypanosome infections in tsetse. *Parasitology,* 134**,** 827-31.

MACOSKO, E. Z., BASU, A., SATIJA, R., NEMESH, J., SHEKHAR, K., GOLDMAN, M., TIROSH, I., BIALAS, A. R., KAMITAKI, N., MARTERSTECK, E. M., TROMBETTA, J. J., WEITZ, D. A., SANES, J. R., SHALEK, A. K., REGEV, A. & MCCARROLL, S. A. 2015. Highly Parallel Genome-wide Expression Profiling of Individual Cells Using Nanoliter Droplets. *Cell,* 161**,** 1202-1214.

MANDELL, M. A. & BEVERLEY, S. M. 2017. Continual renewal and replication of persistent Leishmania major parasites in concomitantly immune hosts. *Proc Natl Acad Sci U S A,* 114**,** E801-E810.

MARIC, D., EPTING, C. L. & ENGMAN, D. M. 2010. Composition and sensory function of the trypanosome flagellar membrane. *Curr Opin Microbiol,* 13**,** 466-72.

MARTIN, M. 2011. Cutadapt removes adapter sequences from high-throughput sequencing reads. *EMBnet. J.,* 17.

MASOPUST, D., SIVULA, C. P. & JAMESON, S. C. 2017. Of Mice, Dirty Mice, and Men: Using Mice To Understand Human Immunology. *J Immunol,* 199**,** 383-388.

MATTHEWS, K. R., TSCHUDI, C. & ULLU, E. 1994. A common pyrimidine-rich motif governs trans-splicing and polyadenylation of tubulin polycistronic pre-mRNA in trypanosomes. *Genes Dev,* 8**,** 491-501.

MAUDLIN, I., WELBURN, S. C. & MILLIGAN, P. J. 1998. Trypanosome infections and survival in tsetse. *Parasitology,* 116 Suppl**,** S23-8.

MCCULLOCH, R., VASSELLA, E., BURTON, P., BOSHART, M. & BARRY, J. D. 2004. Transformation of monomorphic and pleomorphic Trypanosoma brucei. *Methods Mol Biol,* 262**,** 53-86.

MENARD, R., TAVARES, J., COCKBURN, I., MARKUS, M., ZAVALA, F. & AMINO, R. 2013. Looking under the skin: the first steps in malarial infection and immunity. *Nat Rev Microbiol,* 11**,** 701-12.

MERTSCHING, H., WALLES, T., HOFMANN, M., SCHANZ, J. & KNAPP, W. H. 2005. Engineering of a vascularized scaffold for artificial tissue and organ generation. *Biomaterials,* 26**,** 6610-7.

MEUTER, S. & MOSER, B. 2008. Constitutive expression of CXCL14 in healthy human and murine epithelial tissues. *Cytokine,* 44**,** 248-55.

MOLL, R., DIVO, M. & LANGBEIN, L. 2008. The human keratins: biology and pathology. *Histochem Cell Biol,* 129**,** 705-33.

MOLOO, S. K. 1971. An artificial feeding technique for Glossina. *Parasitology,* 63**,** 507-12.

MOREIRA-LEITE, F. F., SHERWIN, T., KOHL, L. & GULL, K. 2001. A trypanosome structure involved in transmitting cytoplasmic information during cell division. *Science,* 294**,** 610-2.

MORKING, P. A., RAMPAZZO RDE, C., WALRAD, P., PROBST, C. M., SOARES, M. J., GRADIA, D. F., PAVONI, D. P., KRIEGER, M. A., MATTHEWS, K., GOLDENBERG, S., FRAGOSO, S. P. & DALLAGIOVANNA, B. 2012. The zinc finger protein TcZFP2 binds target mRNAs enriched during Trypanosoma cruzi metacyclogenesis. *Mem Inst Oswaldo Cruz,* 107**,** 790-9.

MUGNIER, M. R., CROSS, G. A. & PAPAVASILIOU, F. N. 2015. The in vivo dynamics of antigenic variation in Trypanosoma brucei. *Science,* 347**,** 1470-3.

MUGO, E. & CLAYTON, C. 2017. Expression of the RNA-binding protein RBP10 promotes the bloodstream-form differentiation state in Trypanosoma brucei. *PLoS Pathog,* 13**,** e1006560.

MULLER, L. S. M., COSENTINO, R. O., FORSTNER, K. U., GUIZETTI, J., WEDEL, C., KAPLAN, N., JANZEN, C. J., ARAMPATZI, P., VOGEL, J., STEINBISS, S., OTTO, T. D., SALIBA, A. E., SEBRA, R. P. & SIEGEL, T. N. 2018. Genome organization and DNA accessibility control antigenic variation in trypanosomes. *Nature,* 563**,** 121-125.

MUNOZ-ELIAS, E. J., TIMM, J., BOTHA, T., CHAN, W. T., GOMEZ, J. E. & MCKINNEY, J. D. 2005. Replication dynamics of Mycobacterium tuberculosis in chronically infected mice. *Infect Immun,* 73**,** 546-51.

MURPHY, G. F., FLYNN, T. C., RICE, R. H. & PINKUS, G. S. 1984. Involucrin expression in normal and neoplastic human skin: a marker for keratinocyte differentiation. *J Invest Dermatol,* 82**,** 453-7.

MURPHY, J. P., STEPANOVA, E., EVERLEY, R. A., PAULO, J. A. & GYGI, S. P. 2015. Comprehensive Temporal Protein Dynamics during the Diauxic Shift in Saccharomyces cerevisiae. *Mol Cell Proteomics,* 14**,** 2454-65.

MURRAY, P. J. & WYNN, T. A. 2011. Protective and pathogenic functions of macrophage subsets. *Nat Rev Immunol,* 11**,** 723-37.

NAESSENS, J., MWANGI, D. M., BUZA, J. & MOLOO, S. K. 2003. Local skin reaction (chancre) induced following inoculation of metacyclic trypanosomes in cattle by tsetse flies is dependent on CD4 T lymphocytes. *Parasite Immunol,* 25**,** 413-9.

NAJAFABADI, H. S., LU, Z., MACPHERSON, C., MEHTA, V., ADOUE, V., PASTINEN, T. & SALAVATI, R. 2013. Global identification of conserved post-transcriptional regulatory programs in trypanosomatids. *Nucleic Acids Res,* 41**,** 8591-600.

NATESAN, S. K., PEACOCK, L., MATTHEWS, K., GIBSON, W. & FIELD, M. C. 2007. Activation of endocytosis as an adaptation to the mammalian host by trypanosomes. *Eukaryot Cell,* 6**,** 2029-37.

NAUSEEF, W. M. 2007. How human neutrophils kill and degrade microbes: an integrated view. *Immunol Rev,* 219**,** 88-102.

NDE, P. N., LIMA, M. F., JOHNSON, C. A., PRATAP, S. & VILLALTA, F. 2012. Regulation and use of the extracellular matrix by Trypanosoma cruzi during early infection. *Front Immunol,* 3**,** 337.

NDUNGU, K., THUNGU, D., WAMWIRI, F., MIREJI, P., NGAE, G., GITONGA, P., MULINGE, J., AUMA, J. & THUITA, J. 2019. Route of inoculation influences Trypanosoma congolense and Trypanosoma brucei brucei virulence in Swiss white mice. *PLoS One,* 14**,** e0218441.

NIESSEN, C. M. & GOTTARDI, C. J. 2008. Molecular components of the adherens junction. *Biochim Biophys Acta,* 1778**,** 562-71.

NILSSON, D., GUNASEKERA, K., MANI, J., OSTERAS, M., FARINELLI, L., BAERLOCHER, L., RODITI, I. & OCHSENREITER, T. 2010. Spliced leader trapping reveals widespread alternative splicing patterns in the highly dynamic transcriptome of Trypanosoma brucei. *PLoS Pathog,* 6**,** e1001037.

NOLAN, D. P., ROLIN, S., RODRIGUEZ, J. R., VAN DEN ABBEELE, J. & PAYS, E. 2000. Slender and stumpy bloodstream forms of Trypanosoma brucei display a differential response to extracellular acidic and proteolytic stress. *Eur J Biochem,* 267**,** 18-27.

O'FARRELL, P. H. 2011. Quiescence: early evolutionary origins and universality do not imply uniformity. *Philos Trans R Soc Lond B Biol Sci,* 366**,** 3498-507.

OBERHOLZER, M., LANGOUSIS, G., NGUYEN, H. T., SAADA, E. A., SHIMOGAWA, M. M., JONSSON, Z. O., NGUYEN, S. M., WOHLSCHLEGEL, J. A. & HILL, K. L. 2011. Independent analysis of the flagellum surface and matrix proteomes provides insight into flagellum signaling in mammalian-infectious Trypanosoma brucei. *Mol Cell Proteomics,* 10**,** M111 010538.

OBERLE, M., BALMER, O., BRUN, R. & RODITI, I. 2010. Bottlenecks and the maintenance of minor genotypes during the life cycle of Trypanosoma brucei. *PLoS Pathog,* 6**,** e1001023.

OGBADOYI, E., ERSFELD, K., ROBINSON, D., SHERWIN, T. & GULL, K. 2000. Architecture of the Trypanosoma brucei nucleus during interphase and mitosis. *Chromosoma,* 108**,** 501-13.

ORMEROD, W. E. 1970. Pathogenesis and pathology of trypanosomiasis in man. In *The African trypanosomiases* (Mulligan, H.W. and Potts, W.H., eds). *George Allen and Unwin***,** 587 - 607.

OTIENO, L. H. & DARJI, N. 1979. The abundance of pathogenic African trypanosomes in the salivary secretions of wild Glossina pallidipes. *Ann Trop Med Parasitol,* 73**,** 583-8.

OVERATH, P. & ENGSTLER, M. 2004. Endocytosis, membrane recycling and sorting of GPI-anchored proteins: Trypanosoma brucei as a model system. *Mol Microbiol,* 53**,** 735-44.

PARSONS, M. & RUBEN, L. 2000. Pathways involved in environmental sensing in trypanosomatids. *Parasitol Today,* 16**,** 56-62.

PEACOCK, L., FERRIS, V., BAILEY, M. & GIBSON, W. 2006. Multiple effects of the lectin-inhibitory sugars D-glucosamine and N-acetyl-glucosamine on tsetse-trypanosome interactions. *Parasitology,* 132**,** 651-8.

PEACOCK, L., FERRIS, V., BAILEY, M. & GIBSON, W. 2012. The influence of sex and fly species on the development of trypanosomes in tsetse flies. *PLoS Negl Trop Dis,* 6**,** e1515.

PEREZ-MORGA, D., VANHOLLEBEKE, B., PATURIAUX-HANOCQ, F., NOLAN, D. P., LINS, L., HOMBLE, F., VANHAMME, L., TEBABI, P., PAYS, A., POELVOORDE, P., JACQUET, A., BRASSEUR, R. & PAYS, E. 2005. Apolipoprotein L-I promotes trypanosome lysis by forming pores in lysosomal membranes. *Science,* 309**,** 469-72.

PERRY, K. L., WATKINS, K. P. & AGABIAN, N. 1987. Trypanosome mRNAs have unusual "cap 4" structures acquired by addition of a spliced leader. *Proc Natl Acad Sci U S A,* 84**,** 8190-4.

PHILIPPEOS, C., TELERMAN, S. B., OULES, B., PISCO, A. O., SHAW, T. J., ELGUETA, R., LOMBARDI, G., DRISKELL, R. R., SOLDIN, M., LYNCH, M. D. & WATT, F. M. 2018. Spatial and Single-Cell Transcriptional Profiling Identifies Functionally Distinct Human Dermal Fibroblast Subpopulations. *J Invest Dermatol,* 138**,** 811-825.

PICELLI, S., BJORKLUND, A. K., FARIDANI, O. R., SAGASSER, S., WINBERG, G. & SANDBERG, R. 2013. Smart-seq2 for sensitive full-length transcriptome profiling in single cells. *Nat Methods,* 10**,** 1096-8.

POSCHL, E., SCHLOTZER-SCHREHARDT, U., BRACHVOGEL, B., SAITO, K., NINOMIYA, Y. & MAYER, U. 2004. Collagen IV is essential for basement membrane stability but dispensable for initiation of its assembly during early development. *Development,* 131**,** 1619-28.

RALSTON, K. S., LERNER, A. G., DIENER, D. R. & HILL, K. L. 2006. Flagellar motility contributes to cytokinesis in Trypanosoma brucei and is modulated by an evolutionarily conserved dynein regulatory system. *Eukaryot Cell,* 5**,** 696-711.

RAMAMOORTHI, N., NARASIMHAN, S., PAL, U., BAO, F., YANG, X. F., FISH, D., ANGUITA, J., NORGARD, M. V., KANTOR, F. S., ANDERSON, J. F., KOSKI, R. A. & FIKRIG, E. 2005. The Lyme disease agent exploits a tick protein to infect the mammalian host. *Nature,* 436**,** 573-7.

REDDERSEN, K., WIEGAND, C., ELSNER, P. & HIPLER, U. C. 2019. Three-dimensional human skin model infected with Staphylococcus aureus as a tool for evaluation of bioactivity and biocompatibility of antiseptics. *Int J Antimicrob Agents,* 54**,** 283-291.

REINITZ, D. M. & MANSFIELD, J. M. 1990. T-cell-independent and T-cell-dependent B-cell responses to exposed variant surface glycoprotein epitopes in trypanosome-infected mice. *Infect Immun,* 58**,** 2337-42.

REUTER, C., WALLES, H. & GROEBER, F. 2017. Preparation of a Three-Dimensional Full Thickness Skin Equivalent. *Methods Mol Biol,* 1612**,** 191-198.

RICHARDSON, J. B., EVANS, B., PYANA, P. P., VAN REET, N., SISTROM, M., BUSCHER, P., AKSOY, S. & CACCONE, A. 2016. Whole genome sequencing shows sleeping sickness relapse is due to parasite regrowth and not reinfection. *Evol Appl,* 9**,** 381-93.

RITTERSHAUS, E. S., BAEK, S. H. & SASSETTI, C. M. 2013. The normalcy of dormancy: common themes in microbial quiescence. *Cell Host Microbe,* 13**,** 643-51.

ROBINSON, D. R. & GULL, K. 1991. Basal body movements as a mechanism for mitochondrial genome segregation in the trypanosome cell cycle. *Nature,* 352**,** 731-3.

ROBINSON, D. R., SHERWIN, T., PLOUBIDOU, A., BYARD, E. H. & GULL, K. 1995. Microtubule polarity and dynamics in the control of organelle positioning, segregation, and cytokinesis in the trypanosome cell cycle. *J Cell Biol,* 128**,** 1163-72.

RODITI, I., SCHWARZ, H., PEARSON, T. W., BEECROFT, R. P., LIU, M. K., RICHARDSON, J. P., BUHRING, H. J., PLEISS, J., BULOW, R., WILLIAMS, R. O. & ET AL. 1989. Procyclin gene expression and loss of the variant surface glycoprotein during differentiation of Trypanosoma brucei. *J Cell Biol,* 108**,** 737-46.

RODRIGUEZ, J. A., LOPEZ, M. A., THAYER, M. C., ZHAO, Y., OBERHOLZER, M., CHANG, D. D., KISALU, N. K., PENICHET, M. L., HELGUERA, G., BRUINSMA, R., HILL, K. L. & MIAO, J. 2009. Propulsion of African trypanosomes is driven by bihelical waves with alternating chirality separated by kinks. *Proc Natl Acad Sci U S A,* 106**,** 19322-7.

ROGNONI, E., GOMEZ, C., PISCO, A. O., RAWLINS, E. L., SIMONS, B. D., WATT, F. M. & DRISKELL, R. R. 2016. Inhibition of beta-catenin signalling in dermal fibroblasts enhances hair follicle regeneration during wound healing. *Development,* 143**,** 2522-35.

ROJAS, F., SILVESTER, E., YOUNG, J., MILNE, R., TETTEY, M., HOUSTON, D. R., WALKINSHAW, M. D., PEREZ-PI, I., AUER, M., DENTON, H., SMITH, T. K., THOMPSON, J. & MATTHEWS, K. R. 2019. Oligopeptide Signaling through TbGPR89 Drives Trypanosome Quorum Sensing. *Cell,* 176**,** 306-317 e16.

ROTUREAU, B., MORALES, M. A., BASTIN, P. & SPATH, G. F. 2009. The flagellum-mitogen-activated protein kinase connection in Trypanosomatids: a key sensory role in parasite signalling and development? *Cell Microbiol,* 11**,** 710-8.

ROTUREAU, B., OOI, C. P., HUET, D., PERROT, S. & BASTIN, P. 2014. Forward motility is essential for trypanosome infection in the tsetse fly. *Cell Microbiol,* 16**,** 425-33.

ROTUREAU, B., SUBOTA, I. & BASTIN, P. 2011. Molecular bases of cytoskeleton plasticity during the Trypanosoma brucei parasite cycle. *Cell Microbiol,* 13**,** 705-16.

ROTUREAU, B., SUBOTA, I., BUISSON, J. & BASTIN, P. 2012. A new asymmetric division contributes to the continuous production of infective trypanosomes in the tsetse fly. *Development,* 139**,** 1842-50.

ROTUREAU, B. & VAN DEN ABBEELE, J. 2013. Through the dark continent: African trypanosome development in the tsetse fly. *Front Cell Infect Microbiol,* 3**,** 53.

RUBASHKIN, M. G., OU, G. & WEAVER, V. M. 2014. Deconstructing signaling in three dimensions. *Biochemistry,* 53**,** 2078-90.

RUSSELL, W. M. S. & BURCH, R. L. 1959. *The principles of humane experimental technique*, Methuen.

SAGOT, I. & LAPORTE, D. 2019. Quiescence, an individual journey. *Curr Genet,* 65**,** 695-699.

SALAZAR-ROA, M. & MALUMBRES, M. 2017. Fueling the Cell Division Cycle. *Trends Cell Biol,* 27**,** 69-81.

SANDBY-MOLLER, J., POULSEN, T. & WULF, H. C. 2003. Epidermal thickness at different body sites: relationship to age, gender, pigmentation, blood content, skin type and smoking habits. *Acta Derm Venereol,* 83**,** 410-3.

SCHANZ, J., PUSCH, J., HANSMANN, J. & WALLES, H. 2010. Vascularised human tissue models: a new approach for the refinement of biomedical research. *J Biotechnol,* 148**,** 56-63.

SCHUSTER, S., KRUGER, T., SUBOTA, I., THUSEK, S., ROTUREAU, B., BEILHACK, A. & ENGSTLER, M. 2017. Developmental adaptations of trypanosome motility to the tsetse fly host environments unravel a multifaceted in vivo microswimmer system. *Elife,* 6.

SCHUSTER, S., SUBOTA, I., LISACK, J., ZIMMERMANN, H., REUTER, C., MORRISWOOD, B. & ENGSTLER, M. 2020. Unexpected plasticity in the life cycle of Trypanosoma brucei. *bioRxiv***,** 717975.

SCHWEDE, A., JONES, N., ENGSTLER, M. & CARRINGTON, M. 2011. The VSG C-terminal domain is inaccessible to antibodies on live trypanosomes. *Mol Biochem Parasitol,* 175**,** 201-4.

SEED, J. R. & WENCK, M. A. 2003. Role of the long slender to short stumpy transition in the life cycle of the african trypanosomes. *Kinetoplastid Biol Dis,* 2**,** 3.

SEMENZA, J. C. & MENNE, B. 2009. Climate change and infectious diseases in Europe. *Lancet Infect Dis,* 9**,** 365-75.

SEVILLA, L. M., NACHAT, R., GROOT, K. R., KLEMENT, J. F., UITTO, J., DJIAN, P., MAATTA, A. & WATT, F. M. 2007. Mice deficient in involucrin, envoplakin, and periplakin have a defective epidermal barrier. *J Cell Biol,* 179**,** 1599-612.

SHARMA, R., GLUENZ, E., PEACOCK, L., GIBSON, W., GULL, K. & CARRINGTON, M. 2009. The heart of darkness: growth and form of Trypanosoma brucei in the tsetse fly. *Trends Parasitol,* 25**,** 517-24.

SHARMA, R., PEACOCK, L., GLUENZ, E., GULL, K., GIBSON, W. & CARRINGTON, M. 2008. Asymmetric cell division as a route to reduction in cell length and change in cell morphology in trypanosomes. *Protist,* 159**,** 137-51.

SHERWIN, T. & GULL, K. 1989. The cell division cycle of Trypanosoma brucei brucei: timing of event markers and cytoskeletal modulations. *Philos Trans R Soc Lond B Biol Sci,* 323**,** 573-88.

SHI, L., HU, Y., ULLAH, M. W., ULLAH, I., OU, H., ZHANG, W., XIONG, L. & ZHANG, X. 2019. Cryogenic free-form extrusion bioprinting of decellularized small intestinal submucosa for potential applications in skin tissue engineering. *Biofabrication,* 11**,** 035023.

SIEGEL, T. N., GUNASEKERA, K., CROSS, G. A. & OCHSENREITER, T. 2011. Gene expression in Trypanosoma brucei: lessons from high-throughput RNA sequencing. *Trends Parasitol,* 27**,** 434-41.

SIEGEL, T. N., HEKSTRA, D. R., KEMP, L. E., FIGUEIREDO, L. M., LOWELL, J. E., FENYO, D., WANG, X., DEWELL, S. & CROSS, G. A. 2009. Four histone variants mark the boundaries of polycistronic transcription units in Trypanosoma brucei. *Genes Dev,* 23**,** 1063-76.

SILVA, L. M., MUNOZ-CARO, T., BURGOS, R. A., HIDALGO, M. A., TAUBERT, A. & HERMOSILLA, C. 2016. Far beyond Phagocytosis: Phagocyte-Derived Extracellular Traps Act Efficiently against Protozoan Parasites In Vitro and In Vivo. *Mediators Inflamm,* 2016**,** 5898074.

SILVA PEREIRA, S., TRINDADE, S., DE NIZ, M. & FIGUEIREDO, L. M. 2019. Tissue tropism in parasitic diseases. *Open Biol,* 9**,** 190036.

SIMPSON, C. L., PATEL, D. M. & GREEN, K. J. 2011. Deconstructing the skin: cytoarchitectural determinants of epidermal morphogenesis. *Nat Rev Mol Cell Biol,* 12**,** 565-80.

SINGH, A., MINIA, I., DROLL, D., FADDA, A., CLAYTON, C. & ERBEN, E. 2014. Trypanosome MKT1 and the RNA-binding protein ZC3H11: interactions and potential roles in post-transcriptional regulatory networks. *Nucleic Acids Res,* 42**,** 4652-68.

SMITH, T. K., BRINGAUD, F., NOLAN, D. P. & FIGUEIREDO, L. M. 2017. Metabolic reprogramming during the Trypanosoma brucei life cycle. *F1000Res,* 6.

STEGNER, D., VANEEUWIJK, J. M. M., ANGAY, O., GORELASHVILI, M. G., SEMENIAK, D., PINNECKER, J., SCHMITHAUSEN, P., MEYER, I., FRIEDRICH, M., DUTTING, S., BREDE, C., BEILHACK, A., SCHULZE, H., NIESWANDT, B. & HEINZE, K. G. 2017. Thrombopoiesis is spatially regulated by the bone marrow vasculature. *Nat Commun,* 8**,** 127.

STIJLEMANS, B., CALJON, G., VAN DEN ABBEELE, J., VAN GINDERACHTER, J. A., MAGEZ, S. & DE TREZ, C. 2016. Immune Evasion Strategies of Trypanosoma brucei within the Mammalian Host: Progression to Pathogenicity. *Front Immunol,* 7**,** 233.

SUDARSHI, D., LAWRENCE, S., PICKRELL, W. O., ELIGAR, V., WALTERS, R., QUADERI, S., WALKER, A., CAPEWELL, P., CLUCAS, C., VINCENT, A., CHECCHI, F., MACLEOD, A. & BROWN, M. 2014. Human African trypanosomiasis presenting at least 29 years after infection--what can this teach us about the pathogenesis and control of this neglected tropical disease? *PLoS Negl Trop Dis,* 8**,** e3349.

SUPEK, F., BOSNJAK, M., SKUNCA, N. & SMUC, T. 2011. REVIGO summarizes and visualizes long lists of gene ontology terms. *PLoS One,* 6**,** e21800.

SZOOR, B., SILVESTER, E. & MATTHEWS, K. R. 2020. A Leap Into the Unknown - Early Events in African Trypanosome Transmission. *Trends Parasitol,* 36**,** 266-278.

TAYLOR, A. E. & GODFREY, D. G. 1968. A new organelle of bloodstream salivarian trypanosomes. *J. Protozool,* 16**,** 466 - 470.

TELLERIA, E. L., BENOIT, J. B., ZHAO, X., SAVAGE, A. F., REGMI, S., ALVES E SILVA, T. L., O'NEILL, M. & AKSOY, S. 2014. Insights into the trypanosome-host interactions revealed through transcriptomic analysis of parasitized tsetse fly salivary glands. *PLoS Negl Trop Dis,* 8**,** e2649.

TETLEY, L., TURNER, C. M., BARRY, J. D., CROWE, J. S. & VICKERMAN, K. 1987. Onset of expression of the variant surface glycoproteins of Trypanosoma brucei in the tsetse fly studied using immunoelectron microscopy. *J Cell Sci,* 87 (Pt 2)**,** 363-72.

TOMLIN, H. & PICCININI, A. M. 2018. A complex interplay between the extracellular matrix and the innate immune response to microbial pathogens. *Immunology,* 155**,** 186-201.

TRINDADE, S., RIJO-FERREIRA, F., CARVALHO, T., PINTO-NEVES, D., GUEGAN, F., ARESTA-BRANCO, F., BENTO, F., YOUNG, S. A., PINTO, A., VAN DEN ABBEELE, J., RIBEIRO, R. M., DIAS, S., SMITH, T. K. & FIGUEIREDO, L. M. 2016. Trypanosoma brucei Parasites Occupy and Functionally Adapt to the Adipose Tissue in Mice. *Cell Host Microbe,* 19**,** 837-48.

TSURUTA, D., HASHIMOTO, T., HAMILL, K. J. & JONES, J. C. 2011. Hemidesmosomes and focal contact proteins: functions and cross-talk in keratinocytes, bullous diseases and wound healing. *J Dermatol Sci,* 62**,** 1-7.

TUNGGAL, J. A., HELFRICH, I., SCHMITZ, A., SCHWARZ, H., GUNZEL, D., FROMM, M., KEMLER, R., KRIEG, T. & NIESSEN, C. M. 2005. E-cadherin is essential for in vivo epidermal barrier function by regulating tight junctions. *EMBO J,* 24**,** 1146-56.

TUR, E. 1997. Physiology of the skin--differences between women and men. *Clin Dermatol,* 15**,** 5-16.

TURNER, C. M., BARRY, J. D., MAUDLIN, I. & VICKERMAN, K. 1988. An estimate of the size of the metacyclic variable antigen repertoire of Trypanosoma brucei rhodesiense. *Parasitology,* 97 (Pt 2)**,** 269-76.

URWYLER, S., STUDER, E., RENGGLI, C. K. & RODITI, I. 2007. A family of stage-specific alanine-rich proteins on the surface of epimastigote forms of Trypanosoma brucei. *Mol Microbiol,* 63**,** 218-28.

VAN DEN ABBEELE, J., CLAES, Y., VAN BOCKSTAELE, D., LE RAY, D. & COOSEMANS, M. 1999. Trypanosoma brucei spp. development in the tsetse fly: characterization of the post-mesocyclic stages in the foregut and proboscis. *Parasitology,* 118 (Pt 5)**,** 469-78.

VAN DEN BERGH, B., FAUVART, M. & MICHIELS, J. 2017. Formation, physiology, ecology, evolution and clinical importance of bacterial persisters. *FEMS Microbiol Rev,* 41**,** 219-251.

VAN DEURSEN, F. J., SHAHI, S. K., TURNER, C. M., HARTMANN, C., GUERRA-GIRALDEZ, C., MATTHEWS, K. R. & CLAYTON, C. E. 2001. Characterisation of the growth and differentiation in vivo and in vitro-of bloodstream-form Trypanosoma brucei strain TREU 927. *Mol Biochem Parasitol,* 112**,** 163-71.

VAN MARKEN LICHTENBELT, W. D., DAANEN, H. A., WOUTERS, L., FRONCZEK, R., RAYMANN, R. J., SEVERENS, N. M. & VAN SOMEREN, E. J. 2006. Evaluation of wireless determination of skin temperature using iButtons. *Physiol Behav,* 88**,** 489-97.

VAN ZANDBERGEN, G., KLINGER, M., MUELLER, A., DANNENBERG, S., GEBERT, A., SOLBACH, W. & LASKAY, T. 2004. Cutting edge: neutrophil granulocyte serves as a vector for Leishmania entry into macrophages. *J Immunol,* 173**,** 6521-5.

VASSELLA, E., KRAMER, R., TURNER, C. M., WANKELL, M., MODES, C., VAN DEN BOGAARD, M. & BOSHART, M. 2001. Deletion of a novel protein kinase with PX and FYVE-related domains increases the rate of differentiation of Trypanosoma brucei. *Mol Microbiol,* 41**,** 33-46.

VASSELLA, E., REUNER, B., YUTZY, B. & BOSHART, M. 1997. Differentiation of African trypanosomes is controlled by a density sensing mechanism which signals cell cycle arrest via the cAMP pathway. *J Cell Sci,* 110 (Pt 21)**,** 2661-71.

VIEU, E. & RAHMOUNI, A. R. 2004. Dual role of boxB RNA motif in the mechanisms of termination/antitermination at the lambda tR1 terminator revealed in vivo. J Mol Biol, 339, 1077-87.

VIGNERON, A., O'NEILL, M. B., WEISS, B. L., SAVAGE, A. F., CAMPBELL, O. C., KAMHAWI, S., VALENZUELA, J. G. & AKSOY, S. 2020. Single-cell RNA sequencing of Trypanosoma brucei from tsetse salivary glands unveils metacyclogenesis and identifies potential transmission blocking antigens. *Proc Natl Acad Sci U S A,* 117**,** 2613-2621.

WALSHE, D. P., LEHANE, M. J. & HAINES, L. R. 2011. Post eclosion age predicts the prevalence of midgut trypanosome infections in Glossina. *PLoS One,* 6**,** e26984.

WANG, S., DRUMMOND, M. L., GUERRERO-JUAREZ, C. F., TARAPORE, E., MACLEAN, A. L., STABELL, A. R., WU, S. C., GUTIERREZ, G., THAT, B. T., BENAVENTE, C. A., NIE, Q. & ATWOOD, S. X. 2020. Single cell transcriptomics of human epidermis identifies basal stem cell transition states. *Nat Commun,* 11**,** 4239.

WARD, A. I., OLMO, F., ATHERTON, R. L., TAYLOR, M. C. & KELLY, J. M. 2020. Trypanosoma cruzi amastigotes that persist in the colon during chronic stage murine infections have a reduced replication rate. *Open Biol,* 10**,** 200261.

WATT, F. M. 2014. Mammalian skin cell biology: at the interface between laboratory and clinic. *Science,* 346**,** 937-40.

WEI, G., BULL, H., ZHOU, X. & TABEL, H. 2011. Intradermal infections of mice by low numbers of african trypanosomes are controlled by innate resistance but enhance susceptibility to reinfection. *J Infect Dis,* 203**,** 418-29.

WEINGART, J. 2018. Entwicklungsbiologische Analyse der verschiedenen Säugetierstadien von *Trypanosoma brucei brucei* AnTat 1.1. Supervised Bachelor Thesis, Julius-Maximilians-Universität Würzburg.

WHEELER, R. J. 2010. The trypanolytic factor-mechanism, impacts and applications. *Trends Parasitol,* 26**,** 457-64.

WILGUS, T. A., ROY, S. & MCDANIEL, J. C. 2013. Neutrophils and Wound Repair: Positive Actions and Negative Reactions. *Adv Wound Care (New Rochelle),* 2**,** 379-388.

WILLETT, K. C. 1956. An experiment on dosage in human trypanosomiasis. *Ann Trop Med Parasitol,* 50**,** 75-80.

WILLETT, K. C. & GORDON, R. M. 1957. Studies on the deposition, migration, and development to the blood forms of trypanosomes belonging to the Trypanosoma brucei group. II. An account of the migration of the trypanosomes from the site of their deposition in the rodent host to their appearance in the general circulation, with some observations on their probable routes of migration in the human host. *Ann Trop Med Parasitol,* 51**,** 471-92.

WILSON, K. L., FLANAGAN, K. L., PRAKASH, M. D. & PLEBANSKI, M. 2019. Malaria vaccines in the eradication era: current status and future perspectives. *Expert Rev Vaccines,* 18**,** 133-151.

WITKOWSKI, B., LELIEVRE, J., BARRAGAN, M. J., LAURENT, V., SU, X. Z., BERRY, A. & BENOIT-VICAL, F. 2010. Increased tolerance to artemisinin in Plasmodium falciparum is mediated by a quiescence mechanism. *Antimicrob Agents Chemother,* 54**,** 1872-7.

WURST, M., ROBLES, A., PO, J., LUU, V. D., BREMS, S., MARENTIJE, M., STOITSOVA, S., QUIJADA, L., HOHEISEL, J., STEWART, M., HARTMANN, C. & CLAYTON, C. 2009. An RNAi screen of the RRM-domain proteins of Trypanosoma brucei. *Mol Biochem Parasitol,* 163**,** 61-5.

XONG, H. V., VANHAMME, L., CHAMEKH, M., CHIMFWEMBE, C. E., VAN DEN ABBEELE, J., PAYS, A., VAN MEIRVENNE, N., HAMERS, R., DE BAETSELIER, P. & PAYS, E. 1998. A VSG expression site-associated gene confers resistance to human serum in Trypanosoma rhodesiense. *Cell,* 95**,** 839-46.

YANG, G., MAHADIK, B., CHOI, J. Y. & FISHER, J. P. 2020. Vascularization in tissue engineering: fundamentals and state-of-art. *Progress in Biomedical Engineering,* 2**,** 012002.

YORKE, W. 1911. A Note on the Pathology of Lesions of the Cornea and Skin in Animals Experimentally Infected with T. Rhodesiense. *Annals of Tropical Medicine & Parasitology,* 4**,** 385-394.

YUN, Y. E., JUNG, Y. J., CHOI, Y. J., CHOI, J. S. & CHO, Y. W. 2018. Artificial skin models for animal-free testing. *Journal of Pharmaceutical Investigation,* 48**,** 215-223.

ZHANG, L. J., GUERRERO-JUAREZ, C. F., HATA, T., BAPAT, S. P., RAMOS, R., PLIKUS, M. V. & GALLO, R. L. 2015. Innate immunity. Dermal adipocytes protect against invasive Staphylococcus aureus skin infection. *Science,* 347**,** 67-71.

ZIMMERMANN, H. 2020. *Antigenic variation and stumpy development in Trypanosoma brucei.*

ZIMMERMANN, H., SUBOTA, I., BATRAM, C., KRAMER, S., JANZEN, C. J., JONES, N. G. & ENGSTLER, M. 2017. A quorum sensing-independent path to stumpy development in Trypanosoma brucei. *PLoS Pathog,* 13**,** e1006324.

ZOMER, H. D. & TRENTIN, A. G. 2018. Skin wound healing in humans and mice: Challenges in translational research. *J Dermatol Sci,* 90**,** 3-12.

Supervised bachelor and master theses

FEY, P. 2017. Standardisation and scientific validation of a 3D full-thickness skin equivalent based on a biophysical optimised collagen hydrogel. Co-supervised Master Thesis, Julius-Maximilians-Universität Würzburg.

FINGER, T. 2016. Entwicklung eines technischen Verfahrens zur Herstellung von verdichteten Kollagenhydrogelen für *in-vitro*-Hautmodelle. Supervised Bachelor Thesis, Julius-Maximilians-Universität Würzburg.

HAUF, L. 2019. The differentiation of metacyclic to bloodstream form trypanosomes in bioartificial human skin. Supervised Master Thesis, Julius-Maximilians-Universität Würzburg.

WEINGART, J. 2018. Entwicklungsbiologische Analyse der verschiedenen Säugetierstadien von *Trypanosoma brucei brucei* AnTat 1.1. Supervised Bachelor Thesis, Julius-Maximilians-Universität Würzburg.

WUTSIOS, D. 2018. Klonierung und Validierung eines entwicklungsbiologischen Markers in *Trypanosoma brucei brucei* AnTat 1.1. Supervised Bachelor Thesis, Julius-Maximilians-Universität Würzburg.

VII. Annex

7.1 List of Figures

Figure 1: Anatomical properties of the human skin. 2
Figure 2: Microarchitecture of the human epidermis. 3
Figure 3: Architecture of the human dermis. 6
Figure 4: Cell architecture and cell cycle of *Trypanosoma brucei brucei*. 11
Figure 5: The life cycle of *T. brucei*. 15
Figure 6: Basic concept of tissue engineering. 25
Figure 7: Computer-assisted compression system. 31
Figure 8: Plastic compression of dermal equivalents reduces dermal shrinkage and weight loss. 34
Figure 9: High-density dermal equivalents have improved mechanical properties. 35
Figure 10: Trypanosomes and skin equivalents can be cultured with the same medium without detrimental effects. 37
Figure 11: The high-density skin equivalent resembles native human skin. 40
Figure 12: Workflow, statistics, and quality control of the single-cell RNA sequencing experiment of high-density skin equivalents. 42
Figure 13: Defining cell populations in the high-density skin equivalent using single-cell RNA sequencing. 44
Figure 14: Differential gene expression analysis of the keratinocyte subclusters. 45
Figure 15: Differential gene expression analysis of extracellular matrix-associated genes in the high-density skin equivalent. 46
Figure 16: Endothelial cells form a continuous monolayer on the basal side of the high-density skin equivalent. 48
Figure 17: Workflow to implement the high-density skin equivalent as an infection model to study the pathogenesis of African trypanosomes in mammalian skin. 49
Figure 18: The transgenic strain AnTat 1.1 tdTomato + GFP:PAD1$_{UTR}$ shows similar growth and infection kinetics as the wildtype. 53
Figure 19: Simulation of natural vector transmission by using tsetse flies to infect high-density skin equivalents with *T. brucei*. 54

Figure 20: Microscopic analysis of the skin lesion caused by the tsetse bite and the transmitted trypanosome population in the high-density skin equivalent. 56
Figure 21: Testing of an alternative clearing protocol for light sheet fluorescence microscopy. 57
Figure 22: Tsetse borne *T. brucei* parasites infect the skin equivalent. 59
Figure 23: Trypanosomes are entangled by collagen fibers and are in direct contact with dermal fibroblasts. 60
Figure 24: Tsetse-transmitted cell cycle-arrested metacyclic parasites rapidly re-enter the cell cycle and acquire a bloodstream form morphology in the skin equivalent. 62
Figure 25: Tsetse-transmitted cell cycle-arrested metacyclic parasites rapidly activate protein synthesis in the skin equivalent. 63
Figure 26: Workflow and quality control of the single-cell RNA sequencing experiment of trypanosomes. 65
Figure 27: Detection of fly-stage specific BARB-genes and principal component analysis. 67
Figure 28: Time-resolved differential gene expression analysis. 68
Figure 29: Single-parasite RNA sequencing reveals genes upregulated during skin infection. 70
Figure 30: Gene ontology reveals biological processes of trypanosomes during skin infection. 71
Figure 31: Gene ontology reveals biological processes of trypanosomes during early skin infection. 72
Figure 32: Tsetse-transmitted parasites remain at and migrate from the dermal inoculation site. 74
Figure 33: Tsetse-transmitted parasites increase their movement speed in the skin equivalent. 75
Figure 34: Skin-residing parasites can develop into stumpy forms and are infectious to tsetse flies. 77
Figure 35: Skin-dwelling parasites reversible reduce their protein synthesis during infection. 80
Figure 36: Skin-dwelling parasites reversible reduce their metabolism during infection. 81

Figure 37: The transcriptome of the quiescent forms in the skin differs from those of skin-resident parasites at 24 hpi and metacyclic forms.....83
Figure 38: Gene ontology reveals differences in several biological processes of skin-residing trypanosomes at 24 hpi and 7 dpi. 84
Figure 39: Gene ontology reveals differences in several biological processes of metacyclic forms and skin-residing trypanosomes at 7 dpi. 85
Figure 40: Metacyclic forms re-enter the cell cycle and re-acquire an AnTat 1.1 VSG coat in suspension culture. 88
Figure 41: The trypanosome population recovered from metacyclic forms cultured in suspension is developmentally competent to differentiate into stumpy forms and to re-infect tsetse flies. 89

7.2 List of tables

Table 1: Human diseases caused by arthropod-borne protozoan parasites. 7
Table 2: Media, buffers, and solutions 115
Table 3: Instruments and devices 119
Table 4: Glass/plastic ware and consumables 121
Table 5: Antibodies and dyes 122
Table 6: Synthetic DNA oligonucleotides 123
Table 7: Commercial kits 124
Table 8: Trypanosome wildtype strains 125
Table 9: Transgenic trypanosome cell lines 125
Table 10: Software 126
Table 11: Protocol for paraffin embedding 141
Table 12: Protocol for H&E staining 142
Table 13: Tissue clearing protocol for lightsheet microscopy 145
Table 14: PCR conditions and program 155

7.3 List of movies

Movie 1: Related to Figure 19. Natural transmission of *T. brucei* parasites to skin equivalents by tsetse fly. Three hdSEs were stacked on top of each other and subsequently tsetse flies with a mature salivary gland infection were allowed to bite into the stack.

Movie 2: Related to Figure 20. Skin equivalents were infected with *T. brucei* parasites by tsetse flies. Immediately after infection, the injected metacyclic trypanosomes could be detected in the dermis of the skin equivalents through their cytoplasmic expression of the fluorescent reporter tdTomato. The movie was recorded with a fluorescence stereomicroscope for 12 sec at 4 fps. Video plays at 3x speed.

Movie 3: Related to Figure 33. Tracking of trypanosomes in skin equivalents at various timepoints post-infection. Skin equivalents were infected with *T. brucei* parasites by tsetse flies and cultured for 3 days. At the times indicated individual trypanosomes were recorded using a fluorescence stereomicroscope. Movies were acquired for 5 min 20 sec at 4 fps and analyzed with Imaris software. Video plays at 20x speed.

Movie 4: Related to Figure 34. Skin-resident trypanosome at 7 dpi expressing the stumpy marker PAD1. Skin equivalents were infected with *T. brucei* parasites by tsetse flies and cultured for 7 days. The movie was recorded with a fluorescence stereomicroscope for 1 min at 4 fps. Video plays at 3x speed.

7.4 List of supplementary spreadsheets

Table S1: Related to Figures 12 - 15. scRNAseq analysis of skin equivalents.

Table S2: Related to Figures 28 - 29. scRNAseq analysis of trypanosomes.

Table S3: Related to Figure 37. scRNAseq analysis of trypanosomes.

Table S4: Related to Figures 30 - 31 and 38 - 39. GO term enrichment of trypanosomes.

Enclosed to this thesis is a USB memory stick containing all movies and spreadsheets described in this work, which belong to the corresponding figures in the text.

IX. List of Publications

Manuscripts related to this PhD thesis, which are submitted:

Reuter C., Imdahl F., Hauf L., Vafadarnejad E., Fey P., Finger T., Walles H., Saliba AE., Groeber-Becker F., Engstler M. (2021). Vector-borne *Trypanosoma brucei* parasites develop in artificial human skin and persist as skin tissue forms. *bioRxiv* 2021.05.13.443986. https://doi.org/10.1101/2021.05.13.443986

Publications associated to the present work:

Schuster S., Subota I., Lisack J., Zimmermann H., **Reuter C**., Morriswood B., Engstler M. (2020). Unexpected plasticity in the life cycle of *Trypanosoma brucei*. *bioRxiv* 717975. https://doi.org/10.1101/717975

Publications that are not part of this thesis:

Zhang Y., Zhu H., Layritz F., Luo H., Wohlfahrt T., Chen CW., Soare A., Bergmann C., Ramming A., Groeber F., **Reuter C**., Fornasini G., Soukhareva N., Schreiber B., Ramamurthy S., Amann K., Schett G., Distler JHW. (2020). Recombinant Adenosine Deaminase Ameliorates Inflammation, Vascular Disease, and Fibrosis in Preclinical Models of Systemic Sclerosis. *Arthritis Rheumatol*, 72: 1385-1395. https://doi.org/10.1002/art.41259

Reuter C., Oelschlaeger TA. (2018). Enhancement of Mucus Production in Eukaryotic Cells and Quantification of Adherent Mucus by ELISA. *Bio-protocol*, 8(12): e2879. DOI: 10.21769/BioProtoc.2879.

Reuter C., Alzheimer M., Walles H., Oelschlaeger TA. (2018). An adherent mucus layer attenuates the genotoxic effect of colibactin. *Cellular Microbiology*, 20(2): e12812. https://doi.org/10.1111/cmi.12812

Reuter C., Walles H., Groeber F. (2017). Preparation of a Three-Dimensional Full Thickness Skin Equivalent. *In: Koledova Z. (eds) 3D Cell Culture. Methods in Molecular Biology*, vol 1612. Humana Press, New York, NY. https://doi.org/10.1007/978-1-4939-7021-6_14

Jacobs GB., Bock S., Schuch A., Moschall R., Schrom EM., Zahn J., **Reuter C**., Preiser W., Rethwilm A., Engelbrecht S., Kerkau T., Bodem J. (2012). Construction of a High Titer Infectious HIV-1 Subtype C Proviral Clone from South Africa. *Viruses*, 4, no. 9: 1830-1843. https://doi.org/10.3390/v4091830

X. Acknowledgment

Finally, I would like to thank all the people, who contributed with their expertise, time, and energy to the completion of this thesis.

First, I would like to express my sincere gratitude to my supervisors, Markus Engstler, Heike Walles, and Florian Groeber-Becker. Also, I thank Prof. Dr. Markus Sauer for chairing the doctoral committee and the defense of this thesis.

Thank you, Markus, for your mentorship, encouragement, and valuable suggestions through the course of the study. You gave me the opportunity to perform this work in an inspiring academic environment, with the freedom to design and carry out the project independently, and to improve my scientific thinking and experimental skills. Thank you for your support and trust, it's been a pleasure.

I am also very grateful to Heike. You already supported me during my master thesis with your expertise as second supervisor and introduced me to the fantastic world of tissue engineering. Thank you for your support over all these years.

Florian you have warmly welcomed me into your group and introduced me to the field of skin tissue engineering. Thank you for your continuous support, encouragement, and motivation.

Many thanks go to Emmanuel Saliba and his group for the great as well as successful collaboration. Thank you for giving me the opportunity to work in your lab and introducing me to the world of single-cell RNA sequencing.

I would like to thank all the current and previous members of the Chair of Cell and Developmental Biology for their support and for creating a friendly working atmosphere. Thank you for an incredible time, the moral and practical support during my thesis, and a lot of good discussions, talks and laughs in the lab. Thanks to the Mensa crew, I was always well fed. Special thanks to Ines, Tim, and Brooke for their support and the tsetse fly team for the fantastic teamwork (...the flies want to be pampered even on holidays). Many thanks also to the people who kept the lab running: Reinhild, Kathrin, Beate, Elisabeth, Silke, Isabell, Conny, Elina, Lidia and of course Uli, Manu, and Patrick.

Many thanks to all past and present members of the Chair of Tissue Engineering and the Fraunhofer ISC for having a great time. Special thanks to the 'Hautgruppe' and the 'Werkstatt' for your support, critical feedback, and putting my thoughts on the compression reactor into practice.

Thanks also to my talented students Tamara, Philipp, Julia, Doro, Elizabeth, and Laura who made a great contribution to many projects with their interest and hard work.

I am particularly grateful to Marie and Stephan for proofreading this thesis, their critical comments, and helpful suggestions.

I would also like to thank the *Graduate School of Life Sciences* and the research training group GRK 2157 (3D tissue models for studying microbial infections by human pathogens) for providing a structured doctoral program and for enabling the participation at diverse workshops and conferences.

Neben der Arbeit bin ich auch meiner Freundin Marie und meinen Freunden unendlich dankbar, vor allem für die wunderbare gemeinsame Freizeit, welche für die nötige Balance und Würze im Leben sorgt.

Meiner Familie, insbesondere meinen Eltern, möchte ich für die Unterstützung und euer Vertrauen in all den Jahren danken. Ihr habt mir immer die Freiheit gelassen, selbst zu entscheiden und meinen eigenen Weg zu gehen.